Cover Page

Universiteit Leiden

The handle http://hdl.handle.net/1887/32207 holds various files of this Leiden University dissertation

Author: Ording-Wenker, Erica
Title: Biomimetic redox reactions of the Cu(II) μ-thiolate complex
Issue Date: 2015-03-11

Biomimetic Redox Reactions of the Cu^{II} μ-Thiolate Complex

PROEFSCHRIFT

ter verkrijging van
de graad van Doctor aan de Universiteit Leiden,
op gezag van Rector Magnificus Prof. mr. C. J. J. M. Stolker,
volgens besluit van het College voor Promoties
te verdedigen op woensdag 11 maart 2015
klokke 15.00 uur

door

Erica Cecilia Maria Ording-Wenker
geboren te Hoorn in 1986

Samenstelling Promotiecommissie

Promotor	Prof. dr. E. Bouwman
Overige leden	Prof. dr. K. D. Karlin (John Hopkins University, USA)
	Prof. dr. F. Meyer (Georg-August-University Göttingen, Germany)
	Prof. dr. B. de Bruin (Universiteit van Amsterdam)
	Prof. dr. J. Brouwer (Universiteit Leiden)

This work has been financially supported by the National Graduate School Combination NRSC-Catalysis, a joint activity of the graduate schools NIOK, HRSMC and EPL.

Printed by Ridderprint BV
Cover design by Menno Heijna

Table of Contents

List of Abbreviations..... 7

Chapter 1 Introduction..... 9

Chapter 2 Thermodynamics of the Cu^{II} μ-Thiolate and Cu^{I} Disulfide Equilibrium: A Combined Experimental and Theoretical Study..... 27

Chapter 3 Protonation of the Biologically Relevant Cu^{II} μ-Thiolate Complex: Ligand Dissociation or Formation of a Protonated Cu^{I} Disulfide Species?..... 53

Chapter 4 Cu^{I} Thiolate Reactivity with Dioxygen: The Formation of Cu^{II} Sulfinate and Cu^{II} Sulfonate Species via a Cu^{II} μ-Thiolate Intermediate..... 75

Chapter 5 Coordination of New Disulfide Ligands to Cu^{I} and Cu^{II}: Does a Cu^{II} μ-Thiolate Complex Form?..... 97

Chapter 6 The Study of Cu^{II} Phenolate Redox Chemistry..... 119

Chapter 7 Showing the Similarity Between Cu^{II} μ-Oxo and Cu^{II} μ-Thiolate species by Catalytic Catechol Oxidation..... 137

Chapter 8 Summary, Conclusions & Outlook..... 165

Appendix I: Supplementary Information for Chapter 2..... 173
Appendix II: Supplementary Information for Chapter 3..... 183
Appendix III: Supplementary Information for Chapter 4..... 189
Appendix IV: Supplementary Information for Chapter 5..... 193
Appendix V: Supplementary Information for Chapter 6..... 201
Appendix VI: Supplementary Information for Chapter 7..... 205

Samenvatting (Summary in Dutch)..... 213
Samenvatting voor Niet-Chemici..... 219
List of Publications..... 225
Curriculum Vitae..... 226

List of Abbreviations

3,5-DTBC	3,5-di-*tert*-butylcatechol
3,5-DTBQ	3,5-di-*tert*-butyl-*o*-benzoquinone
a.u.	arbitrary units
Ac	acetyl
atm	atmosphere (1 atm = 101 325 Pa)
ATP	adenosine triphosphate
Bu	butyl
C*c*O	cytochrome c oxidase
Cys	cysteine
d	doublet
DCM	dichloromethane
DFT	density functional theory
DIPEA	N,N-diisopropylethylamine
ESI	electrospray ionization
Glu	glutamic acid
His	histidine
hr	hour
IR	infrared
J	coupling constant
LMCT	ligand-to-metal charge transfer
m	multiplet (NMR); medium (IR)
min	minutes
Me	methyl
Met	methionine
MLCT	metal-to-ligand charge transfer
NMR	nuclear magnetic resonance
MS	mass spectrometry
o	ortho
OTf	trifluoridomethanesulfonate
p	para
Ph	phenyl
Py	2-pyridyl
ppm	parts per million
RT	room temperature
s	singlet (NMR); strong (IR)
t	triplet
THF	tetrahydrofuran
TOF	turnover frequency
TPA	tris(2-pyridylmethyl)amine
Ts	4-toluenesulfonyl
Tyr	tyrosine
UV	ultra-violet
vs	very strong
w	weak

Chapter 1

Introduction

The active sites of copper proteins (Type-1, Type-2, Type-3, Cu_A, Cu_B and Cu_Z) are briefly discussed. An overview of synthetic models that mimic the Cu_A site is provided. Related to the synthetic models for the Cu_A site is the redox isomerization reaction between Cu^{II} μ-thiolate and Cu^{I} disulfide species. The redox interconversion of these copper complexes is described in detail including the different reported ways to exert control over this equilibrium. At the end of the chapter a short overview of the contents of this thesis is given.

1.1 Introduction

Biological systems contain many different enzymes that are able to catalyze reactions very fast and very efficiently. A large number of proteins possess one or more copper ions in their active site to catalyze reactions such as electron transfer and oxidation of organic substrates.[1] To understand in what way these processes can be so effective, synthetic models are used to gain more insight into how these reactions take place within the enzyme and to see whether we can learn from them for other catalytic processes. Study of these models allows for a closer look at the coordination chemistry that is involved in relation to the activity of the enzyme. Model studies have for instance contributed significantly to the understanding of dioxygen activation by copper proteins.[2, 3]

Copper proteins are classified into groups based on the structure of their active sites. In this chapter, the Type-1, Type-2, Type-3, Cu_A, Cu_B and Cu_Z active sites (Figure 1.1) are briefly discussed. Furthermore, an overview of reported synthetic models for the Cu_A site and the related equilibrium between Cu^{II} thiolate and Cu^{I} disulfide species is provided.

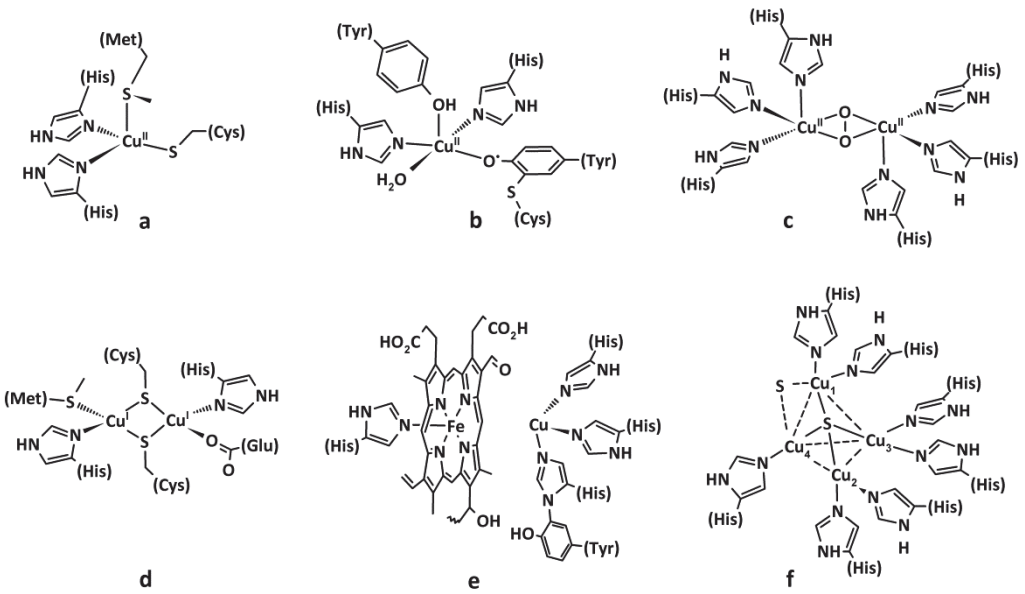

Figure 1.1: Schematic representation of the active sites of the copper proteins (a) plastocyanin (Type-1), (b) galactose oxidase (Type-2), (c) *oxy* hemocyanin (Type-3), (d) cytochrome *c* oxidase (Cu_A site), (e) cytochrome *c* oxidase (Cu_B site) and (f) N_2O reductase (Cu_Z site).

1.2 Copper proteins

1.2.1 Type-1 active site

Type-1 copper proteins are involved in electron-transfer processes and are found in mononuclear proteins such as azurin, amicyanin and plastocyanin (Figure 1.1a), but also in multicopper enzymes like ascorbate oxidase and nitrite reductase.[4] These proteins have an intense blue color due to the absorption band around 600 nm (ε = 5000 M^{-1} cm^{-1}; $Cu^{II} \leftarrow S_{cys}$ LMCT),[5] which is why these proteins are also called "blue copper proteins". These proteins are also characterized by their ground-state EPR signal, which has a unique small hyperfine coupling ($A_{\parallel} \approx 63 \times 10^{-4}$ cm^{-1}). The Cu^{II} ion in the active site has a distorted tetrahedral geometry, which comprises one equatorial, strongly coordinated S(Cys) residue (~2.1 Å), two N(His) ligands and one weakly coordinated axial ligand which is S(Met) in most cases, but can also be an oxygen of glutamine or leucine.

1.2.2 Type-2 active site

Type-2 copper proteins are often called "normal copper proteins", because the proteins lack distinctive spectroscopic features and have EPR features similar to 'common' Cu^{II} complexes containing an N,O chromophore with tetragonal geometry.[6, 7] The coordination sphere of the copper ion in the active site of these proteins consists of four N and/or O donors atoms in a square-pyramidal geometry. The open equatorial coordination position is usually filled by a water molecule. These proteins are predominantly involved in oxidation and oxygenation reactions in enzymes such as galactose oxidase (Figure 1.1b), Cu/Zn superoxide dismutase, amine oxidase and dopamine β-hydroxylase.[1]

1.2.3 Type-3 active site

This class of proteins comprises the enzymes hemocyanin, tyrosinase and catechol oxidase. These enzymes have an active site that contains two copper centers that can reversibly bind dioxygen in ambient conditions.[1] When dioxygen is bound to the enzyme (Figure 1.1c), the Cu^{II} ions are in such close proximity to each other, that they are anti-ferromagnetically coupled and are therefore EPR silent. Hemocyanin is an oxygen-transport protein in arthropods and mollusks, whereas tyrosinase and catechol oxidase bind dioxygen to oxidize phenolic substrates to catechol (tyrosinase) and successively to *o*-quinones (tyrosinase and catechol oxidase), which are then further used for the production of the pigment melanin. The catalytic mechanism by which catechol oxidase oxidizes *o*-bishydroxyarenes to *o*-quinones is still not

completely clarified,[8] but a schematic representation of the catalytic cycle that fits structural, spectroscopic and biochemical data is shown in Figure 1.2.[9]

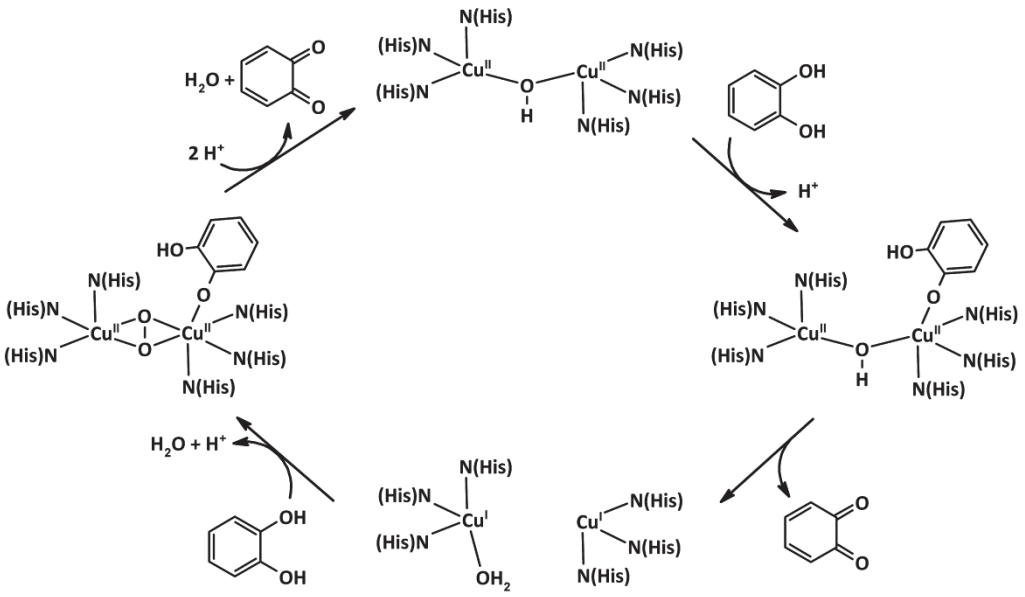

Figure 1.2: Catalytic cycle for the oxidation of catechol by catechol oxidase proposed by Sacchetini et.al.[9]

1.2.4 The Cu_A active site

Like the blue copper proteins, the Cu_A site is involved in electron transfer.[10] The Cu_A site shuttles electrons by varying the oxidation state of one of the two copper centers between Cu^I and Cu^{II} giving a formal oxidation state of $Cu^{1.5}$ in the oxidized state. The two copper ions are bridged by two cysteine thiolate moieties that together form a planar $Cu_2S(Cys)_2$ core with a Cu-Cu distance of ~2.44 Å in the oxidized $Cu^{1.5}Cu^{1.5}$ form and ~2.51 Å in the reduced form.[11] This indicates that there is a bond between the two copper centers, which was the first example of a metal-metal bond in nature.[12] The one-electron reduction of the Cu_A site results in only minor changes in the Cu_2S_2 core giving a slight increase of the Cu-S(Cys) bond from 2.3 Å to 2.33 Å. The Cu-S-Cu bond angles remain unchanged at 65°, which implies that only very low reorganizational energy is needed during electron transfer. Besides coordination to the two S(Cys) residues, each copper ion is coordinated to N(His) and either an S(Met) or a backbone peptide O (from Glu in C_cO and from Trp in N_2O reductase) (Figure 1.1d). The mixed-valence Cu_A site has a purple color and has a seven-line

hyperfine EPR pattern indicating delocalization of the unpaired electron over both copper centers.[13, 14] The Cu_A site is found in cytochrome *c* oxidase (C_cO)[15-17] and N_2O reductase.[18]

1.2.5 The Cu_B active site

In mitochondrial C_cO the electrons enter the Cu_A site (discussed in section 1.2.4) from cytochrome *c*, after which they are passed to the low-spin heme *a* center and subsequently to the high-spin heme a_3/Cu_B center. At this site, the electrons are used for the reduction of dioxygen to water, while generating a transmembrane proton pump that drives the synthesis of ATP.[19, 20] The heme a_3/Cu_B active site belongs to one (Type-A) of the three types of heme-copper oxidases and is the most well studied. The other two types are called Type-B and Type-C oxidases and have a similar active site, but differ in the subunit(s) surrounding the active site.[1, 21] The Cu_B site is located close to the iron center of the heme (~4.3 - 5.4 Å) and is coordinated to three N(His) residues with a vacant site directed towards the coordination sphere of the iron center (Figure 1.1e). Dioxygen is thought to bind between the copper center and the iron center.[22] The tyrosine residue that is covalently linked to a coordinating histidine residue plays a role in the dioxygen reduction.[23-25]

1.2.6 The Cu_Z active site

The Cu_Z active site comprises a tetranuclear copper cluster, which is found in N_2O reductase where it receives electrons from the Cu_A site (discussed in section 1.2.4) for the reduction of N_2O to N_2 and H_2O.[18, 26] The copper cluster is coordinated to seven N(His) residues and two sulfur ions, of which one is bridging all four copper ions (Figure 1.1f).[27] The catalytically active form contains four Cu^I ions. This form coordinates N_2O more easily than the Cu_Z resting state ($Cu^I_3Cu^{II}$).[28, 29]

1.3 Modeling of the Cu_A site

To gain a better understanding of how the rapid electron transfer within the Cu_A site occurs, synthetic models containing copper and bridging thiolate moieties have been designed. The synthesis of Cu^{II} thiolate complexes is complicated by the generally occurring redox reaction in which Cu^{II} is reduced to Cu^I,[30] as shown in equation (1).

$$2\ Cu^{II} + 2\ LS^- \rightarrow 2\ Cu^I + LSSL \qquad (1)$$

It is even more challenging to obtain a dinuclear copper μ-thiolate complex with a $Cu^{1.5}Cu^{1.5}$ oxidation state. Attempts initially led to the synthesis of mononuclear dithiolate Cu^{II} complexes,[31] mixed-valent multicopper complexes containing thiolate bridges,[32-34] dinuclear Cu^{II} complexes containing one thiolate bridge[35] and dinuclear Cu^{I} dithiolate complexes.[36, 37] The dinuclear Cu^{I} μ-thiolate complexes often contain a planar $Cu^{I}_2S_2$ core, like the Cu_A site, with a Cu-Cu distance that can be as small as 2.6 Å.[38, 39] An attempt has been made to oxidize a phenanthroline $Cu^{I}_2S_2$ complex to its mixed-valent state, but the oxidation showed irreversible behavior, although it was possible to form a mixed-valent $Cu^{0}Cu^{I}$ complex by electrochemical reduction.[39]

In 1995, the first dinuclear Cu^{II} dithiolate complex, depicted in Figure 1.3a, was reported by Tolman et.al.[40] Similar to the Cu_A site, this complex has Cu-S distances of ~2.33 Å, but the Cu-Cu distance is much larger with a distance of 3.34 Å. The Cu_2S_2 core has a 'butterfly' structure (Figure 1.3a), characterized by a 146.5° angle between the S-Cu-S planes. The complex displays intense UV-vis bands at 274, 338, 382 and 676 nm in methanol and is EPR-silent due to the anti-ferromagnetic coupling between the two Cu^{II} centers. Reduction to its mixed-valent state was not possible and only irreversible reductions were found with cyclic voltammetry. When the complex was dissolved in acetonitrile, an axial Cu^{II} EPR signal was observed indicating the formation of mononuclear species.

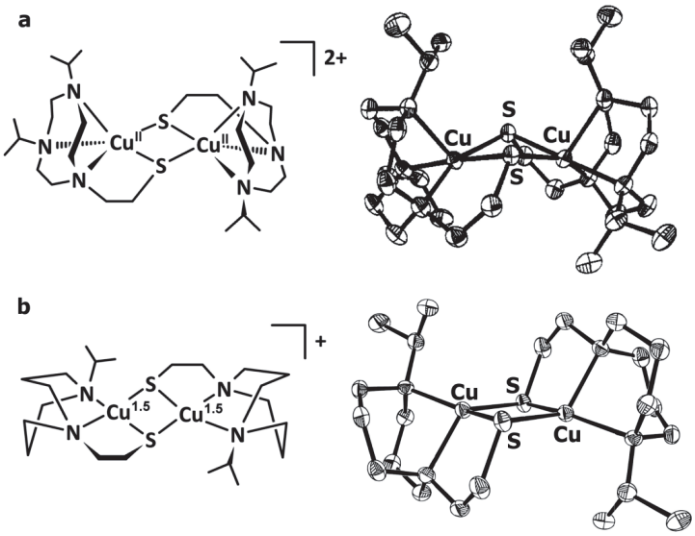

Figure 1.3: Schematic representations and displacement ellipsoid plots (50% probability level) of the cationic parts of (a) the Cu^{II} μ-thiolate complex and (b) $Cu^{1.5}$ μ-thiolate complex published by Tolman et.al.[40, 41] Hydrogen atoms are omitted for clarity.

After publication of the first Cu^{II} μ-thiolate complex, a number of dinuclear Cu^{II} thiolate complexes has been published with different ligands all containing additional nitrogen donors.[42-53] The Cu-Cu distance varies greatly from 2.65 Å[45] to 3.80 Å[53] and in most cases a similar 'butterfly' structure as in the Tolman Cu^{II} thiolate complex is observed (Figure 1.3a). An exception is the Cu^{II} μ-thiolate complex containing a pincer ligand, which has a planar Cu_2S_2 structure.[53]

The first $Cu^{1.5}Cu^{1.5}$ μ-thiolate complex was published one year after the first Cu^{II} thiolate structure.[41] The ligand used to obtain this complex is similar to the ligand in the Cu^{II} thiolate structure, except that it has one nitrogen donor less, generating four-coordinate Cu^{II} centers, similar to the Cu_A site (Figure 1.3b). The mixed-valent complex was synthesized from Cu^{II} and an excess of thiolate ligand, which was partially oxidized during the synthesis as shown in equation (2).

$$6\ LS^- + 4\ Cu^{II} \rightarrow 2\ [Cu^{1.5}{}_2(LS)_2]^+ + LSSL \qquad (2)$$

The mixed-valent complex shows more similarities to the Cu_A site than the Cu^{II} thiolate complexes. The Cu_2S_2 core is planar, with a Cu-Cu distance of 2.92 Å and the complex has an EPR signal consistent with a fully delocalized unpaired electron, as observed for the Cu_A resting state. The UV-vis absorption bands are slightly red-shifted and much less intense than those of the Cu_A site, possibly due to the larger Cu-Cu distance and the differences in donor atoms. Unfortunately, the system does not reproduce the reversible $Cu^ICu^I/Cu^{1.5}Cu^{1.5}$ redox behavior. In a more recent report the structures of both a Cu^ICu^I and $Cu^{1.5}Cu^{1.5}$ complex with the same ligand are discussed (Figure 1.4).[54] Both complexes are stable under inert atmosphere and can be inter-converted electrochemically, although oxidation to the $Cu^{II}Cu^{II}$ state results in complex decomposition. The dinuclear Cu^I complex is formed by a reaction of the precursor dithiolate ligand with dichloromethane, as shown in equation (3); the complex is oxidized with the mild oxidizing agent 4-bromobenzenediazonium tetrafluoridoborate to yield the $Cu^{1.5}Cu^{1.5}$ species.

$$2\ {}^-SLS^- + 2\ Cu^I + CH_2Cl_2 \rightarrow Cu^I{}_2(SLS\text{-}CH_2\text{-}SLS) + 2\ Cl^- \qquad (3)$$

Upon one-electron oxidation of the Cu^ICu^I species the Cu-Cu distance increases from 2.64 Å to 2.93 Å, cleaving the Cu-Cu bond, and flattening the 'butterfly' structure from a 153.1° angle to a 173.0° angle between the S-Cu-S planes (Figure 1.4).

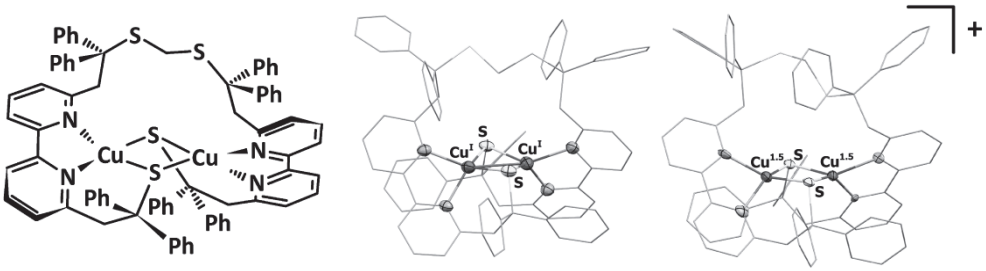

Figure 1.4: Schematic representation and projections of the cationic parts of the Cu^{II} μ-thiolate complex and $Cu^{1.5}$ μ-thiolate complex published by Duboc et.al.[54] Displacement ellipsoids are depicted at the 50% probability level. All hydrogen atoms are omitted, and a large part of the ligand is depicted in wireframe for clarity.

The $Cu^{1.5}Cu^{1.5}$ species has a purple color and shows the EPR signature of an unpaired electron delocalized over two copper centers. The electron self-exchange rate constant of the $Cu^{I}Cu^{I}/Cu^{1.5}Cu^{1.5}$ redox couple was measured to be k = 1.37(2) x 10^6 L mol^{-1} s^{-1},[55] which is faster than that of the Type-1 copper protein plastocyanin (k = 1.5 x 10^5 L mol^{-1} s^{-1}), but slower than that of the Cu_A site (k = 2.2 x 10^8 L mol^{-1} s^{-1}). According to the authors this is due to the cleavage of the Cu-Cu bond upon oxidation.
To date there is only one other report of a $Cu^{1.5}Cu^{1.5}$ complex, containing N-heterocyclic carbene ligands.[56] This species was only characterized in solution.

1.4 Cu^{II} thiolate and Cu^{I} disulfide equilibrium

1.4.1 General introduction

Research directed towards the synthesis of dinuclear Cu^{I}, $Cu^{1.5}$ and Cu^{II} thiolate complexes and their interconversion for mimicking the Cu_A site (section 1.3), has led to the discovery of a redox equilibrium. The redox reaction in which Cu^{II} and thiolate ligands are converted to Cu^{I} and disulfide ligands shown in equation 1, can also occur in the opposite direction depending on the ligand and the reaction conditions. Depending on the ligand set either a dinuclear Cu^{II} μ-thiolate or a Cu^{I} disulfide species can be formed and these species can be in equilibrium with each other. When the Cu^{I} disulfide complexes are converted to the Cu^{II} thiolate species a redox reaction takes place in which the electrons from the sulfur atoms are relocated, thus cleaving the S-S bond to form bridging thiolates and generating Cu^{II} ions. Because this reaction takes place intramolecularly the Cu^{II} thiolate and Cu^{I} disulfide species have the same charge, but different spectroscopic properties which makes it possible to distinguish

between both species. A schematic representation of this equilibrium is shown in Figure 1.5.

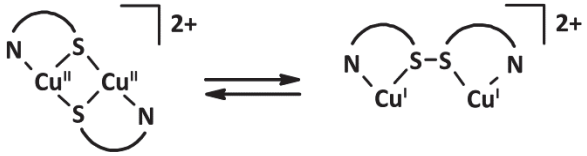

Figure 1.5: Schematic representation of the equilibrium between dinuclear Cu^{II} μ-thiolate and Cu^{I} disulfide complexes and their synthesis.

Investigating the Cu^{II} thiolate/Cu^{I} disulfide redox-equilibrium might provide a better understanding of the copper-sulfur redox reactions occurring in natural systems. Both species are more easily synthesized, compared to the rare mixed-valent $Cu^{1.5}$ complexes, giving the opportunity to study copper complexes with many different ligands. Furthermore, this equilibrium might provide information about other biologically occurring thiolate-disulfide reactions, involving molecules like cysteine and glutathione, that are tuned by the presence of a metal center.[57] For instance, the delivery of copper to the Cu_A site by Sco proteins is thought to occur by such a copper thiolate/disulfide conversion.[58-60] To get more information about the equilibrium it is necessary to be able to regulate the conversion in a controllable manner. This can be accomplished by changing the ligand or the reaction conditions.

1.4.2 Ligand-dependent conversion

The first paper to report both dinuclear Cu^{II} μ-thiolate and Cu^{I} disulfide species with a similar ligand was published in 2001.[46] It was shown that small structural changes in the ligand shift the formation of a Cu^{II} μ-thiolate species (**A**), to two different Cu^{I} disulfide complexes: a Cu^{I} *transoid*-disulfide species (**B**) and a Cu^{I} *cisoid*-disulfide species (**C**). A schematic overview of the complex syntheses starting from a disulfide ligand and two equivalents of Cu^{I} is shown in Figure 1.6.

The three different geometries were confirmed by X-ray structure determination. The Cu^{II} μ-thiolate complex is similar in geometry to other bis(μ-thiolato)dicopper(II) complexes with a Cu-Cu distance of 2.96 Å and a 'butterfly' structure with a 126.9° angle between the S-Cu-S planes. A small change in the R-groups of the ligand results in completely different geometries.

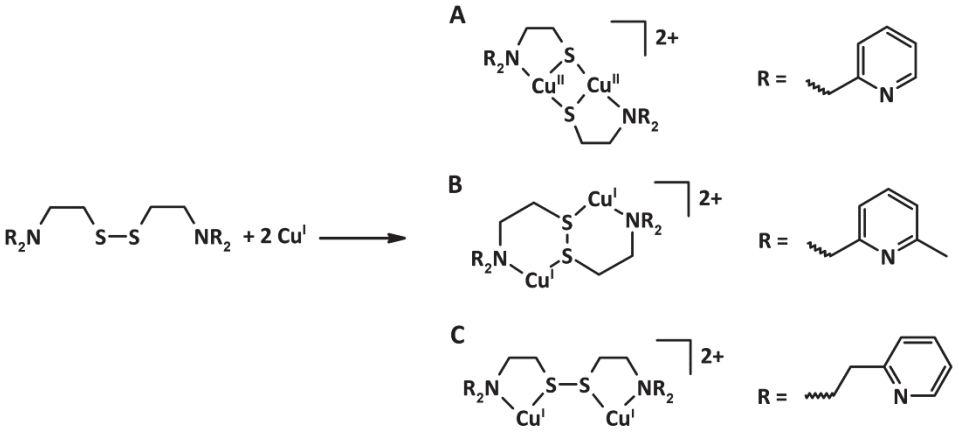

Figure 1.6: Schematic representation of the three different coordination geometries that can be formed starting from a disulfide ligand containing different R-groups and Cu^{I}.[46]

Replacing the methylene group between the tertiary amine and the pyridyl moiety with an ethylene group results in a Cu^{I} disulfide complex with geometry **C**. Geometry **C** is common for Cu^{I} disulfide complexes with the copper ions in a distorted tetrahedral geometry with a Cu-Cu distance of 3.91 Å. When a methyl group is added to the 6-position of the pyridyl moiety, Cu^{I} disulfide geometry **B** is formed. This structure is uncommon with its distorted trigonal pyramidal coordination sphere around the copper center and a large Cu-Cu distance of 5.16 Å. Geometry **B** can be seen as a potential intermediate geometry in going from **A** to **C**.

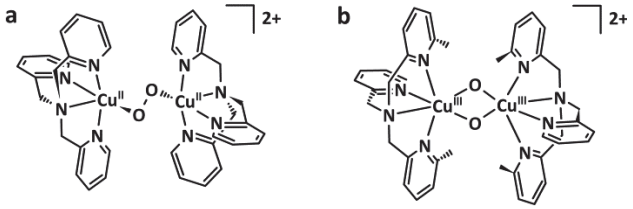

Figure 1.7: Schematic drawing of (a) a Cu^{II} μ-1,2-peroxo species with TPA ligand and (b) a Cu^{III} μ-oxido species with a TPA derived ligand.[61, 62]

It is worthy to note that a similar ligand change, where two 6-methyl groups are added to tris(2-pyridylmethyl)amine (TPA), also leads to a difference in geometry and redox state when the copper complex reacts with dioxygen. The compound $[Cu^{I}(TPA)(CH_3CN)]^{+}$ reacts with dioxygen to form a Cu^{II} μ-1,2-peroxo species,[61] while

the analogous copper complex coordinated to the dimethylated ligand forms a Cu^{III} μ-oxido species when exposed to dioxygen (Figure 1.7).[62] This change in geometry and oxidation states is completely opposite to those in **A** and **B**, indicating that geometry differences as a result of subtle ligand changes are difficult to generalize. The conversion of a Cu^{II} μ-1,2-peroxo species into a Cu^{III} μ-oxido complex was also reported to occur without a change in ligand structure.[63]

1.4.3 Chloride-induced conversion

The first Cu^{II} μ-thiolate to Cu^{I} disulfide conversion with the same ligand was reported to occur by the addition of chloride ions.[47] A ligand very similar to the ligands discussed in section 1.4.2. was reacted with Cu^{I} resulting in the formation of a Cu^{II} μ-thiolate species, even though the ligand provides only four instead of five coordination sites per copper center. Addition of one equivalent of Me_4NCl resulted in conversion to the Cu^{I} disulfide complex as indicated by a color change from dark brown to pale yellow. Addition of another equivalent of chloride anions led to small changes in the UV-vis spectrum and resulted in the formation of a bis(chlorido)dicopper(I) complex as is depicted in Figure 1.8a. The conversion was reversed by addition of $AgBF_4$.

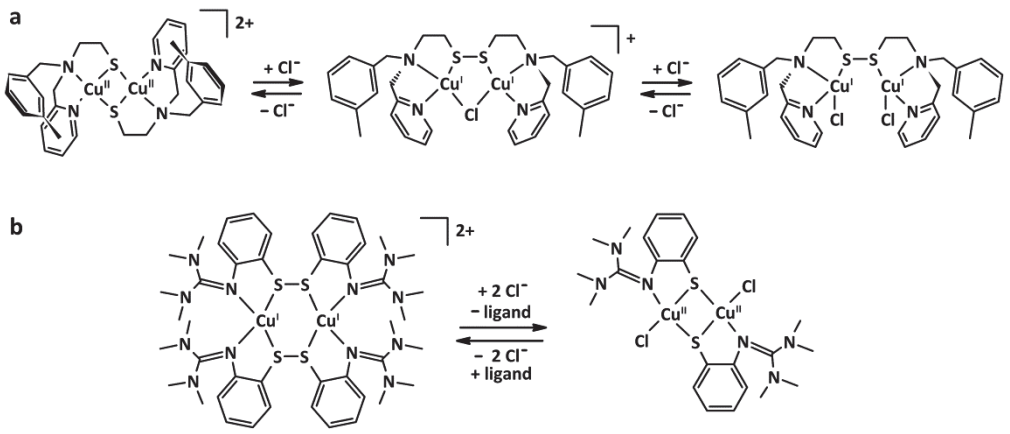

Figure 1.8: Schematic view of the reversible conversion from (a) Cu^{II} thiolate species to Cu^{I} disulfide species[47] and (b) from Cu^{I} disulfide species to Cu^{II} thiolate species[49] upon addition of chloride ions.

The conversion of this Cu^{II} μ-thiolate complex could also be initiated by addition of 2,4-di-*tert*-butylphenolate instead of chloride ions.[64] The authors also briefly mention

that the coordinative properties of the solvent influence the conversion; the use of dichloromethane as a solvent favors the formation of the Cu^{II} μ-thiolate complex while the more strongly coordinating solvent acetonitrile favors the formation of Cu^{I} disulfide species.

A more recent report describes the redox conversion in the opposite direction where a Cu^{I} disulfide complex is converted into a Cu^{II} thiolate complex upon addition of chloride ions in the form of Et_4NCl (Figure 1.8b). The addition of chloride ions leads to dissociation of the ligand thus resulting in tetra-coordinated copper before and after the conversion. The conversion also takes place when bromide ions instead of chloride ions are used and can be reversed by addition of Ag^{+} ions.

1.4.4 Proton-induced conversion

Another interesting example of a Cu^{II} thiolate to Cu^{I} disulfide conversion was published recently.[50] In this paper the conversion is reported to be induced by addition of two equivalents of trifluoridomethanesulfonic acid (HOTf), which results in a color change from dark green to light yellow and disappearance of the Cu^{II} d-d transition bands in the UV-vis absorption spectrum. This reaction can be reversed by addition of N,N-diisopropylethylamine (DIPEA) as depicted in Figure 1.9.

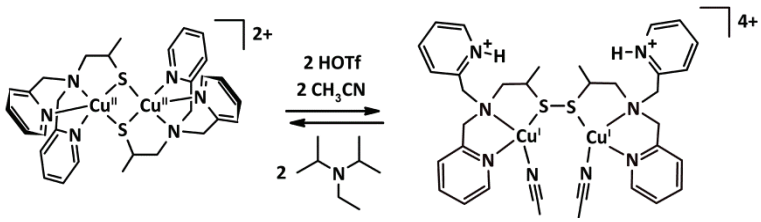

Figure 1.9: Schematic drawing of the conversion of a Cu^{II} thiolate species to a Cu^{I} disulfide species upon addition of HOTf and its reverse reaction by addition of DIPEA.[50]

Protonation of the pyridyl nitrogen of the Cu^{II} thiolate complex is favored over the amine and thiolate moieties, as was determined with ^{1}H NMR NOE enhancements. The presence of Cu^{I} was confirmed with the use of Cu K-edge X-ray Absorbance Spectroscopy.

1.4.5 Thiolate/disulfide equilibrium with cobalt

A similar equilibrium compared to the copper thiolate/disulfide equilibrium was reported for cobalt.[65] The reversible conversion from a mononuclear Co^{III} dithiolate

species to a Co^{II} thiolate/disulfide complex is induced by removal of a chloride ligand by addition of either lithium or silver ions (Figure 1.10)

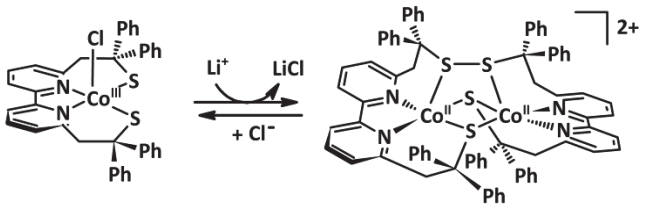

Figure 1.10: Schematic representation of the reversible equilibrium between a Co^{III} thiolate and Co^{II} disulfide complex.[65]

Because of the use of cobalt instead of copper, this conversion can take place under aerobic conditions, which is not the case for the reported copper compounds that can undergo thiolate redox chemistry.

1.5 Aim and outline of this thesis

The focus of the research described in this thesis is on modeling of different aspects of the biomimetic redox reactions between copper ions and sulfur-containing compounds. The dinuclear Cu^{II} μ-thiolate and Cu^{I} disulfide equilibrium can provide a model of the Cu_A site as discussed in section 1.4. As there is limited understanding about why or when Cu^{II} thiolate species form and what determines the conversion to Cu^{I} disulfide complexes the investigations of the effects of small ligand variations on this conversion is described in Chapter 2. Theoretical descriptions of these dinuclear structures are provided, which to the best of our knowledge has not been done before.

In Chapter 3, our investigations of the proton-induced conversion as discussed in section 1.4.4 is reported. The possibility of ligand dissociation instead of conversion to a Cu^{I} disulfide species has been investigated and the experimental results are again supported by DFT calculations.

In Chapter 4, the oxidative degradation of a Cu^{I} thiolate species is described. Oxidation of Cu^{I} thiolate complexes by dioxygen forms a model for possible degradation pathways of copper-sulfur active sites in nature, especially as it is shown that the degradation goes via a Cu^{II} thiolate complex. The Cu^{II} thiolate complex reacts further with dioxygen to form Cu^{II} sulfinate and Cu^{II} sulfonate complexes.

Chapter 5 describes the synthesis of a set of new ligands that are tested for their ability to form Cu^{II} μ-thiolate species. The redox potentials of the Cu^{I} complexes that are formed and crystal structures of Cu^{II} disulfide complexes are discussed.
In Chapter 6, the isolation and analysis of a Cu^{II} phenolate complex is described. This species converts to a Cu^{I} species; a reaction that is reminiscent of the Cu^{II} thiolate to Cu^{I} disulfide conversion. The reaction is of interest since phenols are common substrates in the biological system and are converted to catechols and quinones by copper enzymes (section 1.2.3).
Certain ligands direct copper towards the formation of Cu^{II} μ-thiolate species instead of Cu^{I} disulfide complexes. The copper complexes with these ligands might therefore also stabilize the formation of copper-oxo species, since O and S are in the same group in the periodic table and have similar electron configurations. To test this hypothesis, the reactivity of a large library of Cu^{II} complexes with different ligands have been tested in the oxidation of catechol to *o*-quinone in Chapter 7.
Parts of this thesis have been published,[66-69] are submitted for publication (Chapter 7) or are in preparation for publication (Chapter 6).

1.6 References

1. Solomon, E. I.; Heppner, D. E.; Johnston, E. M.; Ginsbach, J. W.; Cirera, J.; Qayyum, M.; Kieber-Emmons, M. T.; Kjaergaard, C. H.; Hadt, R. G.; Tian, L., *Chem. Rev.* **2014,** *114*, 3659-3853.
2. Mirica, L. M.; Ottenwaelder, X.; Stack, T. D. P., *Chem. Rev.* **2004,** *104*, 1013-1045.
3. Lewis, E. A.; Tolman, W. B., *Chem. Rev.* **2004,** *104*, 1047-1076.
4. Gray, H. B.; Malmstrom, B. G.; Williams, R. J. P., *J. Biol. Inorg. Chem.* **2000,** *5*, 551-559.
5. Solomon, E. I., *Inorg. Chem.* **2006,** *45*, 8012-8025.
6. Solomon, E. I.; Baldwin, M. J.; Lowery, M. D., *Chem. Rev.* **1992,** *92*, 521-542.
7. Solomon, E. I.; Sundaram, U. M.; Machonkin, T. E., *Chem. Rev.* **1996,** *96*, 2563-2605.
8. Koval, I. A.; Gamez, P.; Belle, C.; Selmeczi, K.; Reedijk, J., *Chem. Soc. Rev.* **2006,** *35*, 814-840.
9. Eicken, C.; Krebs, B.; Sacchettini, J. C., *Curr. Opin. Struc. Biol.* **1999,** *9*, 677-683.
10. Randall, D. W.; Gamelin, D. R.; LaCroix, L. B.; Solomon, E. I., *J. Biol. Inorg. Chem.* **2000,** *5*, 16-29.
11. Blackburn, N. J.; de Vries, S.; Barr, M. E.; Houser, R. P.; Tolman, W. B.; Sanders, D.; Fee, J. A., *J. Am. Chem. Soc.* **1997,** *119*, 6135-6143.
12. Savelieff, M. G.; Lu, Y., *J. Biol. Inorg. Chem.* **2010,** *15*, 461-483.
13. Antholine, W. E.; Kastrau, D. H. W.; Steffens, G. C. M.; Buse, G.; Zumft, W. G.; Kroneck, P. M. H., *Eur. J. Biochem.* **1992,** *209*, 875-881.
14. Solomon, E. I.; Xie, X.; Dey, A., *Chem. Soc. Rev.* **2008,** *37*, 623-638.

15. Iwata, S.; Ostermeier, C.; Ludwig, B.; Michel, H., *Nature* **1995,** *376*, 660-669.
16. Tsukihara, T.; Aoyama, H.; Yamashita, E.; Tomizaki, T.; Yamaguchi, H.; Shinzawaitoh, K.; Nakashima, R.; Yaono, R.; Yoshikawa, S., *Science* **1995,** *269*, 1069-1074.
17. Wilmanns, M.; Lappalainen, P.; Kelly, M.; SauerEriksson, E.; Saraste, M., *P. Natl. Acad. Sci. USA* **1995,** *92*, 11955-11959.
18. Brown, K.; Tegoni, M.; Prudencio, M.; Pereira, A. S.; Besson, S.; Moura, J. J.; Moura, I.; Cambillau, C., *Nat. Struct. Biol.* **2000,** *7*, 191-195.
19. Malmstrom, B. G., *J. Biol. Inorg. Chem.* **1998,** *3*, 339-343.
20. Wikstrom, M., *Nature* **1989,** *338*, 776-778.
21. Daskalakis, V.; Pinakoulaki, E.; Stavrakis, S.; Varotsis, C., *J. Phys. Chem. B* **2007,** *111*, 10502-10509.
22. Aoyama, H.; Muramoto, K.; Shinzawa-Itoh, K.; Hirata, K.; Yamashita, E.; Tsukihara, T.; Ogura, T.; Yoshikawa, S., *P. Natl. Acad. Sci. USA* **2009,** *106*, 2165-2169.
23. MacMillan, F.; Kannt, A.; Behr, J.; Prisner, T.; Michel, H., *Biochemistry* **1999,** *38*, 9179-9184.
24. Yu, Y.; Mukherjee, A.; Nilges, M. J.; Hosseinzadeh, P.; Miner, K. D.; Lu, Y., *J. Am. Chem. Soc.* **2014,** *136*, 1174-1177.
25. Wikström, M., *Biochim. Biophys. Acta, Bioenerg.* **2012,** *1817*, 468-475.
26. Gorelsky, S. I.; Ghosh, S.; Solomon, E. I., *J. Am. Chem. Soc.* **2006,** *128*, 278-290.
27. Pomowski, A.; Zumft, W. G.; Kroneck, P. M. H.; Einsle, O., *Nature* **2011,** *477*, 234-237.
28. Ghosh, S.; Gorelsky, S. I.; Chen, P.; Cabrito, I.; Moura, J. J. G.; Moura, I.; Solomon, E. I., *J. Am. Chem. Soc.* **2003,** *125*, 15708-15709.
29. Chan, J. M.; Bollinger, J. A.; Grewell, C. L.; Dooley, D. M., *J. Am. Chem. Soc.* **2004,** *126*, 3030-3031.
30. Ohta, T.; Tachiyama, T.; Yoshizawa, K.; Yamabe, T., *Tetrahedron Lett.* **2000,** *41*, 2581-2585.
31. Bharadwaj, P. K.; Potenza, J. A.; Schugar, H. J., *J. Am. Chem. Soc.* **1986,** *108*, 1351-1352.
32. Bharadwaj, P. K.; John, E.; Xie, C. L.; Zhang, D.; Hendrickson, D. N.; Potenza, J. A.; Schugar, H. J., *Inorg. Chem.* **1986,** *25*, 4541-4546.
33. Houser, R. P.; Tolman, W. B., *Inorg. Chem.* **1995,** *34*, 1632-1633.
34. Coucouvanis, D.; Kanodia, S.; Swenson, D.; Chen, S. J.; Studemann, T.; Baenziger, N. C.; Pedelty, R.; Chu, M., *J. Am. Chem. Soc.* **1993,** *115*, 11271-11278.
35. Aoi, N.; Matsubayashi, G. E.; Tanaka, T., *J. Chem. Soc., Dalton Trans.* **1987**, 241-247.
36. Chadha, R. K.; Kumar, R.; Tuck, D. G., *Can. J. Chem.* **1987,** *65*, 1336-1342.
37. Gómez-Saiz, P.; García-Tojal, J.; Mendia, A.; Donnadieu, B.; Lezama, L.; Pizarro, José L.; Arriortua, Maria I.; Rojo, T., *Eur. J. Inorg. Chem.* **2003,** *2003*, 518-527.
38. Weng, Z.; He, W.; Chen, C.; Lee, R.; Tan, D.; Lai, Z.; Kong, D.; Yuan, Y.; Huang, K.-W., *Angew. Chem. Int. Ed.* **2013,** *52*, 1548-1552.
39. Stange, A. F.; Waldhor, E.; Moscherosch, M.; Kaim, W., *Z. Naturforsch., B: Chem. Sci.* **1995,** *50*, 115-122.

40. Houser, R. P.; Halfen, J. A.; Young, V. G.; Blackburn, N. J.; Tolman, W. B., *J. Am. Chem. Soc.* **1995,** *117*, 10745-10746.
41. Houser, R. P.; Young, V. G.; Tolman, W. B., *J. Am. Chem. Soc.* **1996,** *118*, 2101-2102.
42. Branscombe, N. D. J.; Blake, A. J.; MarinBecerra, A.; Li, W. S.; Parsons, S.; RuizRamirez, L.; Schroder, M., *Chem. Commun.* **1996**, 2573-2574.
43. Uraev, A. I.; Vasilchenko, I. S.; Ikorskii, V. N.; Shestakova, T. A.; Burlov, A. S.; Lyssenko, K. A.; Vlasenko, V. G.; Kuz'menko, T.; Divaeva, L. N.; Pirog, I. V.; Borodkin, G. S.; Uflyand, I. E.; Antipin, M. Y.; Ovcharenko, V. I.; Garnovskii, A. D.; Minkin, V. I., *Mendeleev Commun.* **2005**, 133-135.
44. Rammal, W.; Belle, C.; Beguin, C.; Duboc, C.; Philouze, C.; Pierre, J.-L.; Le Pape, L.; Bertaina, S.; Saint-Aman, E.; Torelli, S., *Inorg. Chem.* **2006,** *45*, 10355-10362.
45. Roy, N.; Sproules, S.; Bothe, E.; Weyhermueller, T.; Wieghardt, K., *Eur. J. Inorg. Chem.* **2009**, 2655-2663.
46. Itoh, S.; Nagagawa, M.; Fukuzumi, S., *J. Am. Chem. Soc.* **2001,** *123*, 4087-4088.
47. Ueno, Y.; Tachi, Y.; Itoh, S., *J. Am. Chem. Soc.* **2002,** *124*, 12428-12429.
48. Raja, D. S.; Bhuvanesh, N. S. P.; Natarajan, K., *Eur. J. Med. Chem.* **2011,** *46*, 4584-4594.
49. Neuba, A.; Haase, R.; Meyer-Klaucke, W.; Flörke, U.; Henkel, G., *Angew. Chem. Int. Ed.* **2012,** *51*, 1714-1718.
50. Thomas, A. M.; Lin, B.-L.; Wasinger, E. C.; Stack, T. D. P., *J. Am. Chem. Soc.* **2013,** *135*, 18912-18919.
51. Gil-Garcia, R.; Fraile, R.; Donnadieu, B.; Madariaga, G.; Januskaitis, V.; Rovira, J.; Gonzalez, L.; Borras, J.; Arnaiz, F. J.; Garcia-Tojal, J., *New J. Chem.* **2013,** *37*, 3568-3580.
52. Ali, M. A.; Mirza, A. H.; Hamid, M. H. S. A.; Aminath, N.; Bernhardt, P. V., *Polyhedron* **2012,** *47*, 79-86.
53. Okamoto, K.; Kuwabara, J.; Kanbara, T., *J. Organomet. Chem.* **2011,** *696*, 1305-1309.
54. Gennari, M.; Pecaut, J.; DeBeer, S.; Neese, F.; Collomb, M.-N.; Duboc, C., *Angew. Chem. Int. Ed.* **2011,** *50*, 5661-5665.
55. Weaver, M. J., *J. Phys. Chem.* **1990,** *94*, 8608-8613.
56. Zhang, S.; Warren, T. H., *Chem. Sci.* **2013,** *4*, 1786-1792.
57. Jacob, C.; Giles, G. L.; Giles, N. M.; Sies, H., *Angew. Chem. Int. Ed.* **2003,** *42*, 4742-4758.
58. Ye, Q.; Imriskova-Sosova, I.; Hill, B. C.; Jia, Z., *Biochemistry* **2005,** *44*, 2934-2942.
59. Cawthorn, T. R.; Poulsen, B. E.; Davidson, D. E.; Andrews, D.; Hill, B. C., *Biochemistry* **2009,** *48*, 4448-4454.
60. Banci, L.; Bertini, I.; Cavallaro, G.; Ciofi-Baffoni, S., *Febs Journal* **2011,** *278*, 2244-2262.
61. Jacobson, R. R.; Tyeklar, Z.; Farooq, A.; Karlin, K. D.; Liu, S.; Zubieta, J., *J. Am. Chem. Soc.* **1988,** *110*, 3690-3692.
62. Hayashi, H.; Fujinami, S.; Nagatomo, S.; Ogo, S.; Suzuki, M.; Uehara, A.; Watanabe, Y.; Kitagawa, T., *J. Am. Chem. Soc.* **2000,** *122*, 2124-2125.
63. Kieber-Emmons, M. T.; Ginsbach, J. W.; Wick, P. K.; Lucas, H. R.; Helton, M. E.; Lucchese, B.; Suzuki, M.; Zuberbühler, A. D.; Karlin, K. D.; Solomon, E. I., *Angew. Chem. Int. Ed.* **2014,** *53*, 4935-4939.

64. Osako, T.; Ueno, Y.; Tachi, Y.; Itoh, S., *Inorg. Chem.* **2004,** *43*, 6516-6518.
65. Gennari, M.; Gerey, B.; Hall, N.; Pécaut, J.; Collomb, M.-N.; Rouzières, M.; Clérac, R.; Orio, M.; Duboc, C., *Angew. Chem.* **2014,** *126*, 5422-5425.
66. Ording-Wenker, E. C. M.; Siegler, M. A.; Lutz, M.; Bouwman, E., *Inorg. Chem.* **2013,** *52*, 13113-13122.
67. Ording-Wenker, E. C. M.; van der Plas, M.; Siegler, M. A.; Bonnet, S.; Bickelhaupt, F. M.; Fonseca Guerra, C.; Bouwman, E., *Inorg. Chem.* **2014,** *53*, 8494-8504.
68. Ording-Wenker, E. C. M.; van der Plas, M.; Siegler, M. A.; Fonseca Guerra, C.; Bouwman, E., *Chem. Eur. J.* **2014,** *20*, 16913-16921.
69. Ording-Wenker, E. C. M.; Siegler, M. A.; Bouwman, E., *Inorg. Chim. Acta* **2015,** *in press*.

Chapter 2

Thermodynamics of the Cu^{II} μ-Thiolate and Cu^{I} Disulfide Equilibrium: A Combined Experimental and Theoretical Study

*The redox equilibrium between dinuclear Cu^{II} μ-thiolate and Cu^{I} disulfide structures has been analyzed experimentally and via DFT calculations. Two new ligands, **L^2SSL^2** and **L^4SSL^4**, and their Cu^{II} μ-thiolate and Cu^{I} disulfide complexes were synthesized. For **L^2SSL^2**, these two redox-isomeric copper species are shown to be in equilibrium, which depends on both temperature and solvent. For **L^4SSL^4** the μ-thiolate species forms as the kinetic product and further evolves into the disulfide complex under thermodynamic control, which creates the unprecedented possibility to compare both species under the same reaction conditions. The energies of the μ-thiolate and disulfide complexes for two series of related ligands have been calculated with DFT; the results rationalize the experimentally observed structures, and emphasize the important role that steric requirements play in the formation of the Cu^{II} thiolate structure.*

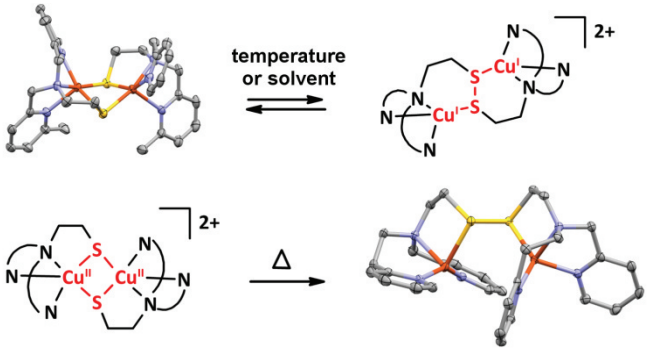

This chapter has been published as a full paper: E. C. M. Ording-Wenker, M. van der Plas, M. A. Siegler, S. Bonnet, F. M. Bickelhaupt, C. Fonseca Guerra, E. Bouwman, *Inorg. Chem.* **2014**, *53*, 8494-8504.

2.1 Introduction

Redox reactions are frequently occurring in biological systems and are the basis for important electron-transfer reactions as for example the binding and reduction of molecules such as dioxygen, nitrite and nitrous oxide.[1] Many of these reactions involve sulfur-containing compounds, such as cysteine or glutathione, which are participating in a thiolate/disulfide equilibrium.[2-5] This thiolate/disulfide equilibrium can be tuned by the presence of a metal center such as copper (Chapter 1). Controlling the interconversion between the Cu^{II} μ-thiolate and Cu^{I} disulfide form of dinuclear copper complexes would allow for the understanding of copper-sulfur redox reactions occurring in natural systems. Up to now, there is limited understanding about why or when the Cu^{II} thiolate complex forms, i.e. whether the electrons are located on copper or sulfur, and as far as we know there are no theoretical descriptions of these dinuclear structures. We considered dipyridylamine ligands as an ideal system to understand the redox equilibrium between the Cu^{II} μ-thiolate and Cu^{I} disulfide form of their dinuclear copper complexes, as small ligand variations have been shown to induce the formation of three different species (Section 1.4.2).[6]

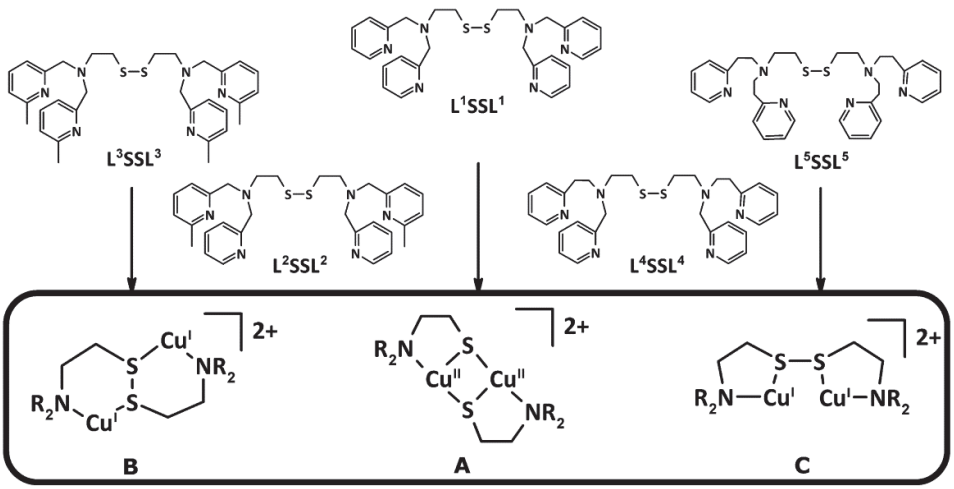

Figure 2.1: Schematic overview of the ligands discussed in this paper and the complexes that are formed when **L^1SSL^1**, **L^3SSL^3** and **L^5SSL^5** are reacted with $[Cu^{I}(CH_3CN)_4]^{+}$.[6]

Minute changes in the ligand structure were shown to induce the preferential formation of either a dinuclear Cu^{II} μ-thiolate compound (Figure 2.1, conformation **A**), a Cu^{I} *transoid*-disulfide (Figure 2.1, conformation **B**) or a Cu^{I} *cisoid*-disulfide

complex (Figure 2.1, conformation **C**).[6] Thus, the two new ligands **L²SSL²** and **L⁴SSL⁴** were designed and synthesized. These ligands combine structural elements of the reported ligand **L¹SSL¹** with either **L³SSL³** or **L⁵SSL⁵** (Figure 2.1). This resulted in two series of ligands with either an increasing number of C6-methylated pyridines, or an increasing number of ethylene bridges between the amine nitrogen and the pyridine rings. In this Chapter we report the unprecedented effects of such small variations on the type of dinuclear copper complexes experimentally formed. DFT calculations have been carried out to quantify the different energies associated with the formation of these species.

2.2 Results

2.2.1 Ligand Synthesis

The ligands **L²SSL²** and **L⁴SSL⁴** were synthesized via the precursor bis-(2-(N-pyridylmethyl)aminoethyl) disulfide (**L^{NH}SSL^{NH}**), which was synthesized following a literature procedure.[7] A schematic representation of the synthesis is provided in Figure 2.2. **L²SSL²** was formed by reductive amination of **L^{NH}SSL^{NH}** with two equivalents of 6-methyl-2-pyridinecarboxaldehyde. The crude product contained side products which were shown by ^{1}H NMR and MS spectra to originate from scrambling of the 2-pyridyl and 6-methyl-2-pyridyl groups during the reaction. After purification by column chromatography **L²SSL²** was obtained as a cream-colored powder that was recrystallized from petroleum ether. **L⁴SSL⁴** was synthesized by alkylation of **L^{NH}SSL^{NH}** with 2-vinylpyridine. The pure product was obtained after column chromatography as a light-brown oil, which darkens over longer periods of time (weeks) indicating degradation of the product.

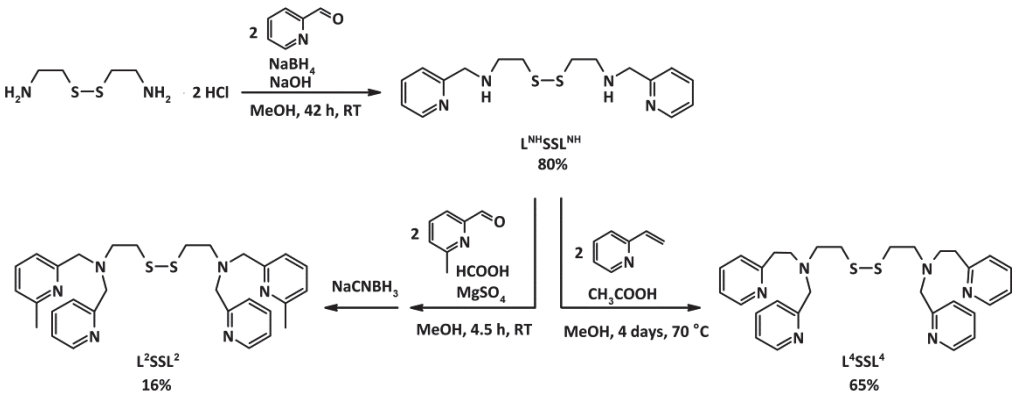

Figure 2.2: Schematic representation of the synthesis of **L²SSL²** and **L⁴SSL⁴** via **L^{NH}SSL^{NH}**.[7]

2.2.2 Synthesis and Structures of $[Cu^{II}_2(\mathbf{L^2S})_2](BF_4)_2{\cdot}C_3H_6O$ and $[Cu^{I}_2(\mathbf{L^4SSL^4})](BF_4)_2$

Addition of $[Cu^{I}(CH_3CN)_4]^+$ to a solution of $\mathbf{L^2SSL^2}$ in weakly or non-coordinating solvents such as dichloromethane or acetone results in a color change from light yellow to dark green. Slow vapor diffusion of pentane into an acetone solution of the complex resulted in the formation of black crystals suitable for X-ray structure determination. The single crystal X-ray analysis confirms the structure of a dinuclear Cu^{II} μ-thiolate complex with the formula $[Cu^{II}_2(\mathbf{L^2S})_2](BF_4)_2{\cdot}C_3H_6O$, which is characterized by the relatively long S-S distance of 3.164(2) Å, whereas a disulfide bond in a Cu^{I} complex is on average ~2.1 Å.[6-8] In contrast, when $[Cu^{I}(CH_3CN)_4]^+$ was added to $\mathbf{L^4SSL^4}$ a bright green solution was obtained independent of the solvent used. When this solution was heated under anaerobic conditions, the color gradually evolved from green to brown. Crystals suitable for X-ray structure determination were obtained by vapor diffusion of hexane into a methanol solution. These crystals appeared to be a Cu^{I} disulfide structure of type **C** (see Figure 2.1) with the chemical formula $[Cu^{I}_2(\mathbf{L^4SSL^4})](BF_4)_2$. Displacement ellipsoid plots of the cationic dinuclear structures of $[Cu^{II}_2(\mathbf{L^2S})_2]^{2+}$ and $[Cu^{I}_2(\mathbf{L^4SSL^4})]^{2+}$ are depicted in Figure 2.3; crystallographic data can be found in Table 2.1 and selected bond distances and angles are given in Table 2.2.

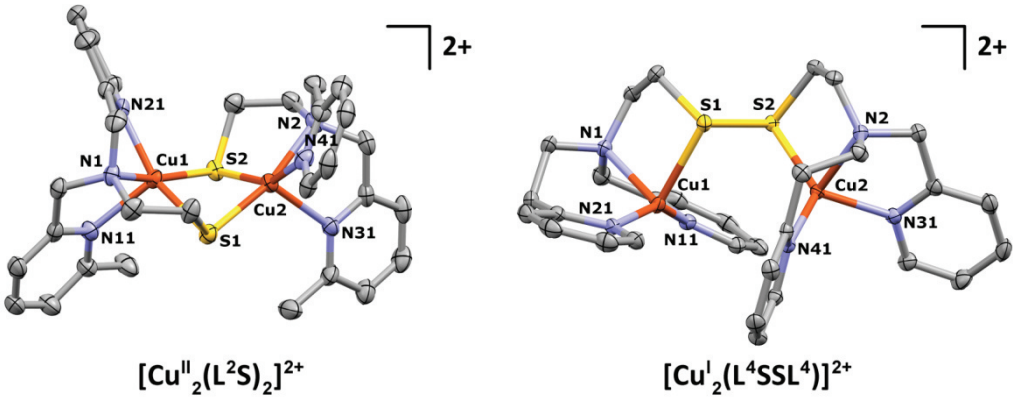

Figure 2.3: Displacement ellipsoid plots (50% probability level) of the cationic parts of $[Cu^{II}_2(\mathbf{L^2S})_2](BF_4)_2{\cdot}C_3H_6O$ and $[Cu^{I}_2(\mathbf{L^4SSL^4})](BF_4)_2$ at 110(2) K. Hydrogen atoms are omitted for clarity.

Table 2.1: Crystallographic and structure refinement data for complexes $[Cu^{II}_2(\mathbf{L^2S})_2](BF_4)_2{\cdot}C_3H_6O$ and $[Cu^{I}_2(\mathbf{L^4SSL^4})](BF_4)_2$

	$[Cu^{II}_2(\mathbf{L^2S})_2](BF_4)_2{\cdot}C_3H_6O$	$[Cu^{I}_2(\mathbf{L^4SSL^4})](BF_4)_2$
empirical formula	$[C_{30}H_{36}Cu_2N_6S_2](BF_4)_2{\cdot}C_3H_6O$	$[C_{30}H_{36}Cu_2N_6S_2](BF_4)_2$
formula weight	903.54	845.47
crystal system	orthorhombic	triclinic
space group	*Pna2₁*	*P*−1
a, Å	21.1268(2)	11.8258(3)
b, Å	10.28491(11)	12.2570(3)
c, Å	35.4103(4)	13.6442(3)
α, deg	90	110.331(2)
β, deg	90	97.1080(19)
γ, deg	90	108.254(2)
V, Å^3	7694.21(14)	1700.05(7)
Z	8	2
D_{calc}, g·cm^3	1.560	1.652
T, Kelvin	110(2)	110(2)
crystal size, mm	0.42 × 0.41 × 0.26	0.34 × 0.28 × 0.11
μ, mm^{-1}	3.045	1.451
no. of reflns measd	27801	31708
no. of unique reflns	13538	7816
no. of reflns obsd.	13151 [$I > 2\sigma(I)$]	6797 [$I > 2\sigma(I)$]
no. of parameters	1111	451
R_1 / wR_2 [$I > 2\sigma(I)$]	0.0497/0.1281	0.0279/0.0711
R_1 / wR_2 [all refl.]	0.0511/0.1291	0.0343/0.0734
goodness of fit	1.086	1.065
$\Delta\rho$, e·Å^{-3}	−0.56 /1.36	−0.53/0.75

The complex $[Cu^{II}_2(\mathbf{L^2S})_2](BF_4)_2{\cdot}C_3H_6O$ crystallizes in the orthorhombic space group *Pna*2$_1$ with two crystallographically independent dinuclear complexes and two acetone molecules in the asymmetric unit. Three of the four crystallographically independent BF_4^- counterions and one of the two acetone solvent molecules are disordered over two orientations. The occupancy factors of their major components refine to 0.843(9), 0.676(12) and 0.69(3) for BF_4^- and 0.58(4) for the acetone molecule. Only one of the two crystallographically independent cations is discussed, as both are very similar. The Cu^{II} ions are in N_3S_2 coordination environments with slightly distorted square-pyramidal geometries. The basal planes are formed by the two thiolate sulfur atoms, the amine nitrogen atom and the unsubstituted pyridyl nitrogen atom; the pyramids are edge-sharing through the bridging thiolate sulfurs. The nitrogen atom of the 6-methylpyridyl group is located at the axial position, and both 6-methyl-2-pyridyl groups are located on the same side of the Cu_2-S_2 average plane. The copper-sulfur distances are all similar (~2.29 Å).

Table 2.2: Selected bond distances and angles of $[Cu^{II}_2(\mathbf{L^2S})_2](BF_4)_2{\cdot}C_3H_6O$ and $[Cu^{I}_2(\mathbf{L^4SSL^4})](BF_4)_2$.

Bond distance (Å)			**Bond angle (°)**		
	$[Cu^{II}_2(\mathbf{L^2S})_2]^{2+}$	$[Cu^{I}_2(\mathbf{L^4SSL^4})]^{2+}$		$[Cu^{II}_2(\mathbf{L^2S})_2]^{2+}$	$[Cu^{I}_2(\mathbf{L^4SSL^4})]^{2+}$
Cu1 - Cu2	3.0444(12)	3.8988(3)	Cu1 - S1 - S2	46.43(5)	97.88(2)
S1 - S2	3.164(2)	2.0643(6)	Cu2 - S2 - S1	46.44(5)	96.18(2)
Cu1 - S1	2.2920(18)	2.4155(5)	Cu1 - S1 - Cu2	83.16(6)	86.82(2)
Cu1 - S2	2.2952(18)	3.3858(5)	Cu1 - S2 - Cu2	83.21(6)	85.31(2)
Cu1 - N1	2.109(6)	2.1625(15)	S1 - Cu1 - S2	87.22(7)	37.15(1)
Cu1 - N11	2.256(6)	1.9669(15)	S1 - Cu1 - N1	88.65(16)	86.97(4)
Cu1 - N21	2.040(6)	1.9449(15)	S1 - Cu2 - S2	87.27(7)	39.93(2)
Cu2 - S1	2.2954(18)	3.1973(5)	S1 - Cu1 - N11	98.22(16)	109.56(4)
Cu2 - S2	2.2897(19)	2.2295(5)	S1 - Cu1 - N21	151.61(18)	101.55(5)
Cu2 - N2	2.104(6)	2.1421(14)	S2 - Cu1 - N1	166.74(18)	93.76(4)
Cu2 - N31	2.236(6)	2.0198(15)	S2 - Cu1 - N11	113.53(15)	73.97(5)
Cu2 - N41	2.027(6)	1.9950(14)	S2 - Cu1 - N21	99.05(18)	135.00(5)
			N1 - Cu1 - N11	79.5(2)	84.31(6)
Dihedral angle (°)			N1 - Cu1 - N21	78.9(2)	102.36(6)
Cu1 - S1 - S2 - Cu2	132.99(9)	−77.015(19)	N11 - Cu1 - N21	104.4(2)	148.52(6)
Cu1 - S1 - Cu2 - S2	−32.26(7)	104.83	S1 - Cu2 - N2	164.93(17)	91.84(4)
			S1 - Cu2 - N31	115.75(16)	161.81(5)
			S1 - Cu2 - N41	97.80(18)	88.77(4)
			S2 - Cu2 - N2	88.49(16)	91.03(4)
			S2 - Cu2 - N31	100.87(16)	122.11(4)
			S2 - Cu2 - N41	152.83(18)	127.83(4)
			N2 - Cu2 - N31	79.3(2)	84.77(6)
			N2 - Cu2 - N41	79.7(2)	101.66(6)
			N31 - Cu2 - N41	100.8(2)	109.43(6)

The Cu-Cu distance is 3.0444(12), which is slightly longer than reported for similar complexes such as $[Cu^{II}_2(\mathbf{L^1S})_2]^{2+}$ (2.960 Å).[6, 7] The Cu-S-Cu-S central unit is in a butterfly arrangement with a dihedral angle of 32.26(7)°. The complex $[Cu^{I}_2(\mathbf{L^4SSL^4})](BF_4)_2$ crystallizes in the triclinic space group *P*–1. The two copper centers are found in different distorted four-coordinate geometries. The Cu1 center is in a 'saw-horse' or 'double T-shaped' geometry. The di(pyridyl)amine group is coordinated in a meridional-type fashion, forming a T-shaped coordination at the copper ion in which the pyridyl groups are roughly in the same plane (N11-Cu1-N21 is 148.52(6)°). The disulfide sulfur atom, together with the pyridyl nitrogen atoms, forms the second T-shape, perpendicular to the other one. The Cu2 center is coordinated in a trigonal-pyramidal geometry, with the two pyridyl nitrogen atoms and the sulfur atom in the trigonal plane, and the amine nitrogen atom in the axial position. Interestingly, an additional copper-hydrogen interaction is present: the

pyridyl hydrogen H16 (*ortho* to N11) is at a distance to Cu2 of *ca.* 2.98 Å.[9-12] When this additional interaction is taken into account, the geometry of Cu2 can be considered as a trigonal bipyramid. The Cu1-Cu2 distance is 3.8988(3) Å, which is similar to what has been reported for $[Cu^{I}_2(\mathbf{L^5SSL^5})]^{2+}$.[6] The Cu-S distance is rather different for each copper center with a longer 2.4155(5) Å distance for Cu1-S1 compared to 2.2295(5) Å for Cu2-S2; the latter being more in agreement with the distances reported previously.[6, 8] The computed structures of $[Cu^{I}_2(\mathbf{L^4SSL^4})]^{2+}$ in conformation **C** (see section 2.4) show a similar difference in Cu-S distances of 2.17 and 2.25 Å in both the gas phase and in acetonitrile. The Cu-H interaction is not visible in these calculations. Even though the difference in Cu-S distances is smaller in the calculated structures, it does show that sterics play a role in the asymmetry of this complex.

2.2.3 Solution Studies of $[Cu^{II}_2(\mathbf{L^2S})_2]^{2+}$ and $[Cu^{I}_2(\mathbf{L^4SSL^4})]^{2+}$

When a more polar (or more strongly coordinating) solvent such as acetonitrile is used in the reaction between $[Cu^{I}(CH_3CN)_4]^{+}$ and $\mathbf{L^2SSL^2}$, a pale greenish-yellow solution is obtained instead of the dark green solution obtained in acetone or dichloromethane. UV-vis spectra (Figure AI.2, Appendix I) of the dark green μ-thiolate complex $[Cu^{II}_2(\mathbf{L^2S})_2]^{2+}$ in dichloromethane show absorption bands at 261 nm (ε = 17 200 M^{-1} cm^{-1}) attributed to the $\pi^* \leftarrow \pi$ transition of the pyridyl groups, two bands at 300 (ε = 7100 M^{-1} cm^{-1}) and 358 nm (ε = 4200 M^{-1} cm^{-1}) attributed to $Cu^{II} \leftarrow S$ LMCT transitions, and three bands at 500 nm (ε = 1200 M^{-1} cm^{-1}), 627 nm (ε = 1100 M^{-1} cm^{-1}) and 928 nm (ε = 410 M^{-1} cm^{-1}) attributed to copper d-d transitions. In acetonitrile, a $\pi^* \leftarrow \pi$ transition is observed at 257 nm (ε = 7950 M^{-1} cm^{-1}) as well as a $Cu^{I} \leftarrow S$ LMCT band at 309 nm (ε = 3150 M^{-1} cm^{-1}), but no d-d transitions are present at higher wavelengths. The lack of d-d transitions in acetonitrile indicates the presence of Cu^{I} instead of Cu^{II} ions. The ^1H NMR spectra of the copper complexes in different solvents were recorded (Figure 2.4) and compared to the spectrum of the free ligand. NMR resonances are observed in the diamagnetic region for $[Cu^{II}_2(\mathbf{L^2S})_2]^{2+}$ in CD_2Cl_2 and the compound was found to be EPR silent, indicating that the Cu^{II} ions in the μ-thiolate complex are anti-ferromagnetically coupled. In the NMR spectrum the signals are relatively broad, most likely because of paramagnetic impurities or some population of the S=1 spin state at room temperature. Using Evans method we found the magnetic moment in CD_2Cl_2 to be μ_{eff} = 1.05 μB, a value which is lower than the spin-only value (2.83 μB for a dinuclear complex) supporting the anti-ferromagnetic coupling.[13, 14]

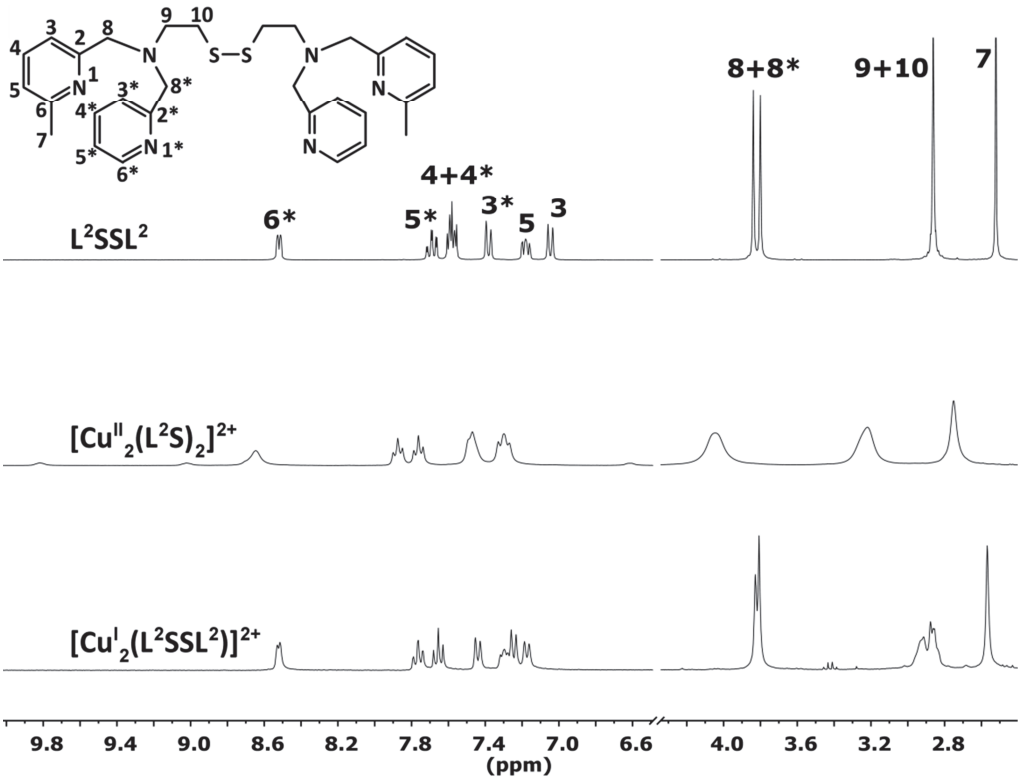

Figure 2.4: ^{1}H NMR spectra of **L²SSL²** and $[Cu^{II}_2(\mathbf{L^2S})_2]^{2+}$ in CD_2Cl_2 and $[Cu^{I}_2(\mathbf{L^2SSL^2})]^{2+}$ in CD_3CN at RT.

The NMR spectrum of the same complex mixture in CD_3CN shows small downfield shifts compared to the spectrum of the free ligand and reveals splitting of the H-8 and H-9 proton peaks, both features indicating coordination of copper to the ligand. The diamagnetic nature of the compound in acetonitrile and the absence of d-d transitions indicate that the complex may be formulated as $[Cu^{I}_2(\mathbf{L^2SSL^2})]^{2+}$. Thus, upon addition of $[Cu^{I}(CH_3CN)_4]^{+}$ to **L²SSL²** in acetonitrile (a polar and coordinating solvent) a Cu^{I} disulfide complex is formed, whereas in dichloromethane and acetone (less polar and weakly coordinating solvents) with the same ligand the Cu^{II} μ-thiolate complex is formed preferentially. Similar behavior with a slightly different ligand has been reported, but this was not thoroughly analyzed.[15] Addition of small amounts of acetonitrile to a solution of $[Cu^{II}_2(\mathbf{L^2S})_2]^{2+}$ in dichloromethane results in a gradual conversion of the Cu^{II} compound to the Cu^{I} disulfide complex, as monitored with UV-vis spectroscopy (Figure 2.5).

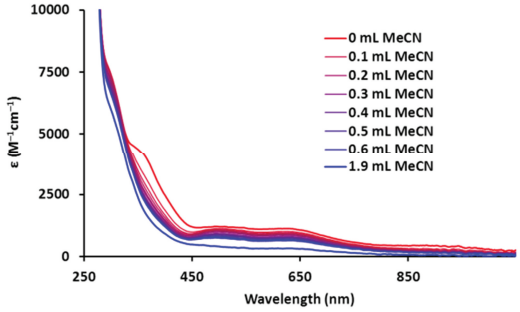

Figure 2.5: UV-vis absorption spectra of **L²SSL²** and 2 equivalents of $[Cu^{I}(CH_3CN)_4](BF_4)$ in 10 mL dichloromethane with variable amounts of added acetonitrile at 1 mM [Cu] concentration recorded with a transmission dipprobe at a path length of 1.2 mm.

These results suggest that in solvents of moderate coordinating properties and/or polarity a mixture of both Cu^{I} disulfide and Cu^{II} μ-thiolate species might be present. Indeed, in methanol a mixture of both the Cu^{II} μ-thiolate and Cu^{I} disulfide compound was observed, as shown with UV-vis spectroscopy (Figure 2.6a). Cooling of such a methanolic solution down to 243 K resulted in an increase in the intensity of the d-d transitions and the $Cu^{II} \leftarrow$ S LMCT characteristic for the Cu^{II} μ-thiolate species. When allowing the solution to warm to room temperature after cooling, we see that this conversion is reversible (red dots, Figure 2.6b). Similar results were obtained when the conversion was measured with ^{1}H NMR spectroscopy, which can be seen in Figure AI.4, Appendix I.

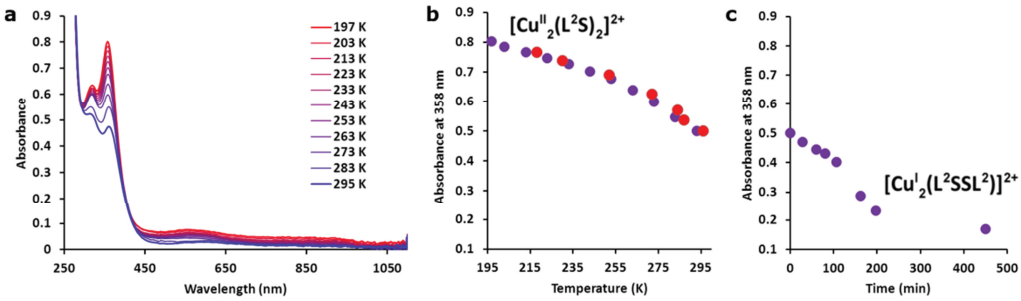

Figure 2.6: UV-vis spectra of $[Cu^{I}(CH_3CN)_4]^{+}$ + **L²SSL²** at different temperatures between 197 K and 295 K (a); the absorption of the $Cu^{II} \leftarrow$ S LMCT at 358 nm plotted vs. temperature while cooling down (purple) and reversing this reaction (red) (b) and plotted vs. time while heating at 333 K (c). Spectra were measured in methanol at 1 mM [Cu] recorded with a transmission dipprobe path length of 2.0 mm.

Reversely, when the solution was heated up to 333 K the d-d transitions and Cu^{II} ← S LMCT became lower in intensity over time, indicating an increase in Cu^{I} disulfide concentration. A plot of the absorbance at 358 nm vs. time is shown in Figure 2.6c. When cooling the solution down to room temperature after heating, there was no increase in the d-d transitions and Cu^{II} ← S LMCT indicating that there is no conversion back to the Cu^{II} μ-thiolate species. Heating the solution for a longer time does not result in any changes in the spectrum. These results show that the Cu^{I} disulfide - Cu^{II} μ-thiolate equilibrium can be temperature controlled at lower temperatures, but at higher temperatures this conversion is not reversible.

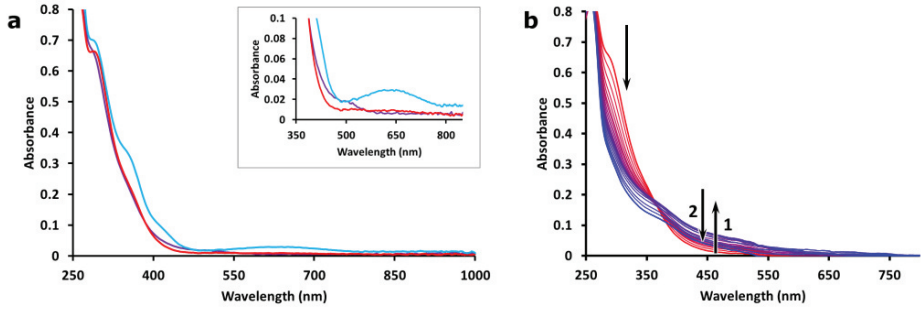

Figure 2.7: UV–vis spectra of $[Cu^{II}_2(\mathbf{L^4S})_2]^{2+}$ (a) in different solvents: MeOH (purple), CH_3CN (red) and dichloromethane (blue) and (b) at 67 °C for 21 h in MeOH at 1 mM [Cu] concentration under argon recorded with a transmission dipprobe with a path length of 1.2 mm. Inset shows the same spectra zoomed in at the d-d transition band at 640 nm. The arrows show the development of the spectra over time.

With $\mathbf{L^4SSL^4}$ a different situation was observed. When $[Cu^{I}(CH_3CN)_4]^{+}$ is added to $\mathbf{L^4SSL^4}$ in methanol a green solution is obtained, with UV-vis absorption bands similar to the bands of $[Cu^{II}_2(\mathbf{L^2S})_2]^{2+}$ in dichloromethane: the π^* ← π transition of the pyridyl groups at 261 nm (ε = 8350 M^{-1} cm^{-1}), Cu^{II} ← S LMCT transitions at 291 nm (ε = 5800 M^{-1} cm^{-1}) and 345 nm (ε = 2900 M^{-1} cm^{-1}), a d-d transition at 616 nm (ε = 245 M^{-1} cm^{-1}) and finally one band at 415 nm (ε = 800 M^{-1} cm^{-1}) that can be ascribed to either another LMCT or d-d transition. Based on the similarities of this UV-vis spectrum with that of $[Cu^{II}_2(\mathbf{L^2S})_2]^{2+}$, the complex in methanol is most likely the Cu^{II} μ-thiolate compound $[Cu^{II}_2(\mathbf{L^4S})_2]^{2+}$. The UV-vis spectrum of this complex was found to depend on the solvent (Figure 2.7a), suggesting that varying amounts of the μ-dithiolate compound $[Cu^{II}_2(\mathbf{L^4S})_2]^{2+}$ and of the disulfide compound $[Cu^{I}_2(\mathbf{L^4SSL^4})]^{2+}$ may be present in different solvents, an effect that was recently reported for ligand $\mathbf{L^1SSL^1}$ and that we also observed for $\mathbf{L^2SSL^2}$.[16] The ^{1}H NMR spectrum of $[Cu^{II}_2(\mathbf{L^4S})_2]^{2+}$ in

CD_3OD shows broad peaks in the diamagnetic region (Figure 2.8 and Figure AI.5, Appendix I). Using the Evans method we found the magnetic moment in CD_3OD to be μ_{eff} = 3.80 μ_B. This value implies that the complex is paramagnetic, which could mean that the anti-ferromagnetic coupling is very weak due to sterics which could lead to a longer Cu-Cu distance in the complex. Another explanation is that the complex forms monomer or oligomers instead of dimers in solution resulting in the disappearance of the anti-ferromagnetic coupling. When the green methanolic solution containing $[Cu^{II}_2(\mathbf{L^4S})_2]^{2+}$ was heated to reflux temperature for a period of ~30 h a brown solution was formed, from which crystals of $[Cu^{I}_2(\mathbf{L^4SSL^4})](BF_4)_2$ (Section 2.2.2) were obtained. The conversion from $[Cu^{II}_2(\mathbf{L^4S})_2]^{2+}$ to $[Cu^{I}_2(\mathbf{L^4SSL^4})]^{2+}$ was monitored using UV-vis spectroscopy (Figure 2.7b). Upon heating the Cu ← S LMCT transition at 345 nm shifted to 297 nm (ε = 2300 M^{-1} cm^{-1}) and became less intense over time. The absence of an isosbestic point indicated formation of an intermediate species in going from $[Cu^{II}_2(\mathbf{L^4S})_2]^{2+}$ to $[Cu^{I}_2(\mathbf{L^4SSL^4})]^{2+}$; the formation of this intermediate is indicated by the arrows in Figure 2.7b.

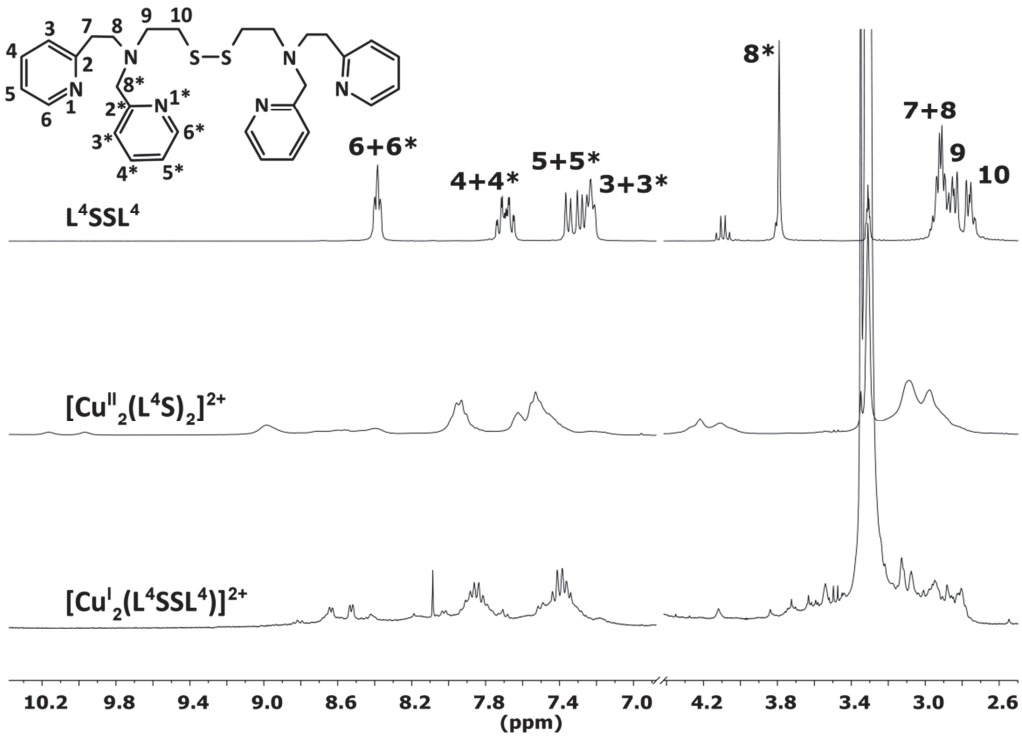

Figure 2.8: ^{1}H NMR spectra of $\mathbf{L^4SSL^4}$, $[Cu^{II}_2(\mathbf{L^4S})_2](BF_4)_2$ and $[Cu^{I}_2(\mathbf{L^4SSL^4})](BF_4)_2$ in CD_3OD at RT.

The conversion was also monitored by ^{1}H NMR spectroscopy. This showed the disappearance of $[Cu^{II}_2(\mathbf{L^4S})_2]^{2+}$ over time and the appearance of very low intensity diamagnetic peaks that can possibly be ascribed to $[Cu^{I}_2(\mathbf{L^4SSL^4})]^{2+}$ (Figure 2.8). The low intensity of the peaks might indicate the presence of paramagnetic species. However, the relatively broad signals obtained for the complexes with $\mathbf{L^4SSL^4}$ may arise from the presence of a mixture of diastereoisomers. Thus in contrast with $[Cu^{II}_2(\mathbf{L^2S})_2]^{2+}$, $[Cu^{II}_2(\mathbf{L^4S})_2]^{2+}$ is found to be a kinetic, less stable product that can convert to $[Cu^{I}_2(\mathbf{L^4SSL^4})]^{2+}$.

Cyclic voltammetry was carried out for $[Cu^{II}_2(\mathbf{L^2S})_2]^{2+}$, $[Cu^{II}_2(\mathbf{L^4S})_2]^{2+}$, $[Cu^{I}_2(\mathbf{L^2SSL^2})]^{2+}$ and $[Cu^{I}_2(\mathbf{L^4SSL^4})]^{2+}$ (Figures AI.6 and AI.7, Appendix I). All complexes show multiple irreversible waves, making assignment of the peaks difficult.

2.2.4 DFT Calculations

Energy of Formation

The formation of a Cu^{II} μ-thiolate complex (**A**) and a Cu^{I} disulfide complex (**B** or **C**) was studied computationally with DFT, calculating the energies for the different geometries for copper compounds of the ligands depicted in Figure 2.1. The Cu^{II} ions in the Cu^{II} μ-thiolate species are anti-ferromagnetically coupled,[6, 16] which has been taken into account computationally (see Section 2.5.3). The energy of formation was calculated according to equation (1) and these values are given in Table 2.3.

$$\mathbf{LSSL} + 2\,[Cu^{I}(CH_3CN)_4]^{+} \rightarrow [Cu_2(\mathbf{LSSL})]^{2+} \text{ or } [Cu_2(\mathbf{LS})_2]^{2+} + 8\,CH_3CN \qquad (1)$$

The computational results corroborate the trends that are witnessed experimentally for the reaction of different ligands with Cu^{I}. A lower energy was found for the Cu^{I} disulfide in *transoid* conformation **B** for $\mathbf{L^1SSL^1}$, $\mathbf{L^2SSL^2}$ and $\mathbf{L^3SSL^3}$, while for $\mathbf{L^4SSL^4}$ and $\mathbf{L^5SSL^5}$ the *cisoid* conformation **C** was found to have a lower energy. These results are in agreement with the crystal structures reported for $[Cu^{I}_2(\mathbf{L^3SSL^3})]^{2+}$ and $[Cu^{I}_2(\mathbf{L^5SSL^5})]^{2+}$.[6] When comparing the energy difference, $\Delta\Delta E$, between structure **A** and the most stable Cu^{I} disulfide structure for each ligand, an increase of $\Delta\Delta E$ was observed following the series $\mathbf{L^1SSL^1}$, $\mathbf{L^2SSL^2}$ and $\mathbf{L^3SSL^3}$, i.e., when the number of *ortho*-methyl groups increased from zero to four. $\mathbf{L^1SSL^1}$, which has been reported to form a Cu^{II} μ-thiolate complex, shows an almost negligible energy difference (–4 kJ mol^{-1}). This energy difference is in the order of the accuracy that can be obtained with our methodology.

Table 2.3: Energies of formation (kJ mol^{-1}) of Cu^{II} μ-thiolate (**A**) and Cu^{I} disulfide (**B** or **C**) complexes for different **LSSL** ligands and 2 [Cu^{I}(CH$_3$CN)$_4$]$^+$ in acetonitrile.[a]

	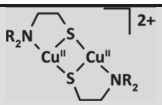 **A**	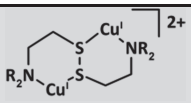 **B**	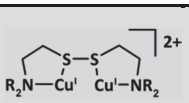 **C**	$\Delta\Delta E$ = $\Delta E_B - \Delta E_A$[b]	$\Delta\Delta E$ = $\Delta E_C - \Delta E_A$[b]
L^{1}SSL^1	−80	**−83**	−73	−4 (−3)	7 (9)
L^{2}SSL^2	−73	**−86**	−83	−13 (−11)	−9 (−4)
L^{3}SSL^3	−63	**−102**	−97	−39 (−35)	−34 (−27)
L^{4}SSL^4	−44	−60	**−93**	−16 (−11)	−49 (−32)
L^{5}SSL^5	27	−20	**−83**	−47 (−41)	−110 (−99)

[a]See equation (1). Computed at ZORA-OPBE/TZ2P in CH$_3$CN (COSMO).

[b]The energy differences in parentheses are the Gibbs free energies, $\Delta\Delta G$ (kJ mol^{-1}).

$\Delta\Delta E$ was found to be larger between **A** and **C** for **L^{4}SSL^4** and **L^{5}SSL^5**; –49 kJ mol^{-1} and –110 kJ mol^{-1} respectively. For **L^{4}SSL^4** the energy difference between **A** and **C** was found to be of a similar magnitude as the energy of formation of **A** (–44 kJ mol^{-1}), showing that the Cu^{II} μ-thiolate complex is intermediary in its formation energy between the starting point (**L^{4}SSL^4** + 2 [Cu^{I}(CH$_3$CN)$_4$]$^+$) and the Cu^{I} disulfide species. The formation of **A** appears even to be unfavorable for **L^{5}SSL^5** (+27 kJ mol^{-1}) which leads to a large energy difference between **A** and **C**. For **L^{2}SSL^2** and **L^{4}SSL^4** three different geometries were calculated for the μ-thiolate species **A**, as a result of the asymmetry caused by the pyridyl groups (Figures AI.8 and AI.9, Appendix I); only the energy of the complexes with the lowest energy is given in Table 2.3. The computed global minimum for [Cu$^{II}_2$(**L^{2}S**)$_2$]$^{2+}$ was found to have the same conformation as that found in the X-ray crystal structure (Figure 2.3). The differences in Gibbs energy, $\Delta\Delta G$, between **A** and **B**, or **A** and **C** are somewhat smaller than $\Delta\Delta E$, but the general trends are the same. The energies of formation in the gas phase show similar trends (Table AI.3 and AI.4, Appendix I).

No computational evidence was found for coordination of acetonitrile to Cu^{II} μ-thiolate or Cu^{I} disulfide complexes. This was established by bringing an acetonitrile molecule in close vicinity (coordination distance) of the copper center and calculating whether it would coordinate to the metal center. This in silico experiment was done for [Cu$^{II}_2$(**L^{2}S**)$_2$]$^{2+}$, [Cu$^{II}_2$(**L^{4}S**)$_2$]$^{2+}$, [Cu$^{I}_2$(**L^{2}SSL^2**)]$^{2+}$ (conformation **B**) and [Cu$^{I}_2$(**L^{4}SSL^4**)]$^{2+}$ (conformation **C**) and in all cases the acetonitrile molecule moved away from the copper complex. Dissociation of one of the pyridyl groups in order to allow the coordination of acetonitrile was suggested for [Cu^{I}(tris(2-pyridylmethyl)amine)]$^+$ by Karlin and coworkers.[17] To see whether this is the case for our complexes, we have

calculated the energies for **A**, **B** and **C** for all five ligands with two dissociated pyridyl groups and one CH_3CN molecule per copper ion. These calculations show that dissociation of the pyridyl groups in favor of an acetonitrile molecule is always less favorable compared to its analogue with no CH_3CN coordinated (Table AI.5, Appendix I). Furthermore the dissociation of the S atom in the Cu^I complexes in favor of CH_3CN has been calculated for all ligands and again shows to be less favorable compared to no coordination of acetonitrile. These experiments indicate that the solvent-induced interconversion between the Cu^{II} μ-thiolate and Cu^I disulfide species are likely due to polarity differences rather than coordination of the solvent.

Bonding Energy

To gain more insight as to *why* either the μ-thiolate or the disulfide complex forms, the bond energy ΔE_{bond} between the two Cu^I ions and the different ligands was analyzed in more detail in the gas phase. Note that the key trends found for the condensed phase computations also occur in the gas phase that is, the thiolate (**A**) and the disulfide forms (**B** or **C**) are essentially at the same energy for $\mathbf{L^1SSL^1}$ whereas the disulfide form is clearly more stable for the other ligands. The ΔE_{bond} comprises the deformation energy of the ligand (ΔE_L), the electrostatic repulsion between the two Cu^I ions ($\Delta E_{Cu\text{-}Cu}$) and the copper-ligand interaction energy (ΔE_{int}).

$$\Delta E_{bond} = \Delta E_L + \Delta E_{Cu\text{-}Cu} + \Delta E_{int} \qquad (2)$$

ΔE_L is the strain energy that is needed to distort the ligand from its lowest energy conformation to the conformation in the complex. $\Delta E_{Cu\text{-}Cu}$ represents the energy that is needed to bring the two Cu^I ions from infinity to the distance that they have in the complex. The term ΔE_{int} accounts for the interaction energy between the deformed ligand and the fragment of two Cu^I ions. The results are given in Table 2.4. The values for ΔE_L show that the energy it takes to change the ligand to the complex conformation is much higher for the μ-thiolate complexes than for the disulfide complexes **B** and **C**. The reason for this is that in the thiolate complex **A** the S-S bond is broken, whereas in the disulfide complexes **B** and **C** it is preserved. ΔE_{bond} differs slightly for ligands $\mathbf{L^1SSL^1}$, $\mathbf{L^2SSL^2}$ and $\mathbf{L^3SSL^3}$ in conformation **A** and shows only small energy differences between geometries **B** and **C**.

Table 2.4: The ligand distortion energy (ΔE_L), Cu^I-Cu^I electrostatic repulsion energy ($\Delta E_{Cu\text{-}Cu}$), interaction energy (ΔE_{int}), and bonding energy (ΔE_{bond}) in kJ mol^{-1} for complexes with geometry A, B and C in the gas phase.[a]

	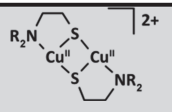 A				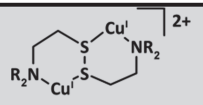 B				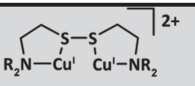 C			
	ΔE_L[b]	$\Delta E_{Cu\text{-}Cu}$	ΔE_{int}	ΔE_{bond}	ΔE_L	$\Delta E_{Cu\text{-}Cu}$	ΔE_{int}	ΔE_{bond}	ΔE_L	$\Delta E_{Cu\text{-}Cu}$	ΔE_{int}	ΔE_{bond}
L^1SSL^1	400	1854	–3161	–907	119	1730	–2772	–923	128	1724	–2774	–922
L^2SSL^2	374	1849	–3140	–917	100	1728	–2772	–944	101	1717	–2767	–949
L^3SSL^3	376	1841	–3113	–897	104	1727	–2773	–942	105	1718	–2767	–944
L^4SSL^4	448	1855	–3197	–894	165	1724	–2781	–893	146	1725	–2793	–922
L^5SSL^5	487	1842	–3163	–835	200	1720	–2783	–863	156	1727	–2810	–927

[a] Computed at ZORA-OPBE/TZ2P.

[b] The deformed ligand was computed as a singlet biradical (see Section 2.5.3).

For **L**^{4}**SSL**^{4} and **L**^{5}**SSL**^{5}, a large increase for ΔE_L is observed for **A**, leading to somewhat less stabilizing ΔE_{bond} values of –894 and –835 kJ mol^{-1} respectively. For **B** and **C** a similar trend can be seen with significantly more destabilizing ligand strain energy ΔE_L in combination with slightly more stabilizing ΔE_{int} values. This indicates that the energy necessary to distort **L**^{4}**SSL**^{4} and **L**^{5}**SSL**^{5} to the binding conformation is much larger than for **L**^{1}**SSL**^{1}, **L**^{2}**SSL**^{2} and **L**^{3}**SSL**^{3}. The electrostatic repulsion $\Delta E_{Cu\text{-}Cu}$ between the two copper ions is nearly constant going down the column from **L**^{1}**SSL**^{1} to **L**^{5}**SSL**^{5}, showing that complex formation is predominantly dependent on the ligand deformation. The ΔE_L values for **L**^{4}**SSL**^{4} and **L**^{5}**SSL**^{5} also reveal a large preference for the formation of geometry **C** over **B**.

2.3 Discussion

Two new ligands **L**^{2}**SSL**^{2} and **L**^{4}**SSL**^{4} were synthesized with structural properties intermediate to those of ligand **L**^{1}**SSL**^{1} and **L**^{3}**SSL**^{3} or **L**^{5}**SSL**^{5} respectively. When these ligands are reacted with $[Cu^I(CH_3CN)_4]^+$ in solution, either a Cu^{II} μ-thiolate (**A**) or a Cu^I disulfide (*transoid* **B** or *cisoid* **C**) species is formed depending on the structure of the ligand, the coordinating properties of the solvent and the temperature. For the ligand **L**^{2}**SSL**^{2} the formation of **A** is confirmed by X-ray structure determination of $[Cu^{II}_2(\mathbf{L^2S})_2](BF_4)_2{\cdot}C_3H_6O$, which is further characterized by its specific LMCT and d-d transitions in the UV-vis spectrum. For the ligand **L**^{4}**SSL**^{4} the formation of $[Cu^I_2(\mathbf{L^4SSL^4})]^{2+}$ was determined by X-ray crystallography, which confirms conformation **C** for $[Cu^I_2(\mathbf{L^4SSL^4})]^{2+}$. For comparison, single crystals of $[Cu^I_2(\mathbf{L^3SSL^3})](BF_4)_2$ were also prepared; X-ray structure determination showed the *transoid*-disulfide conformation **B** (see Figure AI.1 and Table AI.1 and AI.2, Appendix I) to be in agreement with an earlier report.[6]

Modeling these systems computationally with DFT is challenging because of the large number of atoms, but the calculations and the experimental facts give a consistent view. The formation energies calculated for the different copper compounds using DFT show clear trends in the two ligand series, which have been plotted in Figure 2.9. When the geometry optimizations are done in the gas phase similar trends are obtained (Table AI.3 and AI.4, Appendix I), indicating that the calculated energies are not strongly dependent on the solvent, but are inherent to the system. For **L**^{1}**SSL**^{1}, the energy difference between the Cu^{II} thiolate species and the Cu^I disulfide complex is very small, but with increasing steric bulk (methyl groups) or increasing number of ethylene bridges (between the tripodal amine and the pyridine rings) on the ligand the energy differences become larger.

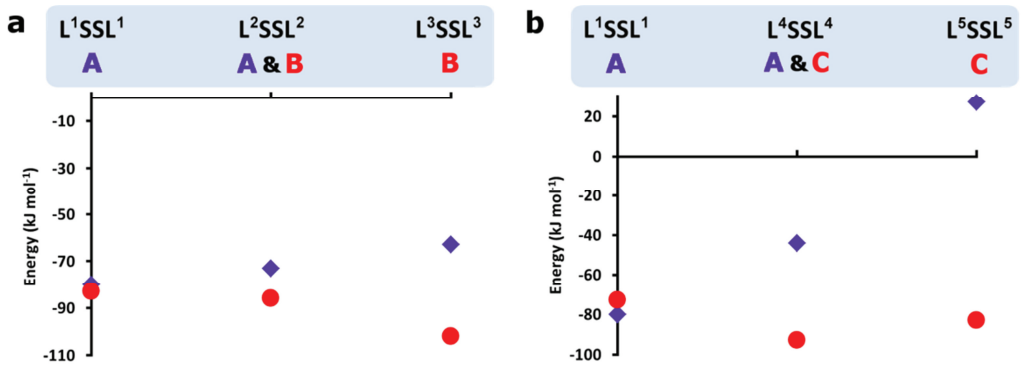

Figure 2.9: Plot of the formation energies (kJ mol^{-1}) of the μ-thiolato Cu^{II} (◆) and Cu^{I} disulfide (●) species a) for ligands **L^{1}SSL^1**, **L^{2}SSL^2** and **L^{3}SSL^3** (conformation **A** and **B**) and b) for ligands **L^{1}SSL^1**, **L^{4}SSL^4** and **L^{5}SSL^5** (conformation **A** and **C**). The blue and red letters indicate the conformation found experimentally for each ligand.

The presence of an ethylene bridge seems to destabilize the Cu^{II} μ-thiolate species to a greater extent than the introduction of a methyl group on the pyridyl ring. This is to be expected considering that the methylene-bridged ligands, like **L^{1}SSL^1**, form five-membered chelate rings with copper whereas the ethylene-bridged ligands, like **L^{5}SSL^5**, form six-membered chelate rings with copper (Figure 2.10). In the μ-thiolate compounds, the Cu^{II} ions have square-pyramidal geometries and therefore prefer coordination angles close to 90°, which means that they would prefer a five-membered chelate ring over a six-membered ring. The larger Cu^{I} ions prefer tetrahedral geometries and can therefore also cope with larger coordination angles such as those found in a six-membered chelate ring.

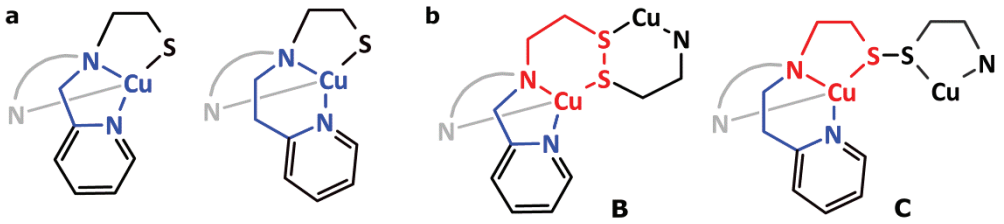

Figure 2.10: Schematic representation of the five- and six-membered rings formed by copper and the pyridyl groups in blue (a) and the five- and six-membered rings formed by copper and the disulfide bridge in geometry **B** and **C** in red (b).

Considering this, it is not surprising that **L**^{5}**SSL**^{5} and to some extent **L**^{4}**SSL**^{4} form Cu^I disulfide compounds in conformation **C**, which is also reflected in ΔE_L (Table 2.4). The deformation energy of the ligand is much higher for **L**^{4}**SSL**^{4} and for **L**^{5}**SSL**^{5}, than it is for the other three ligands indicating that formation of either **A** or **C** is largely induced by steric effects, i.e., the preference of Cu^I and Cu^{II} to form six- and five-membered rings in combination with the length of the ethylene vs. methylene bridges in the ligands. In this respect, **L**^{4}**SSL**^{4} is a unique ligand with its ability to form both five-membered and six-membered rings, ultimately leading to the Cu^I disulfide conformation **C**, but with the ability to also form the Cu^{II} μ-thiolato complex.

A novel discovery is that the equilibrium between the Cu^{II} μ-thiolate and the Cu^I disulfide species can be temperature-dependent. **L**^{2}**SSL**^{2} favors formation of the μ-thiolate complex at low temperatures and the disulfide compound at higher temperatures, although it must be noted that this equilibrium is only reversible at lower temperatures. Whether the compound $[Cu^I_2(\mathbf{L}^2\mathbf{SSL}^2)]^{2+}$ adopts conformation **B** and/or **C** is rather difficult to determine. As far as we know, clear spectroscopic differences between these two coordination isomers do not exist. Since **L**^{2}**SSL**^{2} is similar to **L**^{3}**SSL**^{3}, which has been crystallized with Cu^I in geometry **B**,[6] it would not be surprising if **L**^{2}**SSL**^{2} gives the same conformation as confirmed by the energies calculated for the complexes of **L**^{2}**SSL**^{2} that indicate a slight preference for geometry **B** (Table 2.3).

The UV-vis absorption spectra of $[Cu^{II}_2(\mathbf{L}^4\mathbf{S})_2]^{2+}$ show varying absorption intensities in different solvents (Figure 2.7a). A similar effect was recently reported by the group of Stack who studied the interaction of Cu^I with the ligand **L**^{1}**SSL**^{1}, which they ascribed to the formation of a higher concentration of μ-thiolate species **A** in less coordinating solvents.[16] In the temperature-controlled conversion of $[Cu^{II}_2(\mathbf{L}^4\mathbf{S})_2]^{2+}$ to $[Cu^I_2(\mathbf{L}^4\mathbf{SSL}^4)]^{2+}$ the formation of an intermediate species was observed, which may be ascribed to the intermediate formation of conformation **B** before isomerization to **C** occurs. This is in agreement with the DFT results, showing that geometry **B** with –60 kJ mol^{-1} is in between geometry **A** (–44 kJ mol^{-1}) and geometry **C** (–93 kJ mol^{-1}) in terms of formation energy. Since there is no evidence of the reverse reaction from **C** to **A**, the μ-thiolato Cu^{II} species **A** can be described as a kinetic product and the Cu^I disulfide species **C** as the thermodynamic product. A schematic overview of the experimental results is provided in Figure 2.11.

Considering the results from both the experiments and the calculations, it seems that whether the Cu^{II} μ-thiolate species forms largely depends on the activation barrier in going from **A** to **B** or **C**. For **L**^{2}**SSL**^{2} this barrier appears to be low, which makes studying the equilibrium in methanol possible. In contrast, for **L**^{4}**SSL**^{4} this barrier is

high, resulting in initial formation of conformation **A**, which can be irreversibly converted to **C** by heating. Future work will be directed to quantifying these activation barriers, which is even more challenging. This might provide important additional information concerning this biologically highly relevant equilibrium.

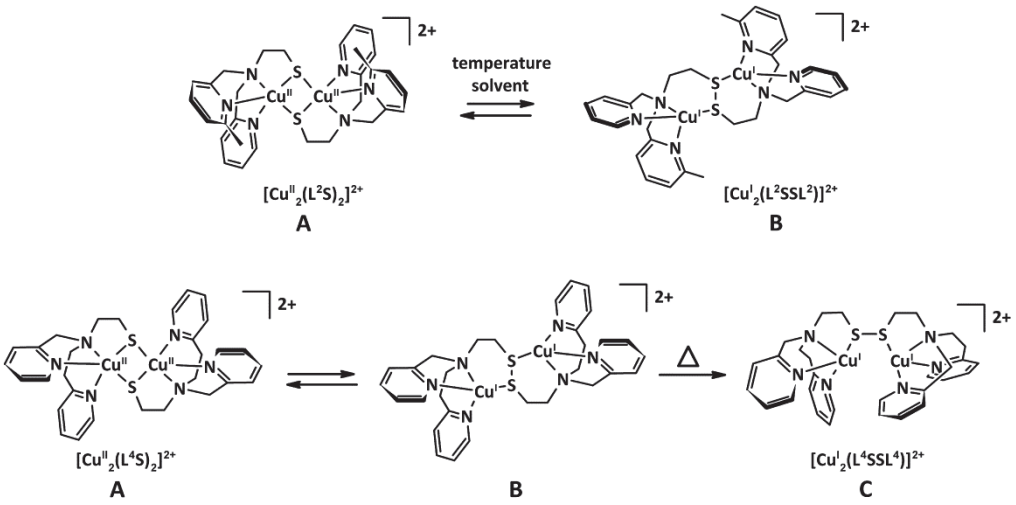

Figure 2.11: Schematic representation of the formation of Cu^{II} μ-thiolate and Cu^{I} disulfide complexes with **L^{2}SSL^2** and **L^{4}SSL^4**.

2.4 Conclusion

Two new dissymmetric ligands, **L^{2}SSL^2** and **L^{4}SSL^4**, were synthesized with an intermediate number of methyl groups (**L^{2}SSL^2**) or ethyl bridges (**L^{4}SSL^4**) compared with the known ligands **L^{1}SSL^1**, **L^{3}SSL^3**, and **L^{5}SSL^5**. Their Cu^{II} μ-thiolate and Cu^{I} disulfide complexes were characterized in the solid state as well as in solution. For **L^{2}SSL^2** the two redox isomeric forms are shown to be in an equilibrium that depends both on temperature and on solvent. The behavior of **L^{4}SSL^4** is unique as it forms the Cu^{II} μ-thiolate species as the kinetic product and the Cu^{I} disulfide complex as the thermodynamic product in methanol. These ligands opened the unique opportunity to compare both Cu^{II} μ-thiolate and Cu^{I} disulfide complexes in the same experimental conditions. DFT calculations provide theoretical insight into the energies involved in the formation of Cu^{II} μ-thiolate and Cu^{I} disulfide complexes and yield a picture that is consistent with the experimental results. An increase in energy difference between the Cu^{II} μ-thiolate and the Cu^{I} disulfide species was observed with increasing steric bulk (methyl groups) or increasing number of ethylene bridges (between the tripodal

amine and the pyridine rings) on the ligands. This implies that deformation of the ligand from its equilibrium structure to the geometry in the complex plays a large role as to whether the Cu^{II} μ-thiolate complex forms. The equilibrium between the two redox-isomeric species seems to be largely dependent on the activation barrier of going from the thiolate to the disulfide complex. This information provides interesting opportunities for future research as proteins generally use low activation barriers for their catalytic electron transfer reactions. Besides this, control over this biomimetic redox equilibrium allows for further analysis and understanding of biological copper-sulfur reactions and might provide opportunities in the field of electron sources and sinks.

2.5 Experimental Section

2.5.1 General Methods

Reagents and solvents were obtained from commercial sources. The syntheses of all copper complexes were carried out using standard Schlenk-line techniques under an argon atmosphere. Solvents were distilled and deoxygenated by bubbling a stream of argon through the solution and stored on activated molecular sieves under argon prior to use. $[Cu^{I}(CH_3CN)_4](BF_4)$, $[Cu^{I}(CH_3CN)_4](ClO_4)$ and bis-(2-(N-pyridylmethyl)aminoethyl) disulfide were synthesized according to literature procedures.[7] ^{1}H and ^{13}C NMR spectra were recorded on a Bruker 300 DPX spectrometer. NMR experiments under argon were carried out using a J. Young NMR tube. Evans method was carried out with mesitylene as the reference compound. IR spectra were obtained on a Perkin Elmer UATR (Single Reflection Diamond) Spectrum Two device (4000-700 cm^{-1}; resolution 4 cm^{-1}). Mass spectrometry was measured using a Finnigan Aqua Mass Spectrometer (MS) with electrospray ionization (ESI). Sample introduction was achieved through a Dionex ASI-100 automated sample injector with an eluent flow rate of 0.2 mL/min. UV-vis spectra were collected using a transmission dipprobe with variable path length on an Avantes Avaspec-2048 spectrometer with Avalight-DH-S-BAL light source. Elemental analyses were performed by the Microanalytical laboratory Kolbe in Germany. Cyclic voltammetry was performed with an Autolab PGstat10 potentiostat controlled by GPES4 software. A three electrode arrangement with a glassy carbon working electrode (3 mm diameter), an Ag/AgCl double junction reference electrode and a Pt wire counter electrode were used in different solvents with 0.1 M NBu_4PF_6 as the electrolyte. In these conditions the Fc/Fc^{+} couple was found to be located at +417 mV in MeOH, with a peak-to-peak separation of 51 mV; at + 461 mV in dichloromethane, with a peak-to-peak separation of 92 mV; at +433 mV in acetonitrile, with a peak-to-peak separation of 51 mV. Potentials are given relative to the Ag/AgCl electrode.

2.5.2 X-ray Crystallography

$[Cu^{II}_2(\mathbf{L^2S})_2](BF_4)_2 \cdot C_3H_6O$

All reflection intensities for $[Cu^{II}_2(\mathbf{L^2S})_2](BF_4)_2 \cdot C_3H_6O$ were measured at 110(2) K using a SuperNova diffractometer (equipped with Atlas detector) with Cu $K\alpha$ radiation (λ = 1.54178 Å) under the program CrysAlisPro (Version 1.171.36.24 Agilent Technologies, 2012). The program CrysAlisPro was also used to refine the cell dimensions and for data reduction. The structure was solved with the program SHELXS-2013 (Sheldrick, 2013)[18] and was refined on F^2 with SHELXL-2013 (Sheldrick, 2013).[18] Analytical numeric absorption corrections based on a multifaceted crystal model were applied using CrysAlisPro. The temperature of the data collection was controlled using the system Cryojet (manufactured by Oxford Instruments). The H atoms were placed at calculated positions using the instructions AFIX 23, AFIX 43 or AFIX 137 with isotropic displacement parameters having values 1.2 or 1.5 times *U*eq of the attached C atoms.

$[Cu^{I}_2(\mathbf{L^4SSL^4})](BF_4)_2$

All reflection intensities for $[Cu^{I}_2(\mathbf{L^4SSL^4})](BF_4)_2$ were measured at 110(2) K using a KM4/Xcalibur (detector: Sapphire3) with enhanced graphite-monochromated Mo $K\alpha$ radiation (λ = 0.71073 Å) under the program CrysAlisPro (Version 1.171.35.11 Oxford Diffraction Ltd., 2011). The program CrysAlisPro was used to refine the cell dimensions and for data reduction. The structure was solved with the program SHELXS-97 (Sheldrick, 2008)[18] and was refined on F^2 with SHELXL-97 (Sheldrick, 2008).[18] Analytical numeric absorption corrections based on a multifaceted crystal model were applied using CrysAlisPro. The temperature of the data collection was controlled using the system Cryojet (manufactured by Oxford Instruments). The H atoms were placed at calculated positions using the instructions AFIX 23 or AFIX 43 with isotropic displacement parameters having values 1.2 times *U*eq of the attached C atoms.

2.5.3 DFT Calculations

All calculations were performed with the Amsterdam Density Functional (ADF) program,[19, 20] using relativistic DFT at ZORA OPBE/TZ2P for geometry optimization and energies.[21] Solvation in acetonitrile was simulated using the conductor-like screening model (COSMO).[22-25] All stationary points in the gas phase and in the condensed phase were verified to be minima on the potential energy surface (PES) through vibrational analysis. The energies of the singlet state of the Cu^{II} μ-thiolate complexes (E^S) have been obtained from the unrestricted broken-symmetry singlet energies (E^{BS}) and the energy of the triplet (E^T) with the approximate projection method of Noodleman: $E^S = 2E^{BS} - E^T$.[26, 27] The biradical singlet state of the deformed ligand with the elongated S-S bond has also been obtained in this way.

The Gibbs free energies ($\Delta G = \Delta H - T\Delta S$) were evaluated with the following procedure. Enthalpies at 298.15 K and 1 atm (ΔH_{298}) were calculated from electronic bond energies (ΔE) in the solvent and vibrational frequencies using standard thermochemistry relations for an ideal gas, according to:[28] $\Delta H_{298} = \Delta E + \Delta E_{trans,298} + \Delta E_{rot,298} + \Delta E_{vib,0} + \Delta(\Delta E_{vib,0})_{298} + \Delta(pV)$

Here, $\Delta E_{trans,298}$, $\Delta E_{rot,298}$ and $\Delta E_{vib,0}$ are the differences between the two complexes in translational, rotational and zero point vibrational energy, respectively; $\Delta(\Delta E_{vib,0})_{298}$ is the change in the vibrational energy difference as one goes from 0 to 298.15 K. The vibrational energy corrections are based on our frequency calculations in the gas phase. The molar work term $\Delta(pV)$ is (Δn)RT, with n=0 ; Thermal corrections for the electronic energy are neglected. The entropy ΔS was also obtained from the gas phase calculations. Most systems were optimized in C_2 symmetry. CH_3CN was optimized with C_{3v} symmetry.

2.5.4 Ligand Synthesis

L²SSL²

Bis-2-((2-pyridylmethyl)amino)ethyl disulfide (2.86 g, 8.55 mmol) was dissolved in methanol (20 mL). 6-Methylpyridine-2-carboxaldehyde (2.08 g, 17.1 mmol) dissolved in methanol (22.5 mL) was added, followed by a scoop of anhydrous $MgSO_4$ and a few drops of formic acid. The resulting yellow solution was stirred for 4.5 h at RT. $NaCNBH_3$ (1.19 g, 18.8 mmol) was added in small portions over the course of 1 h, after which the solution was stirred for 30 minutes. The solution was filtered and evaporated to dryness. The product was treated with 2 M NaOH (120 mL) and extracted with dichloromethane. The organic layer was dried over $MgSO_4$ and evaporated to dryness yielding a dark yellow oil (4.05 g, 87%). The compound was purified by column chromatography over basic alumina (60/40 EtOAc/petroleum ether) yielding a cream-colored solid (0.71 g, 1.3 mmol, 16%), which can be recrystallized from petroleum ether. ^{1}H NMR (300 MHz, CD_3CN, RT): δ 2.44 (s, 6H, Py-CH_3), 2.77 (m, 8H, S-CH_2-CH_2), 3.72 (s, 4H, Py-CH_2-N), 3.76 (s, 4H, Py-CH_2-N), 7.04 (d, J = 8 Hz, 2H, Py$_{Me}$-H_3), 7.17 (m, 2H, Py$_{Me}$-H_5), 7.32 (d, J = 8 Hz, 2H, Py-H_3), 7.55 (m, 4H, Py-H_4; Py$_{Me}$-H_4), 7.68 (td, J = 8 Hz, 2 Hz, 2H, Py-H_5), 8.45 (m, 2H, Py-H_6). ^{13}C NMR (75 MHz, CD_3CN, RT): δ 24.5 (Py-CH$_3$), 37.3 (S-CH$_2$), 54.2 (S-CH$_2$-CH$_2$), 60.9 (Py-CH$_2$-N), 60.9 (Py-CH$_2$-N), 120.8 (Py$_{Me}$-C_5), 122.3 (Py$_{Me}$-C_3), 123.0 (Py-C_5), 124.0 (Py-C_3), 137.4 (Py$_{Me}$-C_4), 137.7 (Py-C_4), 149.7 (Py-C_6), 158.4 (Py$_{Me}$-C_2), 159.8 (Py$_{Me}$-C_6), 160.5 (Py-C_2). ESI-MS found (calculated) for $[M+H]^+$ m/z 545.1 (545.3). IR (neat, cm^{-1}): 2817m, 1591s, 1578s, 1463s, 1436s, 1360s, 1107s, 788m, 762m, 614s.

L⁴SSL⁴

To bis-2-((2-pyridylmethyl)amino)ethyl disulfide (6.24 g, 18.7 mmol) was added glacial acetic acid (3.0 mL, 52.0 mmol), 2-vinylpyridine (5.2 mL, 48.0 mmol) and 8 mL methanol. The solution was stirred for 4 days at 70 °C and then evaporated to dryness yielding a dark green oil. To this oil a solution of Na_2CO_3 (100 mL, 2 M) was added, and the aqueous mixture was extracted with dichloromethane (3 × 100 mL). The combined layers were dried over Na_2SO_4 and evaporated to dryness giving a dark brown oil. This product was purified by column chromatography over basic alumina (60-70% EtOAc/petroleum ether) yielding a light-brown oil (6.63 g, 12.2 mmol, 65%). ^{1}H NMR (300 MHz, CD_3OD, RT): δ 2.75 (m, 4H, S-CH_2), 2.85 (m, 4H, S-CH$_2$-CH_2), 2.92 (m, 8H, Py-CH_2-CH_2-N), 3.79 (s, 4H, Py-CH_2-N), 7.23 (m, 4H, Py-H_3), 7.29 (d, J = 8 Hz, 2H, Py-H_5), 7.35 (d, J = 8 Hz, 2H, Py-H_5), 7.69 (m, 4H, Py-H_4), 8.39 (m, 4H, Py-H_6). ^{13}C NMR (75 MHz,

CD_3OD, RT): δ 36.5 (Py-CH_2-CH_2-N), 37.3 (S-CH_2), 54.5 (S-CH_2-CH_2), 55.4 (Py-CH_2-CH_2-N), 60.7 (Py-CH_2-N), 122.9 (Py-C_3), 123.7 (Py-C_3), 124.8 (Py-C_5), 125.5 (Py-C_5), 138.5 (Py-C_4), 149.2 (Py-C_6), 149.6 (Py-C_6), 160.8 (Py-C_2), 161.4 (Py-C_2). ESI-MS found (calculated) for $[M+Na]^+$ *m/z* 567.1 (567.2); $[M+H]^+$ *m/z* 545.0 (545.3). IR (neat, cm^{-1}): 2930*m*, 2816*m*, 1589*s*, 1568*m*, 1474*m*, 1433*s*, 993*m*, 752*s*, 403*m*.

2.5.5 Complex Synthesis

$[Cu^{II}_2(\mathbf{L^2S})_2](BF_4)_2$

L^2SSL^2 (68.9 mg, 0.126 mmol) was dissolved in dichloromethane (7.5 mL). To this solution $[Cu^I(CH_3CN)_4](BF_4)$ (79.8 mg, 0.253 mmol) was added, which resulted in a very dark green solution. This solution was stirred for 1 hour after which the solution was added to 80 mL pentane resulting in a greenish blue-grey precipitate (97.7 mg, 0.116 mmol, 91%). Crystals suitable for X-ray structure determination were obtained by slow vapor diffusion of pentane into an acetone solution containing the complex. ^1H NMR (300 MHz, CD_2Cl_2, RT): δ 2.70 (s, 6H, Py-CH_3), 3.16 (s, 8H, S-CH_2-CH_2), 3.99 (s, 8H, Py-CH_2-N), 7.24 (t, *J* = 9 Hz, 4H, Py-*H*), 7.42 (s, 4H, Py-*H*), 7.71 (t, *J* = 7.5 Hz, 2H, Py-*H*), 7.82 (t, *J* = 7.5 Hz, 2H, Py-*H*), 8.59 (s, 2H, Py-H_6). ESI-MS found (calculated) for [½ M + MeOH – $BF_4]^+$ *m/z* 367.0 (367.1). Elemental analysis calcd for $[Cu^{II}_2(\mathbf{L^2S})_2](BF_4)_2$: C 42.62, H 4.29, N 9.94, S 7.59; Found: C 41.95, H 4.62, N 9.99, S 7.69. IR (neat, cm^{-1}): 1606s, 1577s, 1466m, 1442m, 1050vs, 786m, 520s. UV-vis in dichloromethane at 1 mM [Cu] concentration: 261 nm (ε = 17200 M^{-1} cm^{-1}), 300 nm (ε = 7100 M^{-1} cm^{-1}), 358 nm (ε = 4200 M^{-1} cm^{-1}), 500 nm (ε = 1200 M^{-1} cm^{-1}), 627 nm (ε = 1100 M^{-1} cm^{-1}), 928 nm (ε = 410 M^{-1} cm^{-1}).

$[Cu^I_2(\mathbf{L^2SSL^2})](BF_4)_2$

L^2SSL^2 (5.45 mg, 0.01 mmol) was dissolved in acetonitrile (2 mL). To this solution was added $[Cu^I(CH_3CN)_4](BF_4)$ (6.29 mg 0.02 mmol), resulting in a light greenish yellow solution. Attempts to isolate the complex resulted in the formation of oil. ^1H NMR (300 MHz, CD_3CN, RT): δ 2.57 (s, 6H, Py-CH_3), 2.90 (m, 8H, S-CH_2-CH_2), 3.81 (s, 4H, Py-CH_2-N), 3.83 (s, 4H, Py-CH_2-N), 7.17 (d, *J* = 8 Hz, 2H, Py_{Me}-H_3), 7.25 (d, *J* = 8 Hz, 2H, Py-H_3), 7.30 (m, 2H, Py_{Me}-H_4), 7.44 (d, *J* = 8 Hz, 2H, Py_{Me}-H_5), 7.66 (t, *J* = 8 Hz, 2H, Py-H_4) 7.76 (t, *J* = 8 Hz, 2H, Py-H_5), 8.52 (d, *J* = 4 Hz, 2H, Py-H_6). ^{13}C NMR (75 MHz, CD_3CN, RT): δ 26.1 (Py-CH_3), 36.8 (S-CH_2), 56.6 (S-CH_2-CH_2), 60.2 (Py-CH_2), 60.5 (Py-CH_2), 122.0 (Py_{Me}-C_5), 124.9 (Py_{Me}-C_3, Py-C_5), 125.3 (Py-C_3), 139.2 (Py_{Me}-C_4), 139.4 (Py-C_4), 150.1 (Py-C_6), 156.9 (Py_{Me}-C_2), 157.8 (Py_{Me}-C_6), 158.7 (Py_{Me}-C_2). ESI-MS found (calculated) for $[M – 2\ BF_4]^{2+}$ *m/z* 335.1 (335.1); [½ M + MeOH – $BF_4]^+$ *m/z* 367.0 (367.1) $[M – 2\ BF_4]^+$ *m/z* 607.1 (607.2). UV-vis in acetonitrile at 1 mM [Cu] concentration: 257 nm (ε = 7950 M^{-1} cm^{-1}), 309 nm (ε = 3150 M^{-1} cm^{-1}).

$[Cu^{II}_2(\mathbf{L^4S})_2](BF_4)_2$

One equivalent of **L^4SSL^4** was mixed with two equivalents of $[Cu^I(CH_3CN)_4](BF_4)$ in methanol yielding a bright green solution. Attempts to isolate the complex resulted in the formation of

oil. ^{1}H NMR (300 MHz, CD_3OD, RT): δ 2.98 (br, 8H, S-CH_2-CH_2), 3.08 (br, 8H, Py-CH_2-CH_2-N), 4.11 (br, 2H, Py-CH_2-N), 4.22 (br, 2H, Py-CH_2-N), 7.53 (m, 8H, Py-*H*), 7.94 (d, *J* = 8 Hz, 4H, Py-*H*), 8.40 (br, 1H, Py-*H*), 8.60 (m, 1H, Py-*H*), 8.98 (br, 2H, Py-*H*). ESI-MS found (calculated) for $[M - 2\ BF_4]^{2+}$ *m*/*z* 336.1 (335.1); $[M - Cu - 2\ BF_4]^+$ *m*/*z* 607.1 (607.2). UV-vis in dichloromethane at 1 mM [Cu] concentration: 261 nm (ε = 8350 M^{-1} cm^{-1}), 291 nm (ε = 5800 M^{-1} cm^{-1}), 345 nm (ε = 2900 M^{-1} cm^{-1}), 415 nm (ε = 800 M^{-1} cm^{-1}), 616 nm (ε = 245 M^{-1} cm^{-1}).

$[Cu^I_2(\mathbf{L^4SSL^4})](BF_4)_2$

L^4SSL^4 (34.0 mg, 0.062 mmol) was dissolved in methanol (6 mL). To this solution $[Cu^I(CH_3CN)_4](BF_4)$ (39.8 mg, 0.125 mmol) was added, which resulted in a bright green solution. The solution containing $[Cu^{II}_2(\mathbf{L^4S})_2](BF_4)_2$ was stirred for 45 hours at 67 °C resulting in a brown/green solution. This solution was added to 80 mL diethyl ether resulting in a green brown powder (37.1 mg, 0.044 mmol, 70 %). Crystals suitable for X-ray structure determination were obtained by vapor diffusion of *n*-hexane in a methanol solution containing the complex. Elemental analysis calcd for $[Cu^I_2(\mathbf{L^4SSL^4})](BF_4)_2$: C 42.62, H 4.29, N 9.94, S 7.59; Found: C 42.62, H 4.54, N 9.88, S 7.74. ESI-MS found (calculated) for $[½\ M - BF_4]^+$ *m*/*z* 335.0 (335.1); $[½\ M - BF_4 + CH_3O]^+$ *m*/*z* 366.0 (366.1); $[M - Cu - 2\ BF_4]^+$ *m*/*z* 607.1 (607.2). UV-vis in acetonitrile at 1 mM [Cu] concentration: 254 nm (ε = 6900 M^{-1} cm^{-1}), 297 nm (ε = 2300 M^{-1} cm^{-1}).

2.6 References

1. Solomon, E. I.; Sundaram, U. M.; Machonkin, T. E., *Chem. Rev.* **1996,** *96*, 2563-2606.
2. Jacob, C.; Giles, G. L.; Giles, N. M.; Sies, H., *Angew. Chem. Int. Ed.* **2003,** *42*, 4742-4758.
3. Bickelhaupt, F. M.; Sola, M.; Schleyer, P. V., *J. Comput. Chem.* **1995,** *16*, 465-477.
4. Carvalho, A. T. P.; Swart, M.; van Stralen, J. N. P.; Fernandes, P. A.; Ramos, M. J.; Bickelhaupt, F. M., *J. Phys. Chem. B* **2008,** *112*, 2511-2523.
5. Roos, G.; Fonseca Guerra, C.; Bickelhaupt, F. M., *J. Biomol. Struct. Dyn.* **2013**, 0-0.
6. Itoh, S.; Nagagawa, M.; Fukuzumi, S., *J. Am. Chem. Soc.* **2001,** *123*, 4087-4088.
7. Ueno, Y.; Tachi, Y.; Itoh, S., *J. Am. Chem. Soc.* **2002,** *124*, 12428-12429.
8. Ohta, T.; Tachiyama, T.; Yoshizawa, K.; Yamabe, T., *Tetrahedron Lett.* **2000,** *41*, 2581-2585.
9. Willcocks, A. M.; Johnson, A. L.; Raithby, P. R.; Schiffers, S.; Warren, J. E., *Acta Crystallogr. Sect. C* **2011,** *67*, 215-217.
10. Colak, A. T.; Yesilel, O. Z.; Buyukgungor, O., *J. Mol. Struct.* **2011,** *991*, 68-72.
11. Chou, C.-C.; Liu, H.-J.; Su, C.-C., *Dalton Trans.* **2008**, 3358-3362.
12. Creaven, B. S.; Mahon, M. F.; McGinley, J.; Moore, A. M., *Inorg. Chem. Commun.* **2006,** *9*, 231-234.
13. Evans, D. F., *J. Chem. Soc.* **1959**, 2003-2005.
14. Bain, G. A.; Berry, J. F., *J. Chem. Educ.* **2008,** *85*, 532-536.
15. Osako, T.; Ueno, Y.; Tachi, Y.; Itoh, S., *Inorg. Chem.* **2004,** *43*, 6516-6518.

16. Thomas, A. M.; Lin, B.-L.; Wasinger, E. C.; Stack, T. D. P., *J. Am. Chem. Soc.* **2013,** *135*, 18912-18919.
17. Lee, D. H.; Wei, N.; Murthy, N. N.; Tyeklar, Z.; Karlin, K. D.; Kaderli, S.; Jung, B.; Zuberbuhler, A. D., *J. Am. Chem. Soc.* **1995,** *117*, 12498-12513.
18. Sheldrick, G. M., *Acta Crystallogr. Sect. A* **2008,** *64*, 112-122.
19. te Velde, G.; Bickelhaupt, F. M.; Baerends, E. J.; Guerra, C. F.; Van Gisbergen, S. J. A.; Snijders, J. G.; Ziegler, T., *J. Comput. Chem.* **2001,** *22*, 931-967.
20. http://www.scm.com/
21. Swart, M.; Ehlers, A. W.; Lammertsma, K., *Mol. Phys.* **2004,** *102*, 2467-2474.
22. Klamt, A., *J. Phys. Chem.* **1995,** *99*, 2224-2235.
23. Klamt, A.; Schuurmann, G., *J. Chem. Soc., Perkin Trans. 2* **1993**, 799-805.
24. Pye, C. C.; Ziegler, T., *Theor. Chem. Acc.* **1999,** *101*, 396-408.
25. Swart, M.; Roesler, E.; Bickelhaupt, F. M., *Eur. J. Inorg. Chem.* **2007**, 3646-3654.
26. Noodleman, L., *J. Chem. Phys.* **1981,** *74*, 5737-5743.
27. Noodleman, L.; Baerends, E. J., *J. Am. Chem. Soc.* **1984,** *106*, 2316-2327.
28. Jensen, F., *Introduction to Computational Chemistry*. 2nd ed.; Wiley: Chichester, West Sussex, UK, **2006**.

Chapter 3

Protonation of the Biologically Relevant Cu^{II} μ-Thiolate Complex: Ligand Dissociation or Formation of a Protonated Cu^{I} Disulfide Species?

The proton-induced electron-transfer reaction of a Cu^{II} μ-thiolate complex to a Cu^{I} containing species has been investigated, both experimentally and computationally. The Cu^{II} μ-thiolate complex $[Cu^{II}_2(\mathbf{L^2{*}S})_2]^{2+}$ was isolated with the new pyridyl-containing ligand $\mathbf{L^2{*}SSL^2{*}}$, which has the ability to form both Cu^{II} thiolate and Cu^{I} disulfide complexes depending on the solvent. Both the Cu^{II} and the Cu^{I} complexes show reactivity upon addition of protons. The new multivalent tetranuclear complex $[Cu^{I}_2Cu^{II}_2(\mathbf{L^1{*}S})_2(CH_3CN)_6]^{4+}$ crystallized after addition of two equivalents of strong acid to a solution containing the μ-thiolate complex $[Cu^{II}_2(\mathbf{L^1{*}S})_2]^{2+}$ and was further analyzed in solution. Our studies show that upon addition of protons to the Cu^{II} thiolate compound the ligand dissociates from the copper centers, in contrast to an earlier report describing redox isomerization to a Cu^{I} disulfide species that is protonated at the pyridyl moieties. Computational studies of the protonated Cu^{II} μ-thiolate and Cu^{I} disulfide species with $\mathbf{L^1{*}SSL^1{*}}$ show that already upon addition of two equivalents of protons, ligand dissociation forming $[Cu^{I}(CH_3CN)_4]^{+}$ and protonated ligand is energetically favored over conversion to a protonated Cu^{I} disulfide complex.

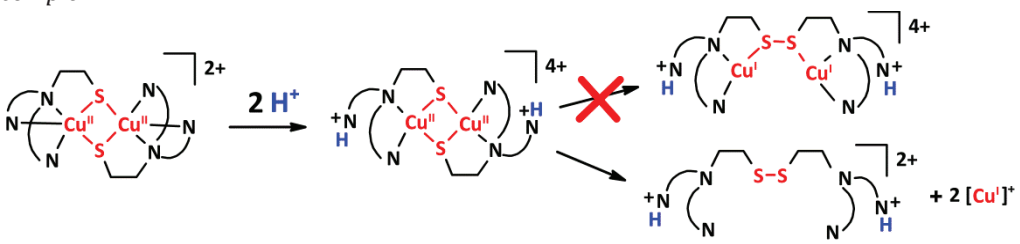

This chapter has been published as a full paper: E. C. M. Ording-Wenker, M. van der Plas, M. A. Siegler, C. Fonseca Guerra, E. Bouwman, *Chem. Eur. J.* **2014**, *20*, 16913-16921.

3.1 Introduction

The abundant occurrence of copper-sulfur redox chemistry in biological systems has attracted attention of inorganic chemists to study the equilibrium between Cu^{I} disulfide and Cu^{II} μ-thiolate species (Chapter 1). We found that upon addition of protons to a Cu^{II} μ-thiolate complex containing ligand **L¹*SSL¹***, a conversion takes place as indicated by a color change from dark green to light yellow. We decided to investigate this proton-induced conversion both with the ligand **L¹*SSL¹*** and a slightly modified analogue **L²*SSL²*** (Figure 3.1). The new ligand **L²*SSL²*** was synthesized, as it resembles the ligand **L²SSL²** for which we reported its solvent and temperature dependent Cu^{II} thiolate/Cu^{I} disulfide equilibrium when coordinated to copper (Chapter 2).[1]

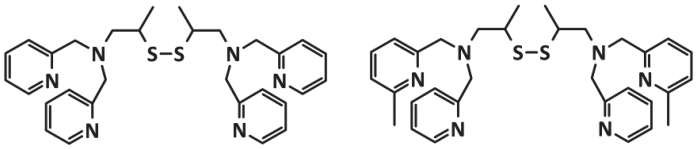

L¹*SSL¹* **L²*SSL²***

Figure 3.1: Schematic drawing of ligands **L¹*SSL¹*** and **L²*SSL²***.

Using protons to shift the redox equilibrium would provide an efficient way to trigger a copper-sulfur redox reaction in a controlled manner, giving new insights in proton-coupled electron transfer reactions in biological systems. During the course of our studies Stack and coworkers reported the dinuclear Cu^{II} μ-thiolate species with ligand **L¹*SSL¹*** upon addition of two equivalents of protons to convert to a Cu^{I} disulfide complex that is protonated at two of the pyridine groups (Section 1.4.4).[2] Addition of base was shown to reverse the reaction. Our studies, however, indicate that indeed the disulfide ligand is formed, but that it dissociates from the Cu^{I} centers already upon the addition of two equivalents of protons. DFT calculations were used to calculate the energies involved in this proton-induced conversion.

3.2 Results

3.2.1 Synthesis and Characterization of $[Cu^{I}_2Cu^{II}_2(\mathbf{L^{1*}S})_2(CH_3CN)_6](BF_4)_4$ and $[Cu^{II}_2(\mathbf{L^{2*}S})_2](BF_4)_2$

The ligands **L¹*SSL¹*** and **L²*SSL²*** were synthesized using a combination of reported procedures (Figure 3.2).[2-4]

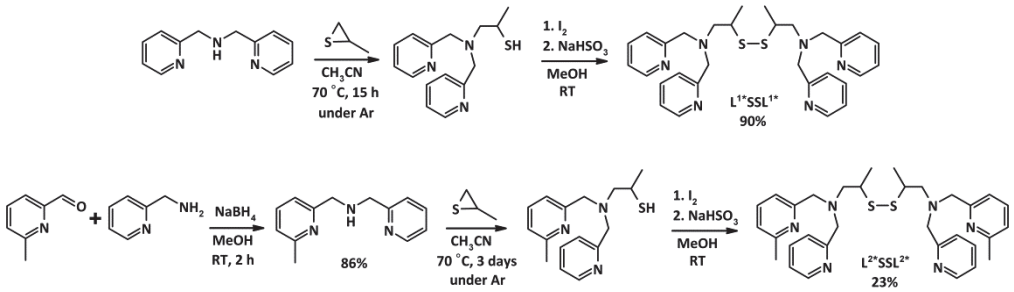

Figure 3.2: Schematic representation of the synthesis of **L¹*SSL¹*** and **L²*SSL²***.

Addition of 2 equivalents of $[Cu^{I}(CH_3CN)_4](BF_4)$ to **L¹*SSL¹*** dissolved in acetonitrile resulted in a dark green solution containing the Cu^{II} thiolate species $[Cu^{II}_2(\mathbf{L^{1*}S})_2]^{2+}$.[2] Subsequent addition of two equivalents of $HBF_4{\cdot}Et_2O$ resulted in a light brown solution to which diethyl ether was slowly added by vapor diffusion. This resulted in small black needle-like crystals of $[Cu^{I}_2Cu^{II}_2(\mathbf{L^{1*}S})_2(CH_3CN)_6](BF_4)_4$ as was unambiguously confirmed by X-ray structure determination. This complex can also be obtained by addition of 4 equivalents of $[Cu^{I}(CH_3CN)_4](BF_4)$ to **L¹*SSL¹*** dissolved in CH_3CN. When 2 equivalents of $[Cu^{I}(CH_3CN)_4](BF_4)$ were added to a solution of **L²*SSL²*** in acetone, again a dark green solution was obtained. Single crystals of the Cu^{II} μ-thiolate compound $[Cu^{II}_2(\mathbf{L^{2*}S})_2](BF_4)_2$ were obtained by vapor diffusion of pentane into this acetone solution; its structure was confirmed by single crystal X-ray crystallography. Projections of the cationic parts of the two structures are depicted in Figure 3.3.

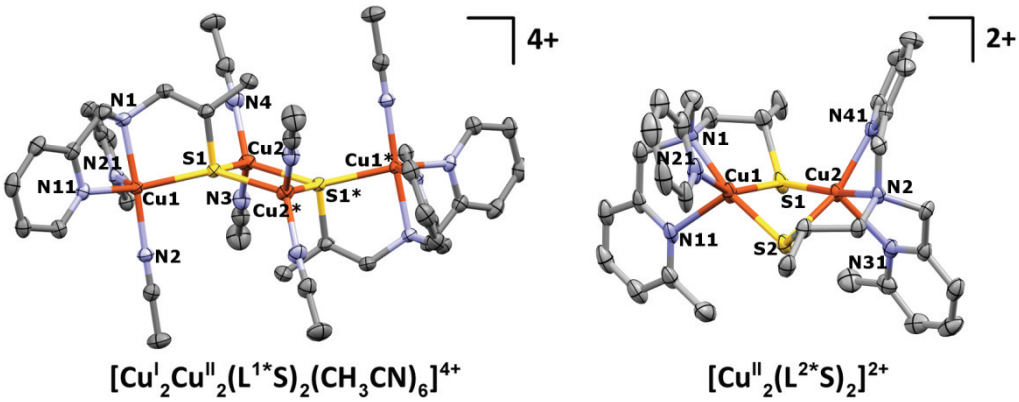

Figure 3.3: Displacement ellipsoid plots (50% probability level) of the cationic parts of $[Cu^{I}_2Cu^{II}_2(\mathbf{L^{1*}S})_2(CH_3CN)_6](BF_4)_4$ and $[Cu^{II}_2(\mathbf{L^{2*}S})_2](BF_4)_2$. Hydrogen atoms are omitted for clarity. Symmetry operation * = 1–x, 1–y, 2–z.

Table 3.1: Crystallographic and structure refinement data for complexes $[Cu^{I}_2Cu^{II}_2(\mathbf{L^{1*}S})_2(CH_3CN)_6](BF_4)_4$ and $[Cu^{II}_2(\mathbf{L^{2*}S})_2](BF_4)_2$.

	$[Cu^{I}_2Cu^{II}_2(\mathbf{L^{1*}S})_2(CH_3CN)_6](BF_4)_4$	$[Cu^{II}_2(\mathbf{L^{2*}S})_2](BF_4)_2$
empirical formula	$[C_{42}H_{54}Cu_4N_{12}S_2](BF_4)_4$	$[C_{32}H_{40}Cu_2N_6S_2](BF_4)_{1.8}(Cl)_{0.2}$
formula weight	1392.49	863.33
crystal system	monoclinic	monoclinic
space group	$P2_1/c$	$P2_1/n$
a, Å	12.2732(2)	10.3463(3)
b, Å	21.0952(2)	34.6731(11)
c, Å	12.1283(2)	11.4305(3)
β, deg	116.609(2)	99.087(2)
V, Å^3	2807.50(8)	4049.1(2)
Z	2	4
D_{calc}, g·cm^3	1.647	1.416
T, K	100(2)	110(2)
crystal size, mm	$0.40 \times 0.06 \times 0.05$	$0.44 \times 0.18 \times 0.03$
μ, mm^{-1}	3.266	2.938
no. of reflns measd	32508	25812
no. of unique reflns	5504	7877
no. of reflns obsd.	4993 [$I > 2\sigma(I)$]	6781 [$I > 2\sigma(I)$]
no. of parameters	457	632
R_1 / wR_2 [$I > 2\sigma(I)$]	0.0442/0.1216	0.0587/0.1657
R_1 / wR_2 [all refl.]	0.0478/0.1254	0.0669/0.1722
goodness of fit	1.084	1.076
$\Delta\rho$, e·Å^{-3}	−1.02 /0.78	−0.64 /0.96

Crystallographic data are provided in Table 3.1 and selected bond distances and angles are provided in Table 3.2 and Table 3.3.

The complex $[Cu^{I}_2Cu^{II}_2(\mathbf{L^{1*}S})_2(CH_3CN)_6](BF_4)_4$ crystallizes in the monoclinic space group $P2_1/c$ with one half of the tetranuclear complex cation and two tetrafluoridoborate anions per asymmetric unit; the tetranuclear complex is found at sites of inversion symmetry. Both BF_4^- counterions are disordered over two orientations; the occupancy factors of the major components of the disorder refine to 0.64(3) and 0.601(8). $[Cu^{I}_2Cu^{II}_2(\mathbf{L^{1*}S})_2(CH_3CN)_6](BF_4)_4$ is a tetranuclear mixed-valent complex containing two Cu^{I} and two Cu^{II} ions. The structure is best described as two Cu^{II} thiolate fragments $[Cu^{II}(\mathbf{L^{1*}S})(CH_3CN)]^+$ connected by two $[Cu^{I}(CH_3CN)_2]^+$ moieties, resulting in a planar four-membered Cu^{I}-S-Cu^{I}-S rhombus with Cu^{I}-S distances of 2.3102(7) Å and 2.4070(7) Å. The Cu^{II}-S distance is 2.3130(6) Å, which is similar to the Cu^{II}-S distances in the related Cu^{II} μ-thiolate structure $[Cu^{II}_2(\mathbf{L^{1*}S})_2]^{2+}$ (2.2909(8) Å and 2.3159(9) Å)[2] and in a similar multivalent complex $[Cu^{II}_4Cu^{I}_4(\mathbf{L^{1*}S})_4(\mu\text{-}OH)_2(CH_3CN)_6]^{6+}$ (2.34-2.36 Å) that is described in Chapter 4.[3]

Table 3.2: Selected bond distances and angles for $[Cu^{I}_2Cu^{II}_2(\mathbf{L^{1*}S})_2(CH_3CN)_6](BF_4)_4$.

Bond distance (Å)		Bond angle (°)	
Cu1 - Cu2	3.8679(5)	Cu1 - S1 - Cu2	113.57(3)
Cu1 - Cu2*	4.4799(5)	Cu1 - S1 - Cu2*	143.28(3)
Cu2 - Cu2*	3.4011(7)	Cu2 - S1 - Cu2*	92.25(2)
S1 - S1*	3.2703(11)	S1 - Cu1 - N1	88.10(6)
Cu1 - S1	2.3130(6)	S1 - Cu1 - N2	95.22(6)
Cu1 - N1	2.033(2)	S1 - Cu1 - N11	136.87(6)
Cu1 - N2	1.983(2)	S1 - Cu1 - N21	105.48(6)
Cu1 - N11	2.056(2)	N1 - Cu1 - N2	176.14(8)
Cu1 - N21	2.128(2)	N1 - Cu1 - N11	81.70(8)
Cu2 - S1	2.3102(7)	N1 - Cu1 - N21	82.61(8)
Cu2* - S1	2.4070(7)	N2 - Cu1 - N11	97.14(9)
Cu2 - N3	1.989(2)	N2 - Cu1 - N21	94.59(8)
Cu2 - N4	2.023(2)	N11 - Cu1 - N21	114.45(8)
		S1 - Cu2 - S1*	87.75(2)
		S1 - Cu2 - N3	132.02(7)
		S1 - Cu2 - N4	114.03(7)
		S1* - Cu2 - N3	105.86(7)
		S1* - Cu2 - N4	124.52(7)
		N3 - Cu2 - N4	95.82(10)

symmetry operation * = 1–x, 1–y, 2–z

The Cu^{II} ions are in an N_4S coordination environment, which can be best described as a highly distorted trigonal bipyramid ($\tau = 0.65$).[5]

$[Cu^{II}_2(\mathbf{L^{2*}S})_2](BF_4)_2$ crystallizes in the monoclinic space group $P2_1/n$. One BF_4^- counterion is found to be disordered over two orientations; the occupancy factor of the major component of the disorder refines to 0.510(6).

Table 3.3: Selected bond distances and angles for $[Cu^{II}_2(\mathbf{L^{2*}S})_2](BF_4)_2$.

Bond distance (Å)		Bond angle (°)	
Cu1 - Cu2	3.0278(7)	Cu1 - S1 - Cu2	82.24(3)
S1 - S2	3.1877(13)	Cu1 - S2 - Cu2	82.05(3)
Cu1 - S1	2.3022(10)	S1 - Cu1 - S2	87.48(4)
Cu1 - S2	2.3087(10)	S1 - Cu1 - N1	88.23(9)
Cu1 - N1	2.081(3)	S1 - Cu1 - N11	98.93(9)
Cu1 - N11	2.278(3)	S1 - Cu1 - N21	153.93(12)
Cu1 - N21	2.026(4)	S2 - Cu1 - N1	168.74(9)
		S2 - Cu1 - N11	111.43(9)
		S2 - Cu1 - N21	100.48(9)
Dihedral angle (°)		N1 - Cu1 - N11	79.53(12)
Cu1 - S1 - S2 - Cu2	–130.95(6)	N1 - Cu1 - N21	79.19(13)
Cu1 - S1 - Cu2 - S2	33.47(4)	N11 - Cu1 - N21	101.08(13)

symmetry operation * = 1–x, 1–y, 2–z

The other BF_4^- counterion is significantly disordered over at least three orientations.[6] The structure is highly similar to those of two reported μ-thiolate complexes $[Cu^{II}_2(\mathbf{L^{1*}S})_2](SbF_6)$ and $[Cu^{II}_2(\mathbf{L^2S})_2](BF_4)$ (Chapter 2).[1, 2] The Cu-Cu distances in $[Cu^{II}_2(\mathbf{L^{2*}S})_2]^{2+}$, $[Cu^{II}_2(\mathbf{L^{1*}S})_2]^{2+}$ and $[Cu^{II}_2(\mathbf{L^2S})_2]^{2+}$ are 3.03 Å, 2.94 Å and 3.04 Å respectively; the S-S distances are 3.19 Å, 3.13 Å and 3.16 Å. The folding angles of the Cu-S butterfly core over the S-S axis are 49°, 59° and 47°. In the structure of $[Cu^{II}_2(\mathbf{L^{2*}S})_2](BF_4)_2$ both methyl-substituted pyridyl rings are located at the same side of the Cu-S plane, as was found in the structure of $[Cu^{II}_2(\mathbf{L^2S})_2](BF_4)$.[1]

3.2.2 $[Cu^{I}_2Cu^{II}_2(\mathbf{L^{1*}S})_2(CH_3CN)_6]^{4+}$ and $[Cu^{II}_2(\mathbf{L^{2*}S})_2]^{2+}$ in Solution

Upon addition of two equivalents of $[Cu^{I}(CH_3CN)_4]^+$ to $\mathbf{L^{1*}SSL^{1*}}$ dissolved in CH_3CN, a solution containing $[Cu^{II}_2(\mathbf{L^{2*}S})_2]^{2+}$ is obtained, showing absorption bands at 248 nm ($\pi^* \leftarrow \pi$ pyridyl groups), 310 nm ($Cu^{II} \leftarrow$ S LMCT), 370 nm ($Cu^{II} \leftarrow$ S LMCT), as well as at 580, 785 and 910 nm (d-d transitions) as depicted in Figure 3.4a. Addition of two additional equivalents of $[Cu^{I}(CH_3CN)_4]^+$ leads to the formation of a brown solution from which $[Cu^{I}_2Cu^{II}_2(\mathbf{L^{1*}S})_2(CH_3CN)_6](BF_4)_4$ can be obtained. The UV-vis spectrum of $[Cu^{I}_2Cu^{II}_2(\mathbf{L^{1*}S})_2(CH_3CN)_6]^{4+}$ is almost identical to that of $[Cu^{II}_2(\mathbf{L^{1*}S})_2]^{2+}$ indicating that the Cu^{II} thiolate moiety is still present. This is confirmed by ^{1}H NMR spectroscopy (Figure 3.5); the resonances observed for $[Cu^{I}_2Cu^{II}_2(\mathbf{L^{1*}S})_2(CH_3CN)_6]^{4+}$ are similar to those for $[Cu^{II}_2(\mathbf{L^{1*}S})_2]^{2+}$, but are broadened indicating loss of the anti-ferromagnetic coupling between the two copper ions that occurs in $[Cu^{II}_2(\mathbf{L^{1*}S})_2]^{2+}$.

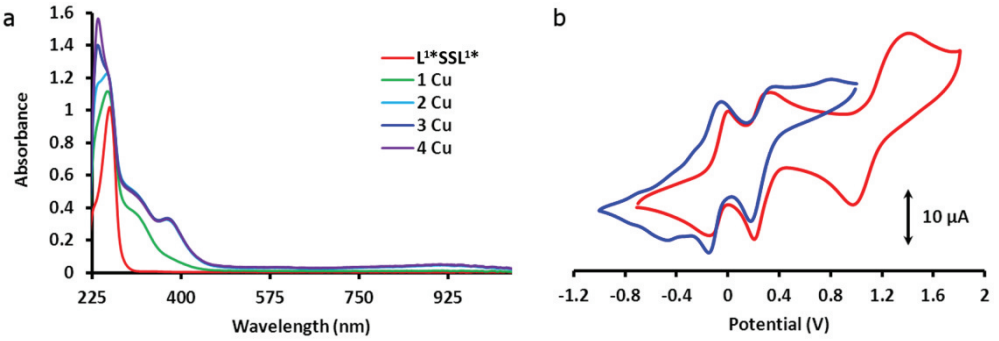

Figure 3.4: UV-vis spectra of $\mathbf{L^{1*}SSL^{1*}}$ (0.5 mM in CH_3CN) with 1, 2, 3 and 4 equivalents of $[Cu^{I}(CH_3CN)_4](BF_4)$ recorded with a transmission dipprobe set at a path length of 1.2 mm (a) and cyclic voltammograms of $\mathbf{L^{1*}SSL^{1*}}$ (0.5 mM) in CH_3CN with 2 equivalents (blue) and 4 equivalents (red) of $[Cu^{I}(CH_3CN)_4](BF_4)$ (b). Potentials are vs Ag/AgCl.

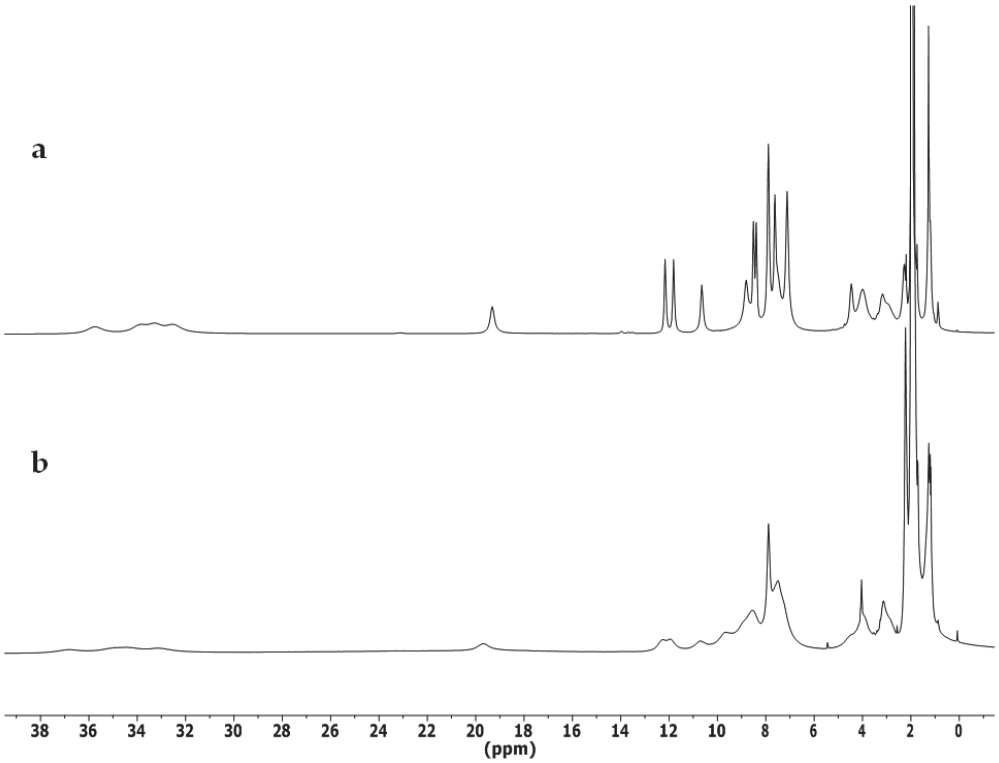

Figure 3.5: ^{1}H NMR spectra of $[Cu^{II}_2(\mathbf{L^{1*}S})_2]^{2+}$ (a) and $[Cu^{I}_2Cu^{II}_2(\mathbf{L^{1*}S})_2(CH_3CN)_6]^{4+}$ (b) in CD_3CN at RT.

Cyclic voltammetry has been carried out with both $[Cu^{II}_2(\mathbf{L^{1*}S})_2]^{2+}$ and $[Cu^{I}_2Cu^{II}_2(\mathbf{L^{1*}S})_2(CH_3CN)_6]^{4+}$; the voltammograms again show similarities (Figure 3.4b). The voltammogram of $[Cu^{II}_2(\mathbf{L^{1*}S})_2]^{2+}$ shows two quasi-reversible waves with $E_{1/2}$ of –0.10 V and 0.25 V and a number of less intense irreversible events. These waves are also present in the voltammogram of $[Cu^{I}_2Cu^{II}_2(\mathbf{L^{1*}S})_2(CH_3CN)_6]^{4+}$, although this species has an additional quasi-reversible wave (at $E_{1/2} \approx 1.20$ V) that can possibly be ascribed to the bridging $[Cu^{I}(CH_3CN)_2]^{+}$ moieties, as the oxidation of $[Cu^{I}(CH_3CN)_4]^{+}$ occurs at a comparable potential ($E_{1/2} = 1.10$ V; Figure AII.1, Appendix II). The ligand $\mathbf{L^{2*}SSL^{2*}}$ upon reaction with Cu^{I} forms a Cu^{II} μ-thiolate compound in both dichloromethane and acetone solutions, which is confirmed by the X-ray structure determination of $[Cu^{II}_2(\mathbf{L^{2*}S})_2](BF_4)_2$ (Section 3.2.1) and the UV-vis spectrum of the dark-green species in dichloromethane (Figure AII.2a, Appendix II). In acetonitrile, however, a light greenish-yellow solution arises after addition of Cu^{I},

which can be attributed to the formation of the disulfide compound $[Cu^{I}_2(\mathbf{L^{2*}SSL^{2*}})]^{2+}$, based on the UV-vis spectra (Figure AII.2b, Appendix II).
Similar behavior has been reported for $\mathbf{L^2SSL^2}$ (Chapter 2).[1] ^{1}H NMR spectra of both the Cu^{I} disulfide and the anti-ferromagnetically coupled Cu^{II} thiolate complex of $\mathbf{L^{2*}SSL^{2*}}$ are shown in Figure 3.6.

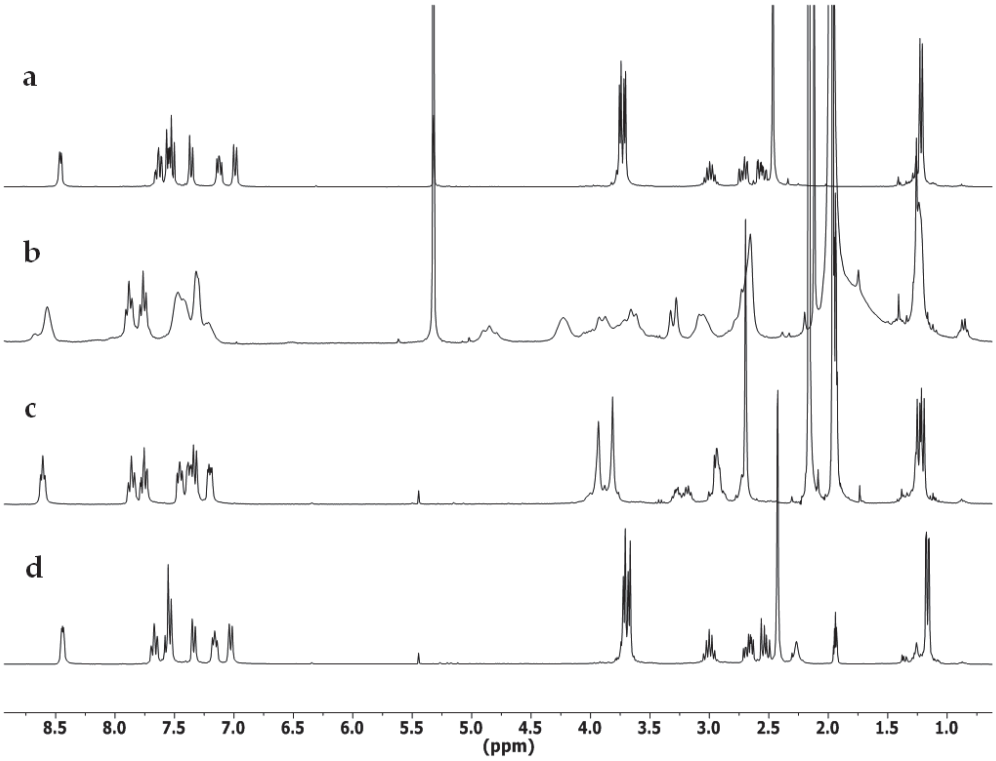

Figure 3.6: ^{1}H NMR spectra of $\mathbf{L^{2*}SSL^{2*}}$ (a) and $[Cu^{II}_2(\mathbf{L^{2*}S})_2]^{2+}$ (b) in CD_2Cl_2 and $\mathbf{L^{2*}SSL^{2*}}$ (d) and $[Cu^{I}_2(\mathbf{L^{2*}SSL^{2*}})]^{2+}$ (c) in CD_3CN at RT.

3.2.3 Spectroscopic Analysis of the Proton-Induced Conversion

Upon addition of protons to an acetonitrile solution of $[Cu^{II}_2(\mathbf{L^{1*}S})_2]^{2+}$ a color change occurs, as has been reported by Stack and coworkers.[2] The addition of 1 – 4 equivalents of HBF_4 (in ratio to the ligand) to the Cu^{II} μ-thiolate containing solution was monitored with ^{1}H NMR; the results are depicted in Figure 3.7. Addition of one equivalent of H^+ leads to broadening of the peaks and a shift of all resonances to the diamagnetic region. Addition of more protons leads to sharper peaks, resulting in a sharp diamagnetic spectrum after addition of four equivalents of protons. This

spectrum is identical with that of the protonated disulfide ligand (Figure 3.8), revealing that the ligand has dissociated giving $[H_4\mathbf{L^{1*}SSL^{1*}}]^{4+}$ and $[Cu^{I}(CH_3CN)_4]^{+}$. The effect of the addition of protons to $[Cu^{II}_2(\mathbf{L^{1*}S})_2]^{2+}$ was also monitored using UV-vis (Figure 3.9a). The addition of two equivalents of acid results not only in the disappearance of the d-d transitions, but also in the disappearance of the $Cu^{II} \leftarrow S$ LMCT band. We would expect to see an $S \leftarrow Cu^{I}$ MLCT band if redox isomerisation to the Cu^{I} disulfide would occur,[1, 7] and its absence indicates that the sulfur center is no longer bound to copper and might be protonated. Again, the UV-vis spectrum of the disulfide ligand in the presence of two equivalents of acid is identical (Figure AII.3, Appendix II). Addition of stoichiometric amounts of NEt_3 completely reverses the reaction, regenerating the Cu^{II} thiolate complex.

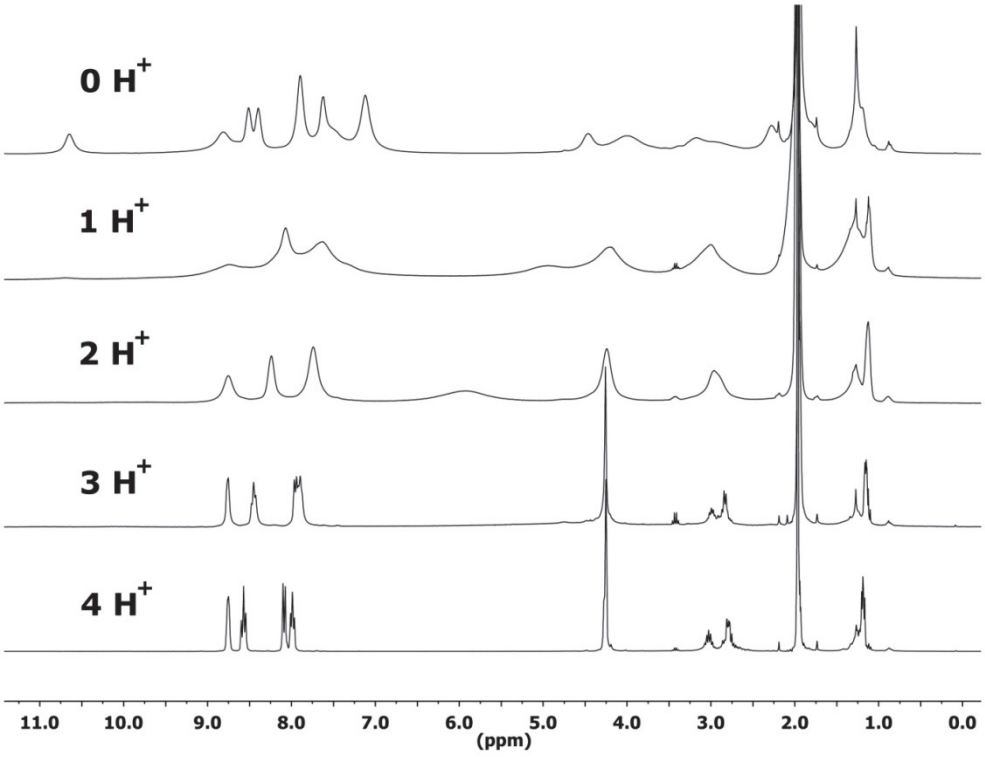

Figure 3.7: ^{1}H NMR spectra of $[Cu^{II}_2(\mathbf{L^{1*}S})_2]^{2+}$ with 0 - 4 equivalents of $HBF_4{\cdot}Et_2O$ in CD_3CN at RT.

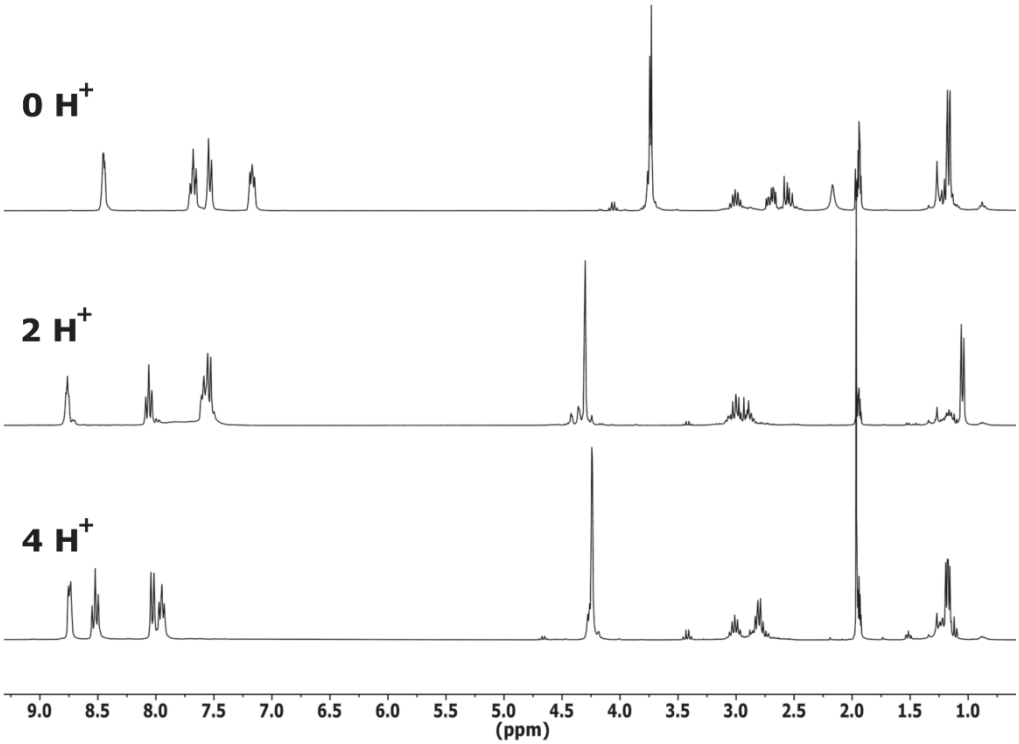

Figure 3.8: ^{1}H NMR spectra of **L^{1}*SSL^{1}*** with 0 - 4 equivalents of $HBF_4 \cdot Et_2O$ in CD_3CN at RT.

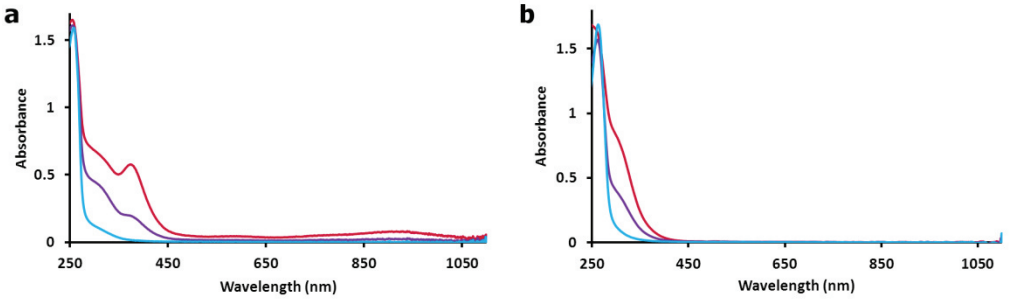

Figure 3.9: UV-vis spectra of $[Cu^{II}_2(\mathbf{L^{1*}S})_2]^{2+}$ (a) and $[Cu^{I}_2(\mathbf{L^{2*}SSL^{2*}})]^{2+}$ (b) with 0 equivalents (red line), 1 equivalent (purple line) and 2 equivalents (blue line) of $HBF_4 \cdot Et_2O$ in CH_3CN at 2 mM [Cu] recorded with a transmission dipprobe set at a path length of 1.2 mm.

Stack et.al.[2] used trifluoridomethanesulfonic acid (HOTf) as the proton source instead of HBF_4. We repeated our experiments with HOTf; the same spectra were obtained as reported by the group of Stack, however, we find that upon addition of HOTf the reaction does not occur stoichiometrically. More HOTf is needed to obtain the same

results as with 4 equiv. HBF_4, as was found with both UV-vis and NMR spectroscopy (Figure AII.5 and AII.7, Appendix II). The use of a solvent that is more easily protonated, such as methanol or acetone, also leads to more gradual protonation of the complex.

As the ligand **L²*SSL²*** can form either the Cu^{I} disulfide or the Cu^{II} thiolate complex depending on the solvent, it is ideally suited to study the effect of protonation of the Cu^{II} or Cu^{I} compounds separately. Addition of just one equivalent of HBF_4 to $[Cu^{II}_2(\mathbf{L^{2*}S})_2]^{+}$ in dichloromethane already leads to precipitation of protonated ligand (Figure AII.6, Appendix II). Upon addition of two equivalents of HBF_4 to $[Cu^{I}_2(\mathbf{L^{2*}SSL^{2*}})]^{2+}$ in acetonitrile again the S ← Cu^{I} MLCT band disappears indicating ligand dissociation (Figure 3.9b).

3.2.4 DFT Analysis of the Proton-Induced Conversion

The experimental and spectroscopic results indicate that addition of two equivalents of protons to $[Cu^{II}_2(\mathbf{L^{1*}S})_2]^{2+}$ leads to ligand dissociation and formation of a mixed-valent tetranuclear cluster, instead of conversion to a protonated Cu^{I} disulfide complex as suggested by Stack et al.[2] However, as the experimental data are not conclusive, we decided to study these complexes computationally with DFT. The calculations were carried out as reported by us recently,[1] taking into account the anti-ferromagnetic coupling between the two Cu^{II} ions in the μ-thiolate complex (Section 3.5.3). Due to the presence of the methyl groups next to the sulfur atom, the ligand **L¹*SSL¹*** has four diastereoisomers (*RR*, *SS*, *RS*, *SR*), which leads to the potential formation of three chemically distinguishable complexes (**X**, **Y** and **Z**, see Figure 3.11). The calculated structures of the three different complexes of the Cu^{II} thiolate complexes (**A**, Figure 3.10) are shown in Figure 3.11 and the relative energies of formation for **A**, **B** and **C** in conformation **X**, **Y** and **Z** are given in Table 3.4. The most stable *RR*/*SS* and *RS*/*SR* thiolate and disulfide complexes were used for the calculations including added protons.

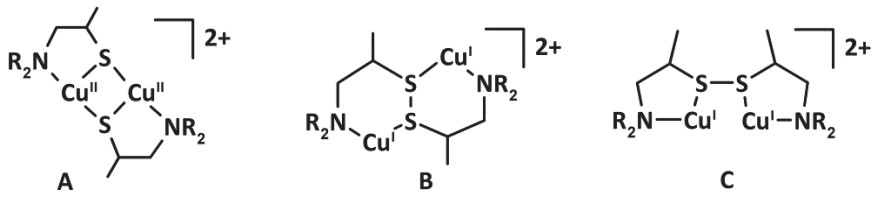

Figure 3.10: Schematic representation of the copper complexes in Cu^{II} μ-thiolate (**A**), Cu^{I} *transoid*-disulfide (**B**) or Cu^{I} *cisoid*-disulfide (**C**) conformation. R = 2-pyridylmethyl.

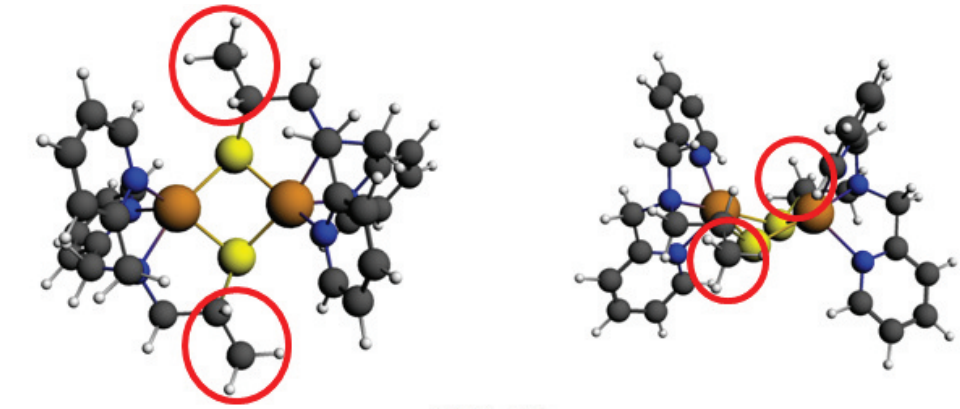

X: *RR* / *SS*
0 kJ mol^{-1}

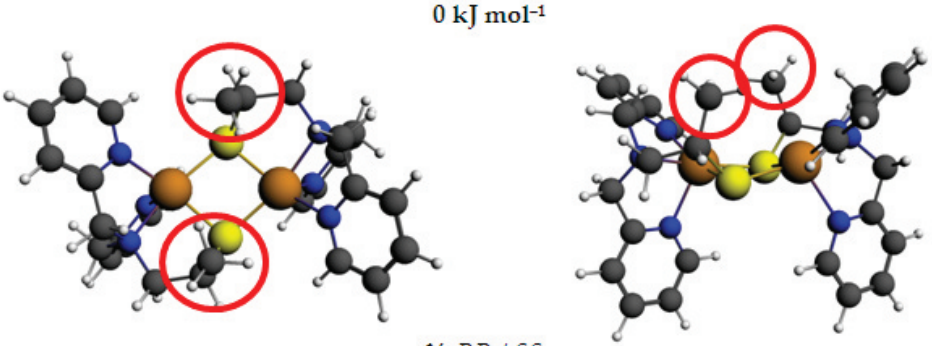

Y: *RR* / *SS*
+43 kJ mol^{-1}

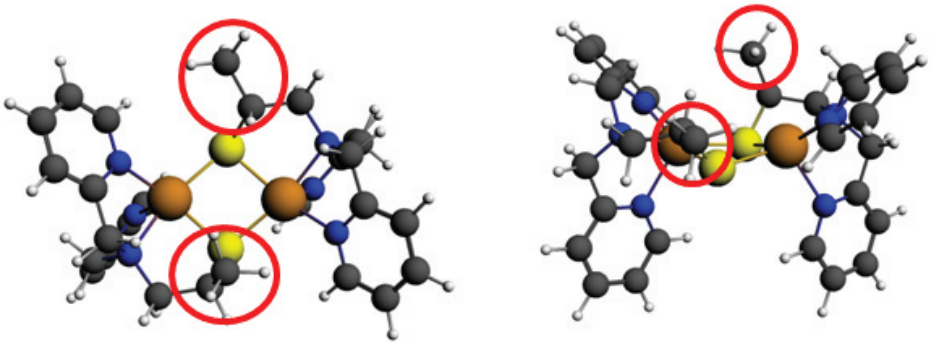

Z: *RS* / *SR*
+31 kJ mol^{-1}

Figure 3.11: Optimized geometries for three chemically distinguishable $[Cu^{II}_2(\mathbf{L^{1*}S})_2]^{2+}$ complexes (**X**; **Y** and **Z**) and their relative energies computed at ZORA-OPBE/TZ2P solvated in CH_3CN (COSMO).

Although it is likely that the pyridyl nitrogen atoms of the ligand are protonated,[2] protonation of the thiolate and tertiary amine atoms were considered as well. The energies of all optimized protonated complexes are given in Table AII.1, Appendix II. The calculations confirm that the pyridyl nitrogen atoms are the most likely site of protonation, as these structures result in the lowest energies. The calculated energies of the protonated μ-thiolate complexes (**A**) and the protonated disulfide complexes (*transoid* **B** and *cisoid* **C**, see Figure 3.10) with or without coordinated acetonitrile molecules are collected in Table 3.5.

A graphical representation of the calculated energies is depicted in Figure 3.12. The calculations show that the protonated disulfide complexes in both geometries (**B** and **C**) with and without coordinated acetonitrile are higher in energy than the protonated Cu^{II} μ-thiolate complex, indicating that formation of a protonated Cu^{I} disulfide species is thermodynamically unfavorable. Ligand dissociation is favored by more than 100 kJ mol^{-1}, supporting that this readily occurs upon protonation.

Table 3.4: Relative formation energies (kJ mol^{-1}) for Cu^{II} μ-thiolate (**A**) and Cu^{I} disulfide (**B** and **C**) complexes in three geometries (**X**, **Y** and **Z,** Figure 3.11) computed at ZORA-OPBE/TZ2P solvated in CH_3CN (COSMO).

	X: *RR* / *SS*	**Y: RR/*SS***	**Z: *RS* / *SR***
L¹*SSL¹* + 2 $[Cu(CH_3CN)_4]^+$	**0**	**0**	4
A + 8 CH_3CN	−94	−51	−64
B + 8 CH_3CN	−88	−54	−76
C + 8 CH_3CN	−70	−77	−77

Table 3.5: Geometry optimization energies (kJ mol^{-1}) for protonated Cu^{II} μ-thiolate (**A**) and Cu^{I} disulfide (**B** and **C**) complexes and protonated ligand **L¹*SSL¹*** computed at ZORA-OPBE/TZ2P in acetonitrile (COSMO).

	Conformation *RR* / *SS*	**Conformation *RS* / *SR***
[**A** + 2 H^+]$^{4+}$ + 8 CH_3CN	**0**	18
[**B** + 2 H^+]$^{4+}$ + 8 CH_3CN	27	30
[**B** + 2 H^+ + 2 CH_3CN]$^{4+}$ + 6 CH_3CN	20	38
[**C** + 2 H^+]$^{4+}$ + 8 CH_3CN	57	51
[**C** + 2 H^+ + 2 CH_3CN]$^{4+}$ + 6 CH_3CN	23	6
[**L¹*SSL¹*** + 2 H^+]$^{2+}$ + 2 $[Cu^I(CH_3CN)_4]^+$	−109	−114

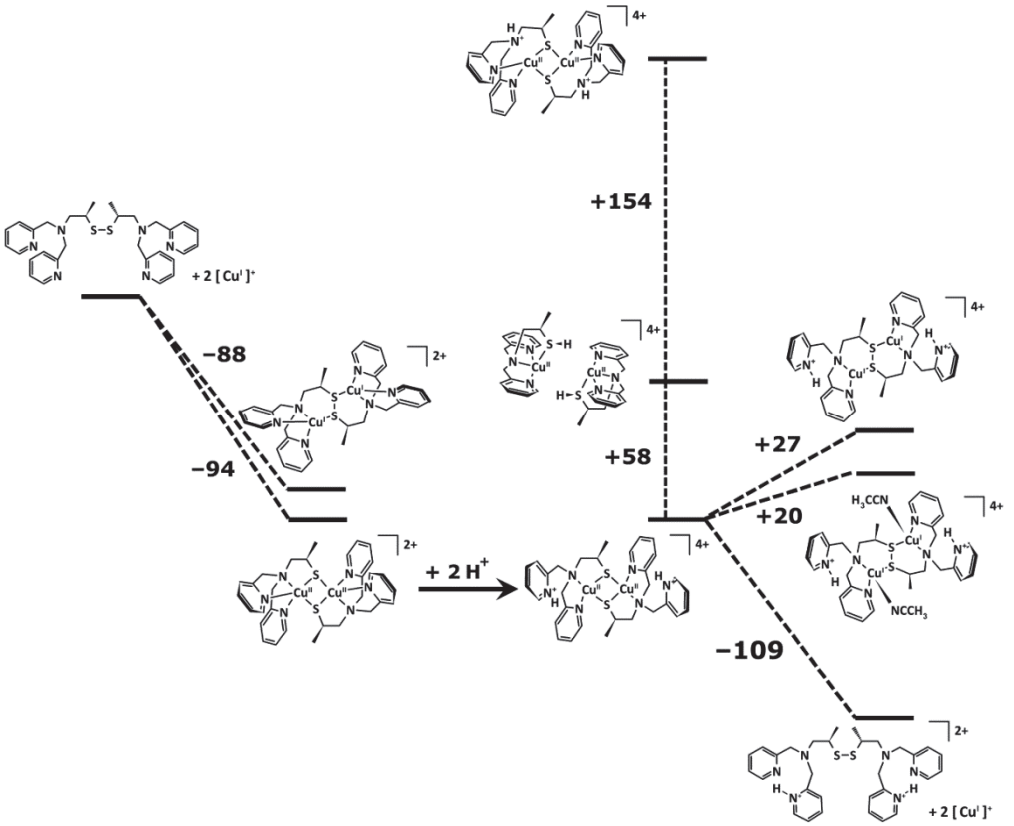

Figure 3.12: Schematic representation of the energies calculated for copper complexes with **L¹*SSL¹*** in the *RR/SS* conformation. For clarity only the *transoid* structures **B** are shown and non-coordinated CH_3CN molecules are omitted.

3.3 Discussion

UV-vis spectra of the titration of $[Cu^{II}_2(\mathbf{L^{1*}S})_2]^{2+}$ with HBF_4 revealed the disappearance of the Cu^{II} d-d transitions and the absence of an S ← Cu^{I} MLCT band after addition of only two equivalents of acid, indicating that the sulfur center no longer binds to copper. Addition of two equivalents of acid to the related compound $[Cu^{II}_2(\mathbf{L^{2*}S})_2]^{2+}$ in dichloromethane resulted in precipitation of $[H_4\mathbf{L^{2*}SSL^{2*}}]^{4+}$, whereas addition to the redox-isomeric compound $[Cu^{I}_2(\mathbf{L^{2*}SSL^{2*}})]^{2+}$ in acetonitrile resulted in disappearance of the S ← Cu^{I} MLCT band similar as observed for $[Cu^{II}_2(\mathbf{L^{1*}S})_2]^{2+}$. The spectroscopic results thus suggest that upon protonation of $[Cu^{II}_2(\mathbf{L^{1*}S})_2]^{2+}$, ligand dissociation takes place via conversion to a Cu^{I} disulfide complex. Crystallization of the complex $[Cu^{I}_2Cu^{II}_2(\mathbf{L^{1*}S})_2(CH_3CN)_6](BF_4)_4$ upon the addition of two equivalents of protons to a solution of $[Cu^{II}_2(\mathbf{L^{1*}S})_2]^{2+}$ suggests that the liberated Cu^{I} acetonitrile

complex, formed after dissociation of the protonated ligand, is accommodated by the remaining Cu^{II} thiolate compound.

Monitoring the titration of H^+ to $[Cu^{II}_2(\mathbf{L^{1*}S})_2]^{2+}$ with ^1H NMR spectroscopy showed the formation of fully protonated ligand after addition of four equivalents of HBF_4. After addition of two equivalents of HBF_4 the ^1H NMR spectrum shows rather broad signals in the diamagnetic region, indicating the presence of a number of different species, which may include an equilibrium between the doubly protonated complex, $[H_4\mathbf{L^{1*}SSL^{1*}}]^{4+}$ and $[Cu^{I}_2Cu^{II}_2(\mathbf{L^{1*}S})_2(CH_3CN)_6]^{4+}$ species. Despite the use of different acids our ^1H NMR spectra are highly similar to those reported by Stack and coworkers. It must be noted that Stack and coworkers have not added more than three equivalents of HOTf in any of their experiments. Even though HOTf is a stronger acid than HBF_4 in water, the acidity could be reversed in acetonitrile as indicated by our experiments. In our experience, OTf^- coordinates more strongly to copper than BF_4^- which suggests weaker acidity of the OTf^- ion in acetonitrile.[3]

The optimized energies calculated using DFT (Table 3.5) show that protonation of the pyridyl nitrogen is most favorable, which was also concluded by Stack and coworkers based on the results of ^1H NMR NOE enhancements.[2] However, the observation of a proton at a pyridine nitrogen with NMR techniques does not tell whether a protonated complex or just a protonated ligand is formed. More importantly, our calculations show that the protonated Cu^{II} thiolate complex is lower in energy than the protonated Cu^{I} disulfide complex, with or without coordination of acetonitrile. Ligand dissociation, on the other hand, is favored by more than 100 kJ mol^{-1}, thus clarifying the experimental results that suggest loss of the copper-sulfur interaction. This means that addition of just two protons per dinuclear copper compound already leads to ligand dissociation for both the Cu^{II} thiolate and the Cu^{I} disulfide complexes.

These proton-coupled reactions form a model for the biological systems, since these Cu^{II} μ-thiolate complexes show resemblance to the Cu_A site. Studies on the Cu_A site in cytochrome *c* oxidase and the artificially engineered Cu_A site in azurin have shown that these active sites are very sensitive to pH changes.[8-12] It is hypothesized that protonation of the Cu_A site induces ligand dissociation of one of the equatorial histidine ligands, which possibly leads to a change in valence state of the copper ions. Furthermore, understanding of this pH dependent behavior can be of importance for other pyridyl-containing metal complexes, which are used as catalysts for reactions such as water oxidation,[13] proton reduction[14] and CO_2 reduction.[15-17] This study shows that the pH can have a large effect on the coordination environment of the metal and might affect the reactivity of the metal center or the mechanism of catalysis.

3.4 Conclusion

We have found that after addition of only two equivalents of protons, a potentially octadentate ligand dissociates from two copper ions, after an intramolecular redox reaction of a dinuclear Cu^{II} dithiolate species to form $[Cu^{I}(CH_3CN)_4]^+$ and the protonated disulfide ligand. Ligand dissociation was found to take place when adding protons to either the Cu^{II} μ-thiolate compound $[Cu^{II}_2(\mathbf{L^{2*}S})_2]^{2+}$ or the Cu^{I} disulfide compound $[Cu^{I}_2(\mathbf{L^{2*}SSL^{2*}})]^{2+}$, showing that this dissociation also readily occurs for Cu^{I} disulfide complexes. Our findings are in contrast to an earlier report describing redox isomerization to a Cu^{I} disulfide species that is protonated at the pyridyl moieties. In the earlier report HOTf was used instead of HBF_4 and although we obtained similar ^{1}H NMR and UV-vis spectra, we found that HOTf is a weaker acid in acetonitrile and does not react stoichiometrically with $[Cu^{II}_2(\mathbf{L^{1*}S})_2]^{2+}$. Our results show that the addition of protons can have an immense effect on the coordination environment of copper ions. The presence of small amounts of acid can already lead to ligand dissociation and possible electron-transfer. The relevance of our findings stretches from biological systems to the field of inorganic chemistry and catalysis. It is of the utmost importance to point out that already small changes in pH may have a significant impact on the coordination environment of the actual catalyst or complex structure in solution.

3.5 Experimental Section

3.5.1 General Methods

Reagents and solvents were purchased from commercial sources. The syntheses of all copper complexes were carried out using standard Schlenk-line techniques under an argon atmosphere. Solvents were distilled and deoxygenated by bubbling a stream of argon through the solution and were stored on activated molecular sieves under argon prior to use. $[Cu^{I}(CH_3CN)_4](BF_4)$ and 1-(6-methyl-2-pyridinyl)-*N*-(2-pyridinylmethyl)methanamine and $[Cu^{II}_2(\mathbf{L^{1*}S})_2]^{2+}$ were synthesized according to literature procedures.[2, 18, 19] NMR spectra were recorded on a Bruker 300 DPX spectrometer. NMR experiments under argon were carried out using a J. Young NMR tube. IR spectra were obtained on a Perkin Elmer UATR (Single Reflection Diamond) Spectrum Two device (4000-700 cm^{-1}; resolution 4 cm^{-1}). Mass spectrometry was measured using a Finnigan Aqua Mass Spectrometer (MS) with electro spray ionization (ESI). Sample introduction was achieved through a Dionex ASI-100 automated sample injector with an eluent flow rate of 0.2 mL/min. Elemental analyses were performed using a Perkin Elmer 2400 Series II CHNS/O analyzer. UV-vis spectra were collected using a transmission dipprobe with variable path length on an Avantes Avaspec-2048 spectrometer with Avalight-DH-S-BAL light source. Cyclic voltammetry was performed with an Autolab PGstat10 potentiostat controlled by GPES4 software. A three electrode arrangement with a

glassy carbon working electrode (3 mm diameter), an Ag/AgCl double junction reference electrode and a Pt wire counter electrode were used in different solvents with 0.1 M NBu_4PF_6 as the electrolyte. In these conditions the Fc/Fc^+ couple was found to be located at +442 mV with a peak-to-peak separation of 60 mV in CH_3CN, and at + 461 mV with a peak-to-peak separation of 92 mV in dichloromethane. Potentials are given relative to the Ag/AgCl electrode.

3.5.2 Single Crystal X-ray Crystallography

All reflection intensities at 100(2) K for $[Cu^{I}_2Cu^{II}_2(\mathbf{L^{1}*S})_2(CH_3CN)_6](BF_4)_4$ were measured and at 110(2) K for $[Cu^{II}_2(\mathbf{L^{2}*S})_2](BF_4)_2$ using a SuperNova diffractometer (equipped with Atlas detector) with Cu $K\alpha$ radiation (mirror optics, λ = 1.54178 Å) under the program CrysAlisPro (Versions 1.171.36.2424 or 1.171.36.32 Agilent Technologies, 2012-2013). The same program was also used to refine the cell dimensions and for data reduction. The structure was solved with the program SHELXS-2013 (Sheldrick, 2013)[20] and was refined on F^2 with SHELXL-2013 (Sheldrick, 2013).[20] Analytical numeric absorption corrections based on a multifaceted crystal model were applied using CrysAlisPro. The temperature of the data collection was controlled using the system Cryojet (manufactured by Oxford Instruments). The H atoms were placed at calculated positions using the instructions AFIX 13, AFIX 23, AFIX 43 or AFIX 137 with isotropic displacement parameters having values 1.2 or 1.5 times *U*eq of the attached C atoms. For the refinement of $[Cu^{II}_2(\mathbf{L^{2}*S})_2](BF_4)_2$, some unresolved electron density – *i.e.*, possibly some amount of disordered solvent molecule (the unresolved electron density did not indicate any additional component of disorder BF_4^-) – has been taken out in the final refinement (SQUEEZE details are provided in the CIF file).

3.5.3 DFT Calculations

All calculations were performed with the Amsterdam Density Functional (ADF) program,[21, 22] using relativistic DFT at ZORA OPBE/TZ2P for geometry optimization and energies.[23] Solvation in acetonitrile was simulated using the conductor-like screening model (COSMO).[24-27] All stationary points in the condensed phase were verified to be minima on the potential energy surface (PES) through vibrational analysis. The energies of the singlet state of the Cu^{II} μ-thiolate complexes (E^S) have been obtained from the unrestricted broken-symmetry singlet energies (E^{BS}) and the energy of the triplet (E^T) with the approximate projection method of Noodleman: $E^S = 2E^{BS} - E^T$.[28, 29]

Some systems were optimized in C_2 symmetry (see Supporting Information). CH_3CN was optimized with C_{3v} symmetry.

3.5.4 Ligand and complex synthesis

L¹*SSL¹*

This ligand was synthesized using a combination of reported syntheses.[2-4] Di-(2-pyridylmethyl)amine (2.0 mL, 11.0 mmol) was dissolved in 10 ml CH_3CN under argon.

Propylene sulfide (1.3 mL, 16.5 mmol) was added, after which the reaction mixture was stirred for 15 hours at 70 °C under argon. After the mixture had cooled down, the solvent and excess propylene sulfide were evaporated. The resulting orange oil was dissolved in 20 mL methanol and titrated with 0.5 M iodine in methanol until a brown color persisted. The reaction was quenched with $NaHSO_3$ (10% in H_2O) regaining the yellow color. The solvent was evaporated and 50 mL H_2O was added. 2 M NaOH was added until pH > 10. The water layer was extracted with 3 x 50 mL $CHCl_3$, the organic layer was dried over Na_2SO_4 and evaporated to yield a brown/yellow oil. The resulting oil was purified by column chromatography (basic alumina, eluent 60% EtOAc in petroleum ether) which yielded a light yellow oil as a mixture of of (*R*,*R*), (*S*,*S*), and (*R*,*S*) stereoisomers (2.69 g, 4.9 mmol, 90%). ^{1}H-NMR (300 MHz, CD_3CN, RT): δ 1.15 (s, 3H, C*-CH_3), 1.17 (s, 3H, C*-CH_3), 2.55 (dd, *J* = 13 Hz, 7.8 Hz, 2H, N-CH_2-C*), 2.70 (m, 2H, N-CH_2-C*), 3.01 (quin, *J* = 6.6 Hz, 2H, C*-*H*), 3.73 (s, 4H, Py-CH_2-N), 3.74 (s, 4H, Py-CH_2-N), 7.14 (m, 4H, Py-H_5), 7.53 (m, 4H, Py-H_3), 7.65 (tt, *J* = 7.5 Hz, 1.8 Hz, 1.5 Hz, 4H, Py-H_4), 8.44 (m, 4H, Py-H_6). ^{13}C-NMR (75 MHz, CD_3CN, RT): δ 19.2 (C*-*C*H$_3$), 19.3 (C*-*C*H$_3$), 45.3 (*C**), 45.4 (*C**), 60.8 (N-*C*H$_2$-C*), 61.0 (N-*C*H$_2$-C*), 61.3 (Py-*C*H$_2$-N), 61.4 (Py-*C*H$_2$-N), 123.0 (Py-*C*$_5$), 124.1 (Py-*C*$_3$), 124.1 (Py-*C*$_3$), 137.2 (Py-*C*$_4$), 149.8 (Py-*C*$_6$), 160.4 (Py-*C*$_2$), 160.5 (Py-*C*$_2$). ESI-MS found (calcd) for $[M + H]^+$: *m*/*z* 545.2 (545.3).

*L²*SSL²**

This ligand was synthesized in a similar way as ligand **L¹*SSL¹*** starting from 1-(6-methyl-2-pyridyl)-*N*-(2-pyridylmethyl)methanamine (3.56 g, 16.7 mmol) dissolved in 25 mL CH_3CN under argon. Propylene sulfide (2.0 mL, 25.0 mmol) was added, after which the reaction mixture was stirred for 3 days at 70 °C under argon. Further workup and reaction with I_2 was done in the same way as for **L¹*SSL¹***. The product was obtained after column chromatography (basic alumina, eluent 20% → 100% EtOAc in petroleum ether) as a yellow oil (1.12 g, 2.0 mmol, 23%). ^{1}H-NMR (300 MHz, CD_3CN, RT): δ 1.15 (d, *J* = 2.1 Hz, 3H, C*-CH_3), 1.18 (d, *J* = 2.4 Hz, 3H, C*-CH_3), 2.42 (s, 3H, Py-CH_3), 2.43 (s, 3H, Py-CH_3), 2.53 (dd, *J* = 13 Hz, 7.8 Hz, 2H, N-CH_2-C*), 2.67 (m, 2H, N-CH_2-C*), 3.00 (quin, *J* = 6.9 Hz, 2H, C*-*H*), 3.67 (s, 2H, Py$_{Me}$-CH_2-N), 3.68 (s, 2H, Py-CH_2-N), 3.71 (s, 2H, Py$_{Me}$-CH_2-N), 3.72 (s, 2H, Py-CH_2-N), 7.03 (d, *J* = 7.5 Hz, 2H, Py$_{Me}$-H_3), 7.16 (tt, *J* = 6.0 Hz, 1.5 Hz, 1.2 Hz, 2H, Py$_{Me}$-H_4), 7.34 (d, *J* = 7.5 Hz, 2H, Py-H_3), 7.55 (t, *J* = 7.8 Hz, 4H, Py$_{Me}$-H_5; Py-H_4), 7.67 (t, *J* = 7.8 Hz, 2H, Py-H_5), 8.44 (m, 2H, Py-H_6). ^{13}C-NMR (75 MHz, CD_3CN, RT): δ 19.1 (C*-*C*H$_3$), 19.2 (C*-*C*H$_3$), 24.5 (Py-*C*H$_3$) 45.2 (*C**), 45.4 (*C**), 60.7 (Py$_{Me}$-*C*H$_2$-N), 60.9 (Py-*C*H$_2$-N), 61.3 (N-*C*H$_2$-C*), 61.3 (N-*C*H$_2$-C*), 61.4 (N-*C*H$_2$-C*), 61.4 (N-*C*H$_2$-C*), 120.8 (Py-*C*$_5$), 120.9 (Py-*C*$_5$), 122.2 (Py$_{Me}$-*C*$_5$), 123.0 (Py$_{Me}$-*C*$_3$), 124.0 (Py-*C*$_3$), 124.1 (Py-*C*$_3$), 137.2 (Py$_{Me}$-*C*$_4$), 137.5 (Py-*C*$_4$), 149.7 (Py-*C*$_6$), 158.3 (Py$_{Me}$-*C*$_2$), 159.7 (Py$_{Me}$-*C*$_6$), 159.7 (Py$_{Me}$-*C*$_6$), 160.4 (Py-*C*$_2$), 160.5 (Py-*C*$_2$). ESI-MS found (calcd) for $[M + H]^+$: *m*/*z* 573.1 (573.3); $[M + Na]^+$: *m*/*z* 595.1 (595.3). IR (neat, cm^{-1}): 1590s, 1577s, 1456m, 1433s, 1365m, 1152m, 1084m, 994s, 976m, 785s, 756m, 614s.

$[Cu^{I}_2Cu^{II}_2(\mathbf{L^{1}*S})_2(CH_3CN)_6](BF_4)_4$

L^{1}*SSL^{1}* (19.8 mg, 0.04 mmol) was dissolved in CH_3CN (4.0 ml). To this solution $[Cu^{I}(CH_3CN)_4](BF_4)$ (46.1 mg, 0.15 mmol) was added, which resulted in a dark brown solution. The solution was stirred for 1 hour after which the solution was added slowly to 100 mL diethyl ether while stirring vigorously. A very oxygen-sensitive greyish purple solid was collected by filtration (41.0 mg, 0.03 mmol, 81%). This compound turned light green when put under vacuum. Crystals suitable for X-ray structure determination were obtained by vapor diffusion of diethyl ether into an CH_3CN solution containing 1 equivalent of **L^{1}*SSL^{1}***, 2 equivalents of $[Cu(CH_3CN)_4](BF_4)$ and 2 equivalents of $HBF_4{\cdot}Et_2O$. Elemental analysis calcd for $C_{30}H_{36}B_4Cu_4F_{16}N_6S_2$ + 2 H_2O: C 30.48, H 3.41, N 7.11, S 5.42. Found: C 29.29, H 3.45, N 6.99, S 5.42. ESI-MS found (calcd) for $[Cu(CH_3CN)_2]^+$: *m/z* 145.1 (145.0); $[Cu(CH_3CN)_3]^+$: *m/z* 186.0 (186.0); [Cu(**L^{1}*S**) – S]$^+$: *m/z* 303.0 (303.1); [Cu(**L^{1}*S**)]$^+$: *m/z* 335.0 (335.1). UV-vis in CH_3CN at 0.5 mM complex concentration: 235 nm (ε = 7000 M^{-1} cm^{-1}), 255 nm (ε = 6150 M^{-1} cm^{-1}), 308 nm (ε = 2500 M^{-1} cm^{-1}), 372 nm (ε = 1700 M^{-1} cm^{-1}), 580 nm (ε = 170 M^{-1} cm^{-1}), 910 nm (ε = 250 M^{-1} cm^{-1}).

$[Cu^{II}_2(\mathbf{L^{2}*S})_2](BF_4)_2$

L^{2}*SSL^{2}* (92.5 mg, 0.16 mmol) was dissolved in acetone (10 ml). To this solution $[Cu^{I}(CH_3CN)_4](BF_4)$ (101 mg, 0.32 mmol) was added, which resulted in a very dark green solution. This solution was stirred for 1 hour after which it was added to 20 mL pentane resulting in a grey powder (88.3 mg, 0.10 mmol, 63%) after filtration. Crystals suitable for X-ray structure determination were obtained by slow vapor diffusion of pentane in an acetone solution containing the complex. ^{1}H NMR (300 MHz, CD_2Cl_2, RT): δ 1.24 (br, 3H, C*-CH_3), 1.26 (s, 3H, C*-CH_3), 2.66 (br, 6H, Py-CH_3), 3.07 (d, *J* = 9.9 Hz, 2H, N-CH_2-C*), 3.30 (d, *J* = 14 Hz, 2H, N-CH_2-C*), 3.76 (m, 6H), 4.23 (br, 2H), 4.86 (t, *J* = 18 Hz, 2H), 7.21 (br, 2H), 7.32 (br, 2H), 7.45 (br, 4H), 7.77 (t, *J* = 7.5 Hz, 2H), 7.88 (t, *J* = 7.5 Hz, 2H), 8.57 (br, 2H, Py-H_6). ESI-MS found (calculated) for [**L^{2}*SSL^{2}*** + Cu]$^{2+}$: *m/z* 317.1 (317.6); $[Cu_2(\mathbf{L^{2}*S})_2]^{2+}$: *m/z* 349.1 (349.1); [**L^{2}*SSL^{2}*** + 3 Cu]$^{2+}$: *m/z* 381.0 (381.5); [**L^{2}*SSL^{2}*** + Cu]$^+$: *m/z* 635.1 (635.2); $[M - BF_4]^+$: *m/z* 785.1 (785.1). UV-vis in dichloromethane at 2 mM [Cu]: 263 nm (ε = 6800 M^{-1} cm^{-1}), 296 nm (ε = 4500 M^{-1} cm^{-1}), 600 nm (ε = 125 M^{-1} cm^{-1}). IR (neat, cm^{-1}): 1607s, 1577s, 1466m, 1445m, 1050w, 868s, 766m, 620s.

$[Cu^{I}_2(\mathbf{L^{2}*SSL^{2}*})](BF_4)_2$

L^{2}*SSL^{2}* (5.73 mg, 0.01 mmol) was dissolved in CH_3CN (2 ml). To this solution was added $[Cu(CH_3CN)_4](BF_4)$ (6.29 mg 0.02 mmol), resulting in a light greenish yellow solution. Attempts to isolate the complex resulted in the formation of oil. ^{1}H NMR (300 MHz, CD_3CN, RT): δ 1.20 (d, *J* = 6.9 Hz, 3H, C*-CH_3), 1.24 (d, *J* = 6.9 Hz, 3H, C*-CH_3), 2.70 (s, 6H, Py-CH_3), 2.94 (m, 4H, N-CH_2-C*), 3.18 (m, 1H, C*-*H*), 3.27 (m, 1H, C*-*H*), 3.82 (s, 4H, Py_{Me}-CH_2-N), 3.93 (s, 4H, Py-CH_2-N), 7.20 (dd, *J* = 7.5 Hz, 3.3 Hz, 2H), 7.33 (d, *J* = 7.5 Hz, 2H), 7.38 (dd, *J* = 7.8 Hz, 3.0 Hz, 2H), 7.46 (m, 2H), 7.76 (td, *J* = 7.8 Hz, 2.4 Hz, 2H), 7.86 (tt, *J* = 7.8 Hz, 1.8 Hz, 2H), 8.61 (t, *J* = 5.1 Hz, 2H, Py-H_6). ESI-MS found (calculated) for $[Cu_2(\mathbf{L^{2}*SSL^{2}*})]^{2+}$: *m/z* 350.1 (349.1); [**L^{2}*SSL^{2}*** + Cu]$^+$: *m/z*

635.1 (635.2); $[M - BF_4]^+$: *m/z* 785.1 (785.1). UV-vis in CH_3CN at 2 mM [Cu]: 260 nm (ε = 6800 M^{-1} cm^{-1}), 305 nm (ε = 3300 M^{-1} cm^{-1}).

3.6 References

1. Ording-Wenker, E. C. M.; van der Plas, M.; Siegler, M. A.; Bonnet, S.; Bickelhaupt, F. M.; Fonseca Guerra, C.; Bouwman, E., *Inorg. Chem.* **2014,** *53*, 8494-8504.
2. Thomas, A. M.; Lin, B.-L.; Wasinger, E. C.; Stack, T. D. P., *J. Am. Chem. Soc.* **2013,** *135*, 18912-18919.
3. Ording-Wenker, E. C. M.; Siegler, M. A.; Lutz, M.; Bouwman, E., *Inorg. Chem.* **2013,** *52*, 13113-13122.
4. Nielsen, M. C.; Ulven, T., *Chem. Eur. J.* **2008,** *14*, 9487-9490.
5. Addison, A. W.; Rao, T. N.; Reedijk, J.; Vanrijn, J.; Verschoor, G. C., *J. Chem. Soc., Dalton Trans.* **1984**, 1349-1356.
6. The BF_4^- anion, that is disordered over at least three orientations, shows residual electron density near the disordered components, which may indicate the presence of traces of some impurities such as Cl^-. The presence of Cl^- can be traced back to the use of chloroform in the synthesis of **L²*SSL²***. The occupancy factors of the three orientations of the disordered BF_4^- counterion and the two positions of Cl^- impurities were refined using free variables (FVAR), and their values refine to 0.382(3), 0.345(3), 0.072(3), 0.165(3), and 0.036(2) (the sum of all occupancy factors being equal to 1 for charge balance).
7. Ohta, T.; Tachiyama, T.; Yoshizawa, K.; Yamabe, T.; Uchida, T.; Kitagawa, T., *Inorg. Chem.* **2000,** *39*, 4358-4369.
8. Alvarez-Paggi, D.; Abriata, L. A.; Murgida, D. H.; Vila, A. J., *Chem. Commun.* **2013,** *49*, 5381-5383.
9. Hay, M. T.; Ang, M. C.; Gamelin, D. R.; Solomon, E. I.; Antholine, W. E.; Ralle, M.; Blackburn, N. J.; Massey, P. D.; Wang, X. T.; Kwon, A. H.; Lu, Y., *Inorg. Chem.* **1998,** *37*, 191-198.
10. Hwang, H. J.; Lu, Y., *P. Natl. Acad. Sci. USA* **2004,** *101*, 12842-12847.
11. Lukoyanov, D.; Berry, S. M.; Lu, Y.; Antholine, W. E.; Scholes, C. P., *Biophys. J.* **2002,** *82*, 2758-2766.
12. Xie, X.; Gorelsky, S. I.; Sarangi, R.; Garner, D. K.; Hwang, H. J.; Hodgsont, K. O.; Hedman, B.; Lu, Y.; Solornon, E. I., *J. Am. Chem. Soc.* **2008,** *130*, 5194-5205.
13. Barnett, S. M.; Goldberg, K. I.; Mayer, J. M., *Nature Chem.* **2012,** *4*, 498-502.
14. Sundstrom, E. J.; Yang, X.; Thoi, V. S.; Karunadasa, H. I.; Chang, C. J.; Long, J. R.; Head-Gordon, M., *J. Am. Chem. Soc.* **2012,** *134*, 5233-5242.
15. Haines, R. J.; Wittrig, R. E.; Kubiak, C. P., *Inorg. Chem.* **1994,** *33*, 4723-4728.
16. Angamuthu, R.; Byers, P.; Lutz, M.; Spek, A. L.; Bouwman, E., *Science* **2010,** *327*, 313-315.
17. Nagao, H.; Mizukawa, T.; Tanaka, K., *Inorg. Chem.* **1994,** *33*, 3415-3420.

18. Hetterscheid, D. G. H.; Smits, J. M. M.; de Bruin, B., *Organometallics* **2004,** *23*, 4236-4246.
19. Pennings, Y. C. M.; Driessen, W. L.; Reedijk, J., *Polyhedron* **1988,** *7*, 2583-2589.
20. Sheldrick, G. M., *Acta Crystallogr. Sect. A* **2008,** *64*, 112-122.
21. te Velde, G.; Bickelhaupt, F. M.; Baerends, E. J.; Guerra, C. F.; Van Gisbergen, S. J. A.; Snijders, J. G.; Ziegler, T., *J. Comput. Chem.* **2001,** *22*, 931-967.
22. http://www.scm.com/
23. Swart, M.; Ehlers, A. W.; Lammertsma, K., *Mol. Phys.* **2004,** *102*, 2467-2474.
24. Klamt, A., *J. Phys. Chem.* **1995,** *99*, 2224-2235.
25. Klamt, A.; Schuurmann, G., *J. Chem. Soc., Perkin Trans. 2* **1993**, 799-805.
26. Pye, C. C.; Ziegler, T., *Theor. Chem. Acc.* **1999,** *101*, 396-408.
27. Swart, M.; Roesler, E.; Bickelhaupt, F. M., *Eur. J. Inorg. Chem.* **2007**, 3646-3654.
28. Noodleman, L., *J. Chem. Phys.* **1981,** *74*, 5737-5743.
29. Noodleman, L.; Baerends, E. J., *J. Am. Chem. Soc.* **1984,** *106*, 2316-2327.

Chapter 4

Cu^{I} Thiolate Reactivity with Dioxygen: The Formation of Cu^{II} Sulfinate and Cu^{II} Sulfonate Species via a Cu^{II} μ-Thiolate Intermediate

*Cu^{I}(**L^{1}*S**) is formed by addition of Cu^{I} to a solution of the pyridyl-thiol ligand N-(2-mercaptopropyl)-N,N-bis(2-pyridylmethyl)amine (**L^{1}*SH**). Oxidation of complex Cu^{I}(**L^{1}*S**) by air leads to the formation of Cu^{II} sulfinate and Cu^{II} sulfonate complexes, providing a model for the oxidative degeneration of copper-sulfur enzymes. Crystal structures were obtained for two Cu^{II} sulfinate complexes, $[Cu^{II}_2(\mathbf{L^{1}*SO_2})_2](BF_4)_2 \cdot 2\ (CH_3)_2CO$ and $[Cu^{II}_2(\mathbf{L^{1}*SO_2})_2(OTf)_2]$, which were further characterized with UV-vis and EPR spectroscopy and cyclic voltammetry. Furthermore, two Cu^{II} sulfonate complexes with the proposed formula $Cu^{II}_2(\mathbf{L^{1}*SO_3})_2(BF_4)_2$ and $Cu^{II}_2(\mathbf{L^{1}*SO_3})_2(OTf)_2$ have been isolated and characterized. Monitoring the oxidation of Cu^{I}(**L^{1}*S**) by UV-vis spectroscopy indicates that the oxidation proceeds via a dinuclear Cu^{II} μ-thiolate complex; as an intermediate an octanuclear mixed-valent $Cu^{I}_4Cu^{II}_4$ cluster with formula $[Cu^{I}_4Cu^{II}_4(\mathbf{L^{1}*S})_4(\mu\text{-}OH)_2(CH_3CN)_6](ClO_4)_6 \cdot 2\ CH_3CN$ was isolated and characterized by X-ray single crystal structure determination.*

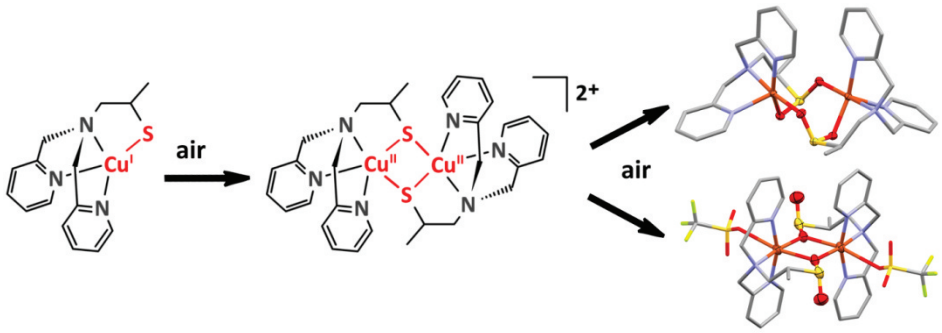

This chapter has been published as a full paper: E. C. M. Ording-Wenker, M. A. Siegler, M. Lutz, E. Bouwman, *Inorg. Chem.* **2013,** *52*, 13113-13122.

4.1 Introduction

Copper plays an essential role in many biological processes. Its ability to cycle between the Cu^{II} and Cu^{I} oxidation states makes it a suitable active site in a wide range of enzymes. A large group of these copper-containing proteins have a coordinating sulfur atom within their active site, which can mediate oxidation and reduction reactions, as discussed in Chapter 1, and many of these copper proteins are involved in O_2 activation reactions. It is therefore important to know how oxidation-sensitive the sulfur ligands are within these enzymes. Besides this, thiols such as cysteine play an important role in biological reduction/oxidation chemistry via disulfide formation, but also further oxidation to sulfenic, sulfinic and sulfonic acids may occur.[1-3] Thus, gaining a better understanding of the oxidation of sulfur ligands in metallo-protein active sites is of interest. In this chapter a Cu^{I} thiolate complex bearing similarity to the Cu_A active site (discussed in Chapter 1) is presented, which is oxidized by dioxygen from air to form Cu^{II} sulfinate and sulfonate complexes via a dinuclear Cu^{II} thiolate intermediate. Synthesis of the Cu^{I} thiolate complex starting from the ligand **L¹*SH** (*N*-(2-mercaptopropyl)-*N*,*N*-bis(2-pyridylmethyl)amine) is depicted in Figure 4.1. The Cu^{II} sulfinate and Cu^{II} sulfonate complexes have been isolated and studied with UV-vis and EPR spectrocopy as well as cyclic voltammetry.

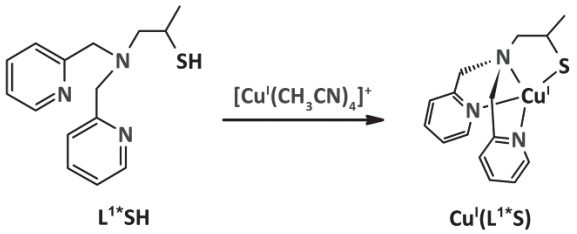

Figure 4.1: Synthesis of the Cu^{I} thiolate compound Cu^{I}(**L¹*S**) from ligand **L¹*SH**.

4.2 Results

4.2.1 Synthesis of Ligands and Complexes

The ligand **L¹*SH** was synthesized by reacting di-(2-picolyl)amine with propylene sulfide as was previously reported.[4] Column chromatography was used to remove unreacted di-(2-picolyl)amine. The thiol ligand **L¹*SH** did not oxidize to the disulfide ligand **L¹*SSL¹*** during the work-up process, which was confirmed by chemically oxidizing **L¹*SH** to **L¹*SSL¹*** with iodine and comparison of the NMR spectra of the two compounds.[5] The ligand slowly degrades and cannot be kept for periods longer than a few months even when stored under argon at –20 °C. **L¹*SH** is obtained as a

mixture of the two enantiomers, as it possesses a chiral center. For all complexation experiments the racemic mixture was used. When either $[Cu^{I}(CH_3CN)_4](BF_4)$ or $[Cu^{I}(CH_3CN)_4](OTf)$ (OTf = trifluoridomethanesulfonate; triflate) was added to a solution of the ligand under argon, a highly oxygen-sensitive, light brown solution is obtained, which likely contains the complex $Cu^{I}(\mathbf{L^{1}*S})$ (as depicted in Figure 4.1). Although ^{1}H-NMR spectroscopy was measured under argon, the NMR spectrum only showed broad peaks in the diamagnetic region. The broadening of the NMR signals is most likely due to the presence of traces of Cu^{II}, or the presence of an equilibrium of different Cu^{I} species with partial coordination of the anions. However, ^{19}F-NMR spectra do not indicate coordination of the counterions to copper species. ESI-MS of the light brown solution showed a peak pattern in agreement with the presence of $[Cu(\mathbf{L^{1}*S})]^{+}$ and $[Cu(\mathbf{L^{1}*SSL^{1}*})]^{+}$. Two smaller signals are also present; one that can tentatively be assigned to a mono-oxygenated compound $[Cu(\mathbf{L^{1}*SO}) + H]^{+}$ or a hydroxide-containing compound $[Cu(\mathbf{L^{1}*S}) + OH]^{+}$ and one signal that can be assigned to the dinuclear compound $[Cu_2(\mathbf{L^{1}*S})_2]^{+}$. Attempts to crystallize $Cu^{I}(\mathbf{L^{1}*S})$ in acetonitrile (starting from the copper perchlorate salt) resulted in the formation of an oil with a number of different crystals. A crystal structure determination of one of those crystals showed the formation of the octanuclear, mixed-valent compound $[Cu^{II}_4Cu^{I}_4(\mathbf{L^{1}*S})_4(\mu\text{-}OH)_2(CH_3CN)_6](ClO_4)_6 \cdot 2\ CH_3CN$ (see below). The presence of Cu^{II} as well as Cu^{I} ions in this octanuclear cluster are in agreement with our explanation of the broad NMR signals observed for $Cu^{I}(\mathbf{L^{1}*S})$. The origin of the Cu^{II} ions in this cluster is ascribed to partial oxidation by air, as no signs of disproportionation (metallic copper) were observed. No other analyses of this compound could be obtained, due to its poor reproducibility. However, as we believe that the formation of this compound is typical for the reactivity of the copper system under study, we judged that it is worthwhile to discuss the structure of this cluster. Further oxidation of $Cu^{I}(\mathbf{L^{1}*S})$ (starting from the copper tetrafluoridoborate or triflate salt) in air resulted in a color change from brown to dark green. After stirring for approximately two hours at room temperature the solution had turned green. Slow diffusion of diethyl ether into the green solution resulted in green crystals, suitable for X-ray structure determination, and a green powder. The crystals and the powder were manually separated; X-ray diffraction showed that the crystals are dinuclear Cu^{II} sulfinate complexes $[Cu^{II}_2(\mathbf{L^{1}*SO_2})_2](BF_4)_2 \cdot 2\ (CH_3)_2CO$ and $[Cu^{II}_2(\mathbf{L^{1}*SO_2})_2(OTf)_2]$, with different connectivity in the structures (see below) depending on the choice of the anion present in the starting Cu^{I} salt. ESI-MS spectra of $[Cu^{II}_2(\mathbf{L^{1}*SO_2})_2](BF_4)_2$ and $[Cu^{II}_2(\mathbf{L^{1}*SO_2})_2(OTf)_2]$ both show a peak pattern that corresponds to one copper ion with one ligand without the SO_2-group. Loss of an SO_2 group upon fragmentation of

sulfinate-containing ligands during ionization has been previously reported for nickel and palladium sulfinate complexes.[6, 7] The spectrum of $[Cu^{II}_2(\mathbf{L^{1*}SO_2})_2](BF_4)_2$ also shows two smaller signals that can be assigned to $[Cu(\mathbf{L^{1*}SO_2})]^+$ and $[Cu(\mathbf{L^{1*}SO_2})$ + $Na]^+$. The HRMS spectrum of $[Cu^{II}_2(\mathbf{L^{1*}SO_2})_2](BF_4)_2$ shows a peak pattern for $[Cu(\mathbf{L^{1*}SO_2})]^+$ and $[Cu_2(\mathbf{L^{1*}SO_2})_2 + F_3CCOO]^+$ together with a range of other signals that indicate the instability of the SO_2 group: $[Cu(\mathbf{L^{1*}SO_2}) - SO_2]^+$, $[Cu(\mathbf{L^{1*}S})]^+$, $[Cu(\mathbf{L^{1*}SO_3} - 2H]^+$. The powder EPR spectra of the sulfinate complexes show an axial signal with $g_{\parallel} = 2.18$ and $g_{\perp} = 2.09$ (Figure AIII.1, Appendix III).

Analyses of the green powders indicate the formation of Cu^{II} sulfonate species. These complexes have been isolated with BF_4^- and OTf^- counterions, and are tentatively described as the dinuclear compounds $Cu^{II}_2(\mathbf{L^{1*}SO_3})_2(BF_4)_2$ and $Cu^{II}_2(\mathbf{L^{1*}SO_3})_2(OTf)_2$. Unfortunately, all attempts to crystallize these Cu^{II} sulfonate species failed. $Cu^{II}_2(\mathbf{L^{1*}SO_3})_2(BF_4)_2$ and $Cu^{II}_2(\mathbf{L^{1*}SO_3})_2(OTf)_2$ have been analyzed with ESI-MS showing peak patterns corresponding to the dicationic complex $[Cu_2(\mathbf{L^{1*}SO_3})_2]^{2+}$ and the mononuclear complex with loss of the SO_3 group. The HRMS spectrum of complex $Cu^{II}_2(\mathbf{L^{1*}SO_3})_2(OTf)_2$ shows a large number of signals resulting from reactivity of the SO_3-group similar to what was observed for the SO_2-group in $[Cu^{II}_2(\mathbf{L^{1*}SO_2})_2](BF_4)_2$: $[Cu(\mathbf{L^{1*}SO_3}) - SO_3]^+$, $[Cu(\mathbf{L^{1*}S})]^+$, $[Cu(\mathbf{L^{1*}SO_2}]^+$, $[Cu(\mathbf{L^{1*}SO_3})(\mathbf{L^{1*}SO_2}) + OH + 2\ Na]^+$. A signal corresponding to a mononuclear species $[Cu(\mathbf{L^{1*}SO_3})]^+$ was also found in HRMS, in contrast to the ESI-MS spectrum in which a peak pattern for the dinuclear species $[Cu_2(\mathbf{L^{1*}SO_3})_2]^{2+}$ is present. Furthermore a signal that may correspond to $[Cu(\mathbf{L^{1*}OSO_3})]^+$ is present, although this signal can also be assigned to $[Cu(\mathbf{L^{1*}SO_2}) + CH_3OH]^+$. Powder EPR spectra of $Cu^{II}_2(\mathbf{L^{1*}SO_3})_2(BF_4)_2$ and $Cu^{II}_2(\mathbf{L^{1*}SO_3})_2(OTf)_2$ both show an isotropic signal with $g = 2.11$ (Figure AIII.2, Appendix III).

4.2.2 X-ray Crystallography

Description of $[Cu^{II}_4Cu^{I}_4(\mathbf{L^{1*}S})_4(\mu\text{-}OH)_2(CH_3CN)_6](ClO_4)_6 \cdot 2\ CH_3CN$

A projection of the structure of the cationic cluster of $[Cu^{II}_4Cu^{I}_4(\mathbf{L^{1*}S})_4(\mu\text{-}OH)_2(CH_3CN)_6]^{6+}$ is depicted in Figure 4.2 and crystallographic data are collected in Table 4.1. Selected bond angles and distances can be found in Table AIII.1, Appendix III. The compound crystallizes in the centrosymmetric monoclinic space group C2/*c*, with one complex cluster, six perchlorate ions and two molecules of acetonitrile per asymmetric unit. The crystal structure is mostly ordered except for three of the six perchlorate ions, which are found to be disordered over two or three orientations. $[Cu^{II}_4Cu^{I}_4(\mathbf{L^{1*}S})_4(\mu\text{-}OH)_2(CH_3CN)_6]^{6+}$ is an octanuclear mixed-

valent copper species with the formula $[Cu^{II}_4Cu^{I}_4(\mathbf{L^{1*}S})_4(\mu\text{-}OH)_2(CH_3CN)_6](ClO_4)_6$. The cluster contains four Cu^{I} and four Cu^{II} ions with two hydroxide and four $\mathbf{L^{1*}S}^-$ ligands.

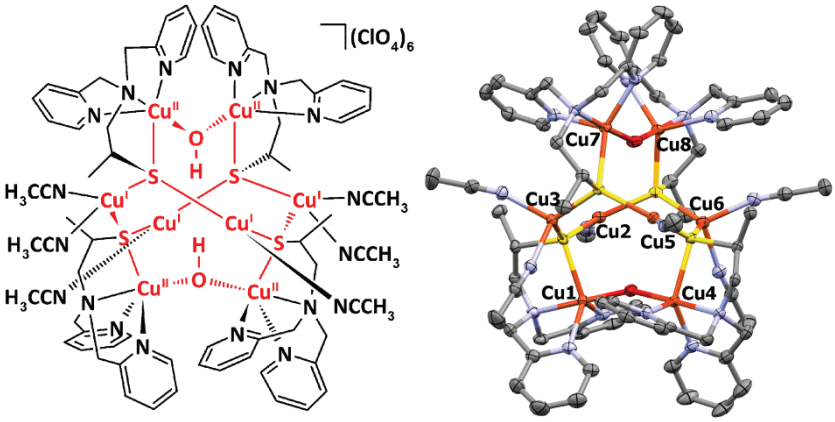

Figure 4.2: Schematic drawing and projection of the structure of the cationic part of $[Cu^{II}_4Cu^{I}_4(\mathbf{L^{1*}S})_4(\mu\text{-}OH)_2(CH_3CN)_6](ClO_4)_6 \cdot 2\ CH_3CN$. Displacement ellipsoids are depicted at the 50% probability level and all hydrogen atoms are omitted for clarity. Bond distance (Å) ranges: Cu^{I}-S, 2.22-2.31; Cu^{II}-S, 2.34-2.36; Cu^{II}-O, 1.91-1.94; Cu^{I}-N, 1.96-2.08; Cu^{II}-N, 2.03-2.05; Cu^{II}-N_{py}, 2.03-2.14.

The structure can be described as two dinuclear $\{Cu^{II}_2(\mathbf{L^{1*}S})_2(OH)\}$ units in which the copper ions are singly bridged by the hydroxide group; these dinuclear units are held together by four Cu^{I} ions. Each Cu^{I} ion is bridging between two different thiolate groups from two ligands (one from each dinuclear unit) and is bound to either one or two acetonitrile ligands. The central bridging structure thus comprises two Cu^{I} ions with trigonal NS_2 coordination and two Cu^{I} ions with tetrahedral N_2S_2 coordination. The Cu^{II} ions are in an N_3OS environment, in a geometry that is best described as a highly distorted trigonal bipyramid with the hydroxide oxygen and amine nitrogen at the axial positions and τ values ranging between 0.63 and 0.82.[8] Contrary to what is expected, the Cu-S distances of the smaller Cu^{II} ion are larger than the Cu-S distances for Cu^{I}. The longer Cu^{II}-S distances might be caused by the presence of the hydroxide ion bridging the two Cu^{II} ions. The hydroxyl hydrogen is positioned between the two thiolate sulfurs forming a bifurcated O–H···S hydrogen bond, with H···S distances of 2.75 – 2.85 Å. An analogous pentanuclear Fe^{II} complex has been reported,[9] which contains a ligand very similar to $\mathbf{L^{1*}S}$. The structure is built up of similar $\{Fe^{II}_2(Py_2NS)_2(OH)\}$ units, but instead of being held together by four metal ions, one

Fe^{II} ion holds these fragments together, and the bridging hydroxide group is pointing away from the thiolate sulfurs.

Description of Structures $[Cu^{II}_2(\mathbf{L^{1*}SO_2})_2](BF_4)_2 \cdot 2\ (CH_3)_2CO$ and $[Cu^{II}_2(\mathbf{L^{1*}SO_2})_2(OTf)_2]$

The crystal structures of two dinuclear Cu^{II} sulfinate complexes with either BF_4^- counterions $[Cu^{II}_2(\mathbf{L^{1*}SO_2})_2](BF_4)_2 \cdot 2\ (CH_3)_2CO$ or OTf^- counterions $[Cu^{II}_2(\mathbf{L^{1*}SO_2})_2(OTf)_2]$ were determined. Projections of the cationic dinuclear structure of $[Cu^{II}_2(\mathbf{L^{1*}SO_2})_2](BF_4)_2$ and $[Cu^{II}_2(\mathbf{L^{1*}SO_2})_2(OTf)_2]$ are depicted in Figure 4.3; crystallographic data and selected bond distances and angles are given in Table 4.1 and Table 4.2, respectively.

Table 4.1: Crystallographic and structure refinement data for complex $[Cu^{II}_4Cu^{I}_4(\mathbf{L^{1*}S})_4(\mu\text{-}OH)_2(CH_3CN)_6]^{6+}$, $[Cu^{II}_2(\mathbf{L^{1*}SO_2})_2](BF_4)_2$ and $[Cu^{II}_2(\mathbf{L^{1*}SO_2})_2(OTf)_2]$.

	$[Cu^{II}_4Cu^{I}_4(\mathbf{L^{1*}S})_4(\mu\text{-}OH)_2(CH_3CN)_6](ClO_4)_6$	$[Cu^{II}_2(\mathbf{L^{1*}SO_2})_2](BF_4)_2$	$[Cu^{II}_2(\mathbf{L^{1*}SO_2})_2(OTf)_2]$
empirical formula	$[C_{72}H_{92}Cu_8N_{18}O_2S_4](ClO_4)_6 \cdot 2\ C_2H_3N$	$[C_{30}H_{36}Cu_2N_6O_4S_2](BF_4)_2 \cdot 2\ C_3H_6O$	$C_{32}H_{36}Cu_2F_6N_6O_{10}S_4$
formula weight	2557.00	1025.62	1033.99
crystal system	monoclinic	monoclinic	monoclinic
space group	*C2/c*	*C2/c*	$P2_1/c$
a, Å	27.0514(3)	29.4214(15)	9.3137(3)
b, Å	38.7599(3)	9.2998(4)	12.4946(4)
c, Å	23.0026(3)	21.3070(7)	16.8065(5)
β, deg	113.4265(15)	130.288(2)	100.346(3)
V, Å^3	22130.4(4)	4447.0(3)	1923.99(10)
Z	8	4	2
D_{calc}, g·cm^3	1.535	1.532	1.785
T, Kelvin	110(2)	150(2)	110(2)
crystal size, mm	$0.40 \times 0.26 \times 0.13$	$0.50 \times 0.30 \times 0.23$	$0.38 \times 0.20 \times 0.13$
μ, mm^{-1}	1.801	1.134	1.417
no. of reflns measd	80859	35196	13441
no. of unique reflns	19488	5082	3378
no. of reflns obsd.	15932 [$I > 2\sigma(I)$]	4465 [$I > 2\sigma(I)$]	2833 [$I > 2\sigma(I)$]
no. of parameters	1434	283	345
R_1 / wR_2 [$I > 2\sigma(I)$]	0.0335 / 0.0889	0.0275 / 0.0692	0.0546 / 0.1516
R_1 / wR_2 [all refl.]	0.0438 / 0.0928	0.0338 / 0.0724	0.0668 / 0.1605
goodness of fit	1.076	1.084	1.069
$\Delta\rho$, e·Å^{-3}	−0.59 / 0.87	−0.47 / 0.64	−0.55 / 1.11

$[Cu^{II}_2(\mathbf{L^{1*}SO_2})_2](BF_4)_2$ crystallizes in the monoclinic space group *C*2/*c*, with half a dinuclear compound, one molecule of acetone and one BF_4^- ion in the asymmetric unit; the dinuclear compound is located on a twofold rotation axis. Compound $[Cu^{II}_2(\mathbf{L^{1*}SO_2})_2(OTf)_2]$ crystallizes in the monoclinic space group $P2_1/c$, with one crystallographically independent half of the dinuclear compound in the asymmetric unit, the dinuclear copper complex is found at sites of inversion symmetry. In complex $[Cu^{II}_2(\mathbf{L^{1*}SO_2})_2](BF_4)_2$ the two symmetry-related Cu^{II} ions are bridged by the two SO_2^- groups, forming an eight-membered ring consisting of Cu1, O1, S1, O2, Cu1′, O1′, S1′, O2′ (Figure 4.3). This configuration is associated with a lower degree of strain than that of the four-membered ring Cu(μ-O)$_2$Cu found in $[Cu^{II}_2(\mathbf{L^{1*}SO_2})_2(OTf)_2]$; the coordination angle O1-Cu1-O2′ is 93.72(5)° in $[Cu^{II}_2(\mathbf{L^{1*}SO_2})_2](BF_4)_2$, whereas the bond angle O1-Cu1-O1′ is 75.56(13)° in $[Cu^{II}_2(\mathbf{L^{1*}SO_2})_2(OTf)_2]$. The copper ions in $[Cu^{II}_2(\mathbf{L^{1*}SO_2})_2](BF_4)_2$ are in an N_3O_2 coordination environment with distorted square-pyramidal geometry (τ = 0.28[8]).

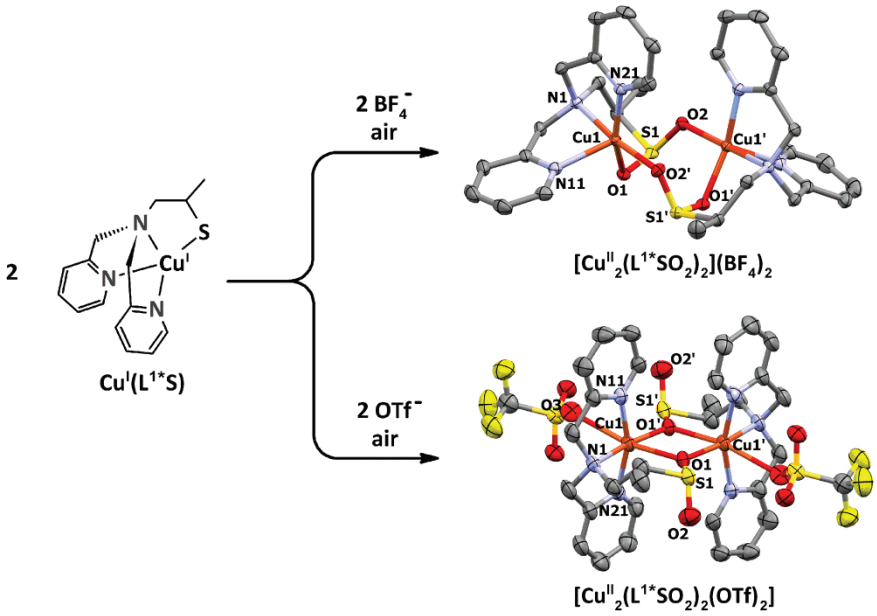

Figure 4.3: Schematic overview of the oxidation of $Cu^I(\mathbf{L^{1*}S})$ to $[Cu^{II}_2(\mathbf{L^{1*}SO_2})_2](BF_4)_2$ and $[Cu^{II}_2(\mathbf{L^{1*}SO_2})_2(OTf)_2]$. Projections of the crystal structures of complex $[Cu^{II}_2(\mathbf{L^{1*}SO_2})_2(OTf)_2]$ and the cationic part of $[Cu^{II}_2(\mathbf{L^{1*}SO_2})_2](BF_4)_2$ are depicted. Displacement ellipsoids are shown at the 50% probability level. All hydrogen atoms are omitted for clarity.

The di(pyridylmethyl)amine group is bound in a facial manner, with the pyridyl groups located in *cis* positions relative to each other. One of the pyridyl groups is located at the axial position at a distance of 2.1706(15) Å; the basal plane is formed by the other pyridyl nitrogen, the amine nitrogen and the two sulfinate oxygens. The S-O distances within the SO_2^- group are more or less equal (1.5247(13) and 1.5377(13) Å), indicating full delocalization of the electrons. Although the Cu^{II} centers are bridged by a three-atom structure, the Cu-Cu distance is relatively short at 3.6322(5) Å because of a weakly chelating interaction of the second sulfinate oxygen: The Cu1-O2 distance is 2.8833(16) Å, which can be considered as semi-coordinating. Taking this interaction into account the coordination geometry of the copper center can be regarded as elongated octahedral with the pyridyl N11 and O2 located on the Jahn-Teller axis. The BF_4^- anion is not coordinated.

The Cu^{II} centers in $[Cu^{II}_2(\mathbf{L^1{*}SO_2})_2(OTf)_2]$ are also symmetry related and are doubly bridged by two oxygens, one of each of the sulfinate groups, resulting in a planar $Cu(\mu\text{-}O)_2Cu$ arrangement.

Table 4.2: Selected bond distances and angles for $[Cu^{II}_2(\mathbf{L^1{*}SO_2})_2](BF_4)_2$ and $[Cu^{II}_2(\mathbf{L^1{*}SO_2})_2(OTf)_2]$.

Bond distance (Å)			**Bond angle (°)**		
	$[Cu^{II}_2(\mathbf{L^1{*}SO_2})_2](BF_4)_2$	$[Cu^{II}_2(\mathbf{L^1{*}SO_2})_2(OTf)_2]$		$[Cu^{II}_2(\mathbf{L^1{*}SO_2})_2](BF_4)_2$	$[Cu^{II}_2(\mathbf{L^1{*}SO_2})_2(OTf)_2]$
Cu1 - Cu1'	3.6322(3)	3.4679(7)	O1 - Cu1 - O2'	93.72(5)	
Cu1 - O1	1.9956(12)	2.415(3)	O1 - Cu1 - O1'		75.56(13)
Cu1 - O1'		1.959(3)	O2 - Cu1 - O2'	84.52(6)	
Cu1 - O2	2.8833(16)		O1 - Cu1 - N1	87.06(5)	170.01(15)
Cu1 - O2'	1.9698(12)		O1 - Cu1 - N11	93.89(5)	97.31(15)
Cu1 - O3		2.600(8)	O1 - Cu1 - N21	155.46(6)	98.11(16)
Cu1 - S1	2.9271(7)		N1 - Cu1 - N11	80.67(6)	83.85(16)
Cu1 - S1'	3.0825(6)	3.1152(13)	N1 - Cu1 - N21	84.43(6)	82.93(18)
Cu1 - N1	2.0417(14)	2.025(4)	N1 - Cu1 - O1		94.47(14)
Cu1 - N11	2.1706(15)	1.990(4)	N1 - Cu1 - O2	172.25(7)	
Cu1 - N21	1.9877(15)	2.016(4)	N11 - Cu1 - N21	107.32(6)	160.83(16)
S1 - O1	1.5247(13)	1.555(3)	N11 - Cu1 - O1		94.43(14)
S1 - O2	1.5377(13)	1.461(4)	N11 - Cu1 - O2	106.96(7)	
			N21 - Cu1 - O1		100.39(14)
			N21 - Cu1 - O2	91.78(7)	
			O1 - S1 - O2	107.88(7)	109.8(2)
			Cu1 - O1 - Cu1		104.44(13)
			Cu1 - O2 - Cu1'	95.05(7)	

'= 1 – x, y, ½ – z for $[Cu^{II}_2(\mathbf{L^1{*}SO_2})_2](BF_4)_2$ and –x, ½ + y, ½ – z for $[Cu^{II}_2(\mathbf{L^1{*}SO_2})_2(OTf)_2]$

The OTf^- counterions are coordinated to the copper centers resulting in an N_3O_3 environment. The OTf^- anions are disordered over two orientations with relative occupancies of 0.638(5) and 0.362(5). The Cu^{II} ions are in a Jahn-Teller elongated octahedral geometry with the triflate O3 and sulfinate O1 atoms in the axial positions at 2.600(8) and 2.415(3) Å, respectively. The di-(2-pyridylmethyl)amine group is bound in a meridional fashion in the equatorial plane, with the pyridyl groups in *trans* position relative to each other; the fourth position of the equatorial plane is occupied by the sulfonate oxygen O1′ of the symmetry-related molecule. In contrast with compound $[Cu^{II}_2(\mathbf{L^{1*}SO_2})_2](BF_4)_2$, the S-O distances within the SO_2^- group in $[Cu^{II}_2(\mathbf{L^{1*}SO_2})_2(OTf)_2]$ are dissimilar. The S1-O1 distance is 1.56 Å and the S1-O2 distance is 1.46 Å. This indicates that the S1-O1 bond has more of a single-bond character while the S1-O2 bond has more of a double bond character; the atom O1 with single-bond characteristics is coordinated to the Cu ions. Similar S-O distances have been reported for other Cu^{II} sulfinate complexes.[10, 11] The Cu-Cu distance of 3.468 Å is slightly smaller than that in $[Cu^{II}_2(\mathbf{L^{1*}SO_2})_2](BF_4)_2$. The $\mathbf{L^{1*}SO_2^-}$ enantiomers form *RR* and *SS* complexes in the crystal structure of $[Cu^{II}_2(\mathbf{L^{1*}SO_2})_2](BF_4)_2$, but are evenly distributed with one *R*-isomer and one *S*-isomer per dinuclear complex in the crystal structure of $[Cu^{II}_2(\mathbf{L^{1*}SO_2})_2(OTf)_2]$.

4.2.3 Solution Studies

Solutions of the sulfinato-Cu^{II} complexes $[Cu^{II}_2(\mathbf{L^{1*}SO_2})_2](BF_4)_2$ and $[Cu^{II}_2(\mathbf{L^{1*}SO_2})_2(OTf)_2]$ in acetonitrile give the same UV-vis spectra (Figure AIII.4a, Appendix III), showing a $\pi^* \leftarrow \pi$ transition of the pyridyl groups at 262 nm, an LMCT of $Cu^{II} \leftarrow O$ at 314 nm and two transitions at 476 and 770 nm. The transition at 770 nm can be ascribed to a d-d transition of the copper(II) ion. The high ε value ($\varepsilon = 450\ M^{-1}\ cm^{-1}$) of the transition at 476 nm indicates that this absorption must be ascribed to a second $Cu^{II} \leftarrow O$ LMCT. The similarity of the spectra indicates that the OTf^- counterion of $[Cu^{II}_2(\mathbf{L^{1*}SO_2})_2(OTf)_2]$ does not remain coordinated in solution. When UV spectra of the complexes are recorded at higher concentrations the absorbance at 476 nm disappears, while a new band arises at 370 nm (see Figure 4.4a). This behavior may indicate that in solution the dinuclear Cu^{II} complex is in equilibrium with its monomeric form depending on the concentration. The sulfonato-Cu^{II} complexes $Cu^{II}_2(\mathbf{L^{1*}SO_3})_2(BF_4)_2$ and $Cu^{II}_2(\mathbf{L^{1*}SO_3})_2(OTf)_2$ also show the same UV-vis spectra in acetonitrile solution, indicating that also in these compounds the counterions do not coordinate to the copper centers in solution (Figure AIII.4b, Appendix III). The absorbance spectra of $Cu^{II}_2(\mathbf{L^{1*}SO_3})_2(BF_4)_2$ and $Cu^{II}_2(\mathbf{L^{1*}SO_3})_2(OTf)_2$ show bands

similar to those of $[Cu^{II}_2(\mathbf{L^{1*}SO_2})_2](BF_4)_2$ and $[Cu^{II}_2(\mathbf{L^{1*}SO_2})_2(OTf)_2]$, with the $\pi^* \leftarrow \pi$ transition of the pyridyl groups at 262 nm, an oxygen to copper LMCT at 306 nm and two d-d transitions at 490 and 740 nm. The effect of the complex concentration on the absorbance, as observed for $[Cu^{II}_2(\mathbf{L^{1*}SO_2})_2](BF_4)_2$, is also present for $Cu^{II}_2(\mathbf{L^{1*}SO_3})_2(BF_4)_2$, but the changes are much smaller (Figure 4.4b). With increasing complex concentration, the absorbance at 490 nm decreases and a small increase in absorbance takes place at 378 nm.

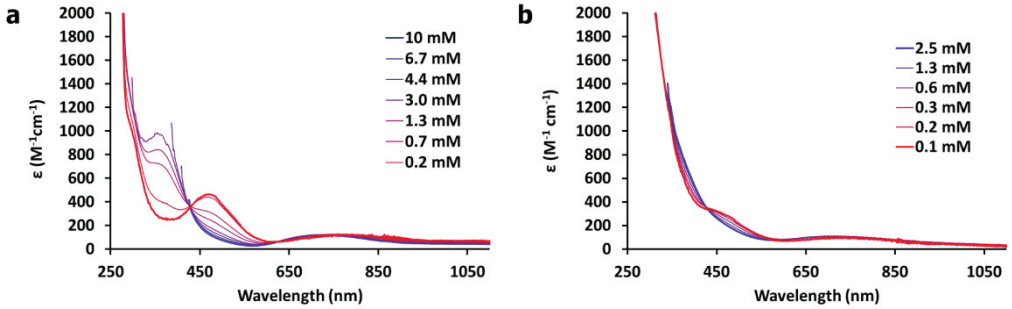

Figure 4.4: UV-vis spectra of $[Cu^{II}_2(\mathbf{L^{1*}SO_2})_2](BF_4)_2$ (a) and $Cu^{II}_2(\mathbf{L^{1*}SO_3})_2(BF_4)_2$ (b) at different concentrations in acetonitrile recorded with a pathlength of 10 mm.

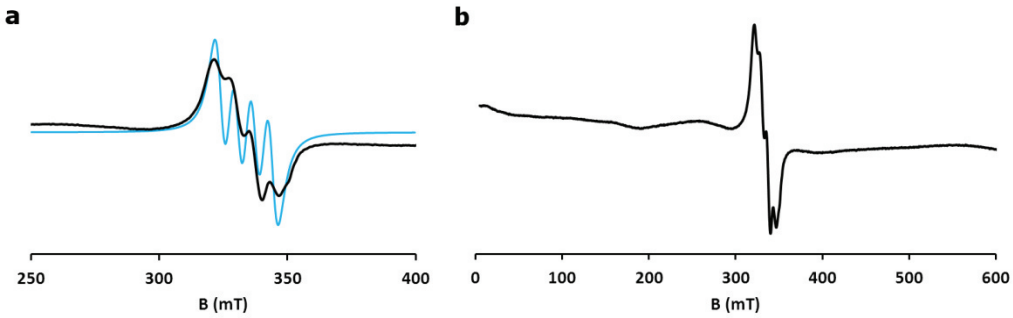

Figure 4.5: X-Band EPR spectrum (ν = 9.874 GHz) of $[Cu^{II}_2(\mathbf{L^{1*}SO_2})_2(OTf)_2]$ at RT dissolved in acetonitrile (black line) plotted from 250 to 400 mT (a) and 0 to 600 mT (b); Simulation with parameters g(iso) = 2.108, A_{Cu}(iso) = 185 MHz, line width w(iso) = 40 MHz (blue line).

The sulfinate compounds $[Cu^{II}_2(\mathbf{L^{1*}SO_2})_2](BF_4)_2$ and $[Cu^{II}_2(\mathbf{L^{1*}SO_2})_2(OTf)_2]$ show highly similar solution EPR spectra in both acetone and acetonitrile solutions at room temperature. The spectra predominantly show a mononuclear isotropic signal at g_i = 2.11 with a copper hyperfine splitting of 63 Gauss (Figure 4.5a, black line). In addition

to the signal of the mononuclear species a weak axial triplet signal is observed, with a half field signal at 1600 Gauss, indicating the presence of two ferromagnetically interacting Cu^{II} ions (Figure 4.5b).[12, 13] The isotropic signal of $[Cu^{II}_2(\mathbf{L^{1*}SO_2})_2(OTf)_2]$ was simulated (Figure 4.5a, blue line) showing the copper hyperfine coupling to be 185 MHz. The broad triplet signal underlying the isotropic signal results in deviation from the baseline. EPR solution spectra of the sulfonate compounds $Cu^{II}_2(\mathbf{L^{1*}SO_3})_2(BF_4)_2$ and $Cu^{II}_2(\mathbf{L^{1*}SO_3})_2(OTf)_2$ are very similar to the spectra of the Cu^{II} sulfinate complexes (Figure AIII.3, Appendix III), showing similar weak axial triplet spectra overlaid with isotropic signals. A weak half-field signal was observed for $Cu^{II}_2(\mathbf{L^{1*}SO_3})_2(BF_4)_2$ and $Cu^{II}_2(\mathbf{L^{1*}SO_3})_2(OTf)_2$ in acetone, but this signal was not visible in acetonitrile.

Cyclic voltammograms of $[Cu^{II}_2(\mathbf{L^{1*}SO_2})_2](BF_4)_2$ were recorded in acetone solutions. The voltammogram shows two quasi-reversible waves (Figure 4.6a). The first wave is located at $E_{1/2}$ = –306 mV with a peak to peak separation of 121 mV; the second electrochemical event is centered at $E_{1/2}$ = –74 mV with a peak to peak separation of 182 mV. When the concentration of the compound was increased from 1 mM [Cu] to 2 mM [Cu] the ratio of the peak currents of the two events (Δ1/Δ2) slightly changed from 1.0 to 1.1, indicating that the two redox events may be ascribed to the presence of a mononuclear and a dinuclear species as observed in the UV-vis spectra; the redox event at –306 mV may thus possibly be attributed to the dinuclear species.

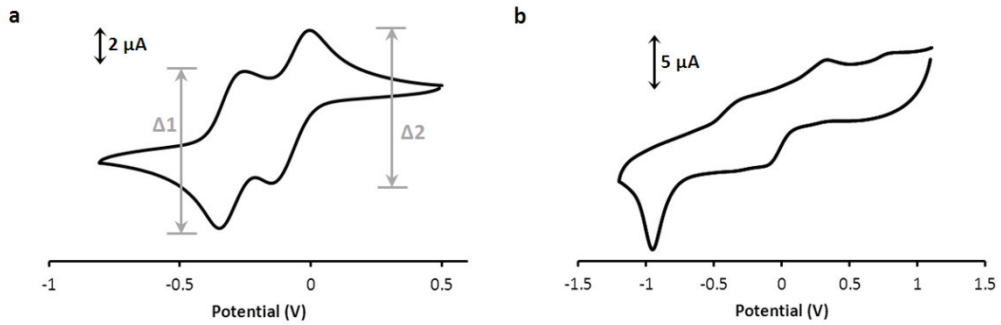

Figure 4.6: Cyclic voltammogram of $[Cu^{II}_2(\mathbf{L^{1*}SO_2})_2](BF_4)_2$ (a) and $Cu^{II}_2(\mathbf{L^{1*}SO_3})_2(BF_4)_2$ (b) in acetone at 1 mM [Cu] concentration at RT. The scan rate is 100 mV/s; potentials are given vs Ag/AgCl.

The cyclic voltammogram of Cu^{II} sulfonate complex $Cu^{II}_2(\mathbf{L^{1*}SO_3})_2(BF_4)_2$ is different from that of $[Cu^{II}_2(\mathbf{L^{1*}SO_2})_2](BF_4)_2$ and shows no reversible electrochemical events

(Figure 4.6b). At least three reduction events (E_{pc} at –103, –345 and –939 mV) and three oxidation waves (E_{pa} at –345, 310 and 783 mV) are observed. The CV of complex $Cu^{II}_2(\mathbf{L^{1*}SO_3})_2(BF_4)_2$ is reproducible when the electrode is polished in between measurements. When this is not done small shifts in the peak potentials are observed. The reduction wave at –939 mV shifts to more positive potentials at higher scan rates and more negative potentials at lower scan rates (Figure 4.7).

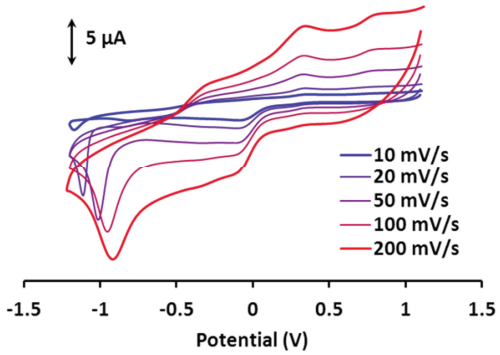

Figure 4.7: Cyclic voltammogram of $Cu^{II}_2(\mathbf{L^{1*}SO_3})_2(BF_4)_2$ in acetone at 1 mM [Cu] concentration measured at different scan rates at RT; potentials are given vs Ag/AgCl.

4.2.4 UV-Vis Monitoring of the Oxidation of $Cu^{I}(\mathbf{L^{1*}S})$

The oxidation of $Cu^{I}(\mathbf{L^{1*}S})$ to the sulfinate and sulfonate species was monitored using UV-vis spectroscopy. When a solution of $Cu^{I}(\mathbf{L^{1*}S})$ is opened to air, a new species starts to form as indicated by a color change from light brown to dark green (Figure 4.8a). The solution was kept homogeneous by bubbling air through the solution and stirring at 400 rpm. An absorbance band at 372 nm arises within three minutes, which is likely to be a thiolate to Cu^{II} LMCT. Two bands at 573 nm and 910 nm of lower intensity appear which may be attributed to d-d transitions. The UV-vis spectrum for the recently reported Cu^{II} μ-thiolate species $[Cu^{II}_2(\mathbf{L^{1*}S})_2]^{2+}$ shows the same characteristic absorption bands.[14] When this solution is left in air for a period of 6 hours, the solution slowly turns green; the characteristic bands for the intermediate species disappear, indicating further oxidation of the copper compound (Figure 4.8b). In the spectrum of the fully oxidized species a broad d-d transition is observed (inset Figure 4.8b) in agreement with the presence of both the sulfinate (770 nm) and sulfonate (740 nm) species.

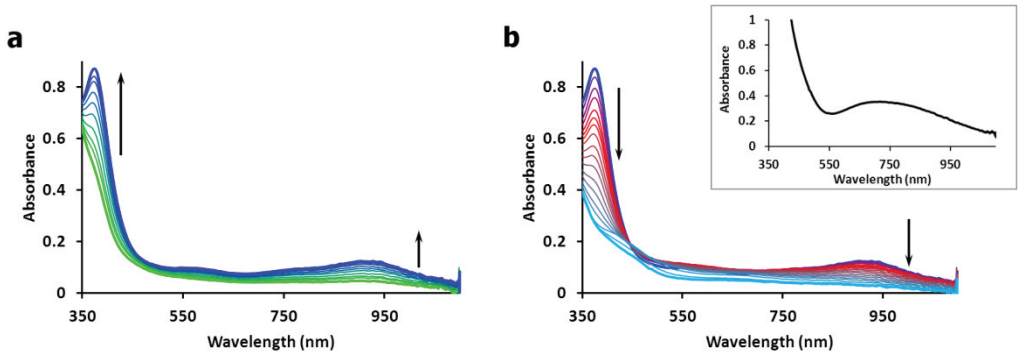

Figure 4.8: UV-vis spectral changes observed for an acetone solution of Cu^{I}(**L¹*S**) with concentration of 2 mM [Cu] exposed to air for 6 hours. Appearance of absorbance bands in first three minutes (a) and decrease of absorbance bands over 6 hours (b); inset shows UV-vis spectrum of the fully oxidized Cu^{I}(**L¹*S**) at 6.0 mM [Cu] recorded with a transmission dipprobe path length of 3.4 mm.

4.3 Discussion

When **L¹*SH** is reacted with $[Cu^{I}(CH_3CN)_4](BF_4)$ in acetone, a species is formed that is tentatively formulated as Cu^{I}(**L¹*S**), although the formation of dinuclear or oligonuclear species cannot be ruled out. Cu^{I}(**L¹*S**) is highly oxidation sensitive, as suggested by the broad NMR signals that are indicative for the presence of traces of Cu^{II}. When Cu^{I}(**L¹*S**) is brought into contact with air, Cu^{I} is oxidized to Cu^{II} before the thiolate ligand is oxidized. In an attempt to crystallize the Cu^{I} thiolate complex, the multivalent compound $[Cu^{II}_4Cu^{I}_4(\mathbf{L^{1*}S})_4(\mu\text{-}OH)_2(CH_3CN)_6](ClO_4)_6$ was isolated, which may be regarded as an intermediate in the oxidation process; in this compound Cu^{II} as well as Cu^{I} centers are present, whereas the thiolate ligands are not yet oxidized. In the initial stage of the oxidation process, the formation of a species with specific absorption bands at 372 nm, 573 nm and 910 nm is indicative for the oxidation of Cu^{I} to Cu^{II}, generating a species that can be formulated as $[Cu^{II}_2(\mathbf{L^{1*}S})_2]^{2+}$ (see Figure 4.9). This is confirmed by comparing the UV-vis spectrum generated upon partial oxidation of the Cu^{I} thiolate solution with the reported UV-vis spectrum for the dinuclear Cu^{II} μ-thiolate complex $[Cu^{II}_2(\mathbf{L^{1*}S})_2]^{2+}$.[14] When $[Cu^{II}_2(\mathbf{L^{1*}S})_2]^{2+}$ is further oxidized by dioxygen, Cu^{II} sulfinate complexes $[Cu^{II}_2(\mathbf{L^{1*}SO_2})_2](BF_4)_2$ and $[Cu^{II}_2(\mathbf{L^{1*}SO_2})_2(OTf)_2]$ and Cu^{II} sulfonate complexes $Cu^{II}_2(\mathbf{L^{1*}SO_3})_2(BF_4)_2$ and $Cu^{II}_2(\mathbf{L^{1*}SO_3})_2(OTf)_2$ are obtained. A complete overview of the observed reactivity of Cu^{I}(**L¹*S**) in air is given in Figure 4.9. The Cu_2S_2 core in the dinuclear species $[Cu^{II}_2(\mathbf{L^{1*}S})_2]^{2+}$ bears some resemblance to the Cu_A site; the oxidation of $[Cu^{II}_2(\mathbf{L^{1*}S})_2]^{2+}$

into Cu^{II} sulfinate and Cu^{II} sulfonate species may thus provide information about possible deactivation pathways of the Cu_A active site and possibly other copper-sulfur enzymes.

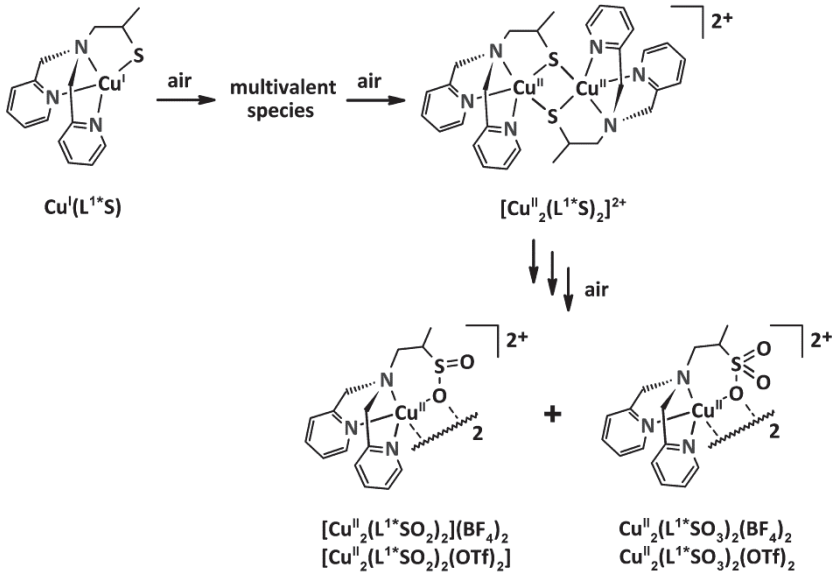

Figure 4.9: Schematic overview of the complete oxidation of Cu^I(**L^{1*}S**).

Quite some research has been carried out on models for dioxygen-induced degradation of enzymes. Most investigations have been focused on nickel,[7, 15-17] but also the oxygenation reactions of thiolate complexes of other metals such as cobalt,[18, 19] iron[20-22] and zinc[23] have been studied. Some studies on the oxidation of copper-sulfur compounds have been reported, but the chemistry is greatly complicated by the ability of copper to catalyze disulfide formation and cleavage.[24, 25] A Cu^I compound has been reported to form a Cu^{II} sulfonate complex starting from either a disulfide or a thiolate ligand.[26] Similarly, the generation of a Cu^{II} sulfinate compound starting from Cu^{II} with a disulfide ligand,[10] or a sulfonate-containing complex starting from a thiolate ligand have been reported.[27] Noteworthy is also the formation of Cu^I disulfide and Cu^{II} sulfinate species from a Cu^{II} disulfide complex under anaerobic conditions in water.[11] The mechanisms behind these reactions are very complicated and seem to differ depending on the ligand. It appears that the ligand largely determines the coordination environment of the copper center and whether a Cu^I disulfide species or a Cu^{II} thiolate species is formed as the most stable configuration.[25] The oxidation reaction of these two species most likely will follow different

mechanisms. The dipyridyl-thiolate ligand **L¹*SH** used in our studies generates a dinuclear Cu^{II} μ-thiolate instead of a Cu^{I} disulfide compound upon reaction with a Cu^{II} salt. This corroborates our finding that the oxidation of Cu^{I}(**L¹*S**) proceeds via the oxidation of Cu^{I} to Cu^{II} before the oxygenation of the ligand takes place.

The exact mechanism of oxygenation of the thiolate ligand is not yet clear. The ESI-MS of Cu^{I}(**L¹*S**) shows a small signal that may tentatively be ascribed to either a copper-sulfenate or a copper-hydroxide species either of which could be intermediates in the oxidation reaction. All attempts at isolation of other intermediates in addition to $[Cu^{II}_4Cu^{I}_4(\mathbf{L^{1*}S})_4(\mu\text{-}OH)_2(CH_3CN)_6](ClO_4)_6$ failed. To the best of our knowledge, there are no previous reports in which both a Cu^{II} sulfinate and a Cu^{II} sulfonate complex were isolated and characterized. This gives us the unique opportunity to compare the properties of both types of complexes.

The UV-vis spectra of the sulfinate and the sulfonate complexes show many similarities. Both spectra show an oxygen to Cu^{II} LMCT and two d-d transitions at roughly the same wavelengths. The EPR and UV-vis spectra of the two sulfinate complexes $[Cu^{II}_2(\mathbf{L^{1*}SO_2})_2](BF_4)_2$ and $[Cu^{II}_2(\mathbf{L^{1*}SO_2})_2(OTf)_2]$ dissolved in either acetone or acetonitrile are highly comparable, indicating that the counterion dissociates and the same $[Cu^{II}_2(\mathbf{L^{1*}SO_2})_2]^{2+}$ species is present in solution. The changes observed in these spectra depending on the concentration of the copper compounds, indicate the presence of both monomeric and dimeric species in an equilibrium reaction. The same behavior is observed for the sulfonate complexes $Cu^{II}_2(\mathbf{L^{1*}SO_3})_2(BF_4)_2$ and $Cu^{II}_2(\mathbf{L^{1*}SO_3})_2(OTf)_2$, indicating that these are most likely also dinuclear in the solid state with general formula $[Cu^{II}_2(\mathbf{L^{1*}SO_3})_2]^{2+}$. For the Cu^{II} sulfonate complexes the equilibrium in solution seems to be more directed towards the dinuclear species; the increase of the band at 490 nm for the Cu^{II} sulfonate compound with dilution is much smaller than the increase at 476 nm for the Cu^{II} sulfinate complex. Furthermore, for the Cu^{II} sulfonate compounds a signal in the ESI-MS can be ascribed to the dicationic, dinuclear species. The solution EPR spectra of the Cu^{II} sulfinate and Cu^{II} sulfonate compounds are also very similar, both showing the presence of the monomeric as well as dimeric species in solution.

Whereas the spectroscopic data for the Cu^{II} sulfinate and Cu^{II} sulfonate complexes are very similar, the electrochemical properties on the other hand are dissimilar. The cyclic voltammogram of $[Cu^{II}_2(\mathbf{L^{1*}SO_2})_2](BF_4)_2$ shows two quasi-reversible waves. These two waves may tentatively be ascribed again to the presence of monomeric and dimeric species, in which case the Cu^{II} to Cu^{I} reduction would take place at different potentials for each species. Alternatively, since the ratio of peak currents shows only a small change upon a small concentration difference, these two waves can be

assigned to two separate one-electron reductions of the dinuclear compound, with a stable $Cu^{II}Cu^{I}$ intermediate.[28] However, for dinuclear systems similar to $[Cu^{II}_2(\mathbf{L^{1*}SO_2})_2](BF_4)_2$ also single isolated two-electron events have been reported.[28] With the available data it is not possible to decide which assignment is appropriate. In contrast, the cyclic voltammogram of Cu^{II} sulfonate compound $Cu^{II}_2(\mathbf{L^{1*}SO_3})_2(BF_4)_2$ shows several irreversible events. A possible explanation for the irreversibility could be the difference in hardness of the sulfonate group as compared to the sulfinate group; the softer sulfinate group is more likely to stabilize the Cu^{I} oxidation state as it can also bind with the sulfur atom. To be able to compare Cu^{II} sulfinate and Cu^{II} sulfonate complexes in more detail, a crystal structure of the sulfonate compound would be helpful. Furthermore, it would be very interesting to isolate other intermediates such as a Cu^{II} sulfenate complex, because up till now such a compound has not been reported.

4.4 Conclusion

Cu^{II} sulfinate and Cu^{II} sulfonate complexes that were formed by the oxidation of a Cu^{I} thiolate species, were isolated and analyzed. Elucidation of the mechanism for oxygenation of the thiolate ligands in the Cu^{II} thiolate species toward the Cu^{II} sulfinate and Cu^{II} sulfonate complexes could give information about the degradation pathways of copper-sulfur enzymes by dioxygen. UV-vis spectroscopy shows that oxidation of the Cu^{I} thiolate complex proceeds via the formation of a dinuclear Cu^{II} thiolate compound that bears resemblance to the Cu_A active site. The oxidation of Cu^{I} to Cu^{II} takes place before the thiolate ligand is oxygenated, which could be caused by the tendency of this type of complexes to form Cu^{II} thiolate species rather than Cu^{I} disulfide species. Spectroscopic and electrochemical analysis of the Cu^{II} sulfinate and Cu^{II} sulfonate complexes showed that both species are spectroscopically very similar, but electrochemically very different. This difference in electrochemical properties is most likely caused by the relative hardness of the sulfonate group that is not suitable for stabilization of the Cu^{I} oxidation state.

4.5 Experimental section

4.5.1 Materials

All chemicals were purchased from commercial sources and used as received. $[Cu^{I}(CH_3CN)_4](BF_4)$, $[Cu^{I}(CH_3CN)_4](ClO_4)$ and $[Cu^{I}(CH_3CN)_4](OTf)$ were synthesized according to literature procedures.[29, 30] All solvents were reagent grade. The synthesis of the ligand **L^1*SH** and the Cu^{I} complexes were carried out using standard Schlenk-line techniques under an argon atmosphere. Solvents for these experiments were distilled, deoxygenated by bubbling a

stream of argon through the solution and stored on activated molecular sieves under argon prior to use.

4.5.2 Analytical Methods

NMR spectra were recorded on a Bruker 300 DPX spectrometer. IR spectra were obtained on a Perkin Elmer Paragon 1000 FTIR spectrophotometer equipped with a Golden Gate ATR device. X-band EPR derivative spectra were recorded with a Bruker EMXplus ESR spectrometer. Elemental analyses were performed using a Perkin Elmer 2400 Series II CHNS/O analyzer. Mass spectrometry was measured using a Finnigan Aqua Mass Spectrometer (MS) with electro spray ionization (ESI). Sample introduction was achieved through a Dionex ASI-100 automated sample injector with an eluent flow rate of 0.2 mL/min. HRMS spectra were recorded on a Thermo Finnigan LTQ Orbitrap equipped with an electro spray ion source in positive mode. UV-vis spectra were collected on a Perkin Elmer Lambda 900 Spectrometer. In situ UV-vis spectra of the oxidation experiments were collected using a transmission dipprobe with variable path length on an Avantes Avaspec-2048 spectrometer with Avalight-DH-S-BAL light source. Cyclic voltammetry was performed with an Autolab PGstat10 potentiostat controlled by GPES4 software. A three electrode arrangement with a glassy carbon working electrode (3 mm diameter), an Ag/AgCl double junction reference electrode and a Pt wire counter electrode in acetone/0.1 M NBu_4PF_6 was used. In these conditions the Fc/Fc^+ couple was found to be located at +525 mV, with a peak-to-peak separation of 62 mV. Potentials are given relative to the Ag/AgCl electrode.

4.5.3 X-ray Structure Determinations

$[Cu^{II}_4Cu^{I}_4(\mathbf{L^{1}*S})_4(\mu\text{-}OH)_2(CH_3CN)_6](ClO_4)_6$ and $[Cu^{II}_2(\mathbf{L^{1}*SO_2})_2(OTf)_2]$

All reflection intensities for compounds $[Cu^{II}_4Cu^{I}_4(\mathbf{L^{1}*S})_4(\mu\text{-}OH)_2(CH_3CN)_6](ClO_4)_6 \cdot 2\ CH_3CN$ and $[Cu^{II}_2(\mathbf{L^{1}*SO_2})_2(OTf)_2]$ were measured at 110(2) K using a KM4/Xcalibur diffractometer (detector: Sapphire3) with enhanced graphite-monochromated Mo $K\alpha$ radiation (λ = 0.71073 Å) under the program CrysAlisPro (Version 1.171.35.11 Oxford Diffraction Ltd., 2011). The program CrysAlisPro was used to refine the cell dimensions and for data reduction. The structures were solved with the program SHELXS-97[31] and were refined on F^2 with SHELXL-97.[31] Analytical numeric absorption corrections based on a multifaceted crystal model were applied using CrysAlisPro. The temperature of the data collection was controlled using the system Cryojet (manufactured by Oxford Instruments). The H atoms (unless otherwise specified) were placed at calculated positions using the instructions AFIX 13, AFIX 23, AFIX 43 or AFIX 137 with isotropic displacement parameters having values 1.2 or 1.5 times U_{eq} of the attached C atoms.

$[Cu^{II}_2(\mathbf{L^1{*}SO_2})_2](BF_4)_2$

Reflections for $[Cu^{II}_2(\mathbf{L^1{*}SO_2})_2](BF_4)_2 \cdot 2\ (CH_3)_2CO$ were measured on a Bruker Kappa Apex II diffractometer with sealed tube and Triumph monochromator (λ = 0.71073 Å). The intensities were integrated with the program Eval15.[32] Absorption correction was performed with SADABS.[33] The structure was solved with Direct Methods using SHELXS-97.[31] Least-squares refinement was performed with SHELXL-2013[31] against F2 of all reflections. Non-hydrogen atoms were refined freely with anisotropic displacement parameters. Hydrogen atoms were located in difference Fourier maps and refined with a riding model. Geometry calculations and checking for higher symmetry was performed with the PLATON program.[34]

4.5.4 Ligand and Complex Synthesis

*N-(2-mercaptopropyl)-N,N-bis(2-pyridylmethyl)amine (**L¹*SH**)*

L¹*SH was synthesized according to a reported procedure[4] with some modifications.

Di-(2-picolyl)amine (0.90 mL, 5.0 mmol) was dissolved in 10 ml acetonitrile under argon. Propylene sulfide (0.59 mL, 7.5 mmol) was added, after which the reaction mixture was stirred for 15 hours at 70 °C under argon. After the mixture had cooled down, the solvent and excess propylene sulfide were evaporated. The resulting yellow oil was purified by column chromatography (silica, eluent 4% methanol in dichloromethane) which yielded a light yellow oil (1.1 g, 4.0 mmol, 80%). ^{1}H-NMR (300 MHz, CD_3CN, RT): δ 1.21 (d, *J* = 7 Hz, 3H, C*-C*H*$_3$), 2.54 (dd, *J* = 13 Hz, 8 Hz, 1H, N-C*H*$_2$-C*), 2.66 (dd, *J* = 13 Hz, 6 Hz, 1H, N-C*H*$_2$-C*), 3.20 (m, 1H, C*-*H*), 3.81 (dd, *J* = 29 Hz, 14 Hz, 4H, Py-C*H*$_2$-N), 7.22 (m, 2H, Py-*H*$_5$), 7.58 (d, *J* = 8 Hz, 2H, Py-*H*$_3$), 7.73 (td, *J* = 8 Hz, 2 Hz, 2H, Py-*H*$_4$), 8.52 (m, 2H, Py-*H*$_6$). ^{13}C-NMR (75 MHz, CD_3CN, RT): δ 22.2 (C*-*C*H$_3$), 33.9 (*C**), 61.1 (Py-*C*H$_2$-N), 64.3 (N-*C*H$_2$-C*), 122.9 (Py-*C*$_5$), 124.1 (Py-*C*$_3$), 137.1 (Py-*C*$_4$), 149.7 (Py-*C*$_6$), 160.3 (Py-*C*$_2$). ESI-MS found (calcd) for [**L¹*SSL¹*** + H]$^+$: *m*/*z* 545.2 (545.3). IR (neat, cm^{-1}): 2820*w*, 1589*m*, 1432*m*, 1148*w*, 1073*w*, 995*w*, 756*s*, 612*w*, 404*m*.

$Cu^I(\mathbf{L^1{*}S})$

One equivalent of **L¹*SH** was mixed with one equivalent of $[Cu^I(CH_3CN)_4]^+$ in either acetonitrile or acetone. This resulted in a light brown solution. For ^{1}H-NMR, a solution of **L¹*SH** (0.24 mmol) and $[Cu^I(CH_3CN)_4](ClO_4)$ (0.24 mmol) in 1.5 mL of deuterated acetonitrile was prepared under argon. NMR experiments were carried out under argon using a J. Young NMR tube. ^{1}H-NMR (300 MHz, CD_3CN, RT): δ 0.85 (br, 1H, C*-C*H*$_3$), 1.22 (br, 2H, C*-C*H*$_3$), 2.80 (br, 1H, N-C*H*$_2$-C*) 3.13 (br, 1H, N-C*H*$_2$-C*), 3.87 (br, 2H, C*-*H* and Py-C*H*$_2$-N), 4.33 (br, 3H, Py-C*H*$_2$-N), 6.24 (br, 2H), 7.57 (br, 4H, Py-*H*), 8.05 (br, 2H, Py-*H*), 8.73 (br, 2H, Py-*H*). ESI-MS found (calcd) for [M]$^+$: *m*/*z* 335.0 (335.1); [M + O + H]$^+$ *m*/*z* 352.1 (352.0); [**L¹*SSL¹*** + Cu]$^+$: *m*/*z* 607.3 (607.2); [2 M]$^+$: *m*/*z* 670.3 (670.1).

Attempts to crystallize Cu^I(**L¹*S**) by vapor diffusion of diethyl ether into an acetonitrile solution (X=ClO_4) resulted in a brown oil with several types of crystals. X-ray crystallography of one of those crystals revealed the formation of a compound with formula $[Cu^{II}_4Cu^I_4(\mathbf{L^1{*}S})_4(\mu\text{-}OH)_2(CH_3CN)_6](ClO_4)_6 \cdot 2\ CH_3CN$.

$[Cu^{II}_2(L^{1*}SO_2)_2](BF_4)_2$ and $Cu^{II}_2(L^{1*}SO_3)_2(BF_4)_2$

$L^{1*}SH$ (32.5 mg, 0.12 mmol) was dissolved in 6 mL acetone under argon. The solution was further deoxygenated by bubbling argon through the solution. $[Cu^{I}(CH_3CN)_4](BF_4)$ (38.4 mg, 0.12 mmol) was added, which resulted in a light brown solution. The solution was opened to the air and stirred for 2 hours until the solution was green. The solution was diluted with 3 mL acetone. Vials containing this reaction mixture were put into a larger container partially filled with diethyl ether, which was then tightly closed. Vapor diffusion of the diethyl ether into the reaction mixture resulted in bright green crystals of $[Cu^{II}_2(L^{1*}SO_2)_2](BF_4)_2$ (13 mg, 0.014 mmol, 24%), which were suitable for X-ray structure determination, together with a green powder of $Cu^{II}_2(L^{1*}SO_3)_2(BF_4)_2$ (19 mg, 0.020 mmol, 34%). The crystals of $[Cu^{II}_2(L^{1*}SO_2)_2](BF_4)_2$ were handpicked from the mixture and dried for analysis.

Elemental analysis calcd for $[Cu^{II}_2(L^{1*}SO_2)_2](BF_4)_2$, $C_{30}H_{36}B_2Cu_2F_8N_6O_4S_2$: C 39.62, H 3.99, N 9.24, S 7.05. Found: C 39.46, H 4.04, N 9.18, S 7.00. ESI-MS found (calcd) for $[^1/_2\ M - BF_4 - SO_2]^+$: *m/z* 302.9 (303.1); $[^1/_2\ M - BF_4]^+$: *m/z* 367.9 (367.0); $[^1/_2\ M - BF_4 + Na]^+$: *m/z* 389.9 (390.0). HRMS found (calcd) for $[^1/_2\ M - BF_4 - SO_2]^+$: *m/z* 303.08 (303.08); $[^1/_2\ M - BF_4 - 2O]^+$: *m/z* 335.07 (335.05); $[^1/_2\ M - BF_4]^+$: *m/z* 367.04 (367.04); $[^1/_2\ M + O - 2\ H - BF_4]^+$: 381.07 (381.03); $[M - 2\ BF_4 + CF_3COO]^+$: *m/z* 849.07 (849.07). IR (neat, cm^{-1}): 1606*w*, 1436*w*, 1046*vs*, 914*s*, 758*m*, 638*w*, 519*w*, 489*w*, 458*w*, 414*w*. UV-vis in acetonitrile at 0.1 mM [Cu] concentration: 262 nm (ε = 5800 M^{-1} cm^{-1}), 314 nm (ε = 900 M^{-1} cm^{-1}), 476 nm (ε = 450 M^{-1} cm^{-1}), 770 nm (ε = 120 M^{-1} cm^{-1}).

Elemental analysis calcd for $Cu^{II}_2(L^{1*}SO_3)_2(BF_4)_2$, $C_{30}H_{36}B_2Cu_2F_8N_6O_6S_2$: C 38.27, H 3.85, N 8.93, S 6.81. Found: C 38.98, H 3.44, N 8.72, S 7.27. ESI-MS found (calcd) for $[^1/_2M - BF_4 - SO_3]^+$: *m/z* 303.1 (303.1); $[M - 2BF_4]^{2+}$: *m/z* 384.1 (384.0). IR (neat, cm^{-1}): 1611*w*, 1448*w*, 1051*vs*, 1028*vs*, 767*m*, 656*w*, 521*w*, 423*w*. UV-vis in acetonitrile at 0.1 mM [Cu] concentration**:** 262 nm (ε = 9800 M^{-1} cm^{-1}), 306 nm (ε = 2200 M^{-1} cm^{-1}), 490 nm (ε = 250 M^{-1} cm^{-1}), 740 nm (ε = 90 M^{-1} cm^{-1}).

$[Cu^{II}_2(L^{1*}SO_2)_2(OTf)_2]$ and $Cu^{II}_2(L^{1*}SO_3)_2(OTf)_2$

Compounds $[Cu^{II}_2(L^{1*}SO_2)_2(OTf)_2]$ and $Cu^{II}_2(L^{1*}SO_3)_2(OTf)_2$ were synthesized in the same way as $[Cu^{II}_2(L^{1*}SO_2)_2](BF_4)_2$ and $Cu^{II}_2(L^{1*}SO_3)_2(BF_4)_2$, starting from **$L^{1*}SH$** (60.8 mg, 0.22 mmol) and $[Cu^{I}(CH_3CN)_4](OTf)$ (82.9 mg, 0.22 mmol). Diethyl ether diffusion yielded green crystals of $[Cu^{II}_2(L^{1*}SO_2)_2(OTf)_2]$ (22 mg, 0.021 mmol, 21%) with green powder of $Cu^{II}_2(L^{1*}SO_3)_2(OTf)_2$ (37 mg, 0.035 mmol, 31%).

Elemental analysis calcd for $[Cu^{II}_2(L^{1*}SO_2)_2(OTf)_2]$, $C_{32}H_{36}Cu_2F_6N_6O_{10}S_4$: C 37.17, H 3.51, N 8.13, S 12.40. Found: C 37.21, H 3.46, N 8.09, S 12.36. ESI-MS found (calcd) for $[^1/_2\ M - OTf - SO_2]^+$: *m/z* 303.0 (303.1). IR (neat, cm^{-1}): 1611*w*, 1448*w*, 1256*s*, 1142*m*, 1088*s*, 1030*s*, 852*m*, 766*m*, 632*s*, 573*w*, 516*m*, 420*m*.

Elemental analysis calcd for $Cu^{II}_2(L^{1*}SO_3)_2(OTf)_2$, $C_{32}H_{36}Cu_2F_6N_6O_{12}S_4$: C 36.05, H 3.40, N 7.88, S 12.03. Found: C 36.49, H 3.52, N 7.71, S 12.58. ESI-MS found (calcd) $[^1/_2\ M - OTf - SO_3]^+$: *m/z* 303.0 (303.1); $[M - 2\ OTf]^{2+}$: *m/z* 383.9 (384.0). HRMS found (calcd) for $[^1/_2\ M - OTf - SO_3]^+$: *m/z* 303.08 (303.08); $[^1/_2\ M - OTf - 3O]^+$: *m/z* 335.07 (335.05); $[^1/_2\ M - OTf - O]^+$: *m/z* 367.04 (367.04); $[^1/_2\ M - OTf]^+$: *m/z* 383.04 (383.04); $[^1/_2\ M - OTf + O]^+$: *m/z* 399.01 (399.03); $[(L^{1*}SO_3)(L^{1*}SO_2)$ +

Na]$^+$: *m*/*z* 647.46 (647.21); [Cu(**L^1*SO$_3$**)(**L^1*SO$_2$**) + OH + 2 Na]$^+$: *m*/*z* 750.41 (750.13). IR (neat, cm^{-1}): 3441*br*, 1611*w*, 1448*w*, 1249*s*, 1155*s*, 1027*vs*, 767*m*, 636*vs*, 516*m*, 420*w*.

*4.5.5 UV-Vis Spectroscopic Monitoring of Cu^I(L^1*S) Oxidation*

L^1*SH (5.5 mg, 0.02 mmol) was dissolved in acetone (2 mL) under argon. [Cu^I(CH$_3$CN)$_4$](BF$_4$) (6.3 mg, 0.02 mmol) was added, which resulted in a light brown solution. The UV-vis setup with transmission dipprobe (set at 1.2 mm path length) was put under argon and blanked with 8 mL acetone, while stirring at 400 rpm. The solution of Cu^I(**L^1*S**) was added to the UV-vis setup, giving a 2 mM [Cu] solution. Air was bubbled through the solution while measuring the absorbance spectrum for a period of six hours.

4.6 References

1. Jacob, C.; Giles, G. L.; Giles, N. M.; Sies, H., *Angew. Chem. Int. Ed.* **2003,** *42*, 4742-4758.
2. Katayama, Y.; Hashimoto, K.; Nakayama, H.; Mino, H.; Nojiri, M.; Ono, T.; Nyunoya, H.; Yohda, M.; Takio, K.; Odaka, M., *J. Am. Chem. Soc.* **2006,** *128*, 728-729.
3. Shigehiro, S.; Nakasako, M.; Dohmae, N.; Tsujimura, M.; Tokoi, K.; Odaka, M.; Yohda, M.; Kamiya, N.; Endo, I., *Nat. Struct. Biol.* **1998,** *5*, 347-351.
4. Angamuthu, R.; Byers, P.; Lutz, M.; Spek, A. L.; Bouwman, E., *Science* **2010,** *327*, 313-315.
5. ^{1}H-NMR of **L^1*SSL^1*** (300 MHz, CD$_3$CN, RT): δ 1.16 (dd, *J* = 6 Hz, 1 Hz, 6H, C*-C*H*$_3$), 2.55 (dd, *J* = 13 Hz, 8 Hz, 2H, N-C*H*$_2$-C*), 2.70 (m, 2H, N-C*H*$_2$-C*), 3.01 (m, 2H, C*-*H*), 3.73 (s, 4H, Py-C*H*$_2$-N), 3.74 (s, 4H, Py-C*H*$_2$-N), 7.14 (m, 4H, Py-*H*$_5$), 7.52 (d, *J* = 8 Hz, 4H, Py-*H*$_3$), 7.65 (td, *J* = 8 Hz, 2 Hz, 4H, Py-*H*$_4$), 8.44 (m, 2H, Py-*H*$_6$).
6. Tuntulani, T.; Musie, G.; Reibenspies, J. H.; Darensbourg, M. Y., *Inorg. Chem.* **1995,** *34*, 6279-6286.
7. Buonomo, R. M.; Font, I.; Maguire, M. J.; Reibenspies, J. H.; Tuntulani, T.; Darensbourg, M. Y., *J. Am. Chem. Soc.* **1995,** *117*, 963-973.
8. Addison, A. W.; Rao, T. N.; Reedijk, J.; Vanrijn, J.; Verschoor, G. C., *J. Chem. Soc., Dalton Trans.* **1984**, 1349-1356.
9. Krishnamurthy, D.; Sarjeant, A. N.; Goldberg, D. P.; Caneschi, A.; Totti, F.; Zakharov, L. N.; Rheingold, A. L., *Chem. Eur. J.* **2005,** *11*, 7328-7341.
10. Odani, A.; Maruyama, T.; Yamauchi, O.; Fujiwara, T.; Tomita, K., *J. Chem. Soc., Chem. Commun.* **1982**, 646-647.
11. Higashi, L. S.; Lundeen, M.; Hilti, E.; Seff, K., *Inorg. Chem.* **1977,** *16*, 310-313.
12. Koolhaas, G. J. A. A.; Driessen, W. L.; Reedijk, J.; van der Plas, J. L.; de Graaff, R. A. G.; Gatteschi, D.; Kooijman, H.; Spek, A. L., *Inorg. Chem.* **1996,** *35*, 1509-1517.
13. Mabbs, F. E.; Collison, D., *Elsevier, Amsterdam* **1992**.
14. Thomas, A. M.; Lin, B.-L.; Wasinger, E. C.; Stack, T. D. P., *J. Am. Chem. Soc.* **2013,** *135*, 18912-18919.

15. Mirza, S. A.; Pressler, M. A.; Kumar, M.; Day, R. O.; Maroney, M. J., *Inorg. Chem.* **1993,** *32*, 977-987.
16. Henderson, R. K.; Bouwman, E.; Spek, A. L.; Reedijk, J., *Inorg. Chem.* **1997,** *36*, 4616-4617.
17. Hosler, E. R.; Herbst, R. W.; Maroney, M. J.; Chohan, B. S., *Dalton Trans.* **2012,** *41*, 804-816.
18. Bourles, E.; de Sousa, R. A.; Galardon, E.; Giorgi, M.; Artaud, I., *Angew. Chem. Int. Ed.* **2005,** *44*, 6162-6165.
19. Adzamli, I. K.; Libson, K.; Lydon, J. D.; Elder, R. C.; Deutsch, E., *Inorg. Chem.* **1979,** *18*, 303-311.
20. Lugo-Mas, P.; Dey, A.; Xu, L.; Davin, S. D.; Benedict, J.; Kaminsky, W.; Hodgson, K. O.; Hedman, B.; Solomon, E. I.; Kovacs, J. A., *J. Am. Chem. Soc.* **2006,** *128*, 11211-11221.
21. Sallmann, M.; Siewert, I.; Fohlmeister, L.; Limberg, C.; Knispel, C., *Angew. Chem. Int. Ed.* **2012,** *51*, 2234-2237.
22. McQuilken, A. C.; Goldberg, D. P., *Dalton Trans.* **2012,** *41*, 10883-10899.
23. de Sousa, R. A.; Galardon, E.; Rat, M.; Giorgi, M.; Artaud, I., *J. Inorg. Biochem.* **2005,** *99*, 690-697.
24. Ohta, T.; Tachiyama, T.; Yoshizawa, K.; Yamabe, T., *Tetrahedron Lett.* **2000,** *41*, 2581-2585.
25. Itoh, S.; Nagagawa, M.; Fukuzumi, S., *J. Am. Chem. Soc.* **2001,** *123*, 4087-4088.
26. Lee, Y.; Lee, D.-H.; Sarjeant, A. A. N.; Karlin, K. D., *J. Inorg. Biochem.* **2007,** *101*, 1845-1858.
27. Stange, A.; Schurr, T.; Klein, A.; Kaim, W., *Z. Anorg. Allg. Chem.* **2005,** *631*, 663-671.
28. Zanello, P.; Tamburini, S.; Vigato, P. A.; Mazzocchin, G. A., *Coord. Chem. Rev.* **1987,** *77*, 165-273.
29. Irangu, J.; Ferguson, M. J.; Jordan, R. B., *Inorg. Chem.* **2005,** *44*, 1619-1625.
30. Pennings, Y. C. M.; Driessen, W. L.; Reedijk, J., *Polyhedron* **1988,** *7*, 2583-2589.
31. Sheldrick, G. M., *Acta Crystallogr. Sect. A* **2008,** *64*, 112-122.
32. Schreurs, A. M. M.; Xian, X.; Kroon-Batenburg, L. M. J., *J. Appl. Crystallogr.* **2010,** *43*, 70-82.
33. Sheldrick, G. M., *SADABS: Area-Detector Absorption Correction;* Universität Göttingen: Göttingen, Germany, **1999**.
34. Spek, A. L., *Acta Crystallogr. Sect. D. Biol. Crystallogr.* **2009,** *65*, 148-155.

Chapter 5

Coordination of New Disulfide Ligands to Cu^{I} and Cu^{II}: Does a Cu^{II} μ-Thiolate Complex Form?

*Interest in dinuclear Cu^{II} μ-thiolate and Cu^{I} disulfide complexes is triggered by their similarity with the Cu_A site and the possibility to control this redox equilibrium. Three new disulfide ligands **L^1SXSL^1**, **$L^{Pz}SSL^{Pz}$** and **$L^{MPz}SSL^{MPz}$** were synthesized and reacted with Cu^{I} salts to investigate whether thiolate or disulfide species would form. The nature of **L^1SXSL^1** precludes the formation of Cu^{II} μ-thiolate species, resulting in the formation of $[Cu^{I}_2(\mathbf{L^1SXSL^1})(CH_3CN)](BF_4)_2$ which was characterized via single crystal X-ray crystallography. Pyrazole-containing ligands **$L^{Pz}SSL^{Pz}$** and **$L^{MPz}SSL^{MPz}$** form Cu^{I} complexes that are stable in solution in air for hours with half-wave potentials of approximately +0.55 V vs. Ag/AgCl, indicating high stability of the Cu^{I} state rather than the Cu^{II} state. The half-wave potentials of the Cu^{I} complexes with **L^1SXSL^1** and **L^4SSL^4** are less positive, indicating that in order to allow formation of both Cu^{II} μ-thiolate and Cu^{I} disulfide species, a half-wave potential of roughly 0 V vs Ag/AgCl would be ideal. Furthermore, Cu^{II} crystal structures with **L^1SXSL^1**, **L^4SSL^4**, **$L^{Pz}SSL^{Pz}$** and **$L^{MPz}SSL^{MPz}$** and different counterions were compared and analyzed. Pyrazolyl-containing ligands **$L^{Pz}SSL^{Pz}$** and **$L^{MPz}SSL^{MPz}$** form complexes that are very similar to the complexes with pyridyl-containing ligands **L^1SXSL^1** and **L^4SSL^4**.*

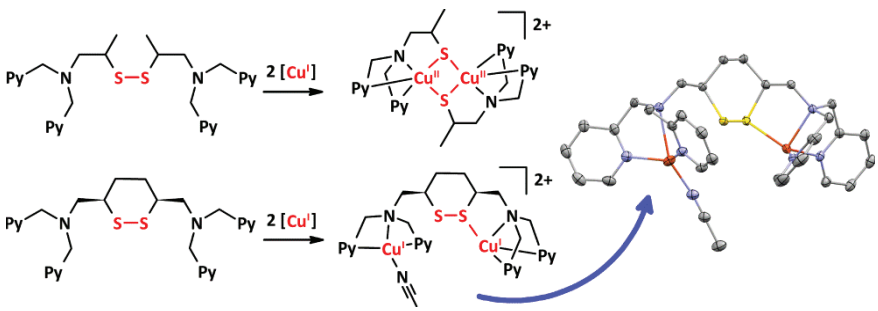

This chapter has been submitted as a full paper: E. C. M. Ording-Wenker, M. A. Siegler, E. Bouwman, *Inorg. Chim. Acta* **2015,** *in press.*

5.1 Introduction

Many biological redox processes involve copper and sulfur, because of their ability to mediate efficient electron transfer. To model these types of reactions, the redox reaction between dinuclear Cu^{II} μ-thiolate and Cu^{I} disulfide complexes is investigated (Chapter 1). It has been reported that small ligand changes can determine the formation of either a Cu^{II} μ-thiolate or a Cu^{I} disulfide complex (Section 1.4.2).[1, 2] To further investigate the effect of ligand changes on the formation of either Cu^{II} or Cu^{I} species we have synthesized three new disulfide ligands **L^1SXSL^1**, **L^{Pz}SSL^{Pz}** and **L^{MPz}SSL^{MPz}.** These ligands show similarities to the ligand **L^1*SSL^1*** that has been shown to form a stable Cu^{II} μ-thiolate complex when reacted with Cu^{I}, as is discussed in Chapter 3 (Figure 5.1).[3, 4]

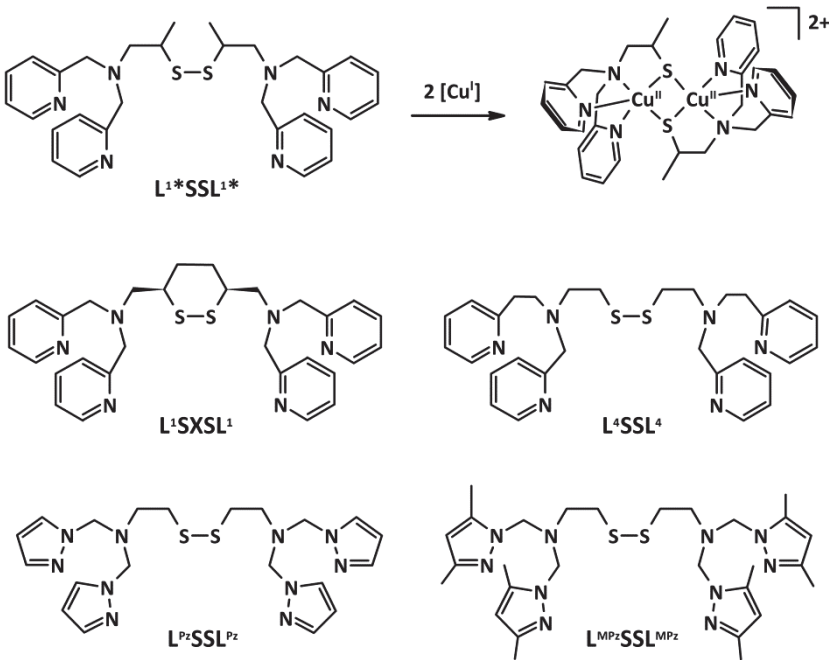

Figure 5.1: Schematic representation of the reaction between **L^1*SSL^1*** and Cu^{I} forming a Cu^{II} μ-thiolate species and ligands **L^1SXSL^1**, **L^4SSL^4**, **L^{Pz}SSL^{Pz}** and **L^{MPz}SSL^{MPz}**.

Ligand **L^1SXSL^1** only differs from **L^1*SSL^1*** in the bond between the two methyl groups in the α-position with respect to the sulfur atoms. This connection generates a six-membered ring, which inhibits the intramolecular, but perhaps not the intermolecular formation of Cu^{II} μ-thiolate species. We further investigated the

replacement of pyridyl groups by pyrazolyl moieties in **L^{Pz}SSL^{Pz}**. The difference between **L^{Pz}SSL^{Pz}** and **L^{MPz}SSL^{MPz}** lies in the methyl groups on the pyrazole rings, as addition of a methyl group to a pyridyl moiety has shown to have a large effect on the complex formation.[2] Ligand **L^{4}SSL^{4}** was used for comparative purposes, because of its ability to form both Cu^{II} μ-thiolate and Cu^{I} disulfide complexes.[1] The three new ligands have been reacted with Cu^{I} salts to study ligand effects on the formation of Cu^{II} μ-thiolate species. Furthermore, new Cu^{II} complexes with all four ligands are reported.

5.2 Results and Discussion

5.2.1 Ligand Synthesis

Ligand **L^{1}SXSL^{1}** was synthesized from the enantiomerically pure compound (3*R*,6*S*)-*meso*-3,6-bis(*tert*-butyloxycarbonylaminomethyl)-1,2-dithiacyclohexane, which was synthesized based on a reported 7-step reaction.[5] The amine groups were deprotected using trifluoridoacetic acid, after which a reductive amination with 2-pyridinecarboxaldehyde gave **L^{1}SXSL^{1}** in 75% yield. The synthetic scheme for **L^{1}SXSL^{1}** is shown in Figure 5.2.

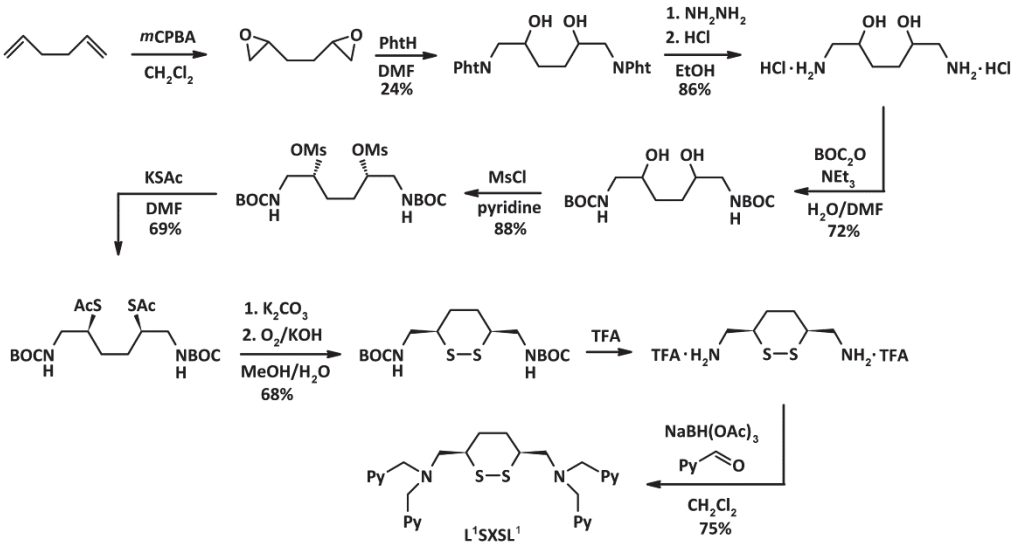

Figure 5.2: Synthesis scheme for **L^{1}SXSL^{1}**.[5, 6] Abbreviations: *m*CPBA = *meta*-chloroperoxybenzoic acid; DMF = *N*,*N*-dimethylformamide; Pht = phthalimide; BOC = di-*tert*-butyl dicarbonate; Ms = methanesulfonyl; Ac = acetyl; TFA = trifluoroacetic acid; Py = 2-pyridyl.

L^{1}SXSL^1 is a *meso* compound containing two stereocenters. Recrystallization of the compound from ethyl acetate resulted in colorless crystals that were suitable for X-ray structure determination; the crystallographic data are presented in Appendix IV. The crystal structure confirms that the ligand is enantiomerically pure, containing an *R* and *S* stereocenter. The two di-(2-pyridylmethyl)amine moieties attached to the six-membered ring are in equatorial and axial position, which is expected to be the most stable isomer. Refluxing **L^{1}SXSL^1** overnight in ethanol results in a 1:1 mixture of the *R*,*S* : *R*,*R*/*S*,*S* isomers, as confirmed by ^{1}H NMR; a longer reflux time does not change this enantiomeric ratio. The pyrazole-containing ligands **L^{Pz}SSL^{Pz}** and **L^{MPz}SSL^{MPz}** were synthesized from *N*-hydroxymethylpyrazole and *N*-hydroxymethyl-3,5-dimethylpyrazole respectively (Figure 5.3).[7] Reaction of the hydroxymethylpyrazoles with cystamine dihydrochloride and triethylamine resulted in **L^{Pz}SSL^{Pz}** and **L^{MPz}SSL^{MPz}** in almost quantitative yields. The ligands were sufficiently pure for further use. Interestingly, ESI-MS spectra of both ligands showed signals indicating loss of one, two, three or four of the carbon fragments originating from the pyrazole groups to form -NH-NH$_2$ moieties. This means that the net weight loss is C$_3$ for the loss of each carbon fragment of **L^{Pz}SSL^{Pz}** and C$_5$H$_4$ for **L^{MPz}SSL^{MPz}**.

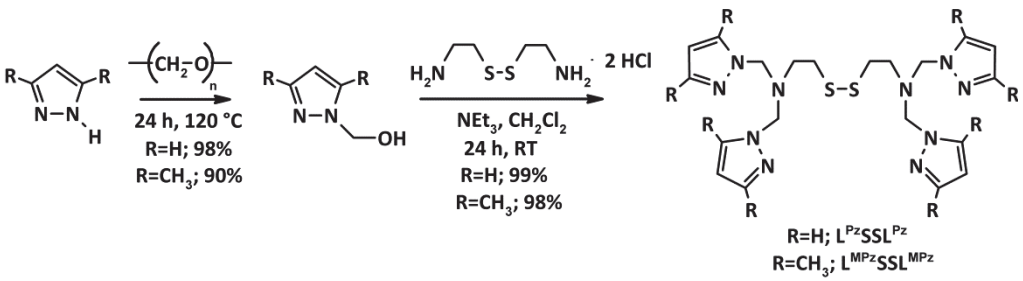

Figure 5.3: Synthesis scheme for **L^{Pz}SSL^{Pz}** and **L^{MPz}SSL^{MPz}**.[7]

5.2.2 Synthesis and analyses of Cu^I complexes

Addition of two equivalents of [Cu^I(CH$_3$CN)$_4$](BF$_4$) to **L^{1}SXSL^1** resulted in a bright yellow solution, which turns green in the presence of air due to oxidation of Cu^I to Cu^{II}. Slow vapor diffusion of diethyl ether into the yellow solution under argon atmosphere yielded crystals suitable for X-ray structure determination, which confirmed a Cu^I complex (see Figure 5.4) with formula [Cu$^I_2$(**L^{1}SXSL^1**)(CH$_3$CN)](BF$_4$)$_2$ · CH$_3$CN. Crystallographic data and selected bond distances are given in Table 5.1 and Table 5.2.

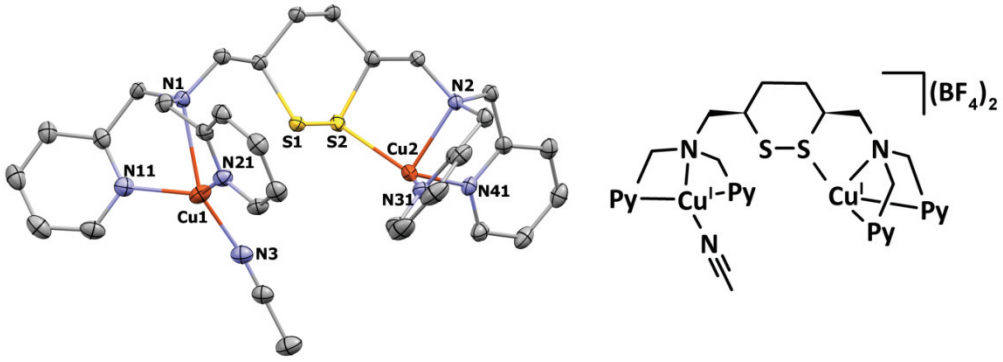

Figure 5.4: Schematic drawing and projection of the cationic part of $[Cu^{I}_2(\mathbf{L^1SXSL^1})(CH_3CN)](BF_4)_2 \cdot CH_3CN$. Displacement ellipsoids are set at 50% probability level. Hydrogen atoms are omitted for clarity.

The two copper centers in $[Cu^{I}_2(\mathbf{L^1SXSL^1})(CH_3CN)](BF_4)_2$ have different coordination geometries. Cu1 coordinates to one of the di-(2-pyridylmethyl)amine moieties of the ligand and an acetonitrile group, resulting in a strongly flattened tetrahedral geometry with an N_4 environment and one N-Cu-N angle of 153°. Cu2 coordinates to the other di-(2-pyridylmethyl)amine moiety and a sulfur donor of the ligand. This gives Cu2 an N_3S environment in a trigonal pyramidal geometry. The 6-membered ring in the backbone of $\mathbf{L^1SXSL^1}$ shows the same chair conformation within the complex as in the free ligand with one axial and one equatorial substitution. The ^1H NMR spectrum of $[Cu^{I}_2(\mathbf{L^1SXSL^1})(CH_3CN)](BF_4)_2$ shows slightly broadened peaks in the diamagnetic region, indicating that the ligand induces quite a steric environment limiting free rotation (Figure AIV.3, Appendix IV). The much more rigid structure of $\mathbf{L^1SXSL^1}$ compared to $\mathbf{L^{1*}SSL^{1*}}$ may possibly hinder the formation of a Cu^{II} μ-thiolate structure. Furthermore, coordination of both copper ions to the sulfur centers is needed for electron transfer to occur and the crystal structure of $[Cu^{I}_2(\mathbf{L^1SXSL^1})(CH_3CN)](BF_4)_2$ shows that at least in the solid state this is not the case for one of the two copper ions. However, it cannot be ruled out that both copper centers are bound to sulfur when the complex is in solution.

Upon addition of two equivalents of $[Cu^{I}(CH_3CN)_4](BF_4)$ to $\mathbf{L^{Pz}SSL^{Pz}}$ or $\mathbf{L^{MPz}SSL^{MPz}}$, colorless solutions are obtained that are stable for several hours in the presence of air; these solutions most likely contain the species $[Cu^{I}_2(\mathbf{L^{Pz}SSL^{Pz}})](BF_4)_2$ and $[Cu^{I}_2(\mathbf{L^{MPz}SSL^{MPz}})](BF_4)_2$, respectively. Unfortunately, all crystallization attempts for both complexes resulted in the formation of residual colorless oils.

Table 5.1: Crystallographic and structure refinement data for complexes $[Cu^{I}_2(\mathbf{L^1SXSL^1})(CH_3CN)](BF_4)_2$, $[Cu^{II}_4(\mathbf{L^1SXSL^1})_2(Cl)_4(Cu^{II}Cl_4)_2]$, $[Cu^{II}_2(\mathbf{L^4SSL^4})(H_2O)(F)(BF_4)](BF_4)_2$, $[Cu^{II}_2(\mathbf{L^{Pz}SSL^{Pz}})(Cl)_2]_n(BF_4)_{2n}$ and $[Cu^{II}_2(\mathbf{L^{MPz}SSL^{MPz}})(CH_3CN)_2(BF_4)_2]_n(BF_4)_{2n}$.

	$[Cu^{I}_2(\mathbf{L^1SXSL^1})(CH_3CN)](BF_4)_2$	$[Cu^{II}_4(\mathbf{L^1SXSL^1})_2(Cl)_4(Cu^{II}Cl_4)_2]$	$[Cu^{II}_2(\mathbf{L^4SSL^4})(H_2O)(F)(BF_4)](BF_4)_2$	$[Cu^{II}_2(\mathbf{L^{Pz}SSL^{Pz}})(Cl)_2]_n(BF_4)_{2n}$	$[Cu^{II}_2(\mathbf{L^{MPz}SSL^{MPz}})(CH_3CN)_2(BF_4)_2]_n(BF_4)_{2n}$
empirical formula	$[C_{32}H_{37}Cu_2N_7S_2](BF_4)_2 \cdot CH_3CN$	$C_{60}H_{68}Cl_{12}Cu_6N_{12}S_4 \cdot 2\,CH_3OH$	$[C_{30}H_{38}BCu_2F_5N_6OS_2](BF_4)_2$	$[C_{20}H_{28}Cl_2Cu_2N_{10}S_2](BF_4)_2 \cdot 2\,CH_3CN$	$[C_{32}H_{50}B_2Cu_2F_8N_{12}S_2](BF_4)_2 \cdot 2\,CH_3CN \cdot C_4H_{10}O$
formula weight	925.56	1954.88	969.29	926.35	1297.50
crystal system	monoclinic	monoclinic	monoclinic	monoclinic	triclinic
space group	*Cc*	$P2_1/c$	$P2_1/c$	$P2_1/n$	*P*-1
a, Å	22.0386(4)	13.25184(17)	13.7798(8)	13.1387(3)	12.4961(3)
b, Å	16.8210(2)	17.8395(3)	12.7963(7)	22.9250(5)	14.7450(3)
c, Å	11.37505(17)	18.4599(2)	22.5595(13)	13.3035(3)	16.3715(2)
α, deg	90	90	90	90	98.5626(14)
β, deg	111.2630(18)	94.7369(12)	106.871(6)	110.399(3)	102.8998(16)
γ, deg	90	90	90	90	92.7244(15)
V, Å^3	3929.80(11)	4349.13(10)	3806.7(4)	3755.78(16)	2897.40(10)
Z, *Z'*	4, 1	2, ½	4. 1	4, 1	2, 1
D_{calc}, g·cm^3	1.564	1.493	1.691	1.638	1.487
T, Kelvin	100(2)	100(2)	110(2)	110(2)	110(2)
crystal size, mm	$0.22 \times 0.16 \times 0.15$	$0.19 \times 0.17 \times 0.09$	$0.47 \times 0.11 \times 0.06$	$0.36 \times 0.27 \times 0.26$	$0.30 \times 0.25 \times 0.17$
μ, mm^{-1}	2.994	6.249	1.327	4.439	2.442
no. of reflns measd	11933	25534	30434	22451	30654
no. of unique reflns	6492	8535	10469	7364	10374
no. of reflns obsd.	6421 [$I > 2\sigma(I)$]	7206 [$I > 2\sigma(I)$]	8201 [$I > 2\sigma(I)$]	7084 [$I > 2\sigma(I)$]	9646 [$I > 2\sigma(I)$]
no. of parameters	508	448	521	472	854
R_1 / wR_2 [$I > 2\sigma(I)$]	0.0246/0.0663	0.0571/0.1599	0.0552/0.1218	0.0372/0.0858	0.0498/0.1377
R_1 / wR_2 [all refl.]	0.0248/0.0665	0.0641/0.1683	0.0780/0.1328	0.0384/0.0862	0.0533/0.1401
goodness of fit	1.053	1.050	1.106	1.169	1.065
$\Delta\rho$, e·Å^{-3}	–0.32 /0.60	–1.28 /1.50	–0.69 /0.86	–0.43 /0.47	–0.83 /0.95

Table 5.2: Selected bond distances (Å) and bond angles (°) for complexes $[Cu^{I}_2(\mathbf{L^1SXSL^1})(CH_3CN)](BF_4)_2$, $[Cu^{II}_4(\mathbf{L^1SXSL^1})_2(Cl)_4(Cu^{II}Cl_4)_2]$, $[Cu^{II}_2(\mathbf{L^4SSL^4})(H_2O)(F)(BF_4)](BF_4)_2$, $[Cu^{II}_2(\mathbf{L^{Pz}SSL^{Pz}})(Cl)_2]_n(BF_4)_{2n}$ and $[Cu^{II}_2(\mathbf{L^{MPz}SSL^{MPz}})(CH_3CN)_2(BF_4)_2]_n(BF_4)_{2n}$.

	$[Cu^{I}_2(\mathbf{L^1SXSL^1})(CH_3CN)](BF_4)_2$	$[Cu^{II}_4(\mathbf{L^1SXSL^1})_2(Cl)_4(Cu^{II}Cl_4)_2]$	$[Cu^{II}_2(\mathbf{L^4SSL^4})(H_2O)(F)(BF_4)](BF_4)_2$	$[Cu^{II}_2(\mathbf{L^{Pz}SSL^{Pz}})(Cl)_2]_n(BF_4)_{2n}$	$[Cu^{II}_2(\mathbf{L^{MPz}SSL^{MPz}})(CH_3CN)_2(BF_4)_2]_n(BF_4)_{2n}$
Cu1 - Cu2	5.7535(6)	6.0370(8)	4.9571(9)	5.8687(5)	8.2073(7)
Cu1 - Cu1*/Cu2*		3.6658(8)		3.5128(6)	
Cu1 - S1	3.1251(8)	2.7791(11)	2.7496(14)	2.9522(9)	2.7761(8)
Cu1 - N1	2.443(3)	2.063(3)	2.036(4)	2.126(2)	2.095(2)
Cu1 - N11/N12	2.020(3)	1.987(3)	2.001(4)	1.934(2)	1.978(3)
Cu1 - N21/N22	2.043(3)	1.995(3)	2.005(4)	1.940(2)	1.968(2)
Cu1 - N3/Cl1/O1	1.947(3)	2.2635(11)	1.984(3)	2.2538(7)	1.975(3)
Cu1 - Cl1*/Cl2*/F2/F5*		2.8951(11)	2.598(3)	2.8136(8)	2.4456(17)
Cu2 - S2	2.2324(8)	2.8141(11)	2.7837(14)	2.8278(9)	5.5963(9)
Cu2 - N2	2.181(2)	2.069(3)	2.039(4)	2.117(2)	2.085(2)
Cu2 - N31/N32	2.021(3)	1.985(3)	1.989(4)	1.949(2)	1.971(3)
Cu2 - N41/N42	1.993(3)	1.985(3)	1.999(4)	1.938(2)	1.958(3)
Cu2 - Cl2/F1		2.2362(10)	1.913(3)	2.2562(7)	2.433(9)
Cu2 - Cl6/Cl1#/N4		2.8914(11)		2.8438(8)	1.976(3)
Cu2 - F5*/F7			2.775(3)		2.4450(18)
S1 - Cu1 - N1	67.35(6)	83.61(9)	85.59(11)	81.05(7)	83.85(7)
S1 - Cu1 - N3/Cl1*/F2/Cl2*/F5*	86.30(9)	169.32(3)	175.90(7)	169.62(3)	172.15(5)
N1 - Cu1 - N11/N12	76.39(10)	81.96(13)	82.76(16)	81.96(9)	82.15(11)
N1 - Cu1 - N21/N22	76.46(10)	83.49(13)	93.07(16)	81.93(9)	82.93(10)
N1 - Cu1 - N3/Cl1/O1	153.15(11)	178.47(9)	171.96(15)	176.55(7)	175.50(10)
N11/N12 - Cu1 - N21/N22	122.36(11)	165.01(13)	165.01(16)	163.55(10)	161.61(11)
S2 - Cu2 - N2	90.50(7)	81.72(9)	84.48(12)	83.04(7)	
S2 - Cu2 - Cl6/F5*/Cl1#		170.51(3)	165.45(7)	171.61(3)	
F1 - Cu2 - F7					173.5(3)
N2 - Cu2 - N31/N32	83.44(10)	81.23(13)	83.37(17)	82.02(9)	82.01(10)
N2 - Cu2 - N41/N42	82.69(10)	82.37(14)	95.13(16)	81.76(9)	81.59(10)
N2 - Cu2 - Cl2/F1/N4		179.03(10)	171.03(15)	176.72(7)	170.02(10)
N31/N32 - Cu2 - N41/N42	117.26(11)	163.57(14)	157.81(16)	163.01(10)	163.46(11)

Symmetry operation * = [1–x, 1–y, 1–z] for $[Cu^{II}_4(\mathbf{L^1SXSL^1})_2(Cl)_4(Cu^{II}Cl_4)_2]$; [–x, 1–y, 1–z] for $[Cu^{II}_2(\mathbf{L^4SSL^4})(H_2O)(F)(BF_4)](BF_4)_2$; [½+x, ½–y, ½+z] for $[Cu^{II}_2(\mathbf{L^{Pz}SSL^{Pz}})(Cl)_2]_n(BF_4)_{2n}$; [x, 1+y, z] for $[Cu^{II}_2(\mathbf{L^{MPz}SSL^{MPz}})(CH_3CN)_2(BF_4)_2]_n(BF_4)_{2n}$. Symmetry operation # = [–½+x, ½–y, –½+z].

^{1}H and ^{13}C NMR spectra of $[Cu^{I}_2(\mathbf{L^{Pz}SSL^{Pz}})](BF_4)_2$ and $[Cu^{I}_2(\mathbf{L^{MPz}SSL^{MPz}})](BF_4)_2$ show the presence of diamagnetic species with peaks that are shifted compared to the resonances of the free ligand (Figure AIV.4 and AIV.5, Appendix IV). These results show that displacement of the pyridyl moieties by pyrazolyl groups leads to ligands that stabilize Cu^{I}, even in the presence of air.

As $\mathbf{L^{1}SXSL^{1}}$, $\mathbf{L^{Pz}SSL^{Pz}}$ and $\mathbf{L^{MPz}SSL^{MPz}}$ form Cu^{I} disulfide complexes when reacted with Cu^{I} their redox potentials were compared with that of $[Cu^{I}_2(\mathbf{L^{4}SSL^{4}})](BF_4)_2$. We reported the formation of this unique Cu^{I} complex, that is formed upon heating a solution containing the Cu^{II} μ-thiolate complex of $\mathbf{L^{4}SSL^{4}}$ (Chapter 2).[1] The cyclic voltammograms of $[Cu^{I}_2(\mathbf{L^{1}SXSL^{1}})(CH_3CN)](BF_4)_2$, $[Cu^{I}_2(\mathbf{L^{Pz}SSL^{Pz}})](BF_4)_2$ and $[Cu^{I}_2(\mathbf{L^{MPz}SSL^{MPz}})](BF_4)_2$ are depicted in Figure 5.5. The half-wave potentials ($E_{1/2}$) and the peak-to-peak separations (ΔEp) of the Cu^{I} complexes containing either $\mathbf{L^{1}SXSL^{1}}$, $\mathbf{L^{4}SSL^{4}}$,[1] $\mathbf{L^{Pz}SSL^{Pz}}$ or $\mathbf{L^{MPz}SSL^{MPz}}$ are given in Table 5.3.

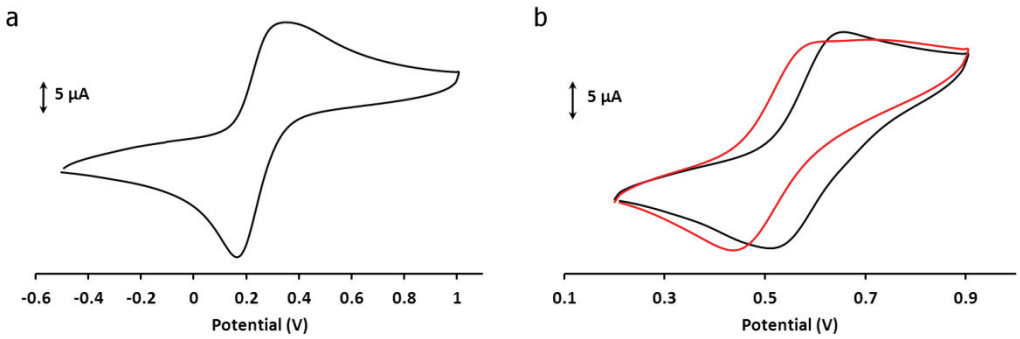

Figure 5.5: Cyclic voltammograms of (a) $[Cu^{I}_2(\mathbf{L^{1}SXSL^{1}})(CH_3CN)](BF_4)_2$ and (b) $[Cu^{I}_2(\mathbf{L^{Pz}SSL^{Pz}})](BF_4)_2$ (black) and $[Cu^{I}_2(\mathbf{L^{MPz}SSL^{MPz}})](BF_4)_2$ (red) in acetonitrile at 2.0 mM [Cu] concentration. Scan rate 100 mV/s; potentials are given vs Ag/AgCl.

All four complexes show a quasi-reversible wave that can be attributed to the Cu^{I}/Cu^{II} redox-couple with relatively large peak separations varying from 140 - 160 mV (Table 5.3). The compounds $[Cu^{I}_2(\mathbf{L^{Pz}SSL^{Pz}})](BF_4)_2$ and $[Cu^{I}_2(\mathbf{L^{MPz}SSL^{MPz}})](BF_4)_2$ also show smaller waves at higher oxidation potentials that are scan-rate dependent and can possibly be attributed to association/dissociation of either acetonitrile or the sulfur group of the ligand (Figure AIV.6 and AIV.7, Appendix IV).

Table 5.3: Electrochemical data for Cu^{I} complexes with **$L^{1}SXSL^{1}$**, **$L^{4}SSL^{4}$**,[1] **$L^{Pz}SSL^{Pz}$** and **$L^{MPz}SSL^{MPz}$** in CH_3CN at 2.0 mM [Cu] concentration. Potentials are given vs Ag/AgCl.

Complex	$E_{1/2}$ (V)	ΔEp (mV)
$[Cu^{I}_2(\mathbf{L^{1}SXSL^{1}})(CH_3CN)](BF_4)_2$	+0.25	150
$[Cu^{I}_2(\mathbf{L^{4}SSL^{4}})](BF_4)_2$[1]	+0.07	150
$[Cu^{I}_2(\mathbf{L^{Pz}SSL^{Pz}})](BF_4)_2$	+0.58	140
$[Cu^{I}_2(\mathbf{L^{MPz}SSL^{MPz}})](BF_4)_2$	+0.52	160

When comparing the $E_{1/2}$ values of the four complexes it can be seen that $E_{1/2}$ is much more positive for $[Cu^{I}_2(\mathbf{L^{Pz}SSL^{Pz}})](BF_4)_2$ ($E_{1/2}$ = +0.58 V) and $[Cu^{I}_2(\mathbf{L^{MPz}SSL^{MPz}})](BF_4)_2$ ($E_{1/2}$ = +0.52 V) than for the two pyridyl-containing complexes. This confirms that the Cu^{I} oxidation state is stabilized by **$L^{Pz}SSL^{Pz}$** and **$L^{MPz}SSL^{MPz}$**, in agreement with the oxidation-insensitive nature of these compounds. The oxidation potential of $[Cu^{I}_2(\mathbf{L^{Pz}SSL^{Pz}})](BF_4)_2$ is slightly higher than that of $[Cu^{I}_2(\mathbf{L^{MPz}SSL^{MPz}})](BF_4)_2$, which is in agreement with the presence of the electron-donating methyl groups in **$L^{MPz}SSL^{MPz}$**. The half-wave potential of $[Cu^{I}_2(\mathbf{L^{1}SXSL^{1}})(CH_3CN)](BF_4)_2$ is more positive than that of $[Cu^{I}_2(\mathbf{L^{4}SSL^{4}})](BF_4)_2$, showing that **$L^{1}SXSL^{1}$** stabilizes Cu^{I} better than **$L^{4}SSL^{4}$**. Apparently to allow formation of both Cu^{II} μ-thiolate and Cu^{I} disulfide species, the half-wave potential needs to be roughly around 0 V (vs. Ag/AgCl); more negative potentials will lead to unstable Cu^{I} complexes and more positive potentials will lead to stabilization of the Cu^{I} complexes.

5.2.3 Synthesis and analyses of Cu^{II} complexes

Cu^{II} compounds of the ligands **$L^{1}SXSL^{1}$**, **$L^{4}SSL^{4}$**, **$L^{Pz}SSL^{Pz}$** and **$L^{MPz}SSL^{MPz}$** were also synthesized and characterized; single crystals were obtained for the compounds $[Cu^{II}_4(\mathbf{L^{1}SXSL^{1}})_2(Cl)_4(Cu^{II}Cl_4)_2]$, $[Cu^{II}_2(\mathbf{L^{4}SSL^{4}})(H_2O)(F)(BF_4)](BF_4)_2$, $[Cu^{II}_2(\mathbf{L^{Pz}SSL^{Pz}})(Cl)_2]_n(BF_4)_{2n}$ and $[Cu^{II}_2(\mathbf{L^{MPz}SSL^{MPz}})(CH_3CN)_2(BF_4)_2]_n(BF_4)_{2n}$. The crystallographic and structure refinement data of the Cu^{II} complexes are provided in Table 5.1. Selected bond distances and angles are given in Table 5.2.

Upon addition of two equivalents of $Cu^{II}Cl_2 \cdot 2\ H_2O$ to **$L^{1}SXSL^{1}$** in CH_3CN, a green precipitate formed, which is insoluble in CH_3CN. Crystals suitable for X-ray structure determination were grown by dissolving the green powder in CH_3OH and slowly diffusing diethyl ether into this solution. The compound was found to be hexanuclear with the formula $[Cu^{II}_4(\mathbf{L^{1}SXSL^{1}})_2(Cl)_4(Cu^{II}Cl_4)_2] \cdot 2\ CH_3OH$. A displacement ellipsoid plot is depicted in Figure 5.6.

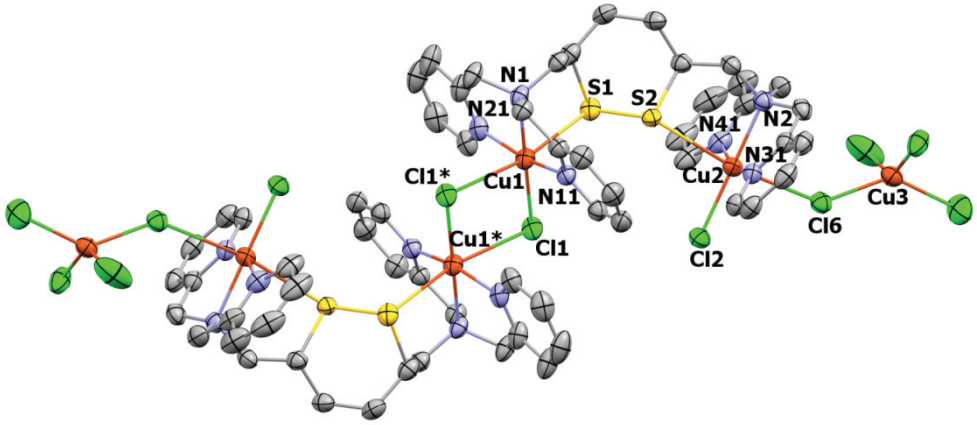

Figure 5.6: Displacement ellipsoid plot (50% probability level) of $[Cu^{II}_4(\mathbf{L^1SXSL^1})_2(Cl)_4(Cu^{II}Cl_4)_2] \cdot 2\ CH_3OH$. Hydrogen atoms and lattice solvent molecules are omitted for clarity. Symmetry operation * = [1–x, 1–y, 1–z].

One third of the added Cu^{II} ions appeared not to coordinate to $\mathbf{L^1SXSL^1}$, but to form the counterion $Cu^{II}Cl_4^{2-}$. The use of three instead of two equivalents of $Cu^{II}Cl_2 \cdot 2\ H_2O$ in the complex synthesis leads to a yield of ca. 96% of the hexanuclear compound. It is remarkable that the formation and coordination of $Cu^{II}Cl_4^{2-}$ is preferred over coordination of terminal Cl^- ions. However, it must be noted that the elemental analysis of the powder indicates the presence of approximately ¼ of terminal Cl^- counterions instead of $CuCl_4^{2-}$ in the crude precipitate.

The compound $[Cu^{II}_4(\mathbf{L^1SXSL^1})_2(Cl)_4(Cu^{II}Cl_4)_2] \cdot 2\ CH_3OH$ crystallizes in the monoclinic space group $P2_1/c$ and is mostly ordered. The compound is located on an inversion center, and thus has three crystallographically independent metal centers. The crystal lattice contains some methanol molecules that are disordered over two orientations (the occupancy factor of the major component of the disorder refines to 0.834(9)) and some other very disordered solvent molecules [8].

In contrast to $[Cu^{I}_2(\mathbf{L^1SXSL^1})(CH_3CN)](BF_4)_2$, the two copper ions in $[Cu^{II}_4(\mathbf{L^1SXSL^1})_2(Cl)_4(Cu^{II}Cl_4)_2]$ that are bound to the ligand are coordinated to sulfur creating a very similar coordination environment for both Cu1 and Cu2. The copper ions have a slightly distorted octahedral geometry with an N_3SCl_2 coordination environment. The Cu^{II} ions are in an elongated Jahn-Teller distorted octahedron with S and Cl at the axial positions at 2.7791(11) (Cu1-S1) / 2.8141(11) (Cu2-S2) and 2.8951(11) (Cu1-Cl1*) / 2.8914(11) Å (Cu2-Cl6), respectively. The di-(2-pyridylmethyl)amine moieties are coordinated in a meridional fashion in the

equatorial plane with Cu^{II}-N(pyr) distances of ca. 2.0 Å. The two symmetry related Cu1 ions are bridged by two chloride ions over an inversion center resulting in a planar Cu(μ-Cl)$_2$Cu arrangement with a Cu1-Cu1* distance of 3.6658(8) Å. The di-(2-pyridylmethyl)amine moieties bound to the Cu(μ-Cl)$_2$Cu core are stacked parallel to each other at a distance of 2.692 Å. The angle between the N11-N1-N21 and N31-N2-N41 meridional planes of Cu1 and Cu2 is 44.21°.

$[Cu^{II}_4(\mathbf{L^1SXSL^1})_2(Cl)_4(Cu^{II}Cl_4)_2]$ dissolved in CH_3OH yields a light blue solution with UV-vis absorptions at 256 nm (LMCT Cu^{II} ← S or Cl), 290 nm (LMCT Cu^{II} ← S or Cl) and 710 nm (Cu^{II} d-d transition). The LMCT for $Cu^{II}Cl_4^{2-}$, which is expected to be around 400 nm, is not observed.[9-11] This indicates that in solution the chlorides might dissociate to a situation where there is just $Cu^{II}Cl_2$ present with and without coordinated $\mathbf{L^1SXSL^1}$. When $[Cu^{II}_4(\mathbf{L^1SXSL^1})_2(Cl)_4(Cu^{II}Cl_4)_2]$ is dissolved in DMF, similar absorption bands are observed and again bands indicating the presence of $Cu^{II}Cl_4^{2-}$ are not present.

When $[Cu^{II}(H_2O)_6](BF_4)_2$ is added to $\mathbf{L^4SSL^4}$ a dark blue solution is formed, from which crystals suitable for X-ray structure determination were grown. These crystals have the formula $[Cu^{II}_2(\mathbf{L^4SSL^4})(H_2O)(F)(BF_4)](BF_4)_2$ (see Figure 5.7) and were isolated in 69% yield indicating that this is the main product of complex formation. Cu^{II} prefers five or six coordination, while the ligand only provides four donor atoms per copper ion. In this case, this results in coordination of the solvent (H_2O), coordination of the usually non-coordinating BF_4^- counterion and remarkably an F^- ion that has been abstracted from BF_4^-. Fluoride abstraction from BF_4^- is a well-known phenomenon that has been reported before.[12-15] $[Cu^{II}_2(\mathbf{L^4SSL^4})(H_2O)(F)(BF_4)](BF_4)_2$ crystallizes in the monoclinic space group $P2_1/c$. The crystal was found to be twinned non-merohedrally, and the twin relationship corresponds a twofold axis found along the reciprocal-space vector **a***. The batch scale factor of the minor component refines to 0.3723(8). The final structure refinement was performed using the HKL5 format. Cu1 is in a slightly distorted octahedral geometry in an N_3SOF environment. The elongated Jahn-Teller axis has S1 and F2 at the axial positions at 2.7496(14) and 2.598(3) Å, respectively. Cu2 is in a slightly distorted square-pyramidal geometry, but when taking into account a somewhat longer interaction between Cu2 and F5* (2.775(3) Å) the geometry can be considered to be octahedral with S2 (2.7837(14) Å) and F5* on the elongated Jahn-Teller axis. The dinuclear molecule is connected to the neighboring molecule, which forms a centrosymmetric dimer *via* a set of four O–H···F hydrogen bonds. One of the two hydrogens (H2) of the water molecule bound to Cu1 is intramolecularly hydrogen-bonded to the F^- counterion coordinated to Cu2 (1.71(3) Å). The other hydrogen (H1) is found to be a bifurcated H-bond donor to F5

(intramolecular hydrogen bond with H···F = 2.04(3) Å) and F1 (intermolecular hydrogen bond with H···F = 2.39(5) Å) atoms. This allows the formation of a quite unique tetranuclear complex with four hydrogen bonds between the cationic units as well as two stabilizing Cu2 - F5* bonds (Figure 5.7).

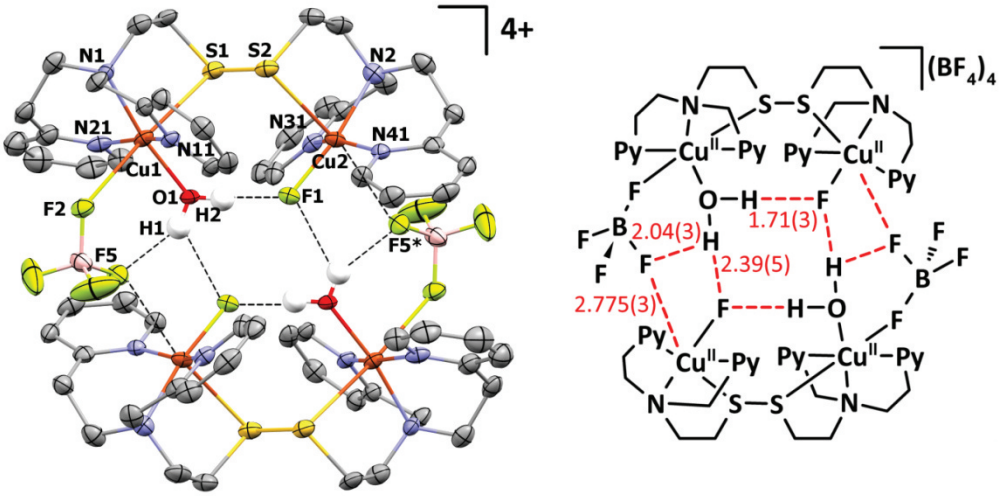

Figure 5.7: Schematic drawing (with distances in Å) and projection of the cationic part of $[Cu^{II}_2(\mathbf{L^4SSL^4})(H_2O)(F)(BF_4)](BF_4)_2$ showing the weaker bonds between two cationic subunits with dotted lines. Displacement ellipsoids are set at 50% probability level. The non-coordinating counterions and hydrogen atoms (except for those of the coordinated water molecules) are omitted for clarity. Symmetry operation * = [–x, 1–y, 1–z].

UV-vis spectra of $[Cu^{II}_2(\mathbf{L^4SSL^4})(H_2O)(F)(BF_4)](BF_4)_2$ in either H_2O or CH_3CN show two absorption bands around 260 nm (LMCT $Cu^{II} \leftarrow S$) and 630 nm (Cu^{II} d-d transition).

As the use of $CuCl_2 \cdot 2\ H_2O$ can lead to formation of $CuCl_4^{2-}$, whereas the use of $[Cu^{II}(H_2O)_6](BF_4)_2$ might result in F^- abstraction, further experiments were carried out starting from one equivalent of $CuCl_2 \cdot 2\ H_2O$ and one equivalent of $[Cu^{II}(H_2O)_6](BF_4)_2$. Reaction of a 1:1 mixture of these salts to $\mathbf{L^{Pz}SSL^{Pz}}$ resulted in the formation of the polymeric complex $[Cu^{II}_2(\mathbf{L^{Pz}SSL^{Pz}})(Cl)_2]_n(BF_4)_{2n} \cdot 2n\ CH_3CN$, as shown by X-ray structure determination (see Figure 5.8). Starting from the ligand $\mathbf{L^{MPz}SSL^{MPz}}$ the very similar compound $[Cu^{II}_2(\mathbf{L^{MPz}SSL^{MPz}})(Cl)_2]_n(BF_4)_{2n}$ was obtained, of which the crystal structure, synthetic procedure, crystallographic data and selected bond distances and angles are reported in Appendix IV.

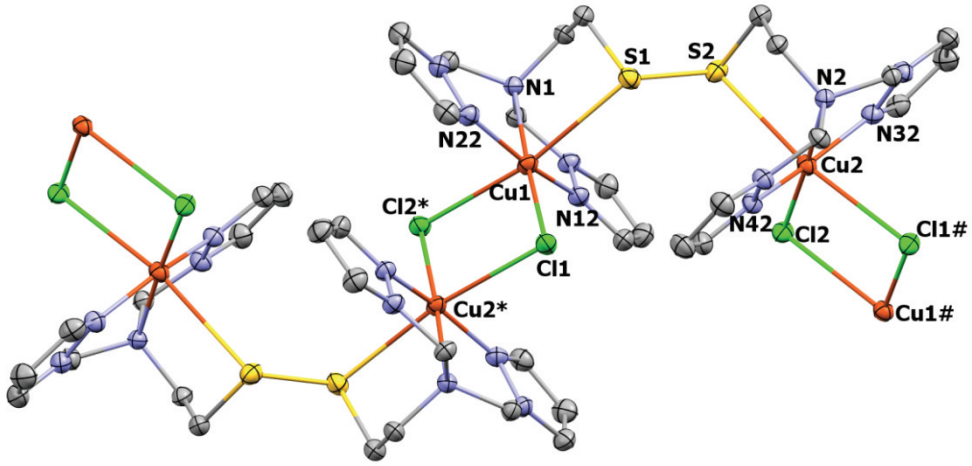

Figure 5.8: Displacement ellipsoid plot (50% probability level) of two of the repeating units in the cationic polymer chain of $[Cu^{II}_2(\mathbf{L^{Pz}SSL^{Pz}})(Cl)_2]_n(BF_4)_{2n}$ · 2n CH_3CN. Hydrogen atoms, counterions and lattice solvent molecules are omitted for clarity. Symmetry operation * = [½+x, ½–y, ½+z] and # = [–½+x, ½–y, –1/2+z].

The ligand $\mathbf{L^{Pz}SSL^{Pz}}$ coordinates to copper in a fashion very similar to $\mathbf{L^1SXSL^1}$ in $[Cu^{II}_4(\mathbf{L^1SXSL^1})_2(Cl)_4(Cu^{II}Cl_4)_2]$ or $\mathbf{L^{1*}SSL^{1*}}$ in the previously reported complex $[Cu^{II}_4(\mathbf{L^{1*}SSL^{1*}})_2(Cl)_4](BF_4)_4$.[16] The angle between the equatorial planes of the copper ions (angle between N12-N1-N22 and N32-N2-N42 planes) is somewhat larger at 59.74°. The Cu(μ-Cl)$_2$Cu core that is formed by the two bridging chlorides is nearly planar with a small torsion angle of 0.87(3)°. The distance between Cu1 and Cu2* is 3.5128(6) Å. Both copper centers are in a slightly distorted octahedral geometry with an N_3SCl_2 environment. The elongated Jahn-Teller axis, like in previously discussed crystal structures, is occupied by the S atom (Cu1-S1 2.9522(9) Å; Cu2-S2 2.8278(9) Å) and the chloride ion (Cu1-Cl2* 2.8136(8) Å; Cu2-Cl1* 2.8438(8) Å).

The UV-vis spectrum of $[Cu^{II}_2(\mathbf{L^{Pz}SSL^{Pz}})(Cl)_2]_n(BF_4)_{2n}$ in acetonitrile shows absorptions at 215 nm (LMCT Cu^{II} ← S or Cl), 284 nm (LMCT Cu^{II} ← S or Cl) and 670 nm (Cu^{II} d-d transition).

When two equivalents of $[Cu^{II}(H_2O)_6](BF_4)_2$ were added to $\mathbf{L^{MPz}SSL^{MPz}}$ in CH_3CN and diethyl was allowed to slowly evaporate into the complex solution, blue crystals suitable for X-ray structure determination were formed with the formula $[Cu^{II}_2(\mathbf{L^{MPz}SSL^{MPz}})(CH_3CN)_2(BF_4)_2]_n(BF_4)_{2n}$ · 2n CH_3CN · n $C_4H_{10}O$ (Figure 5.9). In this case no fluoride ions were abstracted, but CH_3CN and BF_4^- molecules coordinate to

each copper ion. The complex could not be isolated as a powder, because the compound turns into an oil upon evaporation of the lattice (and/or coordinating) solvent molecules. It is important that the complex solution remained within high concentration before vapor diffusion started, as an oil would be obtained rather than crystals, which is likely caused by the formation of monomers and oligomers instead of the polymeric structure. The compound crystallizes in the triclinic space group *P*-1 and is partly disordered. Three of the four crystallographically independent counterions are found to be disordered over two orientations.

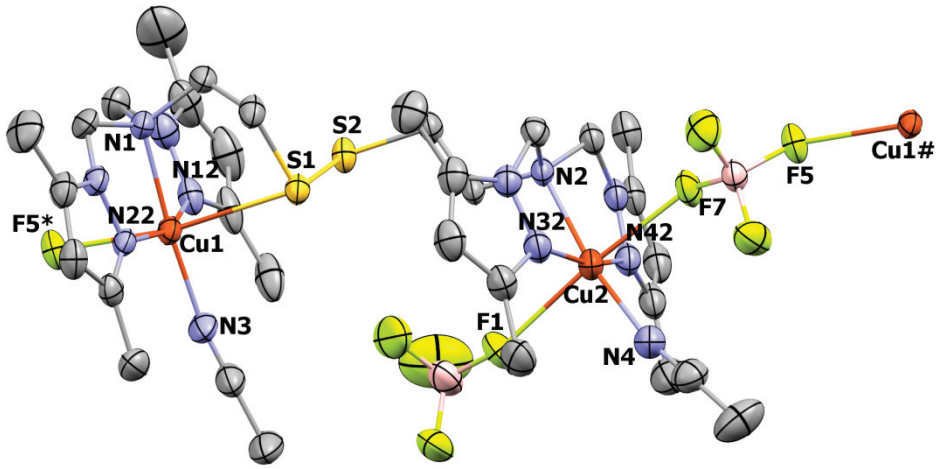

Figure 5.9: Displacement ellipsoid plot (50% probability level) of $[Cu^{II}_2(\mathbf{L}^{MPz}\mathbf{SSL}^{MPz})(CH_3CN)_2(BF_4)_2]_n(BF_4)_{2n}\cdot$ 2n CH_3CN · n $C_4H_{10}O$. Hydrogen atoms, non-coordinating counterions and lattice solvent molecules are omitted for clarity. Symmetry operation * = [x, 1+y, z] and # = [x, –1+y, z].

The polymeric structure formed from $\mathbf{L}^{MPz}\mathbf{SSL}^{MPz}$ with $[Cu^{II}(H_2O)_6](BF_4)$ differs from the structure containing halide ions $[Cu^{II}_2(\mathbf{L}^{MPz}\mathbf{SSL}^{MPz})(Cl)_2]_n(BF_4)_{2n}$. The equatorial planes of the copper centers are only at an angle of 25.58°, whereas they are at an angle of 59.74° in $[Cu^{II}_2(\mathbf{L}^{Pz}\mathbf{SSL}^{Pz})(Cl)_2]_n(BF_4)_{2n}$. Both copper ions are in a slightly distorted octahedral geometry and are coordinated to the di-(*N*-pyrazolylmethyl)amine moiety of the ligand and one CH_3CN solvent molecule in the equatorial plane. One BF_4^- counterion and either another BF_4^- ion or one of the disulfide S atoms of the ligand are in the axial positions. Thus, Cu2 is coordinated by two BF_4^- ions, one of which is bridging towards a neighboring Cu1* ion. The distance

between these copper centers is 6.9966(6) Å, which is shorter than the Cu1-Cu2 distance (8.2073(7) Å). The BF_4^- ions are on the elongated Jahn-Teller axis of Cu2, but the Cu-F distances are significantly shorter (2.433(9) and 2.4450(18) Å), than those of ~2.8 Å found in the other Cu^{II} structures described in this paper.

The UV-vis spectrum of $[Cu^{II}_2(\mathbf{L^{MPz}SSL^{MPz}})(CH_3CN)_2(BF_4)_2]_n(BF_4)_{2n}$ in CH_3CN shows multiple absorption bands. Four bands are in the LMCT region at 204 nm, 223 nm, 272 nm and 335 nm; the absorption at 650 nm can be attributed to a Cu^{II} d-d transition.

5.3 Conclusion

Three new ligands (**L^1SXSL^1**, **L^{Pz}SSL^{Pz}** and **L^{MPz}SSL^{MPz}**) were reacted with Cu^I to investigate whether a Cu^{II} μ-thiolate complex would form, but only Cu^I disulfide species were obtained. The structure of $[Cu^I_2(\mathbf{L^1SXSL^1})(CH_3CN)](BF_4)_2$ shows that only one of the Cu^I centers binds to a disulfide S atom, which perhaps explains why a Cu^{II} μ-thiolate species is not formed. Rearrangement of the molecule would be necessary to allow for intermolecular Cu^{II} thiolate interactions. The pyrazolyl groups in **L^{Pz}SSL^{Pz}** and **L^{MPz}SSL^{MPz}** have a stabilizing effect on Cu^I, inhibiting Cu^{II} μ-thiolate complex formation. Comparison of the half wave potentials of the Cu^I complexes with the four ligands indicate that in order to allow formation of both Cu^{II} μ-thiolate and Cu^I disulfide species, a half-wave potential of roughly 0 V vs Ag/AgCl would be ideal. A number of Cu^{II} complexes with the four ligands but with different counterions were synthesized and discussed. The pyrazolyl-containing ligands **L^{Pz}SSL^{Pz}** and **L^{MPz}SSL^{MPz}** form complexes that are similar to the complexes of the pyridyl-containing ligands **L^1SXSL^1** and **L^4SSL^4**, even though **L^{Pz}SSL^{Pz}** and **L^{MPz}SSL^{MPz}** form much more stable Cu^I complexes.

5.4 Experimental section

5.4.1 General Procedures

Reagents and solvents were purchased from commercial sources. $[Cu^I(CH_3CN)_4](BF_4)$, **L^4SSL^4**, (3*R*,6*S*)-*meso*-3,6-bis(*tert*-butyloxycarbonylaminomethyl)-1,2-dithiacyclohexane, *N*-hydroxymethylpyrazole and *N*-hydroxymethyl-3,5-dimethylpyrazole were synthesized according to literature procedures.[1, 5, 7, 17] NMR spectra were recorded on a Bruker 300 DPX spectrometer. NMR experiments under argon were carried out using a J. Young NMR tube. IR spectra were obtained on a Perkin Elmer UATR (Single Reflection Diamond) Spectrum Two device (4000-700 cm^{-1}; resolution 4 cm^{-1}). Mass spectrometry was measured using a Finnigan Aqua Mass Spectrometer (MS) with electrospray ionization (ESI). Sample introduction was achieved through a Dionex ASI-100 automated sample injector with an eluent flow rate of 0.2

mL/min. Elemental analyses were performed using a Perkin Elmer 2400 Series II CHNS/O analyzer or were performed by the Mircoanalytical laboratory Kolbe in Germany. UV-vis absorbance spectra were recorded on a Varian Cary50 spectrophotometer. Cyclic voltammetry was performed with an Autolab PGstat10 potentiostat controlled by GPES4 software. A three electrode arrangement with a glassy carbon working electrode (3 mm diameter), an Ag/AgCl double junction reference electrode and a Pt wire counter electrode were used in different solvents with 0.1 M NBu_4PF_6 as the electrolyte. In these conditions the Fc/Fc^+ couple was found to be located at +439 mV with a peak-to-peak separation of 65 mV in CH_3CN. Potentials are given relative to the Ag/AgCl electrode.

5.4.2 X-ray Structure Determinations

The reflection intensities for $[Cu^{I}_2(\mathbf{L^1SXSL^1})(CH_3CN)](BF_4)_2$, $[Cu^{II}_4(\mathbf{L^1SXSL^1})_2(Cl)_4(Cu^{II}Cl_4)_2]$, $[Cu^{II}_2(\mathbf{L^{Pz}SSL^{Pz}})(Cl)_2]_n(BF_4)_{2n}$ and $[Cu^{II}_2(\mathbf{L^{MPz}SSL^{MPz}})(CH_3CN)_2(BF_4)_2]_n(BF_4)_{2n}$ were measured at 100(2) or 110(2) K using a SuperNova diffractometer (equipped with Atlas detector) with Cu $K\alpha$ radiation (λ = 1.54178 Å) under the program CrysAlisPro (Version 1.171.36.24 or 1.171.36.28 Agilent Technologies, 2012-2013). The same program was used to refine the cell dimensions and for data reduction. The structures were solved with the program SHELXS-2013 (Sheldrick, 2013)[18] and were refined on F^2 with SHELXL-2013 (Sheldrick, 2013).[18] Analytical numeric absorption corrections based on a multifaceted crystal model were applied using CrysAlisPro. The temperature of the data collection was controlled using the system Cryojet (manufactured by Oxford Instruments). The H atoms were placed at calculated positions using the instructions AFIX 13, AFIX 23, AFIX 43, AFIX 137 or AFIX 147 with isotropic displacement parameters having values 1.2 or 1.5 times *U*eq of the attached C or O atoms.

The reflection intensities for $[Cu^{II}_2(\mathbf{L^4SSL^4})(H_2O)(F)(BF_4)](BF_4)_2$ were measured using a KM4/Xcalibur (detector: Sapphire3) with enhanced graphite-monochromated Mo $K\alpha$ radiation (λ = 0.71073 Å) at 110(2) K under the program CrysAlisPro (Version 1.171.35.11 Oxford Diffraction Ltd., 2011). The same program was used to refine the cell dimensions and for data reduction. The structure was solved with the program SHELXS-97 (Sheldrick, 2008)[18] and was refined on F^2 with SHELXL-97 (Sheldrick, 2008).[18] Analytical numeric absorption corrections based on a multifaceted crystal model were applied using CrysAlisPro. The temperature of the data collection was controlled using the system Cryojet (manufactured by Oxford Instruments). The H atoms (unless otherwise specified) were placed at calculated positions using the instructions AFIX 23 or AFIX 43 with isotropic displacement parameters having values 1.2 times *U*eq of the attached C atoms. The H atoms attached to the coordinated water molecule (O1W) were located from difference Fourier maps; their atomic coordinates were refined freely using the DFIX restraints to keep the O–H and H···H distances within acceptable ranges.

5.4.3 Ligand and Complex Synthesis

L^1SXSL^1

This ligand was synthesized using modified literature procedures.[5, 6] A mixture of (3*R*,6*S*)-*meso*-3,6-bis(*tert*-butyloxycarbonylaminomethyl)-1,2-dithiacyclohexane (0.913 g, 2.41 mmol) and trifluoroacetic acid (5 mL) was stirred for 30 min at RT. The reaction was concentrated *in vacuo* yielding a viscous oil, to which dichloromethane (80 mL) and 2-pyridinecarboxaldehyde (1.4 mL, 14.5 mmol) were added. To this emulsion $NaBH(OAc)_3$ (4.50 g, 21.2 mmol) was added in three portions after which the reaction mixture was stirred for 24 h at RT. The reaction was quenched by addition of $NaHCO_3$ (sat.) and stirred for 15 min. The layers were separated and the aqueous layer was extracted two times with dichloromethane. The combined organic layers were dried over $MgSO_4$ and then evaporated to dryness yielding a yellow oil with white powder. From this impure product, **L^1SXSL^1** could be crystallized with ethyl acetate yielding a white powder (0.986 g, 1.82 mmol, 75%). Crystals suitable for X-ray structure determination were obtained by crystallization from ethyl acetate. The crystal structure of **L^1SXSL^1** is reported in Appendix IV. ^{1}H NMR (300 MHz, CD_3CN, RT): δ 1.47 (br, 2H, S-CH-CH_2-CH_2), 1.67 (m, 2H, S-CH-CH_2-CH_2), 2.52 (br, 2H, S-CH-CH_2-N), 2.76 (br, 2H, S-CH-CH_2-N), 3.03 (q, *J* = 6 Hz, 2H, S-C*H*), 3.72 (m, 8H, N-CH_2-Py), 7.17 (m, 4H, Py-H_5), 7.53 (d, *J* = 8 Hz, 4H, Py-H_3), 7.68 (td, *J* = 8 Hz, 1 Hz, 4H, Py-H_4), 8.43 (d, *J* = 4 Hz, 4H, Py-H_6). ^{1}H NMR (300 MHz, $CDCl_3$, RT): δ 1.50 (br, 2H, S-CH-CH_2-CH_2), 1.70 (m, 2H, S-CH-CH_2-CH_2), 2.72 (m, 4H, S-CH-CH_2-N), 2.95 (br, 2H, S-C*H*), 3.77 (m, 8H, N-CH_2-Py), 7.08 (m, 4H, Py-H_5), 7.52 (d, *J* = 8 Hz, 4H, Py-H_3), 7.59 (td, *J* = 8 Hz, 1 Hz, 4H, Py-H_4), 8.43 (d, *J* = 5 Hz, 4H, Py-H_6). ^{13}C NMR (75 MHz, $CDCl_3$, RT): δ 28.5 (S-CH-CH_2-CH_2), 41.8 (br, S-CH), 56.5 (br, S-CH-CH_2-N), 60.7 (N-CH_2-Py), 122.1 (Py-C_5), 123.4 (Py-C_3), 136.5 (Py-C_4), 148.9 (Py-C_6), 159.4 (Py-C_1). ESI-MS found (calculated) for $[M + H]^+$ *m*/*z* 542.7 (543.2); $[M + 2H]^{2+}$ *m*/*z* 272.1 (272.6); $[M + Na]^+$ *m*/*z* 565.0 (565.2). IR (neat, cm^{-1}): 3050*w*, 3009*w*, 2907*w*, 2821*m*, 1589*s*, 1569*m*, 1473*m*, 1440*m*, 1432*m*, 1369*m*, 1249*m*, 1116*m*, 1048*m*, 984*m*, 964*m*, 873*m*, 768*vs*, 761*vs*, 746*s*, 615*m*, 519*m*. Elemental analysis calcd for **L^1SXSL^1**: C 66.39, H 6.31, N 15.48, S 11.82; Found: C 66.21, H 6.35, N 15.21, S 11.81.

$L^{Pz}SSL^{Pz}$

Cystamine dihydrochloride (1.90 g, 8.43 mmol), *N*-hydroxymethylpyrazole (3.32 g, 33.9 mmol) and triethylamine (1.76 g, 17.5 mmol) dissolved in dichloromethane (50 mL) were stirred for 24 hours at RT. The reaction mixture was extracted with water (30 mL) three times, after which the organic layer was dried over $MgSO_4$ and the solvent was evaporated. This yielded **$L^{Pz}SSL^{Pz}$** as a colorless oil (3.96 g, 8.38 mmol, 99%), which was used without further purification. ^{1}H NMR (300 MHz, CD_3CN, RT): δ 2.65 (t, *J* = 7 Hz, 4H, S-CH_2), 2.94 (t, *J* = 7 Hz, 4H, S-CH_2-CH_2), 5.07 (s, 8H, N-CH_2-Pz), 6.27 (t, *J* = 2 Hz, 4H, N-CH-C*H*), 7.47 (d, *J* = 1 Hz, 4H, N-C*H*), 7.63 (d, *J* = 2 Hz, N-C*H*). ^{13}C NMR (75 MHz, CD_3CN, RT): δ 37.1 (S-CH_2), 50.2 (S-CH_2-CH_2), 68.9 (N-CH_2-Pz), 106.6 (N-CH-*C*H), 130.8 (N-*C*H), 140.1 (N-*C*H). ESI-MS found (calculated) for $[M + Na]^+$ *m*/*z* 495.0 (495.2); $[M - C_3 + Na]^+$ *m*/*z* 459.0 (459.2); $[M - 2\ C_3 + Na]^+$ *m*/*z* 422.9 (423.2); $[M - 3\ C_3 +$

Na]$^+$ *m*/*z* 387.0 (387.2); [M – 4 C_3 + Na]$^+$ *m*/*z* 350.9 (351.2). IR (neat, cm^{-1}): 3110*w*, 2941*w*, 1513*m*, 1393*m*, 1251*m*, 1121*m*, 1084*s*, 1046*s*, 962*m*, 743*vs*, 653*m*, 614*s*.

L^{MPz}SSL^{MPz}

L^{MPz}SSL^{MPz} was synthesized in the same manner as **L^{Pz}SSL^{Pz}** starting from *N*-hydroxymethyl-3,5-dimethylpyrazole (2.89 g, 23.1 mmol), cystamine dihydrochloride (1.27 g, 5.64 mmol) and triethylamine (1.6 mL, 11.5 mmol) in 50 mL dichloromethane. This yielded **L^{MPz}SSL^{MPz}** as a viscous, colorless oil (3.22 g, 5.51 mmol, 98%), which was used without further purification. ^{1}H NMR (300 MHz, CD_3CN, RT): δ 2.11 (s, 12H, C-C*H*$_3$), 2.20 (s, 12H, C-C*H*$_3$), 2.40 (t, *J* = 7 Hz, 4H, S-C*H*$_2$), 2.86 Hz (t, *J* = 7 Hz, 4H, S-CH$_2$-C*H*$_2$), 4.88 (s, 8H, N-C*H*$_2$-Pz), 5.81 (s, 4H, N-C(CH$_3$)-C*H*). ^{13}C NMR (75 MHz, CD_3CN, RT): δ 11.2 (C-*C*H$_3$), 13.7 (C-*C*H$_3$), 36.9 (S-CH$_2$), 49.9 (S-CH$_2$-CH$_2$), 66.3 (N-*C*H$_2$-Pz), 106.4 (N-C(CH$_3$)-*C*H), 140.7 (N-*C*(CH$_3$)), 147.8 (N-*C*(CH$_3$)). ESI-MS found (calculated) for [M – C_5H_4 + Na]$^+$ *m*/*z* 543.0 (543.3); [M – 2 C_5H_4 + Na]$^+$ *m*/*z* 479.0 (479.3); [M – 3 C_5H_4 + Na]$^+$ *m*/*z* 414.9 (415.2); [M – 4 C_5H_4 + Na]$^+$ *m*/*z* 350.9 (351.2). IR (neat, cm^{-1}): 2919*m*, 1555*s*, 1456*s*, 1421*s*, 1376*s*, 1314*s*, 1248*s*, 1096*s*, 1029*s*, 975*s*, 779*vs*, 732*s*, 626*m*.

[Cu^I$_2$(L^{1}SXSL^1)(CH$_3$CN)](BF$_4$)$_2$ · CH$_3$CN

The synthesis of [Cu^I$_2$(**L^{1}SXSL^1**)(CH_3CN)](BF_4)$_2$ was carried out using standard Schlenk-line techniques under an argon atmosphere. To a suspension of **L^{1}SXSL^1** (38.0 mg, 0.070 mmol) in 5 mL CH_3CN was added [Cu^I(CH_3CN)$_4$](BF_4) (44.1 mg, 0.140 mmol). To the resulting bright yellow solution was added 40 mL diethyl ether, which resulted in precipitation. The product was filtered and washed with diethyl ether yielding [Cu^I$_2$(**L^{1}SXSL^1**)(CH_3CN)](BF_4)$_2$ as a yellow powder (9.5 mg, 0.011 mmol, 15%). Crystals suitable for X-ray structure determination were obtained by slow vapor diffusion of diethyl ether into an acetonitrile solution containing the complex under oxygen-free conditions. ^{1}H NMR (300 MHz, CD_3CN, RT): δ 1.61 (br, 2H, S-CH-C*H*$_2$-CH$_2$), 1.86 (br, 2H, S-CH-C*H*$_2$-CH$_2$), 2.78 (br, 4H, S-CH-C*H*$_2$-N), 3.07 (br, 2H, S-C*H*), 3.87 (br, 8H, N-C*H*$_2$-Py), 7.36 (br, 4H, Py-*H*$_3$), 7.45 (br, 4H, Py-*H*$_5$), 7.86 (t, J = 7 Hz, 4H, Py-*H*$_4$), 8.60 (br, 4H, Py-*H*$_6$). ESI-MS found (calculated) for [M – CH_3CN – 2 BF_4]$^{2+}$ m/z 334.1 (334.0); [M – Cu – CH_3CN – 2 BF_4]$^+$ m/z 605.2 (605.2). IR (neat, cm^{-1}): 2907*w*, 1604*m*, 1571*w*, 1480*w*, 1439*m*, 1302*w*, 1284*w*, 1263*w*, 1048*vs*, 1033*vs*, 958*m*, 771*s*, 648*w*, 520*m*. Elemental analysis calcd for [Cu^I$_2$(**L^{1}SXSL^1**)(CH_3CN)](BF_4)$_2$: C 43.45, H 4.22, N 11.08, S 7.25; Found: C 42.59, H 4.14, N 10.75, S 7.35.

[Cu^I$_2$(L^{Pz}SSL^{Pz})](BF$_4$)$_2$

Measurements of [Cu^I$_2$(**L^{Pz}SSL^{Pz}**)](BF_4)$_2$ have been carried out *in situ* by adding two equivalents of [Cu^I(CH_3CN)$_4$](BF_4) to **L^{Pz}SSL^{Pz}** in acetonitrile. Attempts to isolate the complex resulted in the formation of an oil. ^{1}H NMR (300 MHz, CD_3CN, RT): δ 2.56 (t, *J* = 7 Hz, 4H, S-C*H*$_2$), 2.97 (t, *J* = 7 Hz, 4H, S-CH$_2$-C*H*$_2$), 5.12 (s, 8H, N-C*H*$_2$-Pz), 6.39 (t, *J* = 2 Hz, 4H, N-CH-C*H*), 7.63 (d, *J* = 2 Hz, 4H, N-C*H*), 7.76 (d, *J* = 2 Hz, N-C*H*). ^{13}C NMR (75 MHz, CD_3CN, RT): δ 36.5 (S-*C*H$_2$), 49.6

(S-CH_2-CH_2), 68.2 (N-CH_2-Pz), 107.2 (N-CH-*C*H), 132.6 (N-CH), 141.5 (N-*C*H). ESI-MS found (calculated) for [M – Cu – 2 BF_4]$^+$ *m*/*z* 535.2 (535.1).

*[Cu^I_2(**L^{MPz}SSL^{MPz}**)](BF_4)$_2$*

Measurements of [Cu^I_2(**L^{MPz}SSL^{MPz}**)](BF_4)$_2$ have been carried out *in situ* by adding two equivalents of [Cu^I(CH_3CN)$_4$](BF_4) to **L^{MPz}SSL^{MPz}** in acetonitrile. Attempts to isolate the complex resulted in the formation of an oil. ^{1}H NMR (300 MHz, CD_3CN, RT): δ 2.32 (s, 24H, C-C*H*$_3$), 2.78 (t, *J* = 7 Hz, 4H, S-C*H*$_2$), 2.94 Hz (t, *J* = 7 Hz, 4H, S-CH_2-C*H*$_2$), 4.86 (s, 8H, N-C*H*$_2$-Pz), 6.05 (s, 4H, N-C(CH_3)-C*H*). ^{13}C NMR (75 MHz, CD_3CN, RT): δ 11.7 (C-CH_3), 14.0 (C-CH_3), 36.6 (S-CH_2), 50.1 (S-CH_2-CH_2), 62.6 (N-CH_2-Pz), 107.7 (N-C(CH_3)-CH), 142.7 (N-*C*(CH_3)), 150.4 (N-*C*(CH_3)). ESI-MS found (calculated) for [½ M – BF_4]$^+$ *m*/*z* 355.1 (355.1); [M – Cu – 2 BF_4]$^+$ *m*/*z* 647.4 (647.3).

*[Cu^{II}_4(**L^{1}SXSL^1**)$_2$(Cl)$_4$($Cu^{II}Cl_4$)$_2$] · 2 CH_3OH*

To a suspension of **L^{1}SXSL^1** (36.6 mg, 0.067 mmol) in 10 mL CH_3CN was added solid $CuCl_2$ · 2 H_2O (35.0 mg, 0.202 mmol). The mixture was stirred for 1 hour during which **L^{1}SXSL^1** dissolved and a green precipitate formed. The precipitate was filtered and washed with acetonitrile and diethyl ether yielding [Cu^{II}_4(**L^{1}SXSL^1**)$_2$(Cl)$_4$($Cu^{II}Cl_4$)$_2$] as a light green powder (0.061 g, 0.064 mmol, 96%). Crystals suitable for X-ray structure determination were obtained by vapor diffusion of diethyl ether into a methanol solution of the complex. ESI-MS found (calculated) for [Cu_2(**L^{1}SXSL^1**)Cl_2]$^{2+}$ *m*/*z* 370.1 (370.0). IR (neat, cm^{-1}): 3490*m*, 3065*w*, 2939*m*, 1608*s*, 1572*w*, 1482*m*, 1444*s*, 1287*m*, 1160*w*, 1093*w*, 1052*w*, 1030*m*, 899*w*, 855*w*, 778*vs*, 765*s*, 730*w*, 656*w*, 497*w*, 478*w*. Elemental analysis calcd for [Cu^{II}_4(**L^{1}SXSL^1**)$_2$(Cl)$_4$($Cu^{II}Cl_4$)$_2$]: C 38.09, H 3.62, N 8.88, S 6.78; Found: C 39.03, H 3.63, N 9.23, S 7.15. UV-vis in CH_3OH at 0.1 mM [Cu] concentration: 256 nm (11 600 M^{-1} cm^{-1}), 290 nm (3 600 M^{-1} cm^{-1}), 710 nm (90 M^{-1} cm^{-1}). UV-vis in *N*,*N*-dimethylformamide at 0.1 mM [Cu] concentration: 290 nm (3900 M^{-1} cm^{-1}), 730 nm (110 M^{-1} cm^{-1}). X-band EPR powder spectrum (RT, ν = 9.859 GHz): g_{iso} = 2.12.

*[Cu^{II}_2(**L^{4}SSL^4**)(H_2O)(F)(BF_4)](BF_4)$_2$*

To a solution of **L^{4}SSL^4** (0.056 g, 0.103 mmol) in 1.5 mL methanol was added a solution of [Cu^{II}(H_2O)$_6$](BF_4)$_2$ (0.072 g, 0.208 mmol) in water (1 mL), resulting in a dark blue solution. Slow vapor diffusion of diethyl ether into this complex solution resulted in dark blue crystals of [Cu^{II}_2(**L^{4}SSL^4**)(H_2O)(F)(BF_4)](BF_4)$_2$ (0.069 g, 0.071 mmol, 69%) that were suitable for X-ray structure determination. ESI-MS found (calculated) for [½(M – H_2O – F – 3 BF_4)]$^+$ *m*/*z* 335.0 (335.1); [M – Cu – H_2O – F – 3 BF_4]$^+$ *m*/*z* 607.3 (607.2). IR (neat, cm^{-1}): 3517*w*, 2806*w*, 2362*w*, 1616*m*, 1575*w*, 1487*w*, 1447*m*, 1320*w*, 1306*w*, 1046*vs*, 1029*vs*, 1012*vs*, 954*m*, 925*m*, 764*m*, 723*w*, 656*m*, 520*m*, 425*m*. Elemental analysis calcd for [Cu^{II}_2(**L^{4}SSL^4**)(H_2O)(F)(BF_4)](BF_4)$_2$: C 37.17, H 3.95, N 8.67, S 6.62; Found: C 37.52, H 4.28, N 8.70, S 6.49. UV-vis in H_2O at 0.1 mM [Cu] concentration: 256 nm (ε = 11 800 M^{-1} cm^{-1}), 640 nm (ε = 90 M^{-1} cm^{-1}). UV-vis in CH_3CN at 0.1 mM [Cu] concentration: 260 nm (ε = 12 000 M^{-1} cm^{-1}), 620 nm (ε = 200 M^{-1} cm^{-1}). X-band

powder EPR spectrum (RT, ν = 9.858 GHz): g_{iso} = 2.11; X-band EPR spectrum in CH_3CN (RT, ν = 9.875 GHz): g_{iso} = 2.11.

$[Cu^{II}_2(\mathbf{L^{Pz}SSL^{Pz}})(Cl)_2]_n(BF_4)_{2n} \cdot 2n\ CH_3CN$

$\mathbf{L^{Pz}SSL^{Pz}}$ (0.202 g, 0.43 mmol) was dissolved in 5 mL methanol. To this solution solid $[Cu^{II}(H_2O)_6](BF_4)_2$ (0.149 g, 0.43 mmol) and $CuCl_2 \cdot 2\ H_2O$ (0.073 g, 0.43 mmol) were added and the mixture was stirred for 10 minutes. The formed precipitate was filtered and washed with methanol and diethyl ether giving the product $[Cu^{II}_2(\mathbf{L^{Pz}SSL^{Pz}})(Cl)_2]_n(BF_4)_{2n}$ (0.342 g, 0.41 mmol, 94%) as a light blue powder. Crystals suitable for X-ray structure determination were obtained by slow vapor diffusion of diethyl ether into a CH_3CN solution containing the complex. ESI-MS found (calculated) for $[½\ M - BF_4 - Cl]^+$ *m/z* 298.8 (299.0); $[½\ M - BF_4 + Cl]^+$ *m/z* 370.8 (371.0); $[M - Cu - Cl - 2\ BF_4]^+$ *m/z* 569.9 (570.1); $[M - 2\ BF_4]^{2+}$ *m/z* 334.9 (335.0). IR (neat, cm^{-1}): 3131*w*, 1521*w*, 1477*w*, 1426*w*, 1404*w*, 1272*m*, 1036*vs*, 987*s*, 920*m*, 765*vs*, 639*w*, 607*m*, 520*m*. Elemental analysis calcd for $[Cu^{II}_2(\mathbf{L^{Pz}SSL^{Pz}})(Cl)_2](BF_4)_2 \cdot H_2O$: C 27.86, H 3.51, N 16.24, S 7.44; Found: C 28.09, H 3.49, N 16.28, S 7.49. UV-vis in CH_3CN at 0.1 mM [Cu] concentration: 215 nm (11 800 $M^{-1}\ cm^{-1}$), 284 nm (ε = 3 700 $M^{-1}\ cm^{-1}$), 670 nm (ε = 90 $M^{-1}\ cm^{-1}$). X-band powder EPR spectrum (RT, ν = 9.839 GHz): $g_\perp$ = 2.09, $g_\parallel$ = 2.21; X-band EPR spectrum in CH_3CN (RT, ν = 9.875 GHz): g_{iso} = 2.10.

$[Cu^{II}_2(\mathbf{L^{MPz}SSL^{MPz}})(CH_3CN)_2(BF_4)_2]_n(BF_4)_{2n} \cdot 2n\ CH_3CN \cdot n\ C_4H_{10}O$

$\mathbf{L^{MPz}SSL^{MPz}}$ (19 mg; 0.033 mmol) was dissolved in 2 mL acetonitrile giving a colorless solution. To this solution $[Cu^{II}(H_2O)_6](BF_4)_2$ (23 mg; 0.066 mmol) was added resulting in a clear turquoise blue solution. Slow vapor diffusion of diethyl ether into this reaction mixture resulted in blue crystals that were suitable for X-ray structure determination. The crystals of the complex turn into oil when the lattice solvent molecules evaporate from the crystal, thus precluding elemental analysis. ESI-MS found (calculated) for $[½\ M - CH_3CN - 2\ BF_4]^+$ *m/z* 355.2 (355.1); $[M - CH_3CN - 4\ BF_4]^{2+}$ *m/z* 375.2 (375.6). UV-vis in CH_3CN at 0.1 mM [Cu] concentration: 204 nm (17 500 $M^{-1}\ cm^{-1}$), 223 nm (19 800 $M^{-1}\ cm^{-1}$), 272 nm (1 600 $M^{-1}\ cm^{-1}$), 335 nm (800 $M^{-1}\ cm^{-1}$), 650 nm (120 $M^{-1}\ cm^{-1}$). X-band EPR spectrum in CH_3CN (RT, ν = 9.876 GHz): g_{iso} = 2.10.

5.5 References

1. Ording-Wenker, E. C. M.; van der Plas, M.; Siegler, M. A.; Bonnet, S.; Bickelhaupt, F. M.; Fonseca Guerra, C.; Bouwman, E., *Inorg. Chem.* **2014,** *53*, 8494-8504.
2. Itoh, S.; Nagagawa, M.; Fukuzumi, S., *J. Am. Chem. Soc.* **2001,** *123*, 4087-4088.
3. Ording-Wenker, E. C. M.; van der Plas, M.; Siegler, M. A.; Fonseca Guerra, C.; Bouwman, E., *Chem. Eur. J.* **2014,** *20*, 16913-16921.
4. Thomas, A. M.; Lin, B.-L.; Wasinger, E. C.; Stack, T. D. P., *J. Am. Chem. Soc.* **2013,** *135*, 18912-18919.
5. Lee, S. H.; Kohn, H., *Org. Biomol. Chem.* **2005,** *3*, 471-482.
6. Britovsek, G. J. P.; England, J.; White, A. J. P., *Inorg. Chem.* **2005,** *44*, 8125-8134.

7. Driessen, W. L., *Recl. Trav. Chim. Pays-Bas* **1982,** *101*, 441-443.
8. The H atoms of the minor component of the disorder of the lattice methanol molecules could not be found from difference Fourier maps; see CIF file for occupancy factors. For the very disordered solvent molecules (possibly diethyl ether), their contributions have been taken out using the program SQUEEZE for the final refinement. All details of the SQUEEZE refinement are provided in the final CIF file.
9. Solomon, E. I.; Baldwin, M. J.; Lowery, M. D., *Chem. Rev.* **1992,** *92*, 521-542.
10. Winter, A.; Zabel, A.; Strauch, P., *Int. J. Mol. Sci.* **2012,** *13*, 1612-1619.
11. Kovalchukova, O. V.; Palkina, K. K.; Strashnova, S. B.; Zaitsev, B. E., *Russ. J. Coord. Chem.* **2008,** *34*, 830-835.
12. Manzur, J.; Vega, A.; García, A. M.; Acuña, C.; Sieger, M.; Sarkar, B.; Niemeyer, M.; Lissner, F.; Schleid, T.; Kaim, W., *Eur. J. Inorg. Chem.* **2007,** *2007*, 5500-5510.
13. Ackermann, J.; Meyer, F.; Pritzkow, H., *Inorg. Chim. Acta* **2004,** *357*, 3703-3711.
14. Lee, S. C.; Holm, R. H., *Inorg. Chem.* **1993,** *32*, 4745-4753.
15. Reedijk, J., *Comments Inorg. Chem.* **1982,** *1*, 379-389.
16. Angamuthu, R.; Byers, P.; Lutz, M.; Spek, A. L.; Bouwman, E., *Science* **2010,** *327*, 313-315.
17. Pennings, Y. C. M.; Driessen, W. L.; Reedijk, J., *Polyhedron* **1988,** *7*, 2583-2589.
18. Sheldrick, G. M., *Acta Crystallogr. Sect. A* **2008,** *64*, 112-122.

Chapter 6

The Study of Cu^{II} Phenolate Redox Chemistry

The reactions of phenol with copper are numerous and versatile, including biomimetic ring-oxygenations and many different oxidative phenol coupling reactions. We report here an unprecedented redox conversion between Cu^{II} and different phenolate compounds. Controlled oxidation of a Cu^{I} complex coordinated to phenol leads to formation of a purple Cu^{II} phenolate complex that was analyzed by X-ray crystallography, EPR and cyclic voltammetry. This mononuclear complex was found to convert intermolecularly to a Cu^{I} species and a phenol-derived product that can be either a diaryl peroxide or an aromatic ether. UV-vis and NMR spectroscopy confirmed formation of a diamagnetic Cu^{I} species and the Raman spectrum showed the presence of a new aryl-O bond. Interestingly, this new redox chemistry is very similar to the Cu^{II} μ-thiolate/Cu^{I} disulfide redox chemistry.

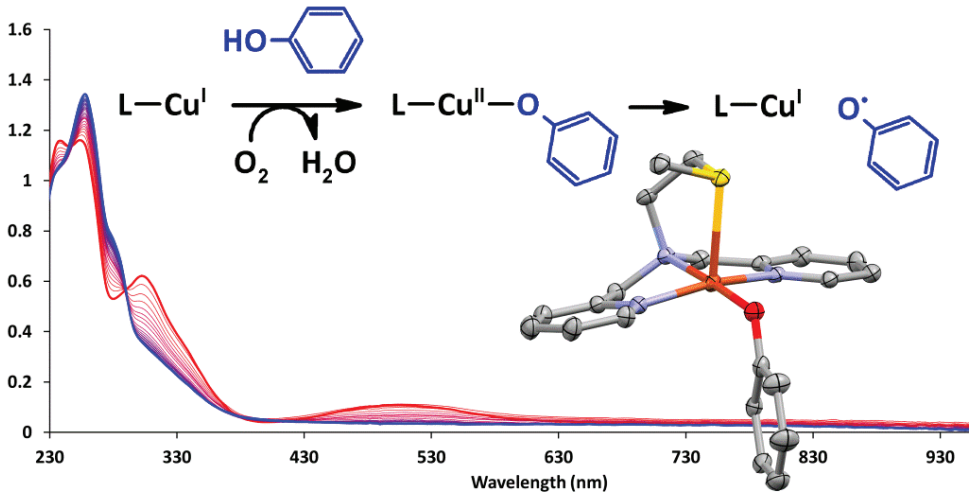

This chapter will be published: E. C. M. Ording-Wenker, M. J. B. Moester, M. A. Siegler, E. Bouwman, *manuscript in preparation*.

6.1 Introduction

Copper-oxygen chemistry is a research field of great interest because of the essential role it plays in many biological processes such as oxygen transfer, hydrogen peroxide generation, methane oxidation and aromatic ring oxygenation.[1, 2] The aromatic ring oxygenation of phenols to catechols and further to *ortho*-quinones has received a lot of attention, owing to its relevance to the tyrosinase and catechol oxidase activity (section 1.2.3; Chapter 7). Furthermore, a large range of substituted phenol substrates is available that allows tweaking of the reaction for mechanistic research.[2-6] Apart from the biomimetic phenol oxygenations, research has been focused on oxidative phenol coupling to form diphenols, diphenoquinones, cyclized products and polymers.[7] Despite the fact that a tremendous amount of research on copper-phenol chemistry has been reported, in this chapter we report unprecedented reactivity in which Cu^{II} and phenolate (PhO^-) form Cu^{I} and a phenolate radical ($PhO^{\bullet}$) that reacts further to an unknown product, as schematically shown in Figure 6.1. This chemistry exhibits similarities to the Cu^{II} μ-thiolate and Cu^{I} disulfide redox chemistry discussed in previous chapters.

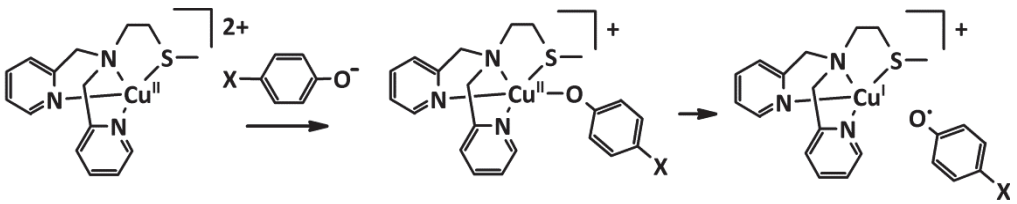

Figure 6.1: Schematic representation of the reaction between $[Cu^{II}(\mathbf{L^1SCH_3})]^{2+}$ and a *para*-substituted phenolate resulting in Cu^{I} and phenolate-peroxide. X = H, halogen, OMe or alkyl.

6.2 Results and Discussion

6.2.1 Synthesis and Analysis of Cu^{II} Complexes

The ligand $\mathbf{L^1SCH_3}$ (Figure 6.1) has been used in our investigations, because it is similar to the ligand $\mathbf{L^1SSL^1}$ that forms Cu^{II} μ-thiolate complexes with Cu^{I} salts (Chapter 2). The presence of the thioether moiety prohibits μ-thiolate formation as the thiolate group has been reported to react with the phenolate moiety.[8] The ligand $\mathbf{L^1SCH_3}$ was synthesized by reductive amination of 2-(methylthio)ethylamine, avoiding the use of toxic 2-chloroethyl methyl sulfide,[9] and increasing the yield from 53% to 99%. The orange/yellow oil of $\mathbf{L^1SCH_3}$ slowly turns dark brown when kept for longer periods of time (weeks). When a flask containing a mixture of equimolar

amounts of $[Cu^{I}(CH_3CN)_4]^+$, **L^1SCH_3** and PhOH in CH_3CN is opened to air an intense dark purple solution is obtained (see Figure 6.2).

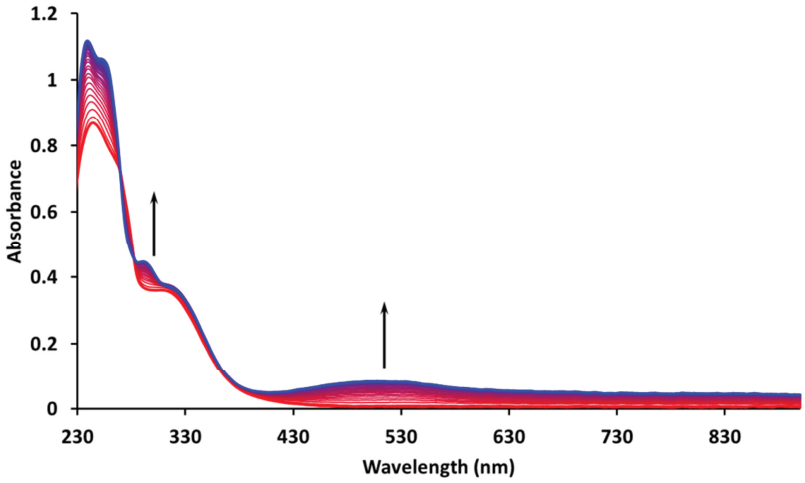

Figure 6.2: UV-vis spectroscopic changes observed for the oxidation of a mixture of $[Cu^{I}(\mathbf{L^1SCH_3})](SbF_6)$ and PhOH by air in CH_3CN at 1.0 mM [Cu] concentration. Spectra were measured over a period of 2 hrs with a transmission dipprobe set at a path length of 1.2 mm.

The UV-vis spectrum shows absorption bands at 238, 255, 293, 320, 510 and 840 nm. The absorption bands at 238, 255, 293 and 320 nm likely arise from LMCT transitions, while the absorptions at 510 and 840 nm can be assigned to Cu^{II} d-d transitions. The bands at 310 and 510 nm are similar to the absorption bands that have been assigned to a Cu^{II}_2 μ-η^2:η^2-peroxide species (~360 nm and 510 nm).[10] To investigate whether a Cu-peroxide species is indeed formed the Raman spectra of copper compounds with a range of different *para*-substituted phenols were measured. Although some of these compounds indeed show a Raman signal close to 740 cm^{-1}, as expected for a Cu_2-peroxide species, for most complexes we observe that the position of this signal shifted depending on the substituent on the *para*-position of the phenyl group. These signals are observed in the range between 580 and 780 cm^{-1} and can possibly be assigned to the C-H out of plane deformations and ring deformations of the phenyl ring (Appendix V, Figure AV.1).[11]

Several reports of purple copper compounds have ascribed the UV-Vis spectra to the presence of Cu^{III}.[12-15] To validate this option, an X-band EPR spectrum of the purple complex in CH_3CN at room temperature was measured. The EPR spectrum shows a

mononuclear isotropic signal with $g_i = 2.10$ and copper hyperfine splitting of 52 Gauss (Appendix V, Figure AV.2), in agreement with the presence of Cu^{II} instead of Cu^{III}. Initially the purple Cu^{II} phenolate complex $[Cu^{II}(\mathbf{L^1SCH_3})(OPh\text{-}X)]^+$ was obtained from a Cu^{I} complex in the presence of phenol and dioxygen, following equation (1). However, the same compound can also be synthesized starting from a Cu^{II} complex and a phenolate salt under oxygen-free conditions, according to equation (2).

$$4\,[Cu^{I}(\mathbf{L^1SCH_3})]^+ + 4\,X\text{-}PhOH + O_2 \rightarrow 4\,[Cu^{II}(\mathbf{L^1SCH_3})(OPh\text{-}X)]^+ + 2\,H_2O \quad (1)$$

$$[Cu^{II}(\mathbf{L^1SCH_3})]^{2+} + X\text{-}PhO^- \rightarrow [Cu^{II}(\mathbf{L^1SCH_3})(OPh\text{-}X)]^+ \quad (2)$$

When the purple complex was prepared in CH_2Cl_2 and the solution was cooled to –84 °C, dark-brown crystals formed. X-ray structure determination showed that the obtained crystals consisted of $[Cu^{II}(\mathbf{L^1SCH_3})(OPh)](SbF_6) \cdot PhOH \cdot 0.38\ CH_2Cl_2$. Attempts to grow crystals at –20 °C of a solution containing *p*-cresol (Me-PhOH), led to formation of single crystals, that by X-ray diffraction were shown to be composed of $[Cu^{II}(\mathbf{L^1SCH_3}^*)(OPh\text{-}Me)](PF_6) \cdot Me\text{-}PhOH \cdot 1.75\ CH_2Cl_2$, in which $\mathbf{L^1SCH_3}^*$ is a degraded ligand. Further analysis of this compound could not be performed, due to its accidental formation in low yield and poor reproducibility. However, as we believe that the formation of this compound is typical for the degradation of this type of complexes, we judged that it is worthwhile to discuss the structure.

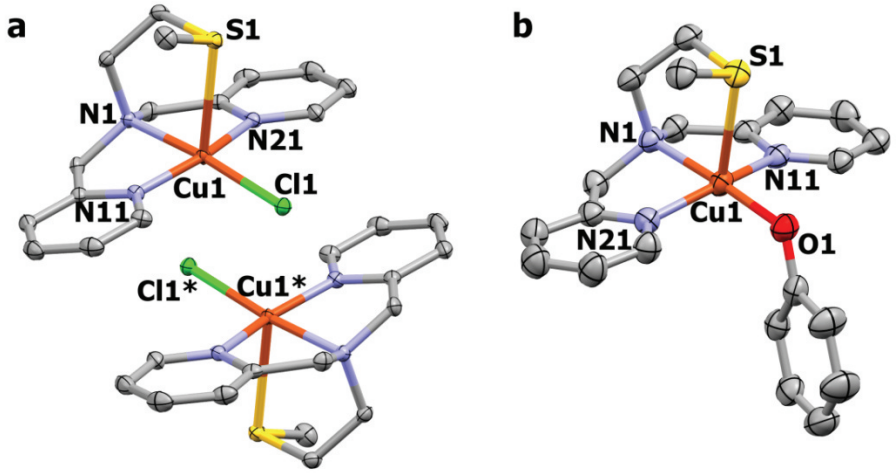

Figure 6.3: Displacement ellipsoid plots (50% probability level) of (a) two cationic complexes of $[Cu^{II}(\mathbf{L^1SCH_3})(Cl)](BF_4)$ and (b) one cationic molecule of $[Cu^{II}(\mathbf{L^1SCH_3})(OPh)](SbF_6) \cdot PhOH \cdot 0.38\ CH_2Cl_2$. The non-coordinating counterions, hydrogen atoms and co-crystallized solvents are omitted for clarity. Symmetry operation * = [1–x, 2–y, 1–z].

For comparison the compound [Cu^{II}(**L^1SCH_3**)(Cl)](BF_4) was synthesized from a mixture containing [$Cu^{II}(H_2O)_6$](BF_4)$_2$, $CuCl_2 \cdot 2\ H_2O$ and **L^1SCH_3** and its structure was determined by X-ray crystallography. Displacement ellipsoid plots of the cationic complexes in [Cu^{II}(**L^1SCH_3**)(Cl)](BF_4), [Cu^{II}(**L^1SCH_3**)(OPh)](SbF_6) and [Cu^{II}(**L^1SCH_3***)(OPh-Me)](PF_6) are shown in Figure 6.3 and Figure 6.4. Crystallographic data and selected bond distances and angles are given in Table 6.1 and Table 6.2. [Cu^{II}(**L^1SCH_3**)(Cl)](BF_4) crystallizes in the triclinic space group *P*-1. The copper ion is in an elongated octahedral coordination geometry with N_3SCl_2 environment, forming a dimer through a weak interaction with a chloride ion (3.1018(4) Å) from a neighboring molecule. The Cu-Cu* distance is 3.8192(3) Å.

Table 6.1: Crystallographic and structure refinement data for complexes [Cu^{II}(**L^1SCH_3**)(Cl)](BF_4), [Cu^{II}(**L^1SCH_3**)(OPh)](SbF_6) and [Cu^{II}(**L^1SCH_3***)(OPh-Me)](PF_6).

	[Cu^{II}(**L^1SCH_3**)(Cl)](BF_4)	[Cu^{II}(**L^1SCH_3**)(OPh)](SbF_6)	[Cu^{II}(**L^1SCH_3***)(OPh-Me)](PF_6)
empirical formula	$[C_{15}H_{19}ClCuN_3S](BF_4)$	$[C_{21}H_{24}CuN_3OS](SbF_6) \cdot C_6H_5OH \cdot 0.38\ CH_2Cl_2$	$[C_{28}H_{29}CuN_4O_2S](PF_6) \cdot C_7H_7OH \cdot 1.75\ CH_2Cl_2$
formula weight	459.19	1583.47	950.51
crystal system	triclinic	monoclinic	triclinic
space group	*P*-1	*C*2/c	*P*-1
a, Å	7.45273(18)	28.9170(8)	11.5835(3)
b, Å	11.2448(3)	22.0004(5)	14.5137(4)
c, Å	12.3634(3)	10.6154(2)	14.5908(4)
α, deg	65.993(3)	90	66.815(3)
β, deg	74.934(2)	90.013(2)	74.239(2)
γ, deg	88.273(2)	90	68.573(3)
V, Å^3	910.58(4)	6753.4(3)	2075.50(11)
Z	2	4	2
D_{calc}, g·cm^3	1.675	1.557	1.518
T, K	110(2)	110(2)	110(2)
crystal size, mm	$0.36 \times 0.28 \times 0.22$	$0.36 \times 0.08 \times 0.07$	$0.64 \times 0.31 \times 0.08$
μ, mm^{-1}	1.504	8.792	4.229
no. of reflns measd	28025	20658	25599
no. of unique reflns	4179	6624	8055
no. of reflns obsd.	3994 [$I > 2\sigma(I)$]	6263 [$I > 2\sigma(I)$]	7606 [$I > 2\sigma(I)$]
no. of parameters	282	502	616
R_1 / wR_2 [$I > 2\sigma(I)$]	0.0187/0.0486	0.0451/0.1256	0.0671/0.1764
R_1 / wR_2 [all refl.]	0.0197/0.0491	0.0479/0.1281	0.0696/0.1783
goodness of fit	1.043	1.077	1.129
$\Delta\rho$, e·Å^{-3}	–0.30/0.36	–0.86/1.01	–0.77/1.10

Table 6.2: Selected bond distances (Å) and bond angles (°) complexes [Cu^{II}(**L^1SCH_3**)(Cl)](BF_4), [Cu^{II}(**L^1SCH_3**)(OPh)](SbF_6) and [Cu^{II}(**L^1SCH_3***)(OPh-Me)](PF_6).

	[Cu^{II}(**L^1SCH_3**)(Cl)](BF_4)	[Cu^{II}(**L^1SCH_3**)(OPh)](SbF_6)	[Cu^{II}(**L^1SCH_3***)(OPh-Me)](PF_6)
Cu1 - Cu1*	3.8192(3)		
Cu1 - S1	2.7152(4)	2.6270(15)	2.5796(11)
Cu1 - N1	2.0558(10)	2.063(4)	2.071(3)
Cu1 - N11	1.9782(11)	1.985(4)	1.993(4)
Cu1 - N21	1.9845(11)	1.984(4)	1.980(3)
Cu1 - Cl1/O1	2.2588(3)	1.929(4)	3.249(3)
Cu1 - Cl1*/F6/O2	3.1018(4)	3.398(4)	1.907(3)
S1 - Cu1 - N1	85.93(3)	87.47(12)	86.17(9)
S1 - Cu1 - N11	101.67(3)	91.62(12)	106.77(10)
S1 - Cu1 - N21	84.59(3)	103.05(13)	97.55(9)
S1 - Cu1 - Cl1/O1/O2	100.430(11)	95.17(12)	93.62(9)
N1 - Cu1 - N11	82.43(4)	83.77(17)	82.29(14)
N1 - Cu1 - N21	83.42(4)	82.59(18)	83.71(13)
N1 - Cu1 - Cl1/O1/O2	173.64(3)	177.09(17)	177.63(13)
N11 - Cu1 - N21	164.06(4)	159.44(18)	150.92(14)

Symmetry operation * = [1–x, 2–y, 1–z]

[Cu^{II}(**L^1SCH_3**)(OPh)](SbF_6) crystallizes in the monoclinic space group *C*2/c. The SbF_6^- counterion and the phenol molecule are both found to be disordered over two orientations; the occupancy factors of the major components of the disorder refines to 0.938(3) and 0.560(11), respectively. Furthermore, the crystal lattice contains CH_2Cl_2 molecules that are located at sites of twofold axial symmetry.[16] In contrast to [Cu^{II}(**L^1SCH_3**)(Cl)](BF_4), [Cu^{II}(**L^1SCH_3**)(OPh)](SbF_6) does not form a dimeric species. The copper ion is in a square-pyramidal geometry (τ = 0.29)[17] and seems to have a weak interaction with the SbF_6^- counterion (Cu – F6 = 3.398(4) Å). The phenol lattice molecule forms a hydrogen bond with the coordinated phenolate molecule at a PhO…H-OPh distance of 1.78 Å. [Cu^{II}(**L^1SCH_3***)(OPh-Me)](PF_6) crystallizes in the triclinic space group *P*-1. The coordinated *p*-cresolate is found to be disordered over two orientations; the occupancy factor of the major component of the disorder refines to 0.722(17). The crystal lattice contains two partially occupied CH_2Cl_2 molecules per asymmetric unit.[18] The copper ion in [Cu^{II}(**L^1SCH_3***)(OPh-Me)](PF_6) has a coordination geometry that is very similar to that in [Cu^{II}(**L^1SCH_3**)(OPh)](SbF_6). The square-pyramidal geometry is more distorted (τ = 0.46) due to the strain in the backbone of the ligand, caused by the oxidative degradation. The degradation of the ligand resulted in formation of a new five-membered ring at the benzylic positions of the pyridyl groups. The five-membered ring seems to have been formed from the

coordinating ligand and an (at the benzylic position) oxidized pyridyl group of another ligand. It has been reported that these benzylic positions can be reactive, which might also explain the rapid degradation of the free ligand **L^{1}SCH$_3$**.[19-22]

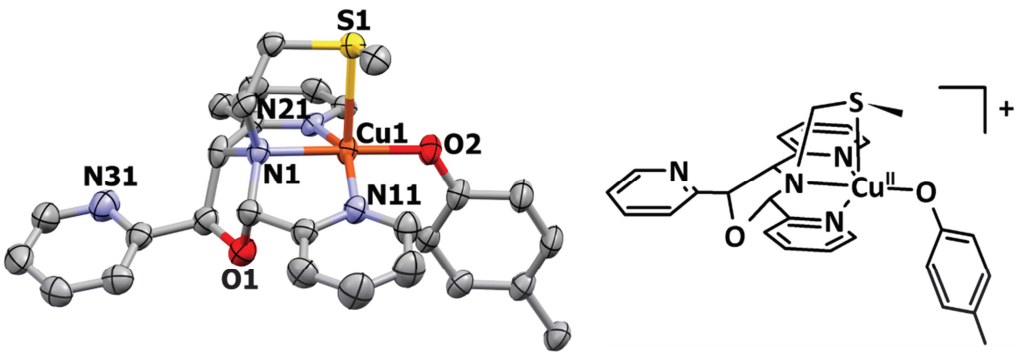

Figure 6.4: Schematic drawing and displacement ellipsoid plot (50% probability level) of the cationic part of [Cu^{II}(**L^{1}SCH$_3$***)(OPh-Me)](PF$_6$) · Me-PhOH · 1.75 CH_2Cl_2. The non-coordinating counterion, hydrogen atoms and lattice molecules have been omitted for clarity.

Cyclic voltammograms were recorded of [Cu^{II}(**L^{1}SCH$_3$**)(OPh-Me)]$^+$ in CH_3CN (see Figure 6.5); this solution is stable for several days at room temperature. An equimolar mixture of **L^{1}SCH$_3$** with Cu^{II}(OTf)$_2$ in CH_3CN shows a reversible redox event corresponding to the Cu^{II}/Cu^{I} redox couple at a half-wave potential of $E_{1/2}$ = +0.19 V vs Ag/AgCl with a peak-to-peak separation of 81 mV. Me-PhO$^-$ (as the potassium salt) in CH_3CN shows two irreversible oxidation events at +0.03 V and +0.31 V vs Ag/AgCl. The oxidation event at +0.03 V likely corresponds to the formation of the cresolate radical: Me-PhO$^-$ → Me-PhO$^\bullet$. The voltammogram of the purple Cu^{II} cresolate compound shows three quasi-reversible and one irreversible redox-event. The irreversible oxidation wave at E_{pa} = 0.81 V and the quasi-reversible event at $E_{1/2}$ = +1.02 V are very similar to the waves observed for M-PhO$^-$, albeit considerably shifted. The quasi-reversible redox couple at $E_{1/2}$ = –0.34 V can be assigned to the Cu^{II}/Cu^{I} couple of the copper cresolate complex; the more negative $E_{1/2}$ value is in agreement with stabilization of the Cu^{II} oxidation state by the coordinating *p*-cresolate anion. The redox event at $E_{1/2}$ = +0.17 V is likely to originate from the Cu^{II}/Cu^{I} redox couple of the complex without a coordinating cresolate group; its intensity is strongly dependent on scan rate (Appendix V, Figure AV.3).

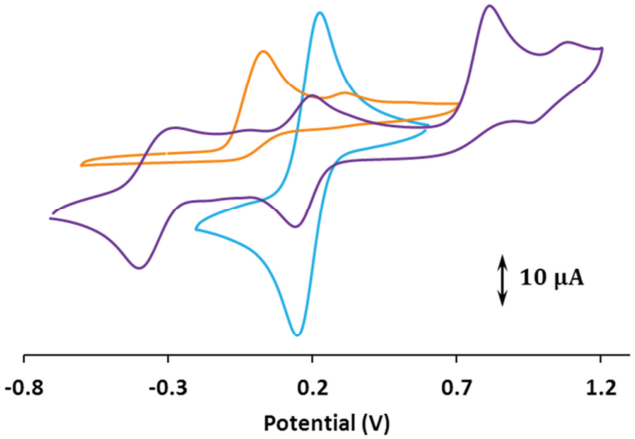

Figure 6.5: Cyclic voltammograms of Me-PhOK (orange), $Cu^{II}(OTf)_2$ + $\mathbf{L^1SCH_3}$ (blue) and $[Cu^{II}(\mathbf{L^1SCH_3})(OPh\text{-}Me)](OTf)$ (purple) in CH_3CN at 2.0 mM [Cu] concentration measured with a scan rate of 100 mV/s. Potentials are given vs Ag/AgCl.

6.2.2 Cu^{II} Phenolate Conversion

Over time the color of a Cu^{II} phenolate solution kept under an argon atmosphere changes from purple to yellow. The change from purple to yellow was monitored with UV-vis spectroscopy for a solution containing $[Cu^{II}(\mathbf{L^1SCH_3})(OPh\text{-}F)](OTf)$ (Figure 6.6). The rate of this conversion depends on the *para*-substituent at the phenol ring. The stability of the purple complexes decreases approximately in the order of X = OMe > tert-butyl ~ iso-propyl ~ CH_3 > H > Cl ~ Br ~ I > F > CF_3. The presence of electron-donating substituents prolongs the lifetime of the purple species, while electron-withdrawing groups result in faster conversion towards the yellow product. In methanol, the purple compound is stable for a short time, but the use of the non-protic solvent CH_3CN increases the lifetime of the purple complex significantly. At low complex concentrations the conversion to the yellow product is much slower (> 50 hrs at 1.0 mM [Cu], Figure 6.6a) than at higher concentrations (~15 min at 10 mM [Cu], Figure 6.6b), indicating that an intermolecular process takes place. The LMCT at 300 nm and the Cu^{II} d-d transitions at 500 and 840 nm disappear, indicating that a Cu^{I} species is formed, and new absorption bands at 257 and 280 nm appear. The formation of Cu^{I} is confirmed by the diamagnetic ^1H NMR spectrum, which resembles that of a 1:1 mixture of $[Cu^{I}(\mathbf{L^1SCH_3})](OTf)$ and F-PhOH (Figure 6.7). The spectrum showed that already some degradation of the ligand had occurred, which is potentially similar as witnessed in $[Cu^{II}(\mathbf{L^1SCH_3}^*)(OPh\text{-}Me)](PF_6)$ (Figure 6.4).

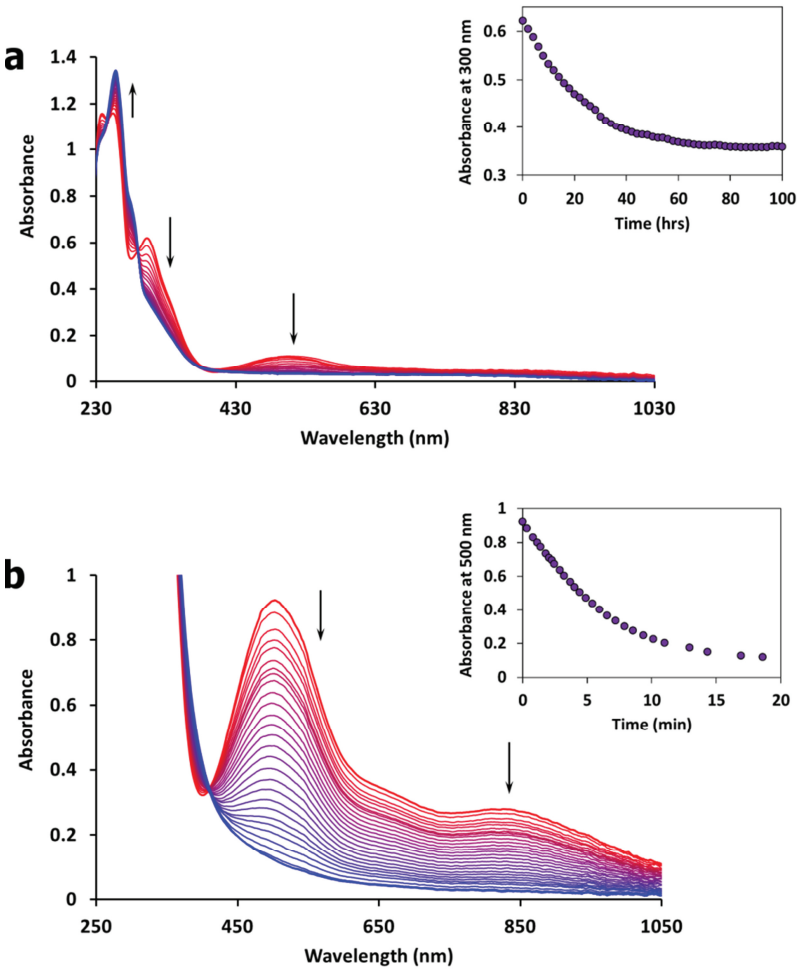

Figure 6.6: UV-vis spectroscopic changes of the conversion of the purple compound [Cu^{II}(**L^1SCH_3**)(OPh-F)](OTf) in CH_3CN to a yellow-colored solution (a) at 1.0 mM [Cu] concentration for 100 hrs and (b) at 10 mM [Cu] concentration for 19 min. Spectra were recorded with a transmission dipprobe set at a path length of 1.2 mm. The inset and the arrows indicate the development of the spectra over time.

The fact that Cu^{II} has reduced to Cu^{I} means that an electron has transferred from PhO^- to copper creating a $PhO^\bullet$ radical that will react further. The concentration-dependence of the conversion indicates that an intermolecular reaction takes place, which could mean that the phenolate radicals react with each other. However, o*rtho*-substitution or oxidative polymerization of the phenol radicals is not likely as this would result in different (asymmetric) NMR spectra. Alternatively, the radical might react with **L^1SCH_3** or the solvent or it may pick up an $H^\bullet$ to reform the phenol

compound. Another option is that two of these phenolate radicals react together to form the peroxide PhO-OPh.

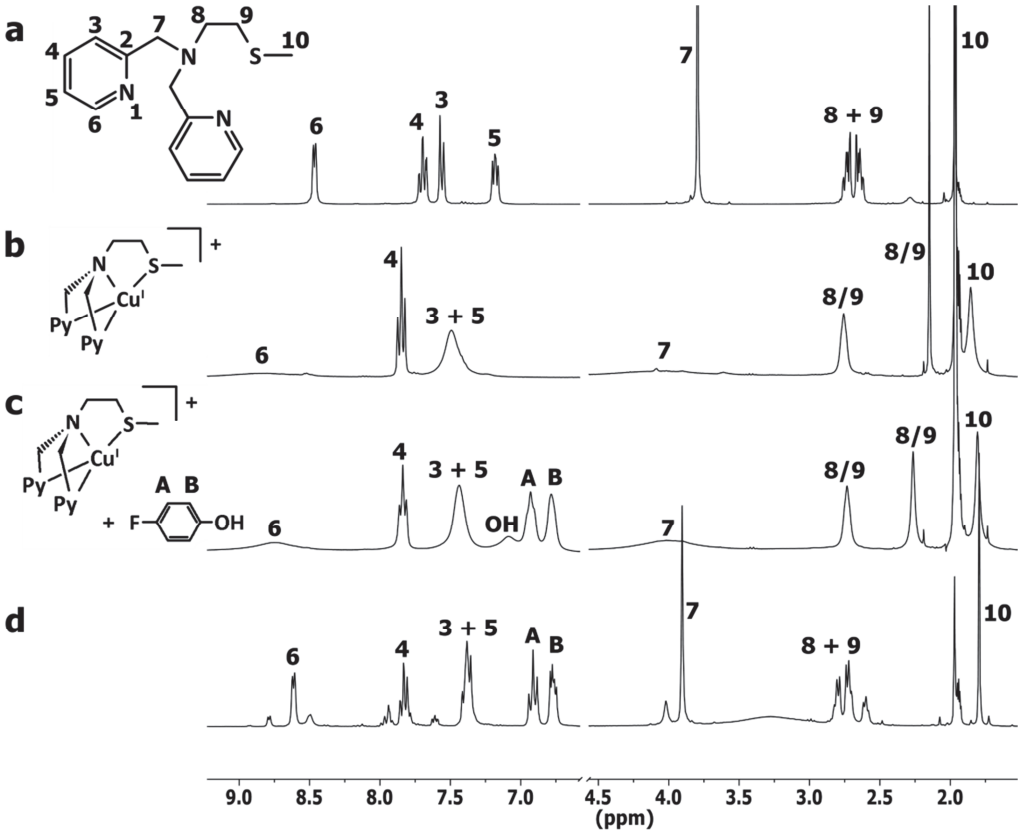

Figure 6.7: ^{1}H NMR spectra of (a) $\mathbf{L^{1}SCH_{3}}$, (b) [Cu^{I}($\mathbf{L^{1}SCH_{3}}$)](OTf), (c) a mixture of [Cu^{I}($\mathbf{L^{1}SCH_{3}}$)](OTf) and F-PhOH and (d) the yellow solution obtained after reaction of [Cu^{II}($\mathbf{L^{1}SCH_{3}}$)](OTf)$_2$ with F-PhO$^-$ in CD_3CN at RT.

To check for the formation of a new bond, Raman spectroscopy was used. The Raman spectra of the purple complex [Cu^{II}($\mathbf{L^{1}SCH_{3}}$)(OPh-F)](OTf) and its converted yellow species are shown in Figure 6.8. The spectra are virtually the same except for an extra Raman signal at 1033 cm^{-1} in the spectrum of the yellow solution. This signal is blue-shifted compared to the O-O stretch vibrations reported for dialkyl-peroxides (~850-900 cm^{-1}).[23] However, this vibration could be assigned to the C-O stretch vibration of an aryl peroxide, which is reported to be located around 1000 cm^{-1}, whereas the C-O stretch vibration for *p*-substituted phenols is located between 1200-1300 cm^{-1}.[11, 24] There are theoretical studies that have shown that the formation of a diaryl peroxide

is unfavorable.[25, 26] Conversely, there are also theoretical studies[27, 28] and some experimental reports in which the formation of diaryl peroxides is thought to occur.[29-36] Alternatively, the signal at 1033 cm^{-1} can be assigned to the C-O stretch vibration of an aromatic ether (1010-1050 cm^{-1})[37] which could form if the $PhO^{\bullet}$ species reacts with the solvent or the ligand. In both cases however, the appearance of this C-O signal indicates the formation of a new species other than phenol.

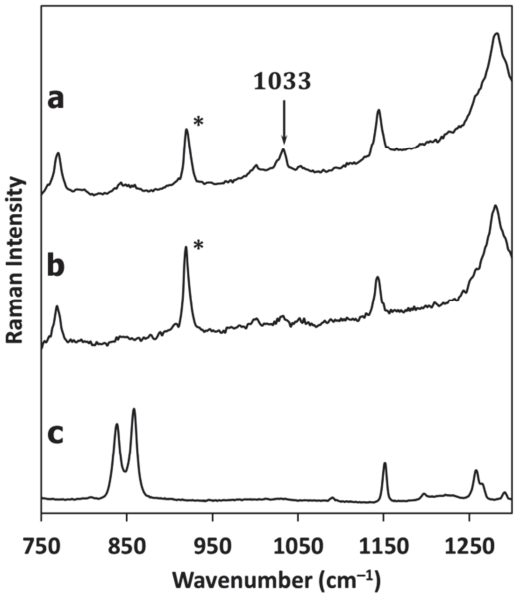

Figure 6.8: Raman spectra of (a) the yellow solution obtained after reaction of $[Cu^{II}(\mathbf{L^1SCH_3})](OTf)_2$ with $F\text{-}PhO^-$, (b) $[Cu^{II}(\mathbf{L^1SCH_3})(OPh\text{-}F)](OTf)$ and (c) F-PhOH recorded with a confocal Raman microscope at an excitation wavelength of 532 nm with 3 s exposure time; the spectra are the average of 25 accumulations. * = CH_3CN.

The formation of a Cu^I species, as confirmed by NMR and UV-vis spectroscopy, together with the appearance of a Raman band at 1033 cm^{-1} suggest the formation of a $PhO^{\bullet}$ radical that further reacts to form either a diaryl peroxide or an aromatic ether via a reaction with the solvent or the ligand. Further research will be directed toward isolation and characterization of this product. It is interesting to note that this reaction of $R\text{-}O^-$ to $R\text{-}O^{\bullet}$ is reminiscent of the Cu^{II} μ-thiolate/Cu^I disulfide redox chemistry (Chapter 1-3), in which $R\text{-}S^-$ is converted to R-S-S-R (Figure 6.9). This type of phenol redox chemistry is unprecedented and might explain the results of similar chemistry,

like for instance for the purple Cu^{II}-N(Sc)-Ts species that was reported to degrade to a Cu^{I} complex in aprotic solvents.[38]

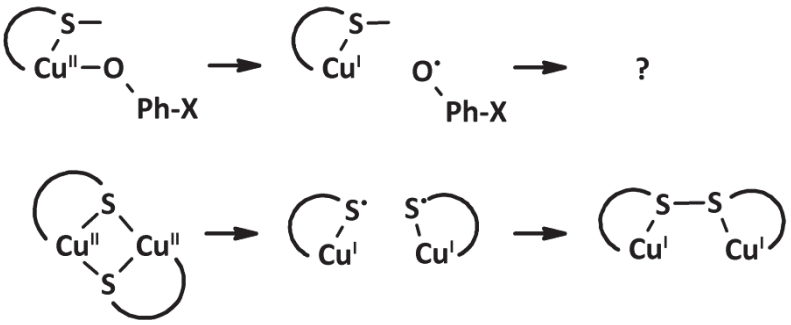

Figure 6.9: Schematic representation of the Cu^{II} μ-thiolate/Cu^{I} disulfide redox chemistry and the related Cu^{II} phenolate conversion to form Cu^{I} and a phenolate radical.

6.3 Conclusion

The unique find of the oxidation of substituted phenolates by Cu^{II} compounds to the corresponding phenolate radicals is described. Oxidation of a mixture of the Cu^{I} compound $[Cu^{I}(\mathbf{L^{1}SCH_{3}})]^{+}$ and phenol by air, results in the formation of a purple Cu^{II} phenolate species of which the structure was determined by X-ray crystallography. Isolation of $[Cu^{II}(\mathbf{L^{1}SCH_{3}}*)(OPh\text{-}Me)](PF_{6})$ indicated that this product degrades by reaction of the ligand at the benzylic positions of the pyridyl groups. The purple product converts to a yellow solution containing Cu^{I}, corroborated by NMR and UV-vis spectroscopy, and either a diaryl peroxide or an aromatic ether, as indicated by the appearance of a new Raman band. This reaction depends on the concentration of the mononuclear species and the *para*-substituent of the phenyl group; electron-donating substituents stabilize the purple Cu^{II} complex whereas electron-withdrawing substituents direct the conversion towards the diaryl peroxide. Interestingly, this reaction is very similar to the Cu^{II} μ-thiolate/Cu^{I} disulfide redox equilibrium. Such a redox reaction with Cu^{II} and phenolate has not been reported before to the best of our knowledge. Future research will be directed to further analysis and characterization of the product that is formed by the phenolate radical.

6.4 Experimental Section

6.4.1 General Methods

Reagents and solvents were purchased from commercial sources. Oxygen-free experiments were carried out using standard Schlenk-line techniques under an argon atmosphere.

$[Cu^{I}(CH_3CN)_4](PF_6)$ and $[Cu^{I}(CH_3CN)_4](SbF_6)$ were synthesized according to a literature procedure.[39] Potassium phenolate salts were obtained by adding potassium *tert*-butoxide to the corresponding phenol in tetrahydrofuran. NMR spectra were recorded on a Bruker 300 DPX spectrometer. NMR experiments under argon were carried out using a J. Young NMR tube. IR spectra were obtained on a Perkin Elmer UATR (Single Reflection Diamond) Spectrum Two device (4000-700 cm^{-1}; resolution 4 cm^{-1}). Mass spectrometry was performed using a Finnigan Aqua Mass Spectrometer (MS) with electro spray ionization (ESI). Sample introduction was achieved through a Dionex ASI-100 automated sample injector with an eluent flow rate of 0.2 mL/min. Elemental analyses were performed by the Microanalytical laboratory Kolbe in Germany. UV-vis spectra were collected using a transmission dipprobe with variable path length on an Avantes Avaspec-2048 spectrometer with Avalight-DH-S-BAL light source. Confocal Raman spectra at 532 nm were recorded using a Renishaw InVia Reflex Raman microscope (Wotton-under-Edge, United Kingdom) with a 300 mW, 785 nm diode laser in combination with a 1200 lines per millimeter (l/mm) grating and an 80 mW, 532 nm frequency doubled Nd:YAG excitation source in combination with a 1800 l/mm grating and a Peltier cooled CCD detector (203 K). The instrument included a Leica light microscope 5× and 20× air objectives. The 521 cm^{-1} Raman shift of an internal silicon standard was used to verify the calibration of the system. Cyclic voltammetry was performed with an Autolab PGstat10 potentiostat controlled by GPES4 software. A three-electrode arrangement with a glassy carbon working electrode (3 mm diameter), an Ag/AgCl double junction reference electrode and a Pt wire counter electrode were used in different solvents with 0.1 M NBu_4PF_6 as the electrolyte. In these conditions the Fc/Fc^+ couple was found to be located at +443 mV with a peak-to-peak separation of 60 mV in CH_3CN. Potentials are given relative to the Ag/AgCl electrode.

6.4.2 X-ray Crystallography

The reflection intensities for $[Cu^{II}(\mathbf{L^1SCH_3})(Cl)](BF_4)$, $[Cu^{II}(\mathbf{L^1SCH_3})(OPh)](SbF_6)$ and $[Cu^{II}(\mathbf{L^1SCH_3}^*)(OPh\text{-}Me)](PF_6)$ were collected at 110(2) K using a SuperNova diffractometer (equipped with Atlas detector) with Mo $K\alpha$ radiation (λ = 0.71073 Å) for $[Cu^{II}(\mathbf{L^1SCH_3})(Cl)](BF_4)$ and Cu Kα radiation (λ = 1.54178 Å) for $[Cu^{II}(\mathbf{L^1SCH_3})(OPh)](SbF_6)$ and $[Cu^{II}(\mathbf{L^1SCH_3}^*)(OPh\text{-}Me)](PF_6)$ under the program CrysAlisPro (Version 1.171.36.32 Agilent Technologies, 2013). The program was used to refine the cell dimensions and for data reduction. The structure was solved with the program SHELXS-2013 or SHELXS-2014 (Sheldrick, 2013-2014)[40] and was refined on F^2 with SHELXL-2013 or SHELXL-2014 (Sheldrick, 2013-2014).[40] Analytical numeric absorption corrections based on a multifaceted crystal model were applied using CrysAlisPro. The temperature of the data collection was controlled using the system Cryojet (manufactured by Oxford Instruments). The H atoms were placed at calculated positions using the instructions AFIX 13, AFIX 23, AFIX 43, AFIX 137 or AFIX 147 with isotropic displacement parameters having values 1.2 or 1.5 times *U*eq of the attached C or O(O2/O2') atoms. The crystals of $[Cu^{II}(\mathbf{L^1SCH_3})(OPh)](SbF_6)$ were found to be pseudo-merohedrally twinned. The twin relationship is defined by the matrix: (1 0 0 / 0 –1 0 / 0 0 –1).

The BASF factor refines to 0.1550(10). The H atom attached to O3 (from the non-coordinated *p*-cresol in [Cu^{II}(**L^1SCH_3***)(OPh-Me)](PF_6)) was found from difference Fourier map, and its coordinates and isotropic temperature factor were refined freely.

6.4.3 Ligand and Complex Synthesis

L^1SCH_3

The synthesis of **L^1SCH_3** was carried out using a slightly modified literature procedure.[41] 2-Pyridinecarboxaldehyde (1.90 mL, 20 mmol) was added to 2-(methylthio)ethylamine (0.93 mL, 10 mmol) dissolved in dichloromethane (20 mL). $NaBH(OAc)_3$ (6.0 g, 28 mmol) was added in small portions over the course of 30 min and the solution was stirred for approximately 5 hours at RT. The reaction was quenched by slowly adding 50 mL NaOH (2 M). The two layers were separated and water layer was washed two more times with dichloromethane. The combined organic layers were dried over Na_2SO_4 after which the solution was evaporated to dryness yielding an orange/yellow oil (2.7 g, 9.9 mmol, 99%). ^{1}H NMR (300 MHz, CD_3CN, RT): δ 1.97 (s, 3H, S-C*H*$_3$), 2.64 (m, 2H, S-C*H*$_2$-C*H*$_2$), 2.74 (m, 2H, S-C*H*$_2$-C*H*$_2$), 3.80 (s, 4H, Py-C*H*$_2$-N), 7.18 (m, 2H, Py-*H*$_5$), 7.56 (d, *J* = 8 Hz, 2H, Py-*H*$_3$), 7.70 (td, *J* = 8 Hz, 2 Hz, 2H, Py-*H*$_4$), 8.47 (m, 2H, Py-*H*$_6$). ^{13}C NMR (75 MHz, CD_3CN, RT): δ 15.6 (S-CH_3), 32.3 (S-CH_2-CH_2), 54.2 (S-CH_2-CH_2), 60.8 (Py-CH_2-N), 122.9 (Py-*C*$_3$ or Py-*C*$_5$), 123.8 (Py-*C*$_3$/Py-*C*$_5$), 137.3 (Py-*C*$_4$), 149.8 (Py-*C*$_6$), 160.7 (Py-*C*$_2$). ESI-MS found (calculated) for $[M+H]^+$ *m*/*z* 274.1 (274.1). IR (neat, cm^{-1}): 2915*w*, 2829*w*, 1589*s*, 1569*m*, 1473*m*, 1432*s*, 1362*m*, 1117*m*, 1047*m*, 994*m*, 755*s*, 616*m*.

*[Cu^{II}(**L^1SCH_3**)(Cl)](BF_4)*

To a solution of **L^1SCH_3** (94 mg, 0.34 mmol) in 8 mL MeOH, [$Cu^{II}(H_2O)_6$](BF_4)$_2$ (59 mg, 0.17 mmol) and $CuCl_2 \cdot 2\ H_2O$ (29 mg, 0.17 mmol) were added, after which a precipitate formed. The precipitate was filtered and washed with MeOH and Et_2O, which yielded the product as a dark blue crystalline solid (110 mg, 0.24 mmol, 70%). Crystals suitable for X-ray structure determination were obtained by slow vapor diffusion of diethyl ether into a methanol solution containing the complex. Elemental analysis calcd for [Cu^{II}(**L^1SCH_3**)(Cl)](BF_4), $C_{15}H_{19}BClCuF_4N_3S$: C 39.23, H 4.17, N 9.15, S 6.98; Found: C 39.73, H 4.44, N 9.25, S 7.05. ESI-MS found (calculated) for $[M - BF_4]^+$ *m*/*z* 370.9 (371.0). IR (neat, cm^{-1}): 1611*m*, 1441*m*, 1284*m*, 1046*vs*, 1029*vs*, 1002*m*, 907*m*, 783*m*, 759*m*, 519*m*. UV-vis in acetonitrile at 0.1 mM [Cu] concentration: 258 nm (ε = 10 800 M^{-1} cm^{-1}), 297 nm (ε = 3 400 M^{-1} cm^{-1}), 700 nm (ε = 130 M^{-1} cm^{-1}), 890 nm (ε = 170 M^{-1} cm^{-1}).

*[Cu^{II}(**L^1SCH_3**)(OPh)](SbF_6)*

L^1SCH_3 (70.5 mg, 0.26 mmol) was dissolved in 35 mL CH_2Cl_2 under argon atmosphere using standard Schlenk-line techniques. To this yellow solution [$Cu^{I}(CH_3CN)_4$](SbF_6) (120 mg, 0.26 mmol) and phenol (25.0 mg, 0.26 mmol) were added. The solution was opened to air and changed color from brown/yellow to intense dark purple. After 15 minutes stirring in air, 70 mL of *n*-pentane was added, which resulted in the formation of a precipitate that was collected

by filtration and was washed with *n*-pentane to yield [Cu^{II}(**L^1SCH_3**)(OPh)](SbF_6) as a dark brown powder (135 mg, 0.20 mmol, 79%). Crystals suitable for X-ray structure determination were obtained by storing a CH_2Cl_2 solution of the complex in an NMR tube in the freezer at –84 °C. Elemental analysis calcd for [Cu^{II}(**L^1SCH_3**)(OPh)](SbF_6), $C_{21}H_{24}CuF_6N_3OSSb$: C 37.88, H 3.63, N 6.31, S 4.82. Found: C 37.69, H 3.74, N 6.29, S 4.79. ESI-MS found (calculated) for [M – OPh – SbF_6]$^+$ *m*/*z* 336.0 (336.1); [M + Cl – OPh – SbF_6]$^+$ *m*/*z* 371.0 (371.0). IR (neat, cm^{-1}): 1609*m*, 1585*w*, 1475*m*, 1447*w*, 1284*w*, 1264*m*, 1239*m*, 1160*w*, 1032*w*, 819*w*, 763*s*, 696*w*, 653*vs*, 574*w*, 541*w*, 515*w*. UV-vis in acetonitrile at 1.0 mM [Cu] concentration: 238 nm (ε = 9 300 M^{-1} cm^{-1}), 255 nm (ε = 8 800 M^{-1} cm^{-1}), 293 nm (ε = 3 700 M^{-1} cm^{-1}), 320 nm (ε = 3 000 M^{-1} cm^{-1}), 510 nm (ε = 700 M^{-1} cm^{-1}) and 840 nm (ε = 380 M^{-1} cm^{-1}).

*[Cu^{II}(**L^1SCH_3***)(OPh-Me)](PF_6)*

Crystals of [Cu^{II}(**L^1SCH_3***)(OPh-Me)](PF_6) were obtained in a similar way as [Cu^{II}(**L^1SCH_3**)(OPh)](SbF_6), but starting from *p*-cresol and [Cu^{I}(CH_3CN)$_4$](PF_6). Crystals suitable for X-ray structure determination were obtained by vapor diffusion at –20 °C of *n*-pentane into a CH_2Cl_2 solution containing the complex mixture.

6.5 References

1. Lewis, E. A.; Tolman, W. B., *Chem. Rev.* **2004,** *104*, 1047-1076.
2. Solomon, E. I.; Heppner, D. E.; Johnston, E. M.; Ginsbach, J. W.; Cirera, J.; Qayyum, M.; Kieber-Emmons, M. T.; Kjaergaard, C. H.; Hadt, R. G.; Tian, L., *Chem. Rev.* **2014,** *114*, 3659-3853.
3. Koval, I. A.; Gamez, P.; Belle, C.; Selmeczi, K.; Reedijk, J., *Chem. Soc. Rev.* **2006,** *35*, 814-840.
4. Sánchez-Ferrer, A.; Rodríguez-López, J. N.; García-Cánovas, F.; García-Carmona, F., *Biochim. Biophys. Acta* **1995,** *1247*, 1-11.
5. Yamazaki, S.; Itoh, S., *J. Am. Chem. Soc.* **2003,** *125*, 13034-13035.
6. Fujieda, N.; Murata, M.; Yabuta, S.; Ikeda, T.; Shimokawa, C.; Nakamura, Y.; Hata, Y.; Itoh, S., *J. Biol. Inorg. Chem.* **2013,** *18*, 19-26.
7. Allen, S. E.; Walvoord, R. R.; Padilla-Salinas, R.; Kozlowski, M. C., *Chem. Rev.* **2013,** *113*, 6234-6458.
8. Osako, T.; Ueno, Y.; Tachi, Y.; Itoh, S., *Inorg. Chem.* **2004,** *43*, 6516-6518.
9. Ambundo, E. A.; Deydier, M. V.; Grall, A. J.; Aguera-Vega, N.; Dressel, L. T.; Cooper, T. H.; Heeg, M. J.; Ochrymowycz, L. A.; Rorabacher, D. B., *Inorg. Chem.* **1999,** *38*, 4233-4242.
10. Mirica, L. M.; Ottenwaelder, X.; Stack, T. D. P., *Chem. Rev.* **2004,** *104*, 1013-1045.
11. Socrates, G., *Infrared and Raman Characteristic Group Frequencies: Tables and Charts*. 3rd ed.; Wiley: **2004**.
12. Donoghue, P. J.; Tehranchi, J.; Cramer, C. J.; Sarangi, R.; Solomon, E. I.; Tolman, W. B., *J. Am. Chem. Soc.* **2011,** *133*, 17602-17605.

13. King, A. E.; Huffman, L. M.; Casitas, A.; Costas, M.; Ribas, X.; Stahl, S. S., *J. Am. Chem. Soc.* **2010,** *132*, 12068-12073.
14. McDonald, M. R.; Scheper, W. M.; Lee, H. D.; Margerum, D. W., *Inorg. Chem.* **1995,** *34*, 229-237.
15. McDonald, M. R.; Fredericks, F. C.; Margerum, D. W., *Inorg. Chem.* **1997,** *36*, 3119-3124.
16. While running checkCIF, the checking procedure generated the following alert type A: *"Structure contains solvent accessible voids of 416 Å^3"*. The highest residual electron density peak and hole are 1.01 (located at 0.94 Å from Sb1) and –0.86 e$^-$ Å^{-3} (located at 0.80 Å from Sb1), respectively. The second largest peak (0.84 e$^-$ Å^{-3}) and two other peaks (0.64 and 0.43 e$^-$ Å^{-3}) that are found in those voids are most likely concerned with some residual disordered solvent molecules with very low occupancy factors. Thus, this alert can be disregarded as there is no significant effect on the correctness of the structure.
17. Addison, A. W.; Rao, T. N.; Reedijk, J.; Vanrijn, J.; Verschoor, G. C., *J. Chem. Soc., Dalton Trans.* **1984**, 1349-1356.
18. One CH_2Cl_2 molecule is found to be disordered over two orientations. The occupancy factors of both major and minor components refine to 0.726(5) and 0.211(5). The other CH_2Cl_2 molecule is ordered, but its occupancy factor refines to 0.809(4).
19. Arnold, P. J.; Davies, S. C.; Dilworth, J. R.; Durrant, M. C.; Griffiths, D. V.; Hughes, D. L.; Richards, R. L.; Sharpe, P. C., *J. Chem. Soc., Dalton Trans.* **2001**, 736-746.
20. Letko, C. S.; Rauchfuss, T. B.; Zhou, X.; Gray, D. L., *Inorg. Chem.* **2012,** *51*, 4511-4520.
21. van der Vlugt, J. I.; Pidko, E. A.; Vogt, D.; Lutz, M.; Spek, A. L., *Inorg. Chem.* **2009,** *48*, 7513-7515.
22. Filonenko, G. A.; Cosimi, E.; Lefort, L.; Conley, M. P.; Copéret, C.; Lutz, M.; Hensen, E. J. M.; Pidko, E. A., *ACS Catal.* **2014,** *4*, 2667-2671.
23. Vacque, V.; Sombret, B.; Huvenne, J. P.; Legrand, P.; Suc, S., *Spectrochim. Acta A* **1997,** *53*, 55-66.
24. Green, J. H. S.; Harrison, D. J.; Kynaston, W., *Spectrochim. Acta A* **1971,** *27*, 2199-2217.
25. Shamovsky, I. L.; Riopelle, R. J.; Ross, G. M., *J. Phys. Chem. A* **2001,** *105*, 1061-1070.
26. Asatryan, R.; Davtyan, A.; Khachatryan, L.; Dellinger, B., *J. Phys. Chem. A* **2005,** *109*, 11198-11205.
27. Drew, M. G. B.; Hopkins, W. A.; Mitchell, P. C. H., *J. Chem. Soc., Faraday Trans.* **1990,** *86*, 47-52.
28. Benassi, R.; Folli, U.; Sbardellati, S.; Taddei, F., *J. Comput. Chem.* **1993,** *14*, 379-391.
29. Li, H.-M.; Zhao, S.-R.; Huo, Q.; Ma, T.; Liu, H.; Lee, J.; Hong, Y.-S.; Wu, C.-Z., *Arch. Pharmacal Res.* **2014**, 1-6.
30. de Mesquita, M. L.; Araújo, R. M.; Bezerra, D. P.; Filho, R. B.; de Paula, J. E.; Silveira, E. R.; Pessoa, C.; de Moraes, M. O.; Costa Lotufo, L. V.; Espindola, L. S., *Biorg. Med. Chem.* **2011,** *19*, 623-630.

31. Palacios-Hernández, T.; Höpfl, H.; Sánchez-Salas, J. L.; González-Vergara, E.; Pérez-Benítez, A.; Quiroz-Alfaro, M. A.; Méndez-Rojas, M. A., *J. Inorg. Biochem.* **2014,** *139*, 85-92.
32. Bayrakçeken, F.; Aktaş, S.; Toptan, M.; Ünlügedik, A., *Spectrochim. Acta A* **2003,** *59*, 135-138.
33. Goyal, R. N.; Sangal, A., *J. Electroanal. Chem.* **2005,** *578*, 185-192.
34. Lin, Y.-W.; Sun, M.-H.; Wan, D.; Liao, L.-F., *Spectrochim. Acta A* **2012,** *96*, 365-369.
35. Tao, Z.; Li, Z., *Int. J. Chem. Kinet.* **1999,** *31*, 65-72.
36. Field, R. J.; Raghavan, N. V.; Brummer, J. G., *J. Phys. Chem.* **1982,** *86*, 2443-2449.
37. Colthup, N. B.; Daly, L. H.; Wiberley, S. E., *Introduction to Infrared and Raman Spectroscopy*. 3rd ed.; Academic Press: San Diego, **1990**.
38. Kundu, S.; Miceli, E.; Farquhar, E.; Pfaff, F. F.; Kuhlmann, U.; Hildebrandt, P.; Braun, B.; Greco, C.; Ray, K., *J. Am. Chem. Soc.* **2012,** *134*, 14710-14713.
39. Kubas, G. J., *Inorg. Synth.* **1990,** *28*, 68-70.
40. Sheldrick, G. M., *Acta Crystallogr. Sect. A* **2008,** *64*, 112-122.
41. Schatz, M.; Leibold, M.; Foxon, S. P.; Weitzer, M.; Heinemann, F. W.; Hampel, F.; Walter, O.; Schindler, S., *Dalton Trans.* **2003**, 1480-1487.

Chapter 7

Showing the Similarity Between Cu^{II} μ-Oxo and Cu^{II} μ-Thiolate species by Catalytic Catechol Oxidation

A large library of Cu^{II} complexes with mononucleating and dinucleating ligands was synthesized to investigate their potential as catalysts for the catalytic oxidation of 3,5-di-tert-butylcatechol (3,5-DTBC). X-ray structure determination of a number of these complexes revealed relatively large Cu…Cu distances and the formation of polymeric species. Comparison of the 3,5-DTBC oxidation rates showed that the ligands that stabilize the biomimetic dinuclear Cu^{II} μ-thiolate complex also result in copper compounds that are much more active in the oxidation of 3,5-DTBC. The activity is inhibited by the presence of chloride ions. The highest turnover frequency that was observed was 7800 h^{-1}, which is one of the highest turnover frequencies for catechol oxidation in CH_3CN. These results demonstrate the similarities between the copper-thiolate and copper-oxygen chemistry.

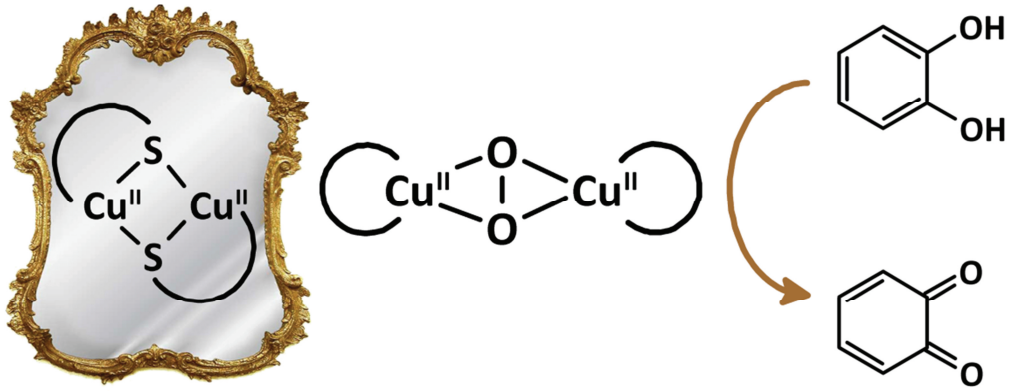

This chapter will be published as a full paper: E. C. M. Ording-Wenker, M. A. Siegler, M. Lutz, E. Bouwman, *submitted for publication*.

7.1 Introduction

The formation and redox properties of synthetic dinuclear Cu^{II} μ-thiolate complexes have been investigated because of their similarity to the Cu_A site (Section 1.3). It was found that small changes in the ligand structure can direct the reaction with copper salts towards the formation of either a Cu^{II} μ-thiolate or a Cu^{I} disulfide complex and that these species can inter-convert (Chapter 2).[1, 2] In Chapter 6 it is shown that this type of complexes exhibits redox chemistry with phenolates that is similar to that with thiolates, indicating that the oxygen chemistry might be very similar to the sulfur chemistry. This is also indicated by the fact that changes in the ligand structure similar to those that influence the Cu^{II} μ-thiolate/Cu^{I} disulfide equilibrium can induce a difference in coordination mode of dioxygen to copper.[3, 4] Additionally, the redox conversion of a Cu^{II}_2 μ-η^2:η^2-peroxide complex into a Cu^{III}_2 (μ-oxo)$_2$ species is reported.[5] To test whether copper-thiolate chemistry is similar to copper-oxygen chemistry the biomimetic catalytic oxidation of 3,5-di-*tert*-butylcatechol (3,5-DTBC) to 3,5-di-*tert*-butyl-*o*-benzoquinone (3,5-DTBQ) was investigated. The oxidation of catechol to quinone by catechol oxidase is thought to go *via* a Cu^{II}_2 μ-η^2:η^2-peroxide species (Section 1.2.3)[6-8] that shows similarities to the Cu^{II} μ-thiolate complex (Figure 7.1), although involvement of other types of Cu_2O_2 intermediates cannot be ruled out.[9] The oxidation of 3,5-DTBC is easy to monitor and is used as a common test reaction for new biomimetic copper complexes.[8] The structural and electronic similarity between the Cu^{II} μ-thiolate and Cu^{II}_2 μ-η^2:η^2-peroxide complex might lead to a more effective or more stabilizing reaction with O_2 by complexes of ligands that promote Cu^{II} μ-thiolate formation. Although it must be noted that if a Cu^{II} μ-thiolate species would form, it might be oxygenated by dioxygen (Chapter 4).[10]

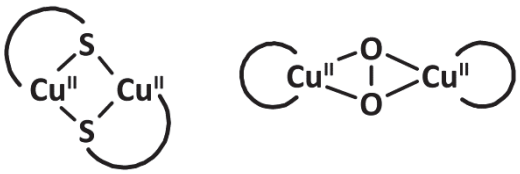

Figure 7.1: Schematic representation of a Cu^{II} μ-thiolate species and a side-on Cu^{II}_2 μ-η^2:η^2-peroxide species showing their similarity.

In this chapter the synthesis of a series of Cu^{II} complexes with mononucleating and dinucleating ligands is described. To have a complete picture of the effect of small ligand changes on the catechol oxidation activity, a large library of ligands was

rationally selected for this study (Figure 7.2). X-ray crystal structures were obtained for a number of the copper complexes and some of these will be discussed.

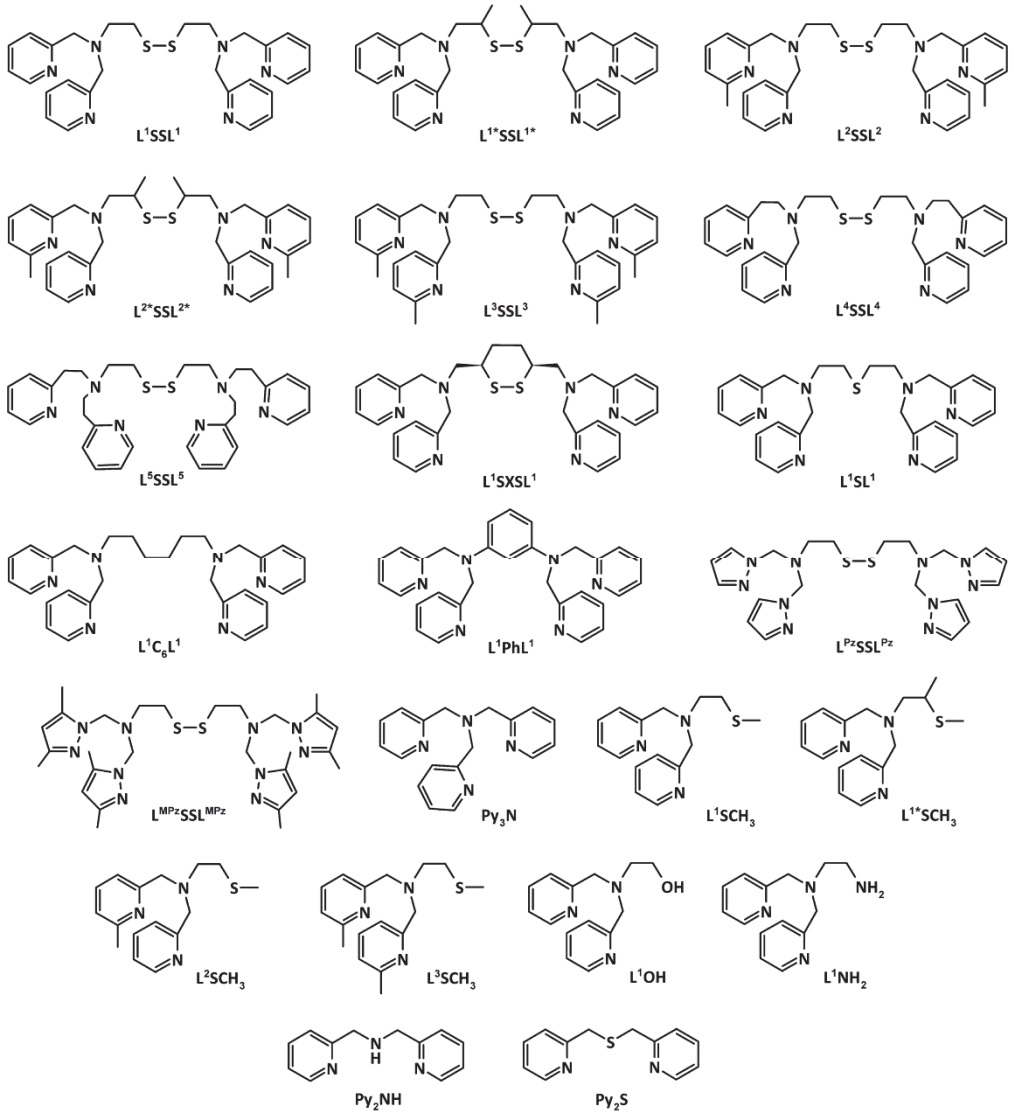

Figure 7.2: Schematic overview of the ligands that were synthesized for the study of the copper-catalyzed oxidation of catechol.

7.2 Results

7.2.1 Ligand and Complex Synthesis

Most of the ligands shown in Figure 7.2 were synthesized according to literature procedures (Chapter 2, 5 and 6)[1, 2, 11-16] or are commercially available. As the ligands are similar to each other, they were systematically named by their structure. For example **L**^{1} stands for the fragment *N*,*N*-bis(2-pyridylmethyl)aminoethyl and **Py** for 2-pyridylmethyl. Four new ligands were synthesized: **L**^{1}**SL**^{1}, **L**^{1}***SCH**$_3$, **L**^{2}**SCH**$_3$ and **L**^{3}**SCH**$_3$. **L**^{1}**SL**^{1} was synthesized by reductive amination of 1,5-diamino-3-thiapentane dihydrobromide, which was made via a 4-step literature procedure.[17] The complete synthesis scheme is depicted in Figure 7.3. Ligand **L**^{1}**SL**^{1} was obtained in 68% yield as a brown oil that turns darker over time. The ligand is not stable and slowly degrades over weeks even when kept under argon at 0 °C. When **L**^{1}**SL**^{1} is coordinated to copper, the complex does not degrade over time.

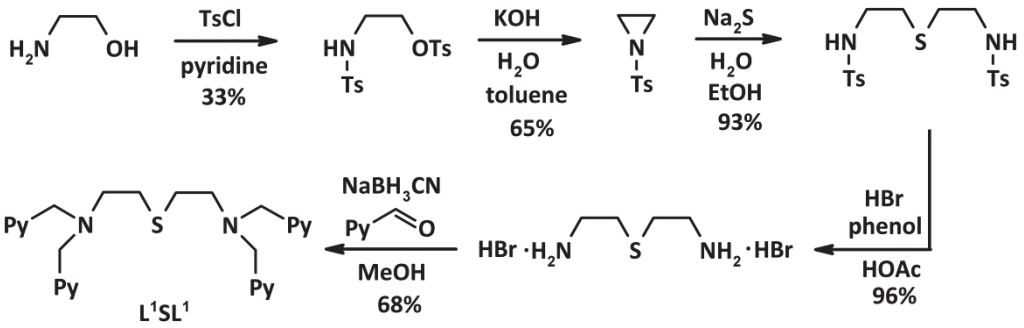

Figure 7.3: Synthesis scheme for **L**^{1}**SL**^{1}.[17] Abbreviations: Ts = 4-toluenesulfonyl; Ac = acetyl; Py = 2-pyridyl.

L^{1}***SCH**$_3$ was synthesized by reaction of propylene sulfide with di-(2-pyridylmethyl)amine in acetonitrile. After solvent evaporation, tetrahydrofuran and NaH were added to deprotonate the thiol. Addition of CH_3I yields **L**^{1}***SCH**$_3$, which was purified by column chromatography, resulting in 86% yield. **L**^{2}**SCH**$_3$ and **L**^{3}**SCH**$_3$ were obtained in relatively moderate yields of 50% and 46% by a two-step reductive amination using $NaBH_4$. The synthesis scheme for **L**^{1}***SCH**$_3$, **L**^{2}**SCH**$_3$ and **L**^{3}**SCH**$_3$ is shown in Figure 7.4. Like **L**^{1}**SL**^{1}, all three ligands degrade over time as indicated by darkening of the oil. The ligand **Py**$_2$**S** has been reported,[18] but its synthesis has not been described elaborately, which is why it is described in Section 7.5.3. **L**^{1}**OH** has also been reported,[19] but a slightly different method has been developed giving an almost quantitative yield of 99%.

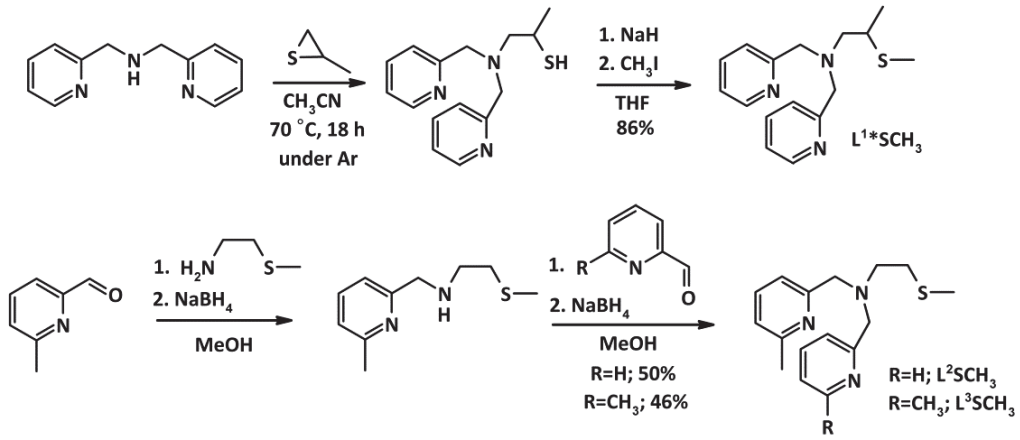

Figure 7.4: Synthesis scheme for $\mathbf{L^1{*}SCH_3}$, $\mathbf{L^2SCH_3}$ and $\mathbf{L^3SCH_3}$. Abbreviation THF = tetrahydrofuran.

With the 22 ligands that were either bought or synthesized, Cu^{II} complexes were formed with one Cl^- and one BF_4^- counterion per copper center. The general synthesis of these complexes entails the addition of a 1:1 mixture of $[Cu^{II}(H_2O)_6](BF_4)_2$ and $Cu^{II}Cl_2 \cdot 2\ H_2O$ to the ligand dissolved in methanol, or in the case of $\mathbf{L^2SSL^2}$ and $\mathbf{L^1NH_2}$ in CH_3CN. If the complex did not precipitate spontaneously, precipitation was induced by addition of diethyl ether. Copper compounds of ligands that can potentially form dinuclear complexes are more likely to form polymeric structures (see Section 7.2.2 and Chapter 5) and are tentatively given the formula: $[Cu^{II}_2(ligand)(Cl)_2]_n(BF_2)_n$. The complexes of ligands that are expected to form mononuclear compounds are indicated with the formula $[Cu^{II}(ligand)(Cl)](BF_4)$.

A copper complex with $\mathbf{L^5SSL^5}$ could not be isolated as a solid; all attempts resulted in the formation of oil. For the catalytic experiments (Section 7.2.3), this complex was formed in situ. In the synthesis of a complex with $\mathbf{L^2SSL^2}$, $[Cu^{II}(H_2O)_6](ClO_4)_2$ was used instead of $[Cu^{II}(H_2O)_6](BF_4)_2$ to grow single crystals suitable for X-ray structure diffraction. However, the complex $[Cu^{II}_2(\mathbf{L^2SSL^2})(Cl)_2]_n(BF_4)_{2n}$ was also synthesized, so that all catalysts used for catechol oxidation have the same counterions.

With the ligand $\mathbf{L^1{*}SCH_3}$ two complexes were formed: $[Cu^{II}(\mathbf{L^1{*}SCH_3})(Cl)]_2(CuCl_4)$ and $[Cu^{II}(\mathbf{L^1{*}SCH_3})(Cl)](BF_4)$. The first compound was obtained by addition of 1 equiv of $Cu^{II}Cl_2 \cdot 2\ H_2O$ to $\mathbf{L^1{*}SCH_3}$, the latter from 0.5 equiv of $Cu^{II}Cl_2 \cdot 2\ H_2O$ and 0.5 equiv. of $[Cu^{II}(H_2O)_6](BF_4)_2$. The X-ray crystal structures were determined of both complexes and the structures of their cationic copper complex were found to be very

similar. Appendix VI contains the crystallographic information for both these structures.

The UV-vis spectra of all the Cu^{II} complexes are highly similar, showing LMCT bands of $Cu^{II} \leftarrow S$ and $Cu^{II} \leftarrow Cl$ in the region between 200 and 400 nm and one or two bands in the range of 650 to 940 nm that can be ascribed to Cu^{II} d-d transitions (Appendix VI, Figure AVI.3).

7.2.2 Description of X-ray Crystal Structures

Single crystals could be obtained for several of the synthesized Cu^{II} complexes. This led to the X-ray crystal structure determination of the polymeric complexes $[Cu^{II}_2(\mathbf{L^1SSL^1})(Cl)_2]_n(BF_4)_{2n}$, $[Cu^{II}_2(\mathbf{L^2SSL^2})(Cl)_2]_n(ClO_4)_{2n}$, $[Cu^{II}_2(\mathbf{L^1SL^1})(Cl)_2]_n(BF_4)_{2n}$ and $[Cu^{II}_2(\mathbf{L^1C_6L^1})(Cl)_2]_n(BF_4)_{2n}$ and of the compounds of mononucleating ligands, namely $[Cu^{II}(\mathbf{L^1{*}SCH_3})(Cl)](BF_4)$, $[Cu^{II}(\mathbf{L^1{*}SCH_3})(Cl)]_2(CuCl_4)$, $[Cu^{II}(\mathbf{L^2SCH_3})(Cl)](BF_4)$, $[Cu^{II}(\mathbf{L^3SCH_3})(Cl)](BF_4)$ and $[Cu^{II}(\mathbf{L^1NH_2})(Cl)](BF_4)$. The copper ions in the polymeric structures $[Cu^{II}_2(\mathbf{L^1SSL^1})(Cl)_2]_n(BF_4)_{2n}$, $[Cu^{II}_2(\mathbf{L^2SSL^2})(Cl)_2]_n(ClO_4)_{2n}$ and $[Cu^{II}_2(\mathbf{L^1SL^1})(Cl)_2]_n(BF_4)_{2n}$ have very similar coordination geometries; $[Cu^{II}_2(\mathbf{L^1SSL^1})(Cl)_2]_n(BF_4)_{2n}$ and $[Cu^{II}_2(\mathbf{L^2SSL^2})(Cl)_2]_n(ClO_4)_{2n}$ will not be discussed, but crystallographic data and selected bond distances and angles can be found in Appendix VI. Similarly the structures of $[Cu^{II}(\mathbf{L^1{*}SCH_3})(Cl)](BF_4)$ and $[Cu^{II}(\mathbf{L^1{*}SCH_3})(Cl)]_2(CuCl_4)$ are comparable to that of $[Cu^{II}(\mathbf{L^2SCH_3})(Cl)](BF_4)$ and information concerning these structures can be found in Appendix VI.

Thus, the structures of $[Cu^{II}_2(\mathbf{L^1SL^1})(Cl)_2]_n(BF_4)_{2n}$, $[Cu^{II}_2(\mathbf{L^1C_6L^1})(Cl)_2]_n(BF_4)_{2n}$, $[Cu^{II}(\mathbf{L^2SCH_3})(Cl)](BF_4)$, $[Cu^{II}(\mathbf{L^3SCH_3})(Cl)](BF_4)$ and $[Cu^{II}(\mathbf{L^1NH_2})(Cl)](BF_4)$ are described. The crystallographic and structure refinement data for these complexes are collected in Table 7.1.

Single crystals of $[Cu^{II}_2(\mathbf{L^1SL^1})(Cl)_2]_n(BF_4)_{2n}$ were obtained by slow evaporation of diethyl ether into a solution of the complex in acetonitrile. A displacement ellipsoid plot of $[Cu^{II}_2(\mathbf{L^1SL^1})(Cl)_2]_n(BF_4)_{2n}$ is shown in Figure 7.5 and selected bond distances and angles are provided in Table 7.2. $[Cu^{II}_2(\mathbf{L^1SL^1})(Cl)_2]_n(BF_4)_{2n}$ crystallizes in the monoclinic space group *C*2/*c*, with half a dinuclear compound and one BF_4^- ion in the asymmetric unit. The structure is very disordered. Both the Cu complex and the BF_4^- counterions are found to be disordered over two orientations. The major and minor components of the Cu complex are related by a pseudo-mirror plane, and the occupancy factor of the major component of the disorder refines to 0.840(3). Both counterions are found at sites of twofold axial symmetry, and are constrained to be disordered with an occupancy factor of 0.5.

Table 7.1: Crystallographic and structure refinement data for complex $[Cu^{II}_2(\mathbf{L^1SL^1})(Cl)_2]_n(BF_4)_{2n}$, $[Cu^{II}_2(\mathbf{L^1C_6L^1})(Cl)_2]_n(BF_4)_{2n}$, $[Cu^{II}(\mathbf{L^2SCH_3})(Cl)](BF_4)$, $[Cu^{II}(\mathbf{L^3SCH_3})(Cl)](BF_4)$ and $[Cu^{II}(\mathbf{L^1NH_2})(Cl)](BF_4)$.

	$[Cu^{II}_2(\mathbf{L^1SL^1})(Cl)_2]_n(BF_4)_{2n}$	$[Cu^{II}_2(\mathbf{L^1C_6L^1})(Cl)_2]_n(BF_4)_{2n}$	$[Cu^{II}(\mathbf{L^2SCH_3})(Cl)](BF_4)$	$[Cu^{II}(\mathbf{L^3SCH_3})(Cl)](BF_4)$	$[Cu^{II}(\mathbf{L^1NH_2})(Cl)](BF_4)$
empirical formula	$[C_{28}H_{32}Cl_2Cu_2N_6S](BF_4)_2$	$[C_{30}H_{36}Cl_2Cu_2N_6](BF_4)_2 \cdot 4\ CH_3CN$	$[C_{16}H_{21}ClCuN_3S](BF_4)$	$[C_{17}H_{23}ClCuN_3S](BF_4)$	$[C_{14}H_{18}ClCuN_4](BF_4)$
formula weight	856.25	1016.46	473.22	487.24	428.12
crystal system	monoclinic	monoclinic	monoclinic	monoclinic	monoclinic
space group	$C2/c$	$C2/m$	$C2/m$	$P2_1/c$	$P2_1/n$
a, Å	10.0603(8)	13.287(2)	13.0671(3)	9.11412(10)	8.92176(15)
b, Å	23.2653(15)	27.558(5)	20.2293(5)	15.17627(13)	12.8949(3)
c, Å	14.5686(9)	6.9232(17)	7.40187(15)	15.31060(15)	14.9606(3)
β, deg	100.321(7)	111.421(13)	101.660(2)	102.6105(10)	102.0565(19)
V, Å^3	3354.7(4)	2359.9(8)	1916.22(8)	2066.65(4)	1683.18(6)
Z	4	2	4	4	4
D_{calc}, g·cm^3	1.695	1.430	1.640	1.566	1.689
T, Kelvin	110(2)	150(2)	110(2)	110(2)	110(2)
crystal size, mm	$0.43 \times 0.14 \times 0.08$	$0.30 \times 0.30 \times 0.30$	$0.35 \times 0.28 \times 0.20$	$0.40 \times 0.32 \times 0.22$	$0.50 \times 0.36 \times 0.14$
μ, mm^{-1}	1.566	1.085	4.318	4.021	1.502
no. of reflns measd	9412	9970	6657	14162	13962
no. of unique reflns	2953	1904	1913	4035	3879
no. of reflns obsd.	2550 [$I > 2\sigma(I)$]	1601 [$I > 2\sigma(I)$]	1791 [$I > 2\sigma(I)$]	3893 [$I > 2\sigma(I)$]	3414 [$I > 2\sigma(I)$]
no. of parameters	444	172	246	303	234
R_1 / wR_2 [$I > 2\sigma(I)$]	0.0538/0.1394	0.0780/0.2007	0.0327/0.0861	0.0240/0.0635	0.0257/0.0675
R_1 / wR_2 [all refl.]	0.0621/0.1452	0.0942/0.2123	0.0346/0.0879	0.0250/0.0641	0.0305/0.0693
goodness of fit	1.029	1.151	1.046	1.054	1.080
$\Delta\rho$, e·Å^{-3}	−0.57/0.81	-1.22/1.04	−0.24/0.45	−0.30/0.39	−0.48/0.31

Table 7.2: Selected bond distances (Å) and bond angles (°) for complexes $[Cu^{II}_2(\mathbf{L^1SL^1})(Cl)_2]_n(BF_4)_{2n}$ and $[Cu^{II}_2(\mathbf{L^1C_6L^1})(Cl)_2]_n(BF_4)_{2n}$.

	$[Cu^{II}_2(\mathbf{L^1SL^1})(Cl)_2]_n(BF_4)_{2n}$	$[Cu^{II}_2(\mathbf{L^1C_6L^1})(Cl)_2]_n(BF_4)_{2n}$
Cu1 - Cu1*	3.6986(7)	3.405(2)
Cu1 - Cu1#	5.0511(7)	12.013(3)
Cu1 - S1	2.6825(7)	
Cu1 - N1	2.057(4)	2.026(9)
Cu1 - N11	2.004(4)	1.987(6)
Cu1 - N21/N11'	1.987(4)	1.987(6)
Cu1 - Cl1	2.278(2)	2.223(3)
Cu1 - Cl1*	2.879(2)	2.865(4)
S1 - Cu1 - N1	84.72(12)	
S1 - Cu1 - N11	83.29(11)	
S1 - Cu1 - N21	100.27(11)	
S1 - Cu1 - Cl1*	166.13(5)	
N1 - Cu1 - N11	82.77(18)	82.88(18)
N1 - Cu1 - N21/N11'	80.87(17)	82.88(18)
N1 - Cu1 - Cl1	177.93(13)	173.7(3)
N11 - Cu1 - N21/N11'	162.84(18)	165.5(4)

Symmetry operation * = [1–x, –y, –z] and # = [1–x, y, ½–z] for $[Cu^{II}_2(\mathbf{L^1SL^1})(Cl)_2]_n(BF_4)_{2n}$; Symmetry operation * = [1–x, y, 1–z]; # = [–x, y, –1–z]; ' = [x, –y, z] for $[Cu^{II}_2(\mathbf{L^1C_6L^1})(Cl)_2]_n(BF_4)_{2n}$.

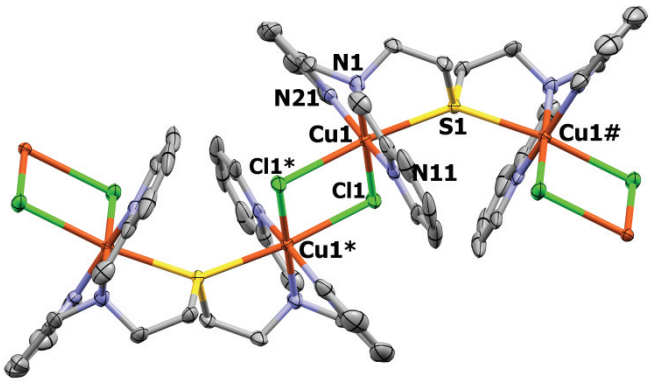

Figure 7.5: Displacement ellipsoid plot (50% probability level) of two of the repeating units in the cationic polymer chain of $[Cu^{II}_2(\mathbf{L^1SL^1})(Cl)_2]_n(BF_4)_{2n}$. The disorder, the non-coordinating counterions and hydrogen atoms are omitted for clarity. Symmetry operation * = [1–x, –y, –z] and # = [1–x, y, ½–z].

The thioether sulfur atom of the dinucleating ligand bridges between the two copper ions, resulting in a distorted octahedral N_3SCl_2 coordination environment for both copper ions. The elongated Jahn-Teller axis is occupied by S1 and Cl1* (Cu1-S1

2.6825(7) Å; Cu1-Cl1* 2.879(2) Å). The chloride ions are bridging between copper ions of neighboring dinuclear complexes resulting in infinite 1D zig-zag chains. The distance between the copper ions in the Cu(μ-Cl)$_2$Cu core is 3.6986(7) Å. This distance is slightly larger than the Cu…Cu distances in [Cu$^{II}_2$(**L^{1}SSL^1**)(Cl)$_2$]$_n$(BF$_4$)$_{2n}$ and [Cu$^{II}_2$(**L^{2}SSL^2**)(Cl)$_2$]$_n$(BF$_4$)$_{2n}$, which are ca. 3.60 Å (average) and 3.6455(4) Å, respectively (Appendix VI, Table AVI.2).

[Cu$^{II}_2$(**L^{1}C$_6$L^1**)(Cl)$_2$]$_n$(BF$_4$)$_{2n}$ · 4 CH$_3$CN crystallized from acetonitrile and di-isopropyl ether. The metal and chloride ions and the 1,6-diaminohexane backbone are lying in a mirror plane and in addition the molecule contains two-fold rotational symmetry; the BF$_4^-$ anion is disordered on a twofold axis, and the acetonitrile molecule is located on a general position. The asymmetric unit consequently contains ¼ of the ligand, half a copper center, half a Cl$^-$ ion, half a BF$_4^-$ ion and one CH$_3$CN molecule. A displacement ellipsoid plot is shown in Figure 7.6a. Selected bond distances and angles can be found in Table 7.2. The copper ions in [Cu$^{II}_2$(**L^{1}C$_6$L^1**)(Cl)$_2$]$_n$(BF$_4$)$_{2n}$ are in an N$_3$Cl$_2$ coordination environment, in a distorted square-pyramidal geometry that resembles that of the copper ions in [Cu$^{II}_2$(**L^{1}SL^1**)(Cl)$_2$]$_n$(BF$_4$)$_{2n}$, except for the coordination of a sulfur atom. The chloride ions are bridging between copper ions of neighboring dinuclear complexes resulting in infinite linear 1D chains. The Cu1-Cu1* distance in the Cu(μ-Cl)$_2$Cu core is 3.405(2) Å, which is significantly smaller than in sulfur-containing complexes such as [Cu$^{II}_2$(**L^{1}SL^1**)(Cl)$_2$]$_n$(BF$_4$)$_{2n}$. The structure of the related dinuclear complex [Cu$^{II}_2$(**L^{1}C$_6$L^1**)(Cl)$_4$], which does not form polymeric structures, was recently reported;[20] the copper ions in the two structures have very similar coordination geometries (Figure 7.6b).

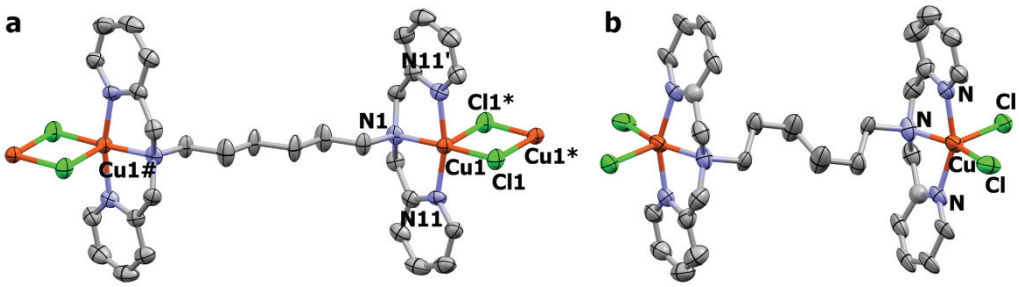

Figure 7.6: Displacement ellipsoid plots (50% probability level) of (a) the cationic part of [Cu$^{II}_2$(**L^{1}C$_6$L^1**)(Cl)$_2$]$_n$(BF$_4$)$_{2n}$ and (b) [Cu$^{II}_2$(**L^{1}C$_6$L^1**)(Cl)$_4$].[20] Non-coordinating counterions and hydrogen atoms are omitted for clarity. Symmetry operation * = [1–x, y, 1–z]; # = [–x, y, –1–z]; ' = [x, –y, z].

The major difference between the structures is that the hexamethylene bridge in $[Cu^{II}_2(\mathbf{L^1C_6L^1})(Cl)_4]$ has a crystallographic C_{2h} symmetry and forms an 'alternating' chain whereas in $[Cu^{II}_2(\mathbf{L^1C_6L^1})(Cl)_2]_n(BF_4)_{2n}$ it forms a linear chain, which is the expected, thermodynamically favored conformation.

The three compounds $[Cu^{II}(\mathbf{L^2SCH_3})(Cl)](BF_4)$, $[Cu^{II}(\mathbf{L^3SCH_3})(Cl)](BF_4)$ and $[Cu^{II}(\mathbf{L^1NH_2})(Cl)](BF_4)$ all crystallized in structures with one mononuclear complex and one BF_4^- counterion in the asymmetric unit. Displacement ellipsoid plots and selected bond distances and angles are given in Figure 7.7 and Table 7.3.

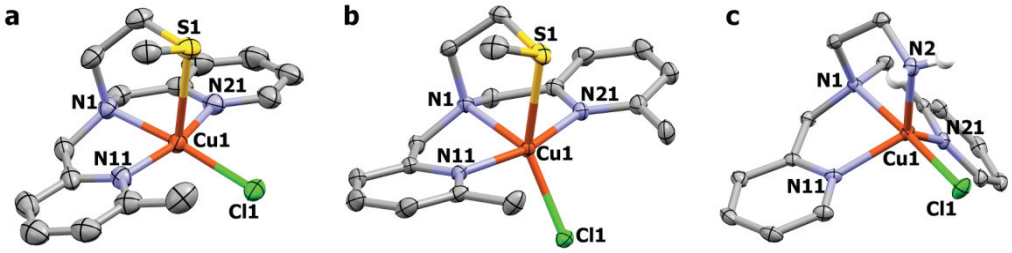

Figure 7.7: Displacement ellipsoid plots (50% probability level) of the cationic parts of (a) $[Cu^{II}(\mathbf{L^2SCH_3})(Cl)](BF_4)$, (b) $[Cu^{II}(\mathbf{L^3SCH_3})(Cl)](BF_4)$ and (c) $[Cu^{II}(\mathbf{L^1NH_2})(Cl)](BF_4)$. The disorder, the non-coordinating counterions and most of the hydrogen atoms are omitted for clarity.

$[Cu^{II}(\mathbf{L^2SCH_3})(Cl)](BF_4)$ crystallizes in the monoclinic space group *C*2/*m*. The copper complex and the BF_4^- counterion are found at sites of mirror and twofold rotation symmetry, respectively. As the complex cation has no mirror symmetry, it is disordered over two orientations with equal occupancy factors (*i.e.*, 0.5 for each component). The BF_4^- counterion is also found to be disordered over two orientations with equal occupancy factors. The copper ion has square-pyramidal geometry (τ = 0.12),[21] but forms a dimer via bridging chloride ions with another cationic subunit, thus creating an octahedral environment with Cl1* and S1 on the elongated Jahn-Teller axis (Cu1-S1 2.7260(9) Å; Cu1-Cl1* 2.9837(9) Å). The Cu1-Cu1* distance of 3.8504(5) Å is larger than in the polymeric species discussed above. Such formation of dimeric structures is also observed for $[Cu^{II}(\mathbf{L^1SCH_3})(Cl)](BF_4)$ (Chapter 6) and $[Cu^{II}(\mathbf{L^{1*}SCH_3})(Cl)](BF_4)$ (Appendix VI, Figure AVI.2).

The compounds $[Cu^{II}(\mathbf{L^3SCH_3})(Cl)](BF_4)$ and $[Cu^{II}(\mathbf{L^1NH_2})(Cl)](BF_4)$ crystallize in monoclinic space groups $P2_1/c$ and $P2_1/n$, respectively. These complexes do not form dimeric species, as their coordination geometry is more distorted towards trigonal bipyramidal with τ parameters of 0.39 and 0.84, respectively.

Table 7.3: Selected bond distances (Å) and bond angles (°) for complexes $[Cu^{II}(\mathbf{L^2SCH_3})(Cl)](BF_4)$, $[Cu^{II}(\mathbf{L^3SCH_3})(Cl)](BF_4)$ and $[Cu^{II}(\mathbf{L^1NH_2})(Cl)](BF_4)$.

	$[Cu^{II}(\mathbf{L^2SCH_3})(Cl)](BF_4)$	$[Cu^{II}(\mathbf{L^3SCH_3})(Cl)](BF_4)$	$[Cu^{II}(\mathbf{L^1NH_2})(Cl)](BF_4)$
Cu1 - Cu1*	3.8504(5)		
Cu1 - S1/N2	2.7260(9)	2.5817(4)	2.0593(15)
Cu1 - N1	2.048(3)	2.0876(12)	2.0439(12)
Cu1 - N11	2.046(5)	1.9914(12)	2.1158(13)
Cu1 - N21	2.002(5)	1.9935(13)	2.0410(13)
Cu1 - Cl1	2.2586(8)	2.2674(4)	2.2381(4)
Cu1 - Cl1*	2.9837(9)		
S1/N2 - Cu1 - N1	86.62(8)	85.75(3)	84.73(5)
S1/N2 - Cu1 - N11	94.7(2)	93.86(4)	109.75(6)
S1/N2 - Cu1 - N21	89.2(2)	82.92(4)	127.21(6)
S1/N2 - Cu1 - Cl1	102.38(3)	141.526(16)	96.44(4)
N1 - Cu1 - N11	80.6(3)	82.13(5)	80.25(5)
N1 - Cu1 - N21	83.4(3)	83.00(5)	81.87(5)
N1 - Cu1 - Cl1	170.52(12)	132.50(4)	177.49(4)
N11 - Cu1 - N21	163.28(15)	164.98(5)	117.72(5)
N11 - Cu1 - Cl1	101.3(2)	95.44(4)	97.26(4)
N21 - Cu1 - Cl1	93.7(2)	96.15(4)	99.12(4)

Symmetry operation * = [x, y, –1+z]

A structure similar to $[Cu^{II}(\mathbf{L^1NH_2})(Cl)](BF_4)$ has been reported in the literature with ClO_4^- instead of BF_4^- as the non-coordinating counterion; the copper ions in the two structures have the same trigonal-bipyramidal coordination geometry with the Cl^- ion and the tertiary nitrogen atom occupying the axial coordination sites.[22] In $[Cu^{II}(\mathbf{L^3SCH_3})(Cl)](BF_4)$ the axial positions are occupied by the pyridyl nitrogens.

7.2.3 Catechol oxidation

The synthesized complexes were tested for their catalytic activity in the oxidation of 3,5-DTBC to 3,5-DTBQ. The rate of oxidation was determined by monitoring the absorbance of 3,5-DTBQ at 400 nm. All catalytic experiments were conducted at 25 °C whilst stirring and bubbling a mixture of N_2 and O_2 (1:1) through the solution. A copper concentration of 0.4 mM, corresponding with 0.4 mM of a mononuclear complex or 0.2 mM of a dinuclear complex, was used together with 20 mM 3,5-DTBC. Upon addition of 20 mM NEt_3 the conversion of 3,5-DTBC started. The results of the catalytic experiments are collected in Table 7.4. Three different types of conversion curves were observed (A, B and C; Figure 7.8). Depending on the type of catalyst the oxidation rate was constant, increasing, or decreasing over time. For this reason both the maximum turnover frequencies (TOFs) and initial TOFs are reported in Table 7.4.

After addition of NEt_3, an abrupt increase in the absorption at 400 nm was observed for all copper complexes with one Cl^- and one BF_4^- counterion (Figure 7.8). The height of this 'jump' was dependent on the catalyst used and appeared to be related to the presence of chloride ions (see below). The initial TOF was determined by taking the tangent of the curve of the first two seconds after the 'jump' in the absorption curve. Blank reactions were performed in the presence and absence of copper (entry 1-2, Table 7.4). The blank reaction with copper was performed using a 1:1 mixture in acetonitrile of $[Cu^{II}(H_2O)_6](BF_4)_2$ and $CuCl_2 \cdot 2\ H_2O$ from which most of the H_2O content was removed by addition of Na_2SO_4. The catalytic activity of the copper complexes with mononucleating ligands is not much higher than for the system containing just the copper salts (entry 2 and 16-24, Table 7.4).

Table 7.4: Turnover frequencies of the oxidation of 3,5-DTBC to 3,5-DTBQ catalyzed by copper complexes with different ligands.[a]

	Ligand	Catalyst	Graph type[c]	max TOF (h^{-1})[d]	initial TOF (h^{-1})
1	-	no catalyst	C	170	15
2	-	$[Cu^{II}(Cl)](BF_4)$[b]	C	450	180
3	**L^1SSL^1**	$[Cu^{II}_2(ligand)(Cl)_2]_n(BF_4)_{2n}$	A	-	2150
4	**L^1*SSL^1***	$[Cu^{II}_2(ligand)(Cl)_2]_n(BF_4)_{2n}$	A	-	4700
5	**L^2SSL^2**	$[Cu^{II}_2(ligand)(Cl)_2]_n(BF_4)_{2n}$	A	-	570
6	**L^2*SSL^2***	$[Cu^{II}_2(ligand)(Cl)_2]_n(BF_4)_{2n}$	A	-	1750
7	**L^3SSL^3**	$[Cu^{II}_2(ligand)(Cl)_2]_n(BF_4)_{2n}$	C	240	190
8	**L^4SSL^4**	$[Cu^{II}_2(ligand)(Cl)_2]_n(BF_4)_{2n}$	A	-	3200
9	**L^5SSL^5**	$[Cu^{II}_2(ligand)(Cl)_2]_n(BF_4)_{2n}$[b]	C	310	120
10	**L^1SXSL^1**	$[Cu^{II}_2(ligand)(Cl)_2]_n(BF_4)_{2n}$	C	430	330
11	**L^1SL^1**	$[Cu^{II}_2(ligand)(Cl)_2]_n(BF_4)_{2n}$	A	-	1800
12	**$L^1C_6L^1$**	$[Cu^{II}_2(ligand)(Cl)_2]_n(BF_4)_{2n}$	A	-	530
13	**L^1PhL^1**	$[Cu^{II}_2(ligand)(Cl)_2]_n(BF_4)_{2n}$	C	580	190
14	**$L^{Pz}SSL^{Pz}$**	$[Cu^{II}_2(ligand)(Cl)_2]_n(BF_4)_{2n}$	C	390	240
15	**$L^{MPz}SSL^{MPz}$**	$[Cu^{II}_2(ligand)(Cl)_2]_n(BF_4)_{2n}$	C	390	170
16	**Py_3N**	$[Cu^{II}(ligand)(Cl)](BF_4)$	A	-	600
17	**L^1SCH_3**	$[Cu^{II}(ligand)(Cl)](BF_4)$	A	-	760
18	**L^1*SCH_3**	$[Cu^{II}(ligand)(Cl)](BF_4)$	C	480	370
19	**L^2SCH_3**	$[Cu^{II}(ligand)(Cl)](BF_4)$	C	330	150
20	**L^3SCH_3**	$[Cu^{II}(ligand)(Cl)](BF_4)$	C	220	110
21	**L^1OH**	$[Cu^{II}(ligand)(Cl)](BF_4)$	B	-	430
22	**L^1NH_2**	$[Cu^{II}(ligand)(Cl)](BF_4)$	B	-	340
23	**Py_2NH**	$[Cu^{II}(ligand)(Cl)](BF_4)$	A	-	440
24	**Py_2S**	$[Cu^{II}(ligand)(Cl)](BF_4)$	C	390	160

[a] Reaction conditions: 0.4 mM [Cu], 20 mM 3,5-DTBC, 20 mM NEt_3 in 3 mL CH_3CN. TOFs were determined from the change in absorbance of 3,5-DTBQ at 400 nm.

[b] Complex was formed in situ.

[c] The three different types of graphs A, B and C are depicted in Figure 7.8.

[d] Only given when maximum TOF is higher than initial TOF (graph type C).

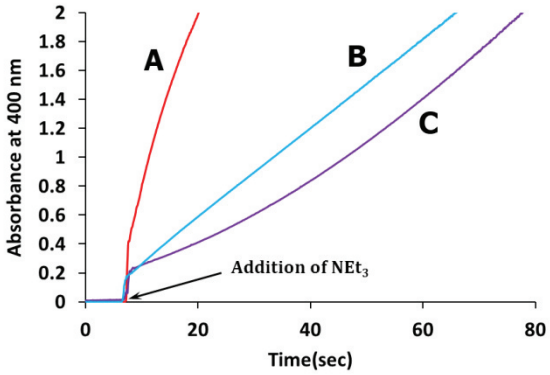

Figure 7.8: Development in time of the absorption at 400 nm due to 3,5-DTBQ formation, catalyzed by $[Cu^{II}_2(\mathbf{L^1SSL^1})(Cl)_2](BF_4)_2$ (red, type A), $[Cu^{II}(\mathbf{L^1OH})(Cl)](BF_4)$ (blue, type B) and $[Cu^{II}_2(\mathbf{L^{Pz}SSL^{Pz}})(Cl)_2](BF_4)_2$ (purple, type C).

In contrast, a number of the dinucleating ligands result in catalytic systems with significantly higher activity, which we will further elaborate on.

The catalytic system comprising the ligand $\mathbf{L^1SSL^1}$ shows reasonably high activity (entry 3), but introduction of methyl groups at the *ortho*-position of the pyridyl rings results in a considerable decrease of the catalytic activity (entry 3, 5 and 7). Addition of a methyl group next to the sulfur in the disulfide bond, however, results in significantly higher activity (entry 3-4, 5-6). Changing the bridge between the tertiary amine and the pyridyl groups from a methylene to an ethylene spacer at two positions leads to an increase in activity (entry 3 vs 8), but at four positions it leads to a dramatic decrease in activity (entry 3 vs 9). The use of pyridyl-containing ligands containing a disulfide bond generally results in higher TOFs, but the high catalytic activity of the system comprising $\mathbf{L^1SL^1}$ indicates that the presence of a thioether instead of a disulfide group can give similar performance (entry 3 vs 11). The presence of an S-donor atom in the ligand does have a positive effect on the catalytic activity of the system, considering that a similar complex with an alkane bridge ($\mathbf{L^1C_6L^1}$) shows a significantly lower TOF (entry 3 vs 12). The complex with ligand $\mathbf{L^1SXSL^1}$ has considerably lower activity than the compound with $\mathbf{L^{1*}SSL^{1*}}$, while these systems only differ in the rigidity of the ligand (entry 4 vs 10). Such rigidity might also be a factor in the low activity of the complex with $\mathbf{L^1PhL^1}$ (entry 13). The presence of pyrazole moieties instead of pyridyl groups stabilizes the Cu^I oxidation state (Chapter 5), which is reflected in the negative effect on the catalytic activity (entry 14-15).

Table 7.5: Turnover frequencies of the oxidation of 3,5-DTBC to 3,5-DTBQ catalyzed by $[Cu^{II}_2(\mathbf{L^{Pz}SSL^{Pz}})]^{4+}$ in the presence of different chloride concentrations.[a]

Catalyst	Graph type[c]	max. TOF (h^{-1})	initial TOF (h^{-1})	Cl^- conc (mM)
$[Cu^{II}_2(\mathbf{L^{Pz}SSL^{Pz}})](BF_4)_4$[b]	C	550	220	0
$[Cu^{II}_2(\mathbf{L^{Pz}SSL^{Pz}})(Cl)_2](BF_4)_2$	C	390	240	0.4
$Cu^{II}_2(\mathbf{L^{Pz}SSL^{Pz}})Cl_4$[b]	C	360	140	0.8
$[Cu^{II}_2(\mathbf{L^{Pz}SSL^{Pz}})(Cl)_2](BF_4)_2$ + Bu_4NCl	C	230	100	20

[a] Reaction conditions: 0.4 mM [Cu], 20 mM 3,5-DTBC, 20 mM NEt_3 in 3 mL CH_3CN. TOFs were determined from the change in absorbance of 3,5-DTBQ at 400 nm.
[b] Complex was formed in situ
[c] The three different types of graphs A, B and C are depicted in Figure 7.8.

The catalytic activity decreases with increasing concentration of chloride ions, as can be seen in Table 7.5. The absorption spectra for $[Cu^{II}_2(\mathbf{L^{Pz}SSL^{Pz}})]^{4+}$ with 1-5 equivalents of chloride ions (in ratio to the dinuclear complex) have been recorded. The spectroscopic changes that are observed upon addition of 1-4 equivalents of chloride ions indicate coordination of the chloride ions to the copper center. During catalysis, the coordinated chloride ions will hamper binding of the substrate or activation of dioxygen. Addition of a fifth equivalent of Cl^- results in formation of an absorption band at 460 nm, which can be attributed to the formation of the complex anion $CuCl_4^{2-}$ (Appendix VI, Figure AVI.5).[23-25] As mentioned before, an abrupt increase is observed in the absorption at 400 nm at the start of the reaction. This 'jump' is likely caused by a change in absorption spectrum when the chloride ions dissociate from the copper center. In other words, the change in absorption at 400 nm can be attributed to a change in the $Cu^{II} \leftarrow Cl$ LMCT. This conclusion is in agreement with the absence of the 'jump' when the 3,5-DTBC oxidation is carried out in either the presence of an excess of chloride ions or the absence of chloride ions (Appendix VI, Figure AVI.6). It is clear that when chloride ions are not present in solution, the change in LMCT will not occur. In the presence of an excess of chloride ions, part of the copper centers dissociate from the ligand to form $CuCl_4^{2-}$ complex anions. Chloride dissociation is suppressed by the excess of chloride ions, resulting in the absence of an abrupt 'jump' in the absorption curve and leading to lower activity.
The catalytic system obtained with $[Cu^{II}_2(\mathbf{L^{1*}SSL^{1*}})(Cl)_2]_n(BF_4)_{2n}$ shows the highest initial TOF with 4700 turnovers h^{-1} (entry 4). As it was found that the presence of chloride ions has a negative effect on the catalytic activity of the catalyst based on the ligand $\mathbf{L^{Pz}SSL^{Pz}}$ (Table 7.5), the catalytic system comprising $\mathbf{L^{1*}SSL^{1*}}$ in the absence of chlorides was also tested. The compound $[Cu^{II}_2(\mathbf{L^{1*}SSL^{1*}})](BF_4)_4$ was formed in situ

by adding two equivalents of $[Cu^{II}(H_2O)_6](BF_4)_2$ to **L¹*SSL¹*** and removing the majority of the H_2O with Na_2SO_4. At 0.4 mM [Cu] concentration the initial TOF of this catalytic system was found to be as high as 7800 h^{-1}. At lower catalyst concentrations the rate of the reaction levels off more quickly (Appendix VI, Figure AVI.7). Since the substrate/catalyst ratio is relatively large at lower catalyst concentrations, this phenomenon is not due to depletion of substrate but can rather be ascribed to more rapid catalyst degradation.

7.3 Discussion

A large library of Cu^{II} complexes has been synthesized and investigated for their catalytic activity in the oxidation of 3,5-DTBC. Crystal structures of a number of the Cu^{II} complexes of dinucleating ligands show that in these cases the chloride ions bridge between the Cu^{II} centers of neighboring molecules, forming polymeric chains. The Cu^{II} complexes with mononucleating ligands form dimeric species in some cases, depending on the coordination geometry of the copper ion. A square-pyramidal geometry of the copper center leaves the sixth coordination site open for coordination to the chloride ion of a molecule in a neighboring subunit.

The oxidation of 3,5-DTBC was carried out with different catalytic systems; three types of reactivity were observed with an increasing, decreasing or constant oxidation rate (Figure 7.8). This variance in catalyst behavior indicates that different activation mechanisms are operative in the formation of the active species depending on the ligand. Catalytic systems that show development of the product following type A have the highest activity at the start of the experiment and become slower over time. For the slower catalytic systems, this type of behavior indicates catalyst degradation over time. However, for the faster catalytic systems like $[Cu^{II}_2(\mathbf{L^{1}*SSL^{1}*})](BF_4)_4$, the decrease in catalytic activity may also be due to depletion of the substrate. The catalysts containing **L¹OH** and **L¹NH₂** show constant activity during the entire experiment (type B), indicating that there is no deactivation of the catalyst. All the other catalysts show an induction period in their activity (type C), which indicates the presence of a pre-catalyst at the beginning of the reaction that is converted to the active catalyst (possibly the Cu^{II} μ-hydroxo species) later on. The ligands **L¹OH** and **L¹NH₂** contain a proton donor/acceptor moiety, which might explain the absence of a similar induction period for these catalysts.

The presence of chloride ions has a negative effect on the catalytic activity. The chloride ions inhibit the reaction either by competing with the substrate for coordination sites or by formation of $CuCl_4^{2-}$, resulting in lower concentration of the

active species in solution. The ease of formation of $CuCl_4^{2-}$ is demonstrated by the structure of the compound $[Cu^{II}(\mathbf{L^1{*}SCH_3})(Cl)]_2(CuCl_4)$, which even formed in the presence of a substoichiometric amount of copper (Appendix VI, Figure AVI.2). Similar behavior was observed for $\mathbf{L^1SXSL^1}$ (Chapter 5).

When comparing the catalytic rates of the different systems (Table 7.4), it is clear that many of the systems under study are not (much) more active than the blank system comprising copper salts in the absence of a ligand. The relative differences however, are very large. The mononuclear catalysts generally have a low TOF, which is not surprising considering that the active species has been proposed to be dinuclear.[7] A number of the systems containing dinucleating ligands behave as mononuclear catalysts, because they are too rigid (entry 10 and 13) or lack bridging sulfur donor atoms (entry 12). Several other dinucleating ligands stabilize the Cu^I oxidation state, also resulting in low activity (entry 7, 9, 14 and 15).[1, 2] The catalytic systems with the highest activity are those containing ligands that stabilize Cu^{II} μ-thiolate complexes ($\mathbf{L^1SSL^1}$, $\mathbf{L^1{*}SSL^1{*}}$, $\mathbf{L^2SSL^2}$, $\mathbf{L^2{*}SSL^2{*}}$, $\mathbf{L^4SSL^4}$).[1, 2, 16, 26] The compound $[Cu^{II}_2(\mathbf{L^2SSL^2})(Cl)_2]_n(BF_4)_{2n}$ forms an exception with its relatively low activity, which can be explained by the fact that $\mathbf{L^2SSL^2}$ forms a Cu^I disulfide complex in CH_3CN which is also the solvent used for catalysis (Chapter 2).[2] These catalytic systems all show catalytic absorption profile A indicating complex degradation, which is not surprising, since Cu^{II} μ-thiolate complexes have been reported either to be oxidized to Cu^{II} sulfinate and sulfonate complexes or to react with the substrate.[10, 27] The rate of 7800 h^{-1} observed for $[Cu^{II}_2(\mathbf{L^1{*}SSL^1{*}})](BF_4)_4$ is the second highest rate reported for 3,5-DTBC oxidation in CH_3CN thus far.[8, 28] It may be argued that this high activity stems from the ability of these complexes to stabilize a Cu^{II}_2 μ-η^2:η^2-peroxide species as it is structurally as well as electronically similar to the Cu^{II} μ-thiolate complex (Figure 7.1), and especially since the formation of this species is proposed to be the rate-determining step of the reaction.[6, 29, 30] Another explanation of the high activity of our catalytic systems might be the participation of the Cu^{II} μ-thiolate complex in catalysis, cycling between Cu^I and Cu^{II} thiolate species. The activity of these catalytic systems can probably be increased even further by using a protic solvent like methanol, but this might also result in faster catalyst degradation.

7.4 Conclusion

Cu^{II} complexes have been synthesized comprising either mononucleating or dinucleating ligands for the catalytic oxidation of 3,5-DTBC. Very high activity for the oxidation of 3,5-DTBC is achieved using ligands that have the ability to form Cu^{II} μ-

thiolate complexes. The presence of chloride ions has a negative effect on the catalytic rates because of coordination to the active sites or the formation of $Cu^{II}Cl_4^{2-}$. The highest TOF reached is 7800 h^{-1} using $[Cu^{II}_2(\mathbf{L^{1*}SSL^{1*}})](BF_4)_4$, which is one of the highest TOFs reported for 3,5-DTBC oxidation in CH_3CN thus far. These results show that there are similarities between thiolato copper and (per)oxido copper chemistry and that ligands that stabilize Cu^{II} μ-thiolate complexes might also induce the formation of Cu^{II}_2 μ-η^2:η^2-peroxide species.

7.5 Experimental section

7.5.1 General methods

Reagents and solvents were purchased from commercial sources. **L^1SSL^1**, **L^2SSL^2**, **L^3SSL^3**, **L^4SSL^4**, **L^5SSL^5**,[1, 2] **$L^{1*}SSL^{1*}$**, **$L^{2*}SSL^{2*}$**,[16] **L^1SXSL^1**, **$L^{Pz}SSL^{Pz}$**, **$L^{MPz}SSL^{MPz}$**, $[Cu^{II}_2(\mathbf{L^{Pz}SSL^{Pz}})(Cl)_2]_n(BF_4)_{2n}$, $[Cu^{II}_2(\mathbf{L^{MPz}SSL^{MPz}})(Cl)_2]_n(BF_4)_{2n}$ (Chapter 5), **$L^1C_6L^1$**,[11] **L^1PhL^1**,[12, 13] **Py_3N**,[14] **L^1SCH_3**, $[Cu^{II}(\mathbf{L^1SCH_3})(Cl)](BF_4)$ (Chapter 6), **L^1NH_2**[22] and 1,5-diamino-3-thiapentane dihydrobromide[17] were synthesized according to literature procedures. NMR spectra were recorded on a Bruker 300 DPX spectrometer. IR spectra were obtained on a Perkin Elmer UATR (Single Reflection Diamond) Spectrum Two device (4000-700 cm^{-1}; resolution 4 cm^{-1}). Mass spectrometry was measured using a Finnigan Aqua Mass Spectrometer (MS) with electro spray ionization (ESI). Sample introduction was achieved through a Dionex ASI-100 automated sample injector with an eluent flow rate of 0.2 mL/min. Elemental analyses were performed using a Perkin Elmer 2400 Series II CHNS/O analyzer or were performed by the Microanalytical laboratory Kolbe in Germany. UV-vis absorbance spectra were recorded on a Varian Cary50 spectrophotometer or using a transmission dipprobe with variable path length on an Avantes Avaspec-2048 spectrometer with Avalight-DH-S-BAL light source.

7.5.2 X-ray Crystallography

$[Cu^{II}_2(\mathbf{L^1SL^1})(Cl)_2]_n(BF_4)_{2n}$ and $[Cu^{II}(\mathbf{L^1NH_2})(Cl)](BF_4)$

The reflection intensities for $[Cu^{II}_2(\mathbf{L^1SL^1})(Cl)_2]_n(BF_4)_{2n}$ and $[Cu^{II}(\mathbf{L^1NH_2})(Cl)](BF_4)$ were measured at 110(2) K using a KM4/Xcalibur (detector: Sapphire3) with enhanced graphite-monochromated Mo *Kα* radiation (λ = 0.71073 Å) under the program CrysAlisPro (Version 1.171.36.24 Agilent Technologies, 2012). The same program was used to refine the cell dimensions and for data reduction. The structures were solved with the program SHELXS-2013 (Sheldrick, 2013)[31] and was refined on F^2 with SHELXL-2013 (Sheldrick, 2013).[31] Analytical numeric absorption corrections based on a multifaceted crystal model were applied using CrysAlisPro. The temperature of the data collection was controlled using the system Cryojet (manufactured by Oxford Instruments). The H atoms were placed at calculated positions using the instructions AFIX 23 or AFIX 43 with isotropic displacement parameters having values 1.2 times *U*eq of the attached C atoms. The H atoms attached to N2 of $[Cu^{II}(\mathbf{L^1NH_2})(Cl)](BF_4)$ were

found from difference Fourier map, and their coordinates and isotropic temperature factors were refined freely.

*[Cu^{II}(**L^{2}SCH$_3$**)(Cl)](BF$_4$) and [Cu^{II}(**L^{3}SCH$_3$**)(Cl)](BF$_4$)*

The reflection intensities for [Cu^{II}(**L^{2}SCH$_3$**)(Cl)](BF$_4$) and [Cu^{II}(**L^{3}SCH$_3$**)(Cl)](BF$_4$) were measured at 110(2) K using a SuperNova diffractometer (equipped with Atlas detector) with Cu *Kα* radiation (λ = 1.54178 Å) under the program CrysAlisPro (Version 1.171.36.32 Agilent Technologies, 2013). The same program was used to refine the cell dimensions and for data reduction. The structures were solved with the program SHELXS-2013 (Sheldrick, 2013)[31] and were refined on F^2 with SHELXL-2013 (Sheldrick, 2013).[31] Analytical numeric absorption corrections based on a multifaceted crystal model were applied using CrysAlisPro. The temperature of the data collection was controlled using the system Cryojet (manufactured by Oxford Instruments). The H atoms were placed at calculated positions using the instructions AFIX 23, AFIX 43 or AFIX 137 with isotropic displacement parameters having values 1.2 or 1.5 times *U*eq of the attached C atoms.

*[Cu$^{II}_2$(**L^{1}C$_6$L^1**)(Cl)$_2$]$_n$(BF$_4$)$_{2n}$*

The reflection intensities for [Cu$^{II}_2$(**L^{1}C$_6$L^1**)(Cl)$_2$]$_n$(BF$_4$)$_{2n}$ were measured on a Bruker Kappa Apex II diffractometer with sealed tube and Triumph monochromator (λ = 0.71073 Å) up to a resolution of $(\sin\theta/\lambda)_{max}$ = 0.57 Å^{-1}. The crystal consisted of several fragments. The four major fragments were taken into account during the integration with the Eval14 software.[32] The second fragment has an arbitrary orientation with respect to the first. The third fragment is generated by a twofold rotation about hkl=(1,0,0) from the first. The fourth fragment has the same twin relation to the second. An absorption correction based on multiple measured reflections was performed with TWINABS (0.57-0.75 correction range).[33] The structure was solved with Direct Methods using SHELXS-97 and refined with SHELXL-97 against F^2 of all reflections.[31] The presence of four fragments was handled with a HKLF-5 reflection file.[34] The twin fractions refined to 0.342(15), 0.267(7), and 0.083(4). Non-hydrogen atoms were refined freely with anisotropic displacement parameters. Hydrogen atoms were introduced in calculated positions and refined with a riding model. The BF_4^- anion was refined with a disorder model of two orientations. Geometry calculations and checking for higher symmetry was performed with the PLATON program.[35]

7.5.3 Ligand synthesis

*Bis-1,5-((2-pyridylmethyl)amino)ethyl-3-thiapentane (**L^{1}SL^1**)*

1,5-Diamino-3-thiapentane dihydrobromide (1.43 g, 5.1 mmol) was dissolved in methanol (40 mL). To this solution 2-pyridinecarboxaldehyde (1.9 mL, 20.3 mmol) was added, after which the reaction mixture was cooled to 0 °C. $NaBH_3CN$ (1.28 g, 20.3 mmol) was added in small portions. The reaction mixture was allowed to warm up to RT and was stirred for 3 days. The reaction mixture was quenched by addition of HCl (37%) until pH = 1. After evaporation of the

solvent, the product was treated with NaOH (50 mL; 5 M) and the aqueous layer was extracted with $CHCl_3$ (3 x 25 mL). The organic fractions were combined, dried over $MgSO_4$ and evaporated to dryness yielding **L^1SL^1** as a brown oil (1.68 g, 3.5 mmol, 68%). ^{1}H NMR (300 MHz, CD_3OD, RT): δ 2.64 (m, 8H, S-CH_2-CH_2), 3.76 (s, 8H, Py-CH_2-N), 7.21 (m, 4H, Py-H_5), 7.62 (d, J = 8 Hz, 4H, Py-H_3), 7.72 (dt, J = 8 Hz, 2 Hz, 4H, Py-H_4), 8.41 (m, 4H, Py-H_6). ^{13}C NMR (75 MHz, CD_3OD, RT): δ 30.5 (S-CH_2-CH_2), 55.1 (S-CH_2-CH_2), 60.7 (Py-CH_2-N), 123.6 (Py-C_5), 124.6 (Py-C_3), 138.4 (Py-C_4), 149.3 (Py-C_6), 160.4 (Py-C_2). ESI-MS found (calculated) for $[M + H]^+$ m/z 485.1 (485.3); $[M + Na]^+$ m/z 507.1 (507.2). IR (neat, cm^{-1}): 3050*w*, 2924*w*, 2821*m*, 1589*s*, 1569*m*, 1473*m*, 1432*s*, 1362*m*, 1265*w*, 1147*m*, 1117*m*, 1086*m*, 1047*m*, 994*m*, 978*m*, 895*w*, 755*vs*, 731*vs*, 701*m*, 613*m*, 465*w*.

*L^1*SCH$_3$*

A mixture of bis(2-pyridylmethyl)amine (1.44 mL, 8.0 mmol) and propylene sulfide (0.94 mL, 12.0 mmol) was stirred in 20 mL CH_3CN at reflux temperature for 18 hrs under Ar atmosphere. The solvent was evaporated, after which the resulting oil was dissolved in 20 mL tetrahydrofuran. NaH (0.37 g, 9.3 mmol, 60% in mineral oil) was added and the reaction mixture was stirred for 2 hrs. To this pink reaction mixture, MeI (0.51 mL, 8.2 mmol) was added and all was stirred for 5 hrs. The reaction was quenched by dropwise addition of H_2O. In total 40 mL H_2O was added after which the water layer was extracted with CH_2Cl_2 (3 × 30 mL). The combined organic layers were dried over Na_2SO_4. The crude product was purified by column chromatography over basic alumina (50/50 EtOAc/petroleum ether) to yield **L^1*SCH$_3$** as a light yellow oil (1.98 g, 6.9 mmol, 86%). ^{1}H NMR (300 MHz, CD_3OD, RT): δ 1.18 (s, 1.5H, C*-CH_3), 1.20 (s, 1.5H, C*-CH_3), 1.99 (s, 3H, S-CH_3), 2.52 (dd, J = 13 Hz, 8 Hz, 1H, N-CH_2-C*), 2.68 (dd, J = 13 Hz, 7 Hz, 1H, N-CH_2-C*), 2.86 (dt, J = 8 Hz, 7 Hz, 1H, C*-H), 3.81 (s, 4H, Py-CH_2-N), 7.30 (ddd, J = 7 Hz, 5 Hz, 1 Hz, 2H, Py-H_5), 7.71 (d, J = 8 Hz, 2H, Py-H_3), 7.82 (td, J = 8 Hz, 2 Hz, 2H, Py-H_4), 8.43 (ddd, J = 5 Hz, 2 Hz, 1 Hz, 2H, Py-H_6). ^{13}C NMR (75 MHz, CD_3OD, RT): δ 13.0 (S-CH_3), 19.5 (C*-CH_3), 40.3 (C*), 61.4 (N-CH_2-C*), 61.5 (Py-CH_2-N), 123.8 (Py-C_5), 125.1 (Py-C_3), 138.5 (Py-C_4), 149.3 (Py-C_6), 160.5 (Py-C_2). ESI-MS found (calculated) for $[M + H]^+$ m/z 288.1 (288.2). IR (neat, cm^{-1}): 3392*br*, 2961*w*, 2919*m*, 2822*w*, 1663*w*, 1589*s*, 1569*m*, 1473*m*, 1432*s*, 1365*m*, 1300*w*, 1247*w*, 1148*m*, 1125*w*, 1075*m*, 1047*m*, 995*m*, 981*m*, 957*m*, 759*vs*, 613*m*, 525*m*, 460*m*.

N-((6-methylpyridin-2-yl)methyl)-2-(methylthio)ethylamine

2-(Methylthio)ethylamine (1.00 g, 11.0 mmol) and 6-methylpyridine-2-carboxaldehyde (1.34 g, 11.0 mmol) were dissolved in 35 mL methanol and stirred at reflux temperature for 24 hrs. The dark orange solution was cooled to RT, after which $NaBH_4$ (0.64 g, 16.9 mmol) was added and the reaction mixture was stirred for 3 hrs. The solvent was evaporated and 30 mL H_2O and 30 mL CH_2Cl_2 were added. The layers were separated and the aqueous layer was extracted CH_2Cl_2 (2 × 30 mL). The combined organic layers were dried over Na_2SO_4 and the solvent was evaporated to yield *N*-((6-methylpyridin-2-yl)methyl)-2-(methylthio)ethylamine in quantitative yield as a red/brown oil. ^{1}H NMR (300 MHz, CD_3OD, RT): δ 2.04 (s, 3H, S-CH_3), 2.52 (s, 3H, Py-

C*H*$_3$), 2.65 (m, 2H, S-C*H*$_2$-C*H*$_2$), 2.79 (m, 2H, S-C*H*$_2$-C*H*$_2$), 3.85 (s, 2H, Py-C*H*$_2$-N), 7.14 (d, *J* = 8 Hz, 1H, Py-*H*$_3$), 7.23 (d, *J* = 8 Hz, 1H, Py-*H*$_5$), 7.66 (t, *J* = 8 Hz, 1H, Py-*H*$_4$). ^{13}C NMR (75 MHz, CD_3OD, RT): δ 15.1 (S-*C*H$_3$), 24.1 (Py-*C*H$_3$), 34.5 (S-*C*H$_2$-*C*H$_2$), 48.1 (S-*C*H$_2$-*C*H$_2$), 54.8 (Py-*C*H$_2$-N), 120.9 (Py-*C*$_5$), 123.1 (Py-*C*$_3$), 138.7 (Py-*C*$_4$), 159.0 (Py-*C*$_6$), 159.5 (Py-*C*$_2$).

L²SCH₃

N-((6-methylpyridin-2-yl)methyl)-2-(methylthio)ethylamine (1.28 g, 6.5 mmol) and 2-pyridinecarboxaldehyde (0.62 mL, 6.5 mmol) were dissolved in 20 mL methanol and stirred at reflux temperature for 2 hrs. The dark brown solution was cooled to RT, $NaBH_4$ (0.39 g, 10.4 mmol) was added and the reaction mixture was stirred for 3 hrs. The solvent was evaporated and 20 mL H_2O and 20 mL CH_2Cl_2 was added. The layers were separated and the aqueous layer was extracted with CH_2Cl_2 (2 × 20 mL). The combined organic layers were dried over Na_2SO_4 and the solvent was evaporated to yield a brown oil (1.84 g). The compound was purified by column chromatography over basic alumina (30/70 EtOAc/petroleum ether) to yield **L²SCH₃** as a yellow/orange oil (0.93 g, 3.2 mmol, 50%). ^{1}H NMR (300 MHz, CD_3OD, RT): δ 1.59 (s, 3H, S-C*H*$_3$), 2.47 (s, 3H, Py$_{Me}$-C*H*$_3$), 2.64 (m, 2H, S-C*H*$_2$-C*H*$_2$), 2.75 (m, 2H, S-C*H*$_2$-C*H*$_2$), 3.79 (s, 2H, Py-C*H*$_2$-N), 3.82 (s, 2H, Py-C*H*$_2$-N), 7.09 (d, *J* = 8 Hz, 1H, Py$_{Me}$-*H*$_3$), 7.24 (ddd, *J* = 7 Hz, 5 Hz, 1 Hz, 1H, Py$_{Me}$-*H*$_5$), 7.47 (d, *J* = 8 Hz, 1H, Py-*H*$_3$), 7.65 (m, 2H, Py-*H*$_4$; Py$_{Me}$-*H*$_4$), 7.77 (td, *J* = 8 Hz, 2 Hz, 1H, Py-*H*$_5$), 8.42 (d, *J* = 5 Hz, 1H, Py-*H*$_6$). ^{13}C NMR (75 MHz, CD_3OD, RT): δ 15.6 (S-*C*H$_3$), 23.9 (Py-*C*H$_3$), 32.5 (S-*C*H$_2$-*C*H$_2$), 54.7 (S-*C*H$_2$-*C*H$_2$), 60.8 (Py-*C*H$_2$-N), 60.8 (Py-*C*H$_2$-N), 121.6 (Py$_{Me}$-*C*$_5$), 123.1 (Py$_{Me}$-*C*$_3$), 123.7 (Py-*C*$_5$), 124.8 (Py-*C*$_3$), 138.5 (Py$_{Me}$-*C*$_4$), 138.7 (Py-*C*$_4$), 149.3 (Py-*C*$_6$), 158.5 (Py$_{Me}$-*C*$_2$), 159.9 (Py$_{Me}$-*C*$_6$), 160.6 (Py-*C*$_2$). ESI-MS found (calculated) for $[M + H]^+$ *m*/*z* 288.1 (288.2). IR (neat, cm^{-1}): 3393*w*, 3061*w*, 2916*m*, 2828*m*, 1591*s*, 1577*s*, 1456*s*, 1433*s*, 1363*m*, 1290*w*, 1152*m*, 1118*m*, 1089*m*, 1047*m*, 994*m*, 783*s*, 756*vs*, 614*m*, 545*m*.

L³SCH₃

N-((6-methylpyridin-2-yl)methyl)-2-(methylthio)ethylamine (1.28 g, 6.5 mmol) and 6-methylpyridine-2-carboxaldehyde (0.79 g, 6.5 mmol) were dissolved in 20 mL methanol and stirred at reflux temperature for 18 hrs. The brown solution was cooled to RT and $NaBH_4$ (0.37 g, 9.8 mmol) was added and the reaction mixture was stirred for 2 hrs. The solvent was evaporated and 20 mL H_2O and 20 mL CH_2Cl_2 were added. The layers were separated and the aqueous layer was extracted two more times with 20 mL CH_2Cl_2. The combined organic layers were dried over Na_2SO_4 and the solvent was evaporated to yield a brown oil (1.93 g). The compound was purified by column chromatography over basic alumina (30/70 EtOAc/petroleum ether) to yield **L³SCH₃** as a yellow/orange oil (0.91 g, 3.0 mmol, 46%). ^{1}H NMR (300 MHz, CD_3OD, RT): δ 1.95 (s, 3H, S-C*H*$_3$), 2.47 (s, 6H, Py-C*H*$_3$), 2.64 (m, 2H, S-C*H*$_2$-C*H*$_2$), 2.74 (m, 2H, S-C*H*$_2$-C*H*$_2$), 3.78 (s, 4H, Py-C*H*$_2$-N), 7.08 (d, *J* = 8 Hz, 2H, Py-*H*$_3$), 7.47 (d, *J* = 8 Hz, 2H, Py-*H*$_5$), 7.63 (t, *J* = 8 Hz, 2H, Py-*H*$_4$). ^{13}C NMR (75 MHz, CD_3OD, RT): δ 15.6 (S-*C*H$_3$), 23.9 (Py-*C*H$_3$), 32.6 (S-*C*H$_2$-*C*H$_2$), 54.7 (S-*C*H$_2$-*C*H$_2$), 60.8 (Py-*C*H$_2$-N), 121.5 (Py-*C*$_5$), 123.1 (Py-*C*$_3$), 138.7 (Py-*C*$_4$), 158.5 (Py-*C*$_6$), 160.1 (Py-*C*$_2$). ESI-MS found (calculated) for $[M + H]^+$ *m*/*z* 302.1

(302.2). IR (neat, cm^{-1}): 3388*w*, 3061*w*, 2917*m*, 2829*w*, 1592*s*, 1577*s*, 1456*s*, 1375*m*, 1355*m*, 1291*w*, 1154*m*, 1117*m*, 1090*m*, 1035*m*, 994*m*, 972*m*, 786*s*, 760*m*, 627*m*, 546*m*.

L^1OH

This ligand was synthesized using a modified literature procedure.[14, 19] 2-Pyridinecarboxaldehyde (1.90 mL, 20.0 mmol) was added to ethanolamine (0.60 mL, 10.0 mmol) dissolved in 30 mL CH_2Cl_2. $NaBH(OAc)_3$ (6.0 g, 28.3 mmol) was added in portions over 15 min. after which the reaction mixture was stirred for 4 hrs. The reaction was quenched by addition of 40 mL $NaHCO_3$ (sat.). The layers were separated and the aqueous layer was extracted two more times with 20 mL CH_2Cl_2. The combined organic layers were dried over Na_2SO_4 and then evaporated to dryness yielding **L^1OH** as a yellow oil. (2.41 g, 9.9 mmol, 99%). ^1H NMR (300 MHz, CD_3CN, RT): δ 2.71 (t, *J* = 6 Hz, 2H, S-CH_2-CH_2), 3.56 (t, *J* = 6 Hz, 2H, S-CH_2-CH_2), 3.83 (s, 4H, Py-CH_2-N), 4.0 (br, CH_2-O*H*), 7.17 (m, 2H, Py-*H*5), 7.43 (d, *J* = 8 Hz, 2H, Py-*H*3), 7.66 (td, *J* = 8 Hz, 2 Hz, 2H, Py-*H*4), 8.47 (d, *J* = 5 Hz, 2H, Py-*H*6). ^{13}C NMR (75 MHz, CD_3CN, RT): δ 57.5 (S-*C*H_2-*C*H_2), 60.3 (S-*C*H_2-*C*H_2), 61.0 (Py-*C*H_2-N), 123.0 (Py-*C*3/Py-*C*5), 123.9 (Py-*C*3/Py-*C*5), 137.4 (Py-*C*4), 149.8 (Py-*C*6), 160.8 (Py-*C*2). ESI-MS found (calculated) for $[M + H]^+$ *m*/*z* 244.2 (244.1). IR (neat, cm^{-1}): 3270*br*, 2939*w*, 2826*m*, 1592*s*, 1570*m*, 1475*m*, 1433*s*, 1363*m*, 1309*w*, 1249*w*, 1149*m*, 1047*s*, 1002*m*, 758*vs*, 616*s*, 502*m*, 469*m*.

Py_2S

This ligand was synthesized using a modified literature procedure.[18] NaOH (0.30 g, 7.5 mmol) was dissolved in a mixture of 10 mL H_2O and 10 mL ethanol. $Na_2S \cdot 9\ H_2O$ (0.60 g, 2.5 mmol) and 2-(chloromethyl)pyridine hydrochloride (0.82 g, 5.0 mmol) were added. The mixture was refluxed at 95°C for 20 hours and left to cool to RT. The resulting bright orange solution was extracted twice with 20 mL CH_2Cl_2. The organic fractions were combined and dried over Na_2SO_4 to yield **Py_2S** as a yellow oil (0.48 g, 2.2 mmol, 88%). ^1H NMR (300 MHz, CD_3OD, RT): δ 3.82 (s, 4H, S-CH_2-N), 7.25 (dd, *J* = 7 Hz, 5 Hz, 2H, Py-*H*5), 7.42 (d, *J* = 8 Hz, 2H, Py-*H*3), 7.73 (td, *J* = 8 Hz, 2 Hz, 2H, Py-*H*4), 8.42 (d, *J* = 5 Hz, 2H, Py-*H*6). ^{13}C NMR (75 MHz, CD_3OD, RT): δ 38.2 (S-*C*H_2-N), 123.5 (Py-*C*5), 124.9 (Py-*C*3), 138.7 (Py-*C*4), 149.7 (Py-*C*6), 159.4 (Py-*C*2). ESI-MS found (calculated) for $[M + H]^+$ *m*/*z* 217.1 (217.1). IR (neat, cm^{-1}): 3369*br*, 3050*w*, 3008*w*, 2925*w*, 1590*s*, 1568*m*, 1471*m*, 1434*vs*, 1307*w*, 1208*w*, 1151*w*, 1088*w*, 1048*w*, 994*m*, 790*m*, 747*vs*, 711*m*, 627*w*, 579*m*, 484*m*.

7.5.4 Complex synthesis

General synthesis procedure

All complexes were synthesized in the same manner unless mentioned otherwise. The ligand was dissolved in methanol, after which $[Cu^{II}(H_2O)_6](BF_4)_2$ and $Cu^{II}Cl_2 \cdot 2\ H_2O$ were added. If there was no formation of powder, diethyl ether was added until precipitation occured. The powder was filtered and washed with diethyl ether to yield the target complex.

*[Cu^{II}_2(**L^1SSL^1**)$(Cl)_2]_n(BF_4)_{2n}$*

From **L^1SSL^1** (67 mg; 0.13 mmol), $[Cu^{II}(H_2O)_6](BF_4)_2$ (46 mg; 0.13 mmol) and $Cu^{II}Cl_2 \cdot 2\ H_2O$ (22 mg; 0.13 mmol), the product $[Cu^{II}_2$(**L^1SSL^1**$)(Cl)_2]_n(BF_4)_{2n}$ (104 mg; 0.12 mmol; 90%) was obtained as a blue powder. Crystals suitable for X-ray structure determination were obtained by slow vapor diffusion of diethyl ether into a CH_3CN solution containing the complex. ESI-MS found (calculated) for $[M - 2\ BF_4]^+$ *m/z* 357.0 (357.0); $[½\ M - Cl - BF_4]^+$ *m/z* 320.9 (321.0); $[½\ M + Cl - BF_4]^+$ *m/z* 392.9 (393.0). IR (neat, cm^{-1}): 1610*m*, 1575*w*, 1486*w*, 1447*m*, 1303*w*, 1286*w*, 1026*vs*, 990*s*, 921*m*, 820*w*, 777*m*, 762*s*, 719*m*, 656*w*, 518*m*, 476*w*, 424*s*. Elemental analysis calcd for $[Cu^{II}_2$(**L^1SSL^1**$)(Cl)_2](BF_4)_2 \cdot H_2O$: C 37.11, H 3.78, N 9.27, S 7.07; Found: C 37.40, H 3.96, N 9.25, S 7.23. UV-vis in CH_3CN at 0.1 mM [Cu] concentration: 258 nm (ε = 10 300 $M^{-1}\ cm^{-1}$), 289 nm (ε = 2 700 $M^{-1}\ cm^{-1}$), 680 nm (ε = 190 $M^{-1}\ cm^{-1}$).

*[Cu^{II}_2(**L^1*SSL^1***$)(Cl)_2]_n(BF_4)_{2n}$*

From **L^1*SSL^1*** (197 mg; 0.36 mmol), $[Cu^{II}(H_2O)_6](BF_4)_2$ (128 mg; 0.36 mmol) and $Cu^{II}Cl_2 \cdot 2\ H_2O$ (62 mg; 0.36 mmol), the product $[Cu^{II}_2$(**L^1*SSL^1***$)(Cl)_2]_n(BF_4)_{2n}$ (245 mg; 0.27 mmol; 74%) was obtained as a blue powder. ESI-MS found (calculated) for $[M - 2\ BF_4]^{2+}$ *m/z* 371.0 (371.0); $[M + 2\ Cl - 2\ BF_4]^{2+}$ *m/z* 407.0 (406.0); $[½\ M - Cl - BF_4]^+$ *m/z* 335.0 (335.1); $[M - Cu - Cl - 2\ BF_4]^+$ *m/z* 642.3 (642.1). IR (neat, cm^{-1}): 1611*w*, 1574*w*, 1484*w*, 1446*m*, 1284*w*, 1162*w*, 1048*vs*, 1030*vs*, 935*m*, 866*m*, 819*w*, 765*s*, 726*w*, 658*w*, 521*m*, 420*m*. Elemental analysis calcd for $[Cu^{II}_2$(**L^1*SSL^1***$)(Cl)_2](BF_4)_2$: C 39.32, H 3.96, N 9.17, S 7.00; Found: C 38.69, H 3.99, N 9.19, S 6.88. UV-vis in CH_3CN at 0.1 mM [Cu] concentration: 258 nm (ε = 10 900 $M^{-1}\ cm^{-1}$), 294 nm (ε = 2 900 $M^{-1}\ cm^{-1}$), 690 nm (ε = 210 $M^{-1}\ cm^{-1}$).

*[Cu^{II}_2(**L^2SSL^2**)$(Cl)_2]_n(BF_4)_{2n}$*

L^2SSL^2 (72 mg; 0.13 mmol), $[Cu^{II}(H_2O)_6](BF_4)_2$ (46 mg; 0.13 mmol) and $Cu^{II}Cl_2 \cdot 2\ H_2O$ (23 mg; 0.13 mmol) were dissolved in 5 mL CH_3CN. Diethyl ether (13 mL) was added to the bright blue solution. After 15 minutes, the suspension was decanted and filtered. This yielded a bright blue powder that was washed with diethyl ether giving $[Cu^{II}_2$(**L^2SSL^2**$)(Cl)_2]_n(BF_4)_{2n}$ (48 mg; 0.05 mmol; 40%). Single crystals suitable for X-ray structure determination were synthesized from $[Cu^{II}(H_2O)_6](ClO_4)_2$ instead of $[Cu^{II}(H_2O)_6](BF_4)_2$. Slow vapor diffusion of diethyl ether into a CH_3CN solution containing the complex, yielded crystals of $[Cu^{II}_2$(**L^2SSL^2**$)(Cl)_2]_n(ClO_4)_{2n}$. ESI-MS found (calculated) for $[M - 2\ BF_4]^{2+}$ *m/z* 371.0 (371.0); $[M + 2\ Cl - 2\ BF_4]^{2+}$ *m/z* 406.9 (406.0); $[½\ M - Cl - BF_4]^+$ *m/z* 335.0 (335.1). IR (neat, cm^{-1}): 3554*w*, 1610*m*, 1577*w*, 1447*m*, 1287*w*, 1052*vs*, 1028*vs*, 921*m*, 790*m*, 764*m*, 724*w*, 654*w*, 520*m*, 474*m*. Elemental analysis calcd for $[Cu^{II}_2$(**L^2SSL^2**$)(Cl)_2](BF_4)_2$: C 39.32, H 3.96, N 9.17, S 7.00; Found: C 39.23, H 4.01, N 9.12, S 6.96. UV-vis in CH_3CN at 0.1 mM [Cu] concentration: 263 nm (ε = 11 600 $M^{-1}\ cm^{-1}$), 303 nm (ε = 2 800 $M^{-1}\ cm^{-1}$), 720 nm (ε = 270 $M^{-1}\ cm^{-1}$).

*[Cu^{II}_2(**$L^{2*}SSL^{2*}$**)(Cl)$_2$]$_n$(BF_4)$_{2n}$*

From **$L^{2*}SSL^{2*}$** (84 mg; 0.15 mmol), [Cu^{II}(H_2O)$_6$](BF_4)$_2$ (51 mg; 0.15 mmol) and $Cu^{II}Cl_2 \cdot 2\ H_2O$ (25 mg; 0.15 mmol), the product [Cu^{II}_2(**$L^{2*}SSL^{2*}$**)(Cl)$_2$]$_n$(BF_4)$_{2n}$ (97 mg; 0.10 mmol; 70%) was obtained as a blue powder. ESI-MS found (calculated) for [M – 2 BF_4]$^{2+}$ *m/z* 386.0 (385.0); [½ M – Cl – BF_4]$^+$ *m/z* 349.1 (349.1); [½ M + Cl – BF_4]$^+$ *m/z* 421.0 (421.0); [M – Cu – Cl – 2 BF_4]$^+$ *m/z* 670.3 (670.2). IR (neat, cm^{-1}): 3565*w*, 2934*w*, 1611*m*, 1576*w*, 1447*m*, 1287*w*, 1052*vs*, 1027*vs*, 867*w*, 771*m*, 729*w*, 654*w*, 521*m*. Elemental analysis calcd for [Cu^{II}_2(**$L^{2*}SSL^{2*}$**)(Cl)$_2$](BF_4)$_2$: C 40.70, H 4.27, N 8.90, S 6.79; Found: C 39.35, H 4.13, N 8.52, S 6.85. UV-vis in CH_3CN at 0.1 mM [Cu] concentration: 264 nm (ε = 11 400 M^{-1} cm^{-1}), 303 nm (ε = 3 000 M^{-1} cm^{-1}), 730 nm (ε = 270 M^{-1} cm^{-1}).

*[Cu^{II}_2(**L^3SSL^3**)(Cl)$_2$]$_n$(BF_4)$_{2n}$*

From **L^3SSL^3** (153 mg; 0.27 mmol), [Cu^{II}(H_2O)$_6$](BF_4)$_2$ (93 mg; 0.27 mmol) and $Cu^{II}Cl_2 \cdot 2\ H_2O$ (46 mg; 0.27 mmol), the product [Cu^{II}_2(**L^3SSL^3**)(Cl)$_2$]$_n$(BF_4)$_{2n}$ (207 mg; 0.22 mmol; 82%) was obtained as a blue powder. ESI-MS found (calculated) for [½ M – Cl – BF_4]$^+$ *m/z* 349.0 (349.1); [M – Cu – 2 Cl – 2 BF_4]$^{2+}$ *m/z* 318.1 (317.6); [M – Cu – 2 Cl – 2 BF_4]$^+$ *m/z* 635.3 (635.2). IR (neat, cm^{-1}): 2938*w*, 1612*m*, 1577*w*, 1474*m*, 1459*m*, 1417*w*, 1386*w*, 1349*w*, 1274*w*, 1243*w*, 1172*w*, 1049*vs*, 986*vs*, 923*m*, 852*m*, 805*m*, 722*m*, 519*m*. Elemental analysis calcd for [Cu^{II}_2(**L^3SSL^3**)(Cl)$_2$](BF_4)$_2$: C 40.70, H 4.27, N 8.90, S 6.79; Found: C 39.90, H 4.21, N 8.86, S 6.81. UV-vis in CH_3CN at 0.1 mM [Cu] concentration: 265 nm (ε = 13 000 M^{-1} cm^{-1}), 343 nm (ε = 1 600 M^{-1} cm^{-1}), 640 nm (ε = 180 M^{-1} cm^{-1}), 750 nm (ε = 200 M^{-1} cm^{-1}).

*[Cu^{II}_2(**L^4SSL^4**)(Cl)$_2$]$_n$(BF_4)$_{2n}$*

From **L^4SSL^4** (96 mg; 0.18 mmol), [Cu^{II}(H_2O)$_6$](BF_4)$_2$ (61 mg; 0.18 mmol) and $Cu^{II}Cl_2 \cdot 2\ H_2O$ (30 mg; 0.18 mmol), the product [Cu^{II}_2(**L^4SSL^4**)(Cl)$_2$]$_n$(BF_4)$_{2n}$ (110 mg; 0.12 mmol; 68%) was obtained as a greyish blue powder. ESI-MS found (calculated) for [M – 2 BF_4]$^{2+}$ *m/z* 371.0 (371.0); [M + 2 Cl – 2 BF_4]$^{2+}$ *m/z* 406.9 (406.0); [½ M – Cl – BF_4]$^+$ *m/z* 335.0 (335.1); [M – Cu – Cl – 2 BF_4]$^+$ *m/z* 642.3 (642.1). IR (neat, cm^{-1}): 3628*w*, 1612*m*, 1574*w*, 1487*w*, 1448*m*, 1319*w*, 1300*w*, 1165*w*, 1054*vs*, 1029*vs*, 946*m*, 769*s*, 724*w*, 655*w*, 588*w*, 520*m*, 479*m*. Elemental analysis calcd for [Cu^{II}_2(**L^4SSL^4**)(Cl)$_2$](BF_4)$_2 \cdot H_2O$: C 38.56, H 4.10, N 8.99, S 6.86; Found: C 38.45, H 4.36, N 9.12, S 7.03. UV-vis in CH_3CN at 0.1 mM [Cu] concentration: 261 nm (ε = 11 500 M^{-1} cm^{-1}), 293 nm (ε = 3 600 M^{-1} cm^{-1}), 580 nm (ε = 200 M^{-1} cm^{-1}), 670 nm (ε = 180 M^{-1} cm^{-1}).

*[Cu^{II}_2(**L^5SSL^5**)(Cl)$_2$]$_n$(BF_4)$_{2n}$*

This complex was formed in situ. CH_3CN at 0.1 mM [Cu] concentration: 263 nm (ε = 10 800 M^{-1} cm^{-1}), 292 nm (ε = 3 600 M^{-1} cm^{-1}), 342 nm (ε = 1 900 M^{-1} cm^{-1}), 710 nm (ε = 170 M^{-1} cm^{-1}).

*[Cu^{II}_2(**L^1SXSL^1**)(Cl)$_2$]$_n$(BF_4)$_{2n}$*

From **L^1SXSL^1** (23 mg; 0.04 mmol), [Cu^{II}(H_2O)$_6$](BF_4)$_2$ (15 mg; 0.04 mmol) and $Cu^{II}Cl_2 \cdot 2\ H_2O$ (7.4 mg; 0.04 mmol) in CH_3CN, the product [Cu^{II}_2(**L^1SXSL^1**)(Cl)$_2$]$_n$(BF_4)$_{2n}$ (34 mg; 0.04 mmol;

86%) was obtained as a light blue powder. ESI-MS found (calculated) for $[M - 2\ BF_4]^{2+}$ *m/z* 370.0 (370.0). IR (neat, cm^{-1}): 3612*w*, 1611*m*, 1574*w*, 1484*w*, 1447*m*, 1287*w*, 1162*w*, 1054*vs*, 1030*vs*, 901*w*, 852*w*, 819*w*, 765*s*, 728*w*, 656*w*, 521*m*. Elemental analysis calcd for $[Cu^{II}_2(\mathbf{L^1SXSL^1})(Cl)_2](BF_4)_2$: C 39.41, H 3.75, N 9.19, S 7.01; Found: C 38.56, H 3.73, N 9.04, S 6.85. UV-vis in CH_3CN at 0.1 mM [Cu] concentration: 257 nm (ε = 10 800 $M^{-1}\ cm^{-1}$), 290 nm (ε = 3 000 $M^{-1}\ cm^{-1}$), 700 nm (ε = 190 $M^{-1}\ cm^{-1}$).

$[Cu^{II}_2(\mathbf{L^1SL^1})(Cl)_2]_n(BF_4)_{2n}$

From $\mathbf{L^1SL^1}$ (275 mg; 0.57 mmol), $[Cu^{II}(H_2O)_6](BF_4)_2$ (196 mg; 0.57 mmol) and $Cu^{II}Cl_2 \cdot 2\ H_2O$ (97 mg; 0.57 mmol), the product $[Cu^{II}_2(\mathbf{L^1SL^1})(Cl)_2]_n(BF_4)_{2n}$ (370 mg; 0.43 mmol; 76%) was obtained as a light blue powder. Crystals suitable for X-ray structure determination were obtained by slow vapor diffusion of diethyl ether into a CH_3CN solution containing the complex. ESI-MS found (calculated) for $[M - 2\ BF_4]^{2+}$ *m/z* 341.0 (341.0). IR (neat, cm^{-1}): 3612*w*, 1611*m*, 1574*w*, 1481*w*, 1444*m*, 1290*w*, 1088*m*, 1049*vs*, 1030*vs*, 995*m*, 973*w*, 946*w*, 906*w*, 819*w*, 777*m*, 761*m*, 717*m*, 654*w*, 521*w*. Elemental analysis calcd for $[Cu^{II}_2(\mathbf{L^1SL^1})(Cl)_2](BF_4)_2$: C 39.28, H 3.77, N 9.81, S 3.74; Found: C 40.13, H 3.85, N 10.15, S 3.67. UV-vis in CH_3CN at 0.1 mM [Cu] concentration: 256 nm (ε = 10 600 $M^{-1}\ cm^{-1}$), 290 nm (ε = 2 900 $M^{-1}\ cm^{-1}$), 690 nm (ε = 110 $M^{-1}\ cm^{-1}$).

$[Cu^{II}_2(\mathbf{L^1C_6L^1})(Cl)_2]_n(BF_4)_{2n}$

From $\mathbf{L^1C_6L^1}$ (102 mg; 0.21 mmol), $[Cu^{II}(H_2O)_6](BF_4)_2$ (74 mg; 0.21 mmol) and $Cu^{II}Cl_2 \cdot 2\ H_2O$ (36 mg; 0.21 mmol), the product $[Cu^{II}_2(\mathbf{L^1C_6L^1})(Cl)_2]_n(BF_4)_{2n}$ (158 mg; 0.19 mmol; 87%) was obtained as a dark blue powder. Crystals suitable for X-ray structure determination were obtained by slow vapor diffusion of di-isopropyl ether into a CH_3CN solution containing the complex. ESI-MS found (calculated) for $[M - 2\ BF_4]^{2+}$ *m/z* 339.1 (339.1). IR (neat, cm^{-1}): 3090*w*, 2933*w*, 2853*w*, 1612*m*, 1574*w*, 1484*w*, 1446*m*, 1283*m*, 1088*m*, 1049*vs*, 1031*vs*, 897*m*, 883*m*, 817*w*, 766*s*, 726*w*, 660*w*, 521*m*, 492*w*. Elemental analysis calcd for $[Cu^{II}_2(\mathbf{L^1C_6L^1})(Cl)_2](BF_4)_2$: C 42.28, H 4.26, N 9.86; Found: C 42.49, H 4.35, N 9.93. UV-vis in CH_3CN at 0.1 mM [Cu] concentration: 256 nm (ε = 11 800 $M^{-1}\ cm^{-1}$), 291 nm (ε = 3 000 $M^{-1}\ cm^{-1}$), 660 nm (ε = 140 $M^{-1}\ cm^{-1}$).

$[Cu^{II}_2(\mathbf{L^1PhL^1})(Cl)_2]_n(BF_4)_{2n}$

From $\mathbf{L^1PhL^1}$ (166 mg; 0.35 mmol), $[Cu^{II}(H_2O)_6](BF_4)_2$ (121 mg; 0.35 mmol) and $Cu^{II}Cl_2 \cdot 2\ H_2O$ (60 mg; 0.35 mmol), the product $[Cu^{II}_2(\mathbf{L^1PhL^1})(Cl)_2]_n(BF_4)_{2n}$ (249 mg; 0.30 mmol; 84%) was obtained as a green powder. ESI-MS found (calculated) for $[M - 2\ BF_4]^{2+}$ *m/z* 335.0 (335.0); $[M - Cu - Cl - 2\ BF_4]^{+}$ *m/z* 570.2 (570.1). IR (neat, cm^{-1}): 2972*w*, 1611*m*, 1575*w*, 1486*w*, 1449*m*, 1288*m*, 1052*vs*, 1031*vs*, 870*m*, 769*s*, 698*m*, 657*m*, 538*w*, 521*m*. Elemental analysis calcd for $[Cu^{II}_2(\mathbf{L^1PhL^1})(Cl)_2](BF_4)_2 \cdot 2\ CH_3CN$: C 44.09, H 3.70, N 12.10; Found: C 43.18, H 3.82, N 11.80. UV-vis in CH_3CN at 0.1 mM [Cu] concentration: 260 nm (ε = 11 500 $M^{-1}\ cm^{-1}$), 310 nm (ε = 2 000 $M^{-1}\ cm^{-1}$), 380 nm (ε = 410 $M^{-1}\ cm^{-1}$), 700 nm (ε = 150 $M^{-1}\ cm^{-1}$).

*[Cu^{II}(**Py_3N**)(Cl)](BF_4)*

From **Py_3N** (160 mg; 0.55 mmol), [$Cu^{II}(H_2O)_6$](BF_4)$_2$ (96 mg; 0.28 mmol) and $Cu^{II}Cl_2 \cdot 2\ H_2O$ (47 mg; 0.28 mmol), the product [Cu^{II}(**Py_3N**)(Cl)](BF_4) (251 mg; 0.53 mmol; 96%) was obtained as a mint green powder. ESI-MS found (calculated) for [M – BF_4]$^+$ *m/z* 388.0 (388.1). IR (neat, cm^{-1}): 2974*w*, 1607*m*, 1575*w*, 1480*w*, 1438*m*, 1307*w*, 1263*w*, 1159*w*, 1113*w*, 1090*m*, 1047*vs*, 1021*s*, 958*m*, 841*w*, 771*m*, 761*s*, 643*w*, 506*m*. Elemental analysis calcd for [Cu^{II}(**Py_3N**)(Cl)](BF_4): C 43.75, H 4.08, N 11.34; Found: C 44.88, H 4.40, N 11.59. UV-vis in CH_3CN at 0.1 mM [Cu] concentration: 230 nm (ε = 7 600 M^{-1} cm^{-1}), 261 nm (ε = 12 100 M^{-1} cm^{-1}), 299 nm (ε = 3 100 M^{-1} cm^{-1}), 730 nm (ε = 90 M^{-1} cm^{-1}), 940 nm (ε = 200 M^{-1} cm^{-1}).

*[Cu^{II}(**L^{1}*SCH_3**)(Cl)](BF_4)*

From **L^{1}*SCH_3** (178 mg; 0.62 mmol), [$Cu^{II}(H_2O)_6$](BF_4)$_2$ (107 mg; 0.31 mmol) and $Cu^{II}Cl_2 \cdot 2\ H_2O$ (53 mg; 0.31 mmol), the product [Cu^{II}(**L^{1}*SCH_3**)(Cl)](BF_4) (157 mg; 0.33 mmol; 54%) was obtained as a blue powder. Crystals suitable for X-ray structure determination were obtained by slow vapor diffusion of diethyl ether into a methanol solution containing the complex. ESI-MS found (calculated) for [M – BF_4]$^+$ *m/z* 385.0 (385.0). IR (neat, cm^{-1}): 1609*m*, 1573*w*, 1483*w*, 1444*m*, 1302*w*, 1285*w*, 1160*w*, 1054*vs*, 1028*vs*, 863*w*, 820*w*, 766*s*, 652*w*, 520*m*. Elemental analysis calcd for [Cu^{II}(**L^{1}*SCH_3**)(Cl)](BF_4): C 40.61, H 4.47, N 8.88, S 6.78; Found: C 40.17, H 4.51, N 8.68, S 7.03. UV-vis in CH_3CN at 0.1 mM [Cu] concentration: 257 nm (ε = 11 000 M^{-1} cm^{-1}), 299 nm (ε = 3 600 M^{-1} cm^{-1}), 690 nm (ε = 130 M^{-1} cm^{-1}), 880 nm (ε = 160 M^{-1} cm^{-1}).

*[Cu^{II}(**$L^{2}SCH_3$**)(Cl)](BF_4)*

From **$L^{2}SCH_3$** (116 mg; 0.40 mmol), [$Cu^{II}(H_2O)_6$](BF_4)$_2$ (70 mg; 0.20 mmol) and $Cu^{II}Cl_2 \cdot 2\ H_2O$ (35 mg; 0.20 mmol), the product [Cu^{II}(**$L^{2}SCH_3$**)(Cl)](BF_4) (96 mg; 0.20 mmol; 50%) was obtained as a blue powder. Crystals suitable for X-ray structure determination were obtained by slow vapor diffusion of diethyl ether into a methanol solution containing the complex. ESI-MS found (calculated) for [M – BF_4]$^+$ *m/z* 385.0 (385.0); [M – Cl – BF_4]$^+$ *m/z* 350.0 (350.1). IR (neat, cm^{-1}): 2932*w*, 1610*m*, 1578*w*, 1460*w*, 1445*m*, 1287*w*, 1175*w*, 1050*vs*, 1026*vs*, 961*m*, 911*m*, 791*m*, 764*m*, 725*w*, 654*w*, 520*m*. Elemental analysis calcd for [Cu^{II}(**$L^{2}SCH_3$**)(Cl)](BF_4): C 40.61, H 4.47, N 8.88, S 6.78; Found: C 40.64, H 4.59, N 8.78, S 6.71. UV-vis in CH_3CN at 0.1 mM [Cu] concentration: 265 nm (ε = 10 300 M^{-1} cm^{-1}), 305 nm (ε = 3 600 M^{-1} cm^{-1}), 350 nm (ε = 2 300 M^{-1} cm^{-1}), 690 nm (ε = 320 M^{-1} cm^{-1}), 870 nm (ε = 310 M^{-1} cm^{-1}).

*[Cu^{II}(**$L^{3}SCH_3$**)(Cl)](BF_4)*

From **$L^{3}SCH_3$** (154 mg; 0.51 mmol), [$Cu^{II}(H_2O)_6$](BF_4)$_2$ (88 mg; 0.26 mmol) and $Cu^{II}Cl_2 \cdot 2\ H_2O$ (44 mg; 0.26 mmol), the product [Cu^{II}(**$L^{3}SCH_3$**)(Cl)](BF_4) (195 mg; 0.40 mmol; 78%) was obtained as a dark blue powder. Crystals suitable for X-ray structure determination were obtained by slow vapor diffusion of diethyl ether into a methanol solution containing the complex. ESI-MS found (calculated) for [M – BF_4]$^+$ *m/z* 399.0 (399.1); [M – Cl – BF_4]$^+$ *m/z* 364.0 (364.1). IR (neat, cm^{-1}): 2929*w*, 1610*m*, 1576*w*, 1474*m*, 1457*m*, 1432*w*, 1349*w*, 1287*w*, 1241*w*,

1094*m*, 1049*vs*, 1027*vs*, 964*m*, 915*w*, 803*s*, 792*m*, 773*m*, 648*w*, 520*m*. Elemental analysis calcd for [Cu^{II}(**L^3SCH_3**)(Cl)](BF_4): C 41.90, H 4.76, N 8.62, S 6.58; Found: C 42.08, H 4.73, N 8.69, S 6.52. UV-vis in CH_3CN at 0.1 mM [Cu] concentration: 267 nm (ε = 11 700 M^{-1} cm^{-1}), 319 nm (ε = 2 600 M^{-1} cm^{-1}), 358 nm (ε = 2 400 M^{-1} cm^{-1}), 650 nm (ε = 300 M^{-1} cm^{-1}), 840 nm (ε = 160 M^{-1} cm^{-1}).

*[Cu^{II}(**L^1OH**)(Cl)](BF_4)*

From **L^1OH** (194 mg; 0.80 mmol), [$Cu^{II}(H_2O)_6$](BF_4)$_2$ (138 mg; 0.40 mmol) and $Cu^{II}Cl_2 \cdot 2\ H_2O$ (68 mg; 0.40 mmol), the product [Cu^{II}(**L^1OH**)(Cl)](BF_4) (307 mg; 0.72 mmol; 90%) was obtained as a blue powder. ESI-MS found (calculated) for [M – BF_4]$^+$ *m*/*z* 341.0 (341.0). IR (neat, cm^{-1}): 3474*br*, 2949*w*, 1611*m*, 1575*w*, 1480*w*, 1443*m*, 1287*m*, 1060*vs*, 1031*vs*, 1005*s*, 983*s*, 955*m*, 871*m*, 798*s*, 763*vs*, 723*m*, 655*m*, 519*m*, 483*m*. Elemental analysis calcd for [Cu^{II}(**L^1OH**)(Cl)](BF_4): C 39.49, H 3.99, N 9.79; Found: C 39.13, H 3.97, N 9.73. UV-vis in CH_3CN at 0.1 mM [Cu] concentration: 256 nm (ε = 11 300 M^{-1} cm^{-1}), 285 nm (ε = 3 400 M^{-1} cm^{-1}), 690 nm (ε = 90 M^{-1} cm^{-1}).

*[Cu^{II}(**L^1NH_2**)(Cl)](BF_4)*

L^1NH_2 (133 mg; 0.55 mmol), [$Cu^{II}(H_2O)_6$](BF_4)$_2$ (95 mg; 0.27 mmol) and $Cu^{II}Cl_2 \cdot 2\ H_2O$ (47 mg; 0.27 mmol) were dissolved in 10 mL CH_3CN. This solution was added drop wise to 100 mL diethyl ether. The powder was filtered and washed with diethyl ether yielding [Cu^{II}(**L^1NH_2**)(Cl)](BF_4) (141 mg; 0.33 mmol; 60%) as a light blue powder. Crystals suitable for X-ray structure determination were obtained by slow vapor diffusion of diethyl ether into a CH_3CN solution containing the complex. ESI-MS found (calculated) for [M – BF_4]$^+$ *m*/*z* 340.1 (340.1). IR (neat, cm^{-1}): 3366*m*, 3303*w*, 1605*m*, 1575*w*, 1477*w*, 1447*m*, 1439*m*, 1265*w*, 1045*vs*, 1021*vs*, 964*s*, 941*m*, 886*w*, 765*vs*, 643*m*, 566*m*, 522*m*, 490*m*. Elemental analysis calcd for [Cu^{II}(**L^1NH_2**)(Cl)](BF_4): C 39.28, H 4.24, N 13.09; Found: C 39.34, H 4.27, N 12.97. UV-vis in CH_3CN at 0.1 mM [Cu] concentration: 258 nm (ε = 9 800 M^{-1} cm^{-1}), 293 nm (ε = 3 900 M^{-1} cm^{-1}), 700 nm (ε = 110 M^{-1} cm^{-1}), 690 nm (ε = 220 M^{-1} cm^{-1}).

*[Cu^{II}(**Py_2NH**)(Cl)](BF_4)*

From **Py_2NH** (223 mg; 1.12 mmol), [$Cu^{II}(H_2O)_6$](BF_4)$_2$ (193 mg; 0.56 mmol) and $Cu^{II}Cl_2 \cdot 2\ H_2O$ (96 mg; 0.56 mmol), the product [Cu^{II}(**Py_2NH**)(Cl)](BF_4) (341 mg; 0.89 mmol; 79%) was obtained as a dark blue powder. ESI-MS found (calculated) for [M – BF_4]$^+$ *m*/*z* 296.9 (297.0). IR (neat, cm^{-1}): 3466*w*, 3215*w*, 1611*m*, 1574*w*, 1483*w*, 1445*m*, 1285*w*, 1051*vs*, 1028*vs*, 1001*vs*, 935*s*, 815*w*, 764*vs*, 727*m*, 656*w*, 520*m*, 483*w*. Elemental analysis calcd for [Cu^{II}(**Py_2NH**)(Cl)](BF_4) $\cdot$ H_2O: C 35.76, H 3.75, N 10.43; Found: C 37.01, H 3.85, N 10.68. UV-vis in CH_3CN at 0.1 mM [Cu] concentration: 255 nm (ε = 12 000 M^{-1} cm^{-1}), 293 nm (ε = 2 100 M^{-1} cm^{-1}), 660 nm (ε = 120 M^{-1} cm^{-1}).

*[Cu^{II}(**Py_2S**)(Cl)](BF_4)*

From **Py_2S** (112 mg; 0.52 mmol), [$Cu^{II}(H_2O)_6$](BF_4)$_2$ (89 mg; 0.26 mmol) and $Cu^{II}Cl_2 \cdot 2\ H_2O$ (44 mg; 0.26 mmol), the product [Cu^{II}(**Py_2S**)(Cl)](BF_4) (159 mg; 0.40 mmol; 76%) was obtained as a turquoise blue powder. ESI-MS found (calculated) for [M – BF_4]$^+$ *m*/*z* 313.9 (314.0); [M + CH_3CN

– Cl – BF_4]$^+$ *m*/*z* 320.0 (320.0). IR (neat, cm^{-1}): 2929*w*, 1602*m*, 1568*w*, 1474*m*, 1446*m*, 1406*m*, 1262*m*, 1106*m*, 1074*s*, 1052*s*, 1024*s*, 997*vs*, 890*m*, 783*vs*, 764*m*, 717*m*, 649*m*, 518*m*, 475*m*. Elemental analysis calcd for [Cu^{II}(**Py_2S**)(Cl)](BF_4): C 35.84, H 3.01, N 6.97, S 7.97; Found: C 34.85, H 2.89, N 6.65, S 8.06. UV-vis in CH_3CN at 0.1 mM [Cu] concentration: 265 nm (ε = 11 600 M^{-1} cm^{-1}), 320 nm (ε = 1 900 M^{-1} cm^{-1}), 360 nm (ε = 2 800 M^{-1} cm^{-1}), 690 nm (ε = 220 M^{-1} cm^{-1}).

7.5.5 Catalysis experiments

To 1 000 μL CH_3CN in a 1 cm quartz cuvette was added 1 000 μL catalyst solution (0.0012 mmol mononuclear complex or 0.0006 mmol dinuclear complex in CH_3CN; when the complex was made in situ Na_2SO_4 was added to remove most of the H_2O present), followed by 1 000 μL 3,5-di-*tert*-butylcatechol solution (0.06 mmol in CH_3CN). The solution was stirred and kept at a temperature of 25 °C using a Cary Single Cell Peltier Accessory from Agilent Technologies (Type SPV-1X0) and a mixture of N_2:O_2(50:50) was bubbled through the solution with a needle. At the start of the measurement NEt_3 was added (8.36 μL, 0.06 mmol) and the formation of 3,5-di-*tert*-butyl-*o*-benzoquinone was monitored by measuring the absorbance at 400 nm every 0.1 sec. Every measurement was carried out in quadruplo or quintuplo. The average value is reported.

7.6 References

1. Itoh, S.; Nagagawa, M.; Fukuzumi, S., *J. Am. Chem. Soc.* **2001,** *123*, 4087-4088.
2. Ording-Wenker, E. C. M.; van der Plas, M.; Siegler, M. A.; Bonnet, S.; Bickelhaupt, F. M.; Fonseca Guerra, C.; Bouwman, E., *Inorg. Chem.* **2014,** *53*, 8494-8504.
3. Jacobson, R. R.; Tyeklar, Z.; Farooq, A.; Karlin, K. D.; Liu, S.; Zubieta, J., *J. Am. Chem. Soc.* **1988,** *110*, 3690-3692.
4. Hayashi, H.; Fujinami, S.; Nagatomo, S.; Ogo, S.; Suzuki, M.; Uehara, A.; Watanabe, Y.; Kitagawa, T., *J. Am. Chem. Soc.* **2000,** *122*, 2124-2125.
5. Kieber-Emmons, M. T.; Ginsbach, J. W.; Wick, P. K.; Lucas, H. R.; Helton, M. E.; Lucchese, B.; Suzuki, M.; Zuberbühler, A. D.; Karlin, K. D.; Solomon, E. I., *Angew. Chem. Int. Ed.* **2014,** *53*, 4935-4939.
6. Koval, I. A.; Gamez, P.; Belle, C.; Selmeczi, K.; Reedijk, J., *Chem. Soc. Rev.* **2006,** *35*, 814-840.
7. Eicken, C.; Krebs, B.; Sacchettini, J. C., *Curr. Opin. Struc. Biol.* **1999,** *9*, 677-683.
8. Allen, S. E.; Walvoord, R. R.; Padilla-Salinas, R.; Kozlowski, M. C., *Chem. Rev.* **2013,** *113*, 6234-6458.
9. Reedijk, J., *Science* **2005,** *308*, 1876-1877.
10. Ording-Wenker, E. C. M.; Siegler, M. A.; Lutz, M.; Bouwman, E., *Inorg. Chem.* **2013,** *52*, 13113-13122.
11. Ertuerk, H.; Hofmann, A.; Puchta, R.; van Eldik, R., *Dalton Trans.* **2007**, 2295-2301.
12. Turba, S.; Walter, O.; Schindler, S.; Nielsen, L. P.; Hazell, A.; McKenzie, C. J.; Lloret, F.; Cano, J.; Julve, M., *Inorg. Chem.* **2008,** *47*, 9612-9623.

13. Schindler, S.; Szalda, D. J.; Creutz, C., *Inorg. Chem.* **1992,** *31*, 2255-2264.
14. Britovsek, G. J. P.; England, J.; White, A. J. P., *Inorg. Chem.* **2005,** *44*, 8125-8134.
15. Malachowski, M. R.; Huynh, H. B.; Tomlinson, L. J.; Kelly, R. S.; Jun, J. W. F., *J. Chem. Soc., Dalton Trans.* **1995**, 31-36.
16. Ording-Wenker, E. C. M.; van der Plas, M.; Siegler, M. A.; Fonseca Guerra, C.; Bouwman, E., *Chem. Eur. J.* **2014,** *20*, 16913-16921.
17. Herges, R.; Dikmans, A.; Jana, U.; Kohler, F.; Jones, P. G.; Dix, I.; Fricke, T.; Konig, B., *Eur. J. Org. Chem.* **2002**, 3004-3014.
18. Martel, H. J. J. B.; Rasmussen, M., *Tetrahedron Lett.* **1971,** *12*, 3843-3846.
19. Sundaravel, K.; Sankaralingam, M.; Suresh, E.; Palaniandavar, M., *Dalton Trans.* **2011,** *40*, 8444-8458.
20. Tse, E. C. M.; Schilter, D.; Gray, D. L.; Rauchfuss, T. B.; Gewirth, A. A., *Inorg. Chem.* **2014,** *53*, 8505-8516.
21. Addison, A. W.; Rao, T. N.; Reedijk, J.; Vanrijn, J.; Verschoor, G. C., *J. Chem. Soc., Dalton Trans.* **1984**, 1349-1356.
22. Schatz, M.; Leibold, M.; Foxon, S. P.; Weitzer, M.; Heinemann, F. W.; Hampel, F.; Walter, O.; Schindler, S., *Dalton Trans.* **2003**, 1480-1487.
23. Winter, A.; Zabel, A.; Strauch, P., *Int. J. Mol. Sci.* **2012,** *13*, 1612-1619.
24. Solomon, E. I.; Baldwin, M. J.; Lowery, M. D., *Chem. Rev.* **1992,** *92*, 521-542.
25. Kovalchukova, O. V.; Palkina, K. K.; Strashnova, S. B.; Zaitsev, B. E., *Russ. J. Coord. Chem.* **2008,** *34*, 830-835.
26. Thomas, A. M.; Lin, B.-L.; Wasinger, E. C.; Stack, T. D. P., *J. Am. Chem. Soc.* **2013,** *135*, 18912-18919.
27. Osako, T.; Ueno, Y.; Tachi, Y.; Itoh, S., *Inorg. Chem.* **2004,** *43*, 6516-6518.
28. Midoes, A. C. D.; Aranha, P. E.; dos Santos, M. P.; Tozzo, E.; Romera, S.; Santos, R. H. d. A.; Dockal, E. R., *Polyhedron* **2008,** *27*, 59-64.
29. Monzani, E.; Quinti, L.; Perotti, A.; Casella, L.; Gullotti, M.; Randaccio, L.; Geremia, S.; Nardin, G.; Faleschini, P.; Tabbi, G., *Inorg. Chem.* **1998,** *37*, 553-562.
30. Selmeczi, K.; Reglier, M.; Giorgi, M.; Speier, G., *Coord. Chem. Rev.* **2003,** *245*, 191-201.
31. Sheldrick, G. M., *Acta Crystallogr. Sect. A* **2008,** *64*, 112-122.
32. Schreurs, A. M. M.; Xian, X.; Kroon-Batenburg, L. M. J., *J. Appl. Crystallogr.* **2010,** *43*, 70-82.
33. Sheldrick, G. M., *SADABS and TWINABS: Siemens Area Detector Absorption Correction*; Universität Göttingen: Göttingen Germany, **1999**.
34. Herbst-Irmer, R.; Sheldrick, G. M., *Acta Crystallogr. Sect. B: Struct. Sci.* **1998,** *54*, 443-449.
35. Spek, A. L., *Acta Crystallogr. Sect. D. Biol. Crystallogr.* **2009,** *65*, 148-155.

Chapter 8

Summary, Conclusions & Outlook

8.1 Summary

8.1.1 Introduction

Chemical reactions in biological systems are catalyzed by a great variety of enzymes. Many of these enzymes contain copper, because of its ability to cycle between Cu^{II} and Cu^{I} oxidation states without difficulty.[1] The catalyzed reactions are very fast and efficient and to understand these processes, synthetic models are used to gain more insight into how these reactions take place within the enzyme and to see whether we can learn from them for other catalytic processes. Our interest was captured by the electron-shuttling Cu_A site which contains two copper ions bridged by two cysteine thiolate moieties and is found in cytochrome *c* oxidase and N_2O reductase.[2-4] Designing synthetic models for this active site is challenging, because of the redox reaction that commonly takes place upon addition of a thiolate compound to a Cu^{II} ion: 2 Cu^{II} + 2 LS^- → 2 Cu^{I} + LSSL. However, it has been reported that this redox reaction actually is an equilibrium, which can be influenced by ligand structure, solvent or the presence of chloride ions.[5-8] A schematic view of this equilibrium is given in Figure 8.1.

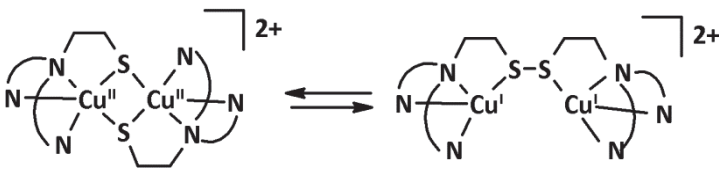

Figure 8.1: Schematic representation of the redox equilibrium between a Cu^{II} μ-thiolate complex and a Cu^{I} disulfide species.

In Chapter 1, an overview is given of different types of copper enzymes and their active sites. This is followed by a sum-up of the different synthetic analogs of the Cu_A site among which are a number of Cu^{II} μ-thiolate complexes. Subsequently different reported Cu^{II} μ-thiolate/Cu^{I} disulfide equilibria are discussed together with a similar cobalt-based equilibrium.

8.1.2 The Cu^{II} μ-Thiolate - Cu^{I} Disulfide Equilibrium

The equilibrium between the Cu^{II} μ-thiolate and Cu^{I} disulfide species can be controlled by inducing small ligand changes, adding chloride ions or changing the solvent. There is, however, limited understanding of why or when the Cu^{II} μ-thiolate complex forms. In Chapter 2, two new ligands **L^2SSL^2** and **L^4SSL^4** are introduced

which, together with three ligands from literature,[5] form two series of ligands with either increasing bulk on the pyridyl ring or an increasing number of (longer) ethylene bridges towards the pyridyl ring. The two new ligands both have the ability to form Cu^{II} μ-thiolate complexes but the complexes differ in their redox-conversion to the Cu^{I} disulfide species. When the ligand **L^2SSL^2** is combined with a Cu^{I} salt, it forms a Cu^{II} μ-thiolate complex in apolar solvents but a Cu^{I} disulfide species in polar solvents. The Cu^{II} μ-thiolate complex can be converted to a Cu^{I} disulfide complex by adding the polar solvent CH_3CN to the less polar CH_2Cl_2. Furthermore, we found that this equilibrium is temperature-dependent and can be reversibly switched at lower temperatures in methanol with the Cu^{I} species being the thermodynamically favored product at higher temperatures. The ligand **L^4SSL^4** forms a Cu^{II} μ-thiolate complex when reacted with a Cu^{I} salt in both polar and apolar solvents, but this Cu^{II} compound is irreversibly converted to the Cu^{I} disulfide complex by heating. So in the case of **L^4SSL^4**, the Cu^{II} μ-thiolate species is formed as the kinetic product whereas the Cu^{I} disulfide complex is the thermodynamic product. To gain insight in the energies that are involved in these equilibria and what causes the observed differences, DFT calculations were carried out on all the Cu^{II} thiolate and Cu^{I} disulfide complexes of the two ligand series. It was found that the Cu^{I} disulfide species is indeed lower in energy than the Cu^{II} μ-thiolate species, but that there is an increase in energy difference between the two states with increasing steric bulk or increasing number of ethylene bridges in the ligands. This implies that the energy of deformation of the ligand from its equilibrium structure to the geometry in the complex determines whether the Cu^{II} μ-thiolate complex forms. The position of the equilibrium between the two redox-isomeric species seems to be largely dependent on the activation barrier of going from the thiolate to the disulfide complex.

Another Cu^{II} μ-thiolate/Cu^{I} disulfide equilibrium with a very similar ligand was reported to be controlled by the presence of protons.[9] Isolation of a complex containing both Cu^{II} thiolate moieties and dissociated Cu^{I} ions directed us to consider the possibility that the proton-induced conversion of a Cu^{II} thiolate compound to a Cu^{I} disulfide species might actually result in dissociation of the ligand. Our investigations in this proton-induced conversion are described in Chapter 3. ^{1}H NMR and UV-vis measurements showed that the ligand dissociates from the copper ions after addition of 4 equiv of protons to the dinuclear Cu^{II} μ-thiolate species; a number of protons that corresponds to one proton per pyridyl group. However, from the experimental data it was not clear what happens after addition of two H^+. To clarify this, the protonation of these complexes was studied computationally with DFT. The calculations showed that indeed the pyridyl-nitrogen is protonated, but in addition

revealed that ligand dissociation is favored by more than 100 kJ mol^{-1} over conversion to a protonated Cu^{I} disulfide complex. The ligand dissociation reaction is schematically shown in Figure 8.2. A similar ligand dissociation reaction was shown experimentally to occur for a Cu^{I} disulfide complex.

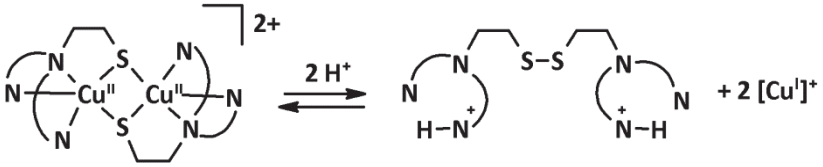

Figure 8.2: Schematic representation of the ligand dissociation that takes place after protonation of a Cu^{II} μ-thiolate complex.

8.1.3 Cu^{II} μ-Thiolate Oxidation

Many copper-containing proteins are involved in O_2 activation reactions and some of these copper enzymes contain sulfur ligands. It is therefore of interest to know how oxidation sensitive these enzymes are. Furthermore, thiols such as cysteine play an important role in biological reduction/oxidation chemistry via disulfide formation, but also via further oxidation to sulfenic, sulfinic and sulfonic acids.[10] In Chapter 4, our studies concerning the oxidation of a Cu^{I} thiolate complex are described. Isolation of a multinuclear Cu^{II}-Cu^{I} thiolate complex that is a potential intermediate in the oxidation reaction, together with UV-vis measurements, indicated that the oxidation proceeds via a Cu^{II} μ-thiolate complex, thus initially via oxidation of copper instead of direct oxidation of the thiolate ligands. The oxidation of the Cu^{I} thiolate species ultimately results in formation of Cu^{II} sulfinate and Cu^{II} sulfonate complexes that were isolated, analyzed and compared.

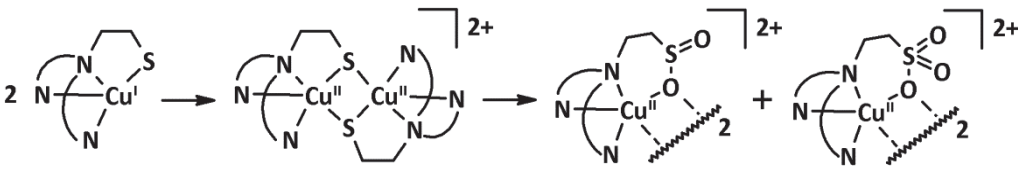

Figure 8.3: Schematic representation of the complete oxidation of a Cu^{I} thiolate complex to Cu^{II} sulfinate and Cu^{II} sulfonate complexes via formation of a Cu^{II} μ-thiolate species.

It was found that the sulfinate and sulfonate complexes are spectroscopically very similar, but electrochemically quite different. This difference is most likely caused by

the relative hardness of the sulfonate group that is not suitable for stabilization of the Cu^{I} oxidation state. A schematic overview of the oxidation process is given in Figure 8.3.

8.1.4 Small Ligand Changes Prevent Cu^{II} μ-Thiolate Formation

The Cu^{II} μ-thiolate complex provides a synthetic model for the Cu_A active site, but its synthesis is complicated by its conversion to a Cu^{I} disulfide complex. Small changes in the ligand structure can determine whether a Cu^{II} μ-thiolate or Cu^{I} disulfide complex is formed. The synthesis of three new disulfide ligands is described in Chapter 5, to analyze the effects on Cu^{II} μ-thiolate formation. The ligand **L^1SXSL^1** is similar to the ligand **L^{1*}SSL^{1*}** that was shown to form Cu^{II} μ-thiolate compounds, but is made more rigid by incorporation of an extra carbon-carbon bond. This ligand precludes Cu^{II} μ-thiolate formation, because of the large rearrangement necessary to allow for intermolecular Cu^{II} thiolate formation. The other ligands described in Chapter 5 have different electronic properties due to substitution of the pyridyl group by a pyrazole or 3,5-dimethylpyrazole moiety. Reaction of these pyrazole-based ligands with Cu^{I} salts resulted in formation of Cu^{I} complexes that are stable in air for days. The half-wave potentials of these three Cu^{I} complexes were determined and compared to the half-wave potential of a Cu^{I} complex that was formed by thermal conversion of a Cu^{II} μ-thiolate compound (Chapter 2). The comparison indicates that in order to allow formation of both Cu^{II} μ-thiolate and Cu^{I} disulfide species, a half-wave potential of roughly 0 V vs Ag/AgCl would be ideal. A number of Cu^{II} complexes obtained with the disulfide ligands and different counterions are also described in Chapter 5.

8.1.5 Similarities Between Copper-Thiolate and Copper-Oxygen Chemistry

A large part of biomimetic copper research reported in literature has been focused on aromatic ring oxidation of phenols and catechols, because these reactions are models for the activity of enzymes like tyrosinase and catechol oxidase.[1, 11] In Chapters 6 and 7 the reaction of copper complexes with phenols and catechol is described; the results reveal the similarities between copper-thiolate and copper-oxygen chemistry.

A mixture of a Cu^{I} complex with phenol was opened to air, which resulted in formation of a dark purple mononuclear Cu^{II} phenolate species. Its structure was determined by X-ray crystallography and described in Chapter 6. The formation of this species is interesting, because usually oxidation leads to ring oxygenation or oxidative phenol coupling.[12] Over time, the purple phenolate complex undergoes a

unique redox reaction to form a yellow Cu^{I} species and a phenolate radical, that reacts further to form a diaryl peroxide or an aromatic ether. This was confirmed by NMR and UV-vis spectroscopy and the appearance of a new Raman band. The rate of conversion is dependent on the concentration of the mononuclear species as well as the *para*-substituent on the phenyl group. A schematic representation of the conversion is given in Figure 8.4; the ligand that is used in this conversion is similar to the ligand used for Cu^{II} μ-thiolate formation. This redox reaction is analogous to the copper thiolate/disulfide redox reaction, only instead of converting 2 R-S^- to 2 R-$S^\bullet$ that reacts further to R-S-S-R, R-O^- is converted to R-$O^\bullet$.

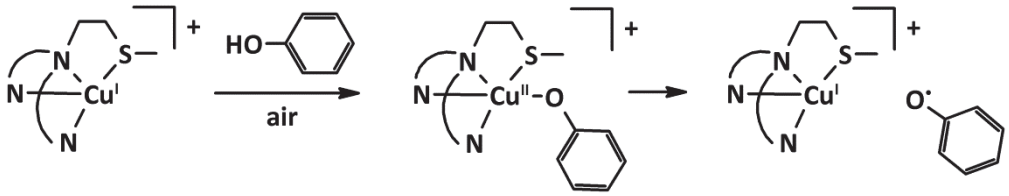

Figure 8.4: Schematic representation of the formation of a Cu^{II} phenolate species and its further redox conversion into a Cu^{I} complex and a phenolate radical.

To further investigate the similarities between the copper-oxygen and copper-sulfur chemistry, the catalytic oxidation of 3,5-di-*tert*-butylcatechol (3,5-DTBC) to 3,5-di-*tert*-butyl-*o*-benzoquinone (3,5-DTBQ) was investigated; the results are reported in Chapter 7. A large library of mononucleating and dinucleating ligands was synthesized and with these ligands [Cu^{II}(ligand)(Cl)](BF_4) complexes were formed to test in catalysis. For a number of these complexes crystal structures were obtained, that showed relatively large Cu…Cu distances for the dinucleating ligands. The catalytic oxidation of 3,5-DTBC occurred with higher turnover frequencies (TOFs) using the catalytic systems based on dinucleating ligands than those containing mononucleating ligands, confirming the need for two copper sites in catalysis. Furthermore, the ligands with the ability to form Cu^{II} μ-thiolate complexes displayed the highest TOFs; the highest initial TOF reached with such a system was 7800 h^{-1}. However, the oxidation of 3,5-DTBC became slower in time indicating catalyst degradation. These results again imply that there is a relation between thiolate formation with copper ions and their reaction with dioxygen. It can be hypothesized that the high activity is caused by the ability of these complexes to stabilize the Cu^{II}_2 μ-η^2:η^2-peroxide intermediate as it is similar to the Cu^{II} μ-thiolate complex. After all,

formation of the Cu^{II}_2 μ-η^2:η^2-peroxide species has been postulated to be the rate-determining step in the reaction.[11, 13]

8.2 Conclusions & Outlook

The equilibrium between Cu^{II} μ-thiolate and Cu^{I} disulfide species has been shown very sensitive to small changes in either ligand structure or reaction conditions. In this thesis, the energies involved in this equilibrium have been clarified to give a better view on why either one or the other species forms. Other aspects such as formation, protonation and oxidation of the Cu^{II} μ-thiolate complex have also been investigated yielding insight in the impact of different possible reactions occurring in biological systems, such as pH changes and oxidative enzyme degradation. However, it is difficult to determine whether these synthetic analogs are representatives for the active sites in metalloenzymes. Most of the reactions described in this thesis have been carried out in acetonitrile, which is polar, but not a protic solvent like water. Furthermore, acetonitrile stabilizes Cu^{I}, whereas H_2O generally leads to disproportionation of Cu^{I} salts into Cu^{II} and Cu^{0} when they are not stabilized by their ligands. Enzymes create an environment around the active site in which hydrogen bonding plays an important role, which is rather difficult to mimic in a small model system. Still, there are indications that the reactions that we investigated are similar to what actually may occur in the biological system. The ligand dissociation we observed after protonation of a Cu^{II} μ-thiolate species, has been postulated to occur similarly in the Cu_A site as well. It has been hypothesized that protonation of the Cu_A site induces dissociation of one of the equatorial histidine ligands, which might also lead to a change in valence state of the copper ions.[14-18] In this case the synthetic model does allow for a more detailed understanding of the natural active site. However, the reactivity of the synthetic models described in this thesis should not be used to draw conclusions about the biological system, but they can be used to support existing data about enzymatic structures and reactions.

The similarities between copper-thiolate and copper-oxide chemistry are demonstrated in Chapter 6 and 7. This is a relatively unexplored field of coordination chemistry. The conversion of a phenolate to a phenolate radical by oxidation with Cu^{II} ions is unprecedented and deserves further attention. The fact that sulfur and oxygen react in a similar way with copper and are interchangeable in some cases, allows for exploring other synthetic reactions with sulfur or oxygen-containing compounds. Furthermore, if the efficiency of 3,5-DTBC oxidation is indeed increased by better stabilization of the Cu^{II}_2 μ-η^2:η^2-peroxide intermediate by ligands that

support Cu^{II} μ-thiolate-type complexes, other types of oxidative catalysis might be worthwhile studying with these systems.

8.3 References

1. Solomon, E. I.; Heppner, D. E.; Johnston, E. M.; Ginsbach, J. W.; Cirera, J.; Qayyum, M.; Kieber-Emmons, M. T.; Kjaergaard, C. H.; Hadt, R. G.; Tian, L., *Chem. Rev.* **2014,** *114*, 3659-3853.
2. Iwata, S.; Ostermeier, C.; Ludwig, B.; Michel, H., *Nature* **1995,** *376*, 660-669.
3. Tsukihara, T.; Aoyama, H.; Yamashita, E.; Tomizaki, T.; Yamaguchi, H.; Shinzawaitoh, K.; Nakashima, R.; Yaono, R.; Yoshikawa, S., *Science* **1995,** *269*, 1069-1074.
4. Brown, K.; Tegoni, M.; Prudencio, M.; Pereira, A. S.; Besson, S.; Moura, J. J.; Moura, I.; Cambillau, C., *Nat. Struct. Biol.* **2000,** *7*, 191-195.
5. Itoh, S.; Nagagawa, M.; Fukuzumi, S., *J. Am. Chem. Soc.* **2001,** *123*, 4087-4088.
6. Osako, T.; Ueno, Y.; Tachi, Y.; Itoh, S., *Inorg. Chem.* **2004,** *43*, 6516-6518.
7. Ueno, Y.; Tachi, Y.; Itoh, S., *J. Am. Chem. Soc.* **2002,** *124*, 12428-12429.
8. Neuba, A.; Haase, R.; Meyer-Klaucke, W.; Flörke, U.; Henkel, G., *Angew. Chem. Int. Ed.* **2012,** *51*, 1714-1718.
9. Thomas, A. M.; Lin, B.-L.; Wasinger, E. C.; Stack, T. D. P., *J. Am. Chem. Soc.* **2013,** *135*, 18912-18919.
10. Jacob, C.; Giles, G. L.; Giles, N. M.; Sies, H., *Angew. Chem. Int. Ed.* **2003,** *42*, 4742-4758.
11. Koval, I. A.; Gamez, P.; Belle, C.; Selmeczi, K.; Reedijk, J., *Chem. Soc. Rev.* **2006,** *35*, 814-840.
12. Allen, S. E.; Walvoord, R. R.; Padilla-Salinas, R.; Kozlowski, M. C., *Chem. Rev.* **2013,** *113*, 6234-6458.
13. Monzani, E.; Quinti, L.; Perotti, A.; Casella, L.; Gullotti, M.; Randaccio, L.; Geremia, S.; Nardin, G.; Faleschini, P.; Tabbi, G., *Inorg. Chem.* **1998,** *37*, 553-562.
14. Alvarez-Paggi, D.; Abriata, L. A.; Murgida, D. H.; Vila, A. J., *Chem. Commun.* **2013,** *49*, 5381-5383.
15. Hay, M. T.; Ang, M. C.; Gamelin, D. R.; Solomon, E. I.; Antholine, W. E.; Ralle, M.; Blackburn, N. J.; Massey, P. D.; Wang, X. T.; Kwon, A. H.; Lu, Y., *Inorg. Chem.* **1998,** *37*, 191-198.
16. Hwang, H. J.; Lu, Y., *P. Natl. Acad. Sci. USA* **2004,** *101*, 12842-12847.
17. Lukoyanov, D.; Berry, S. M.; Lu, Y.; Antholine, W. E.; Scholes, C. P., *Biophys. J.* **2002,** *82*, 2758-2766.
18. Xie, X.; Gorelsky, S. I.; Sarangi, R.; Garner, D. K.; Hwang, H. J.; Hodgsont, K. O.; Hedman, B.; Lu, Y.; Solornon, E. I., *J. Am. Chem. Soc.* **2008,** *130*, 5194-5205.

Appendix I

Supplementary information on Chapter 2

Figure AI.1 Displacement ellipsoid plot of $[Cu^{I}_2(\mathbf{L^3SSL^3})]^{2+}$

Table AI.1 Crystallographic data for $[Cu^{I}_2(\mathbf{L^3SSL^3})](BF_4)_2$

Table AI.2 Selected bond distances and angles of $[Cu^{I}_2(\mathbf{L^3SSL^3})](BF_4)_2$

Figure AI.2 UV-vis absorption spectra of $[Cu^{II}_2(\mathbf{L^2S})_2](BF_4)_2$ and $[Cu^{I}_2(\mathbf{L^2SSL^2})](BF_4)_2$

Figure AI.3 UV-vis absorption spectrum of $[Cu^{I}_2(\mathbf{L^4SSL^4})](BF_4)_2$

Figure AI.4 ^{1}H NMR spectra of $[Cu^{II}_2(\mathbf{L^2S})_2](BF_4)_2$ in CD_3OD at different temperatures

Figure AI.5 ^{1}H NMR spectrum of $[Cu^{II}_2(\mathbf{L^4S})_2](BF_4)_2$ in different solvents

Figure AI.6 Cyclic voltammograms of $[Cu^{II}_2(\mathbf{L^2S})_2](BF_4)_2$ and $[Cu^{II}_2(\mathbf{L^4S})_2](BF_4)_2$

Figure AI.7 Cyclic voltammograms of $[Cu^{I}_2(\mathbf{L^2SSL^2})](BF_4)_2$ and $[Cu^{I}_2(\mathbf{L^4SSL^4})](BF_4)_2$

Figure AI.8 Three optimized geometries for $[Cu^{II}_2(\mathbf{L^2S})_2]^{2+}$

Figure AI.9 Three optimized geometries for $[Cu^{II}_2(\mathbf{L^4S})_2]^{2+}$

Table AI.3 ADF total energies of all Cu^{II} μ-thiolate complexes

Table AI.4 ADF total energies of all Cu^{I} disulfide complexes

Table AI.5 ADF total energies of all copper complexes with MeCN

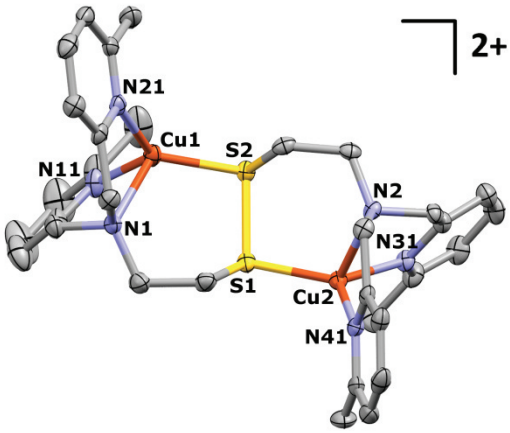

Figure AI.1: Projection of the cationic part of $[Cu^{I}_2(\mathbf{L^3SSL^3})](BF_4)_2$. Displacement ellipsoids are depicted at 50% probability level. All hydrogen atoms are omitted for clarity.

Table AI.1: Crystallographic and structure refinement data for complexes $[Cu^{I}_2(\mathbf{L^3SSL^3})](BF_4)_2$.

	$[Cu^{I}_2(\mathbf{L^3SSL^3})](BF_4)_2$
empirical formula	$[C_{32}H_{40}Cu_2N_6S_2](BF_4)_2$
formula weight	873.52
crystal system	monoclinic
space group	$P2_1/n$
a, Å	11.3108(5)
b, Å	28.8420(11)
c, Å	11.9924(4)
α, deg	90
β, deg	104.604(4)
γ, deg	90
V, Å^3	3785.8(3)
Z	4
D_{calc}, g·cm^3	1.533
T, Kelvin	110(2)
crystal size, mm	$0.21 \times 0.17 \times 0.13$
μ, mm^{-1}	1.306
no. of reflns measd	23924
no. of unique reflns	7045
no. of reflns obsd.	5654
no. of parameters	473
R_1 / wR_2 [$I > 2\sigma(I)$]	0.0431/0.0995
R_1 / wR_2 [all refl.]	0.0595/0.1059
goodness of fit	1.041
$\Delta\rho$, e·Å^{-3}	−0.50/0.78

Structure determination

All reflection intensities for $[Cu^{I}_2(\mathbf{L^3SSL^3})](BF_4)_2$ were measured at 110(2) K using a KM4/Xcalibur (detector: Sapphire3) with enhanced graphite-monochromated Mo *Kα* radiation (λ = 0.71073 Å) under the program CrysAlisPro (Version 1.171.35.11 Oxford Diffraction Ltd., 2011). The program CrysAlisPro was used to refine the cell dimensions and for data reduction. The structure was solved with the program SHELXS-97 (Sheldrick, 2008) and was refined on F^2 with SHELXL-97 (Sheldrick, 2008). Analytical numeric absorption corrections based on a multifaceted crystal model were applied using CrysAlisPro. The temperature of the data collection was controlled using the system Cryojet (manufactured by Oxford Instruments). The H atoms were placed at calculated positions using the instructions AFIX 23, AFIX 43or AFIX 137 with isotropic displacement parameters having values 1.2 or 1.5 times *U*eq of the attached C atoms.

Table AI.2: Selected bond distances and angles for $[Cu^{I}_2(\mathbf{L^3SSL^3})](BF_4)_2$.

Bond distance (Å)		**Bond angle (°)**	
Cu1 - Cu2	5.1494(6)	Cu1 - S1 - Cu2	140.21(4)
S1 - S2	2.0872(12)	Cu1 - S2 - Cu2	137.12(4)
Cu1 - S1	3.2721(8)	S1 - Cu1 - S2	38.96(3)
Cu1 - S2	2.1925(8)	S2 - Cu1 - N1	110.53(7)
Cu1 - N1	2.186(3)	S2 - Cu1 - N11	119.79(8)
Cu1 - N11	2.035(3)	S2 - Cu1 - N21	124.72(8)
Cu1 - N21	2.005(3)	N1 - Cu1 - N11	83.48(11)
Cu2 - S1	2.1901(8)	N1 - Cu1 - N21	81.83(10)
Cu2 - S2	3.3219(8)	N11 - Cu1 - N21	114.99(11)
Cu2 - N2	2.167(3)	S1 - Cu2 - S2	37.94(3)
Cu2 - N31	2.024(3)	S1 - Cu2 - N2	108.51(7)
Cu2 - N41	2.012(3)	S1 - Cu2 - N31	125.10(8)
		S1 - Cu2 - N41	116.95(8)
		N2 - Cu2 - N31	84.04(10)
Dihedral angle (°)		N2 - Cu2 - N41	81.88(10)
Cu1 - S2 - S1 - Cu2	–161.75(4)	N31 - Cu2 - N41	117.70(10)

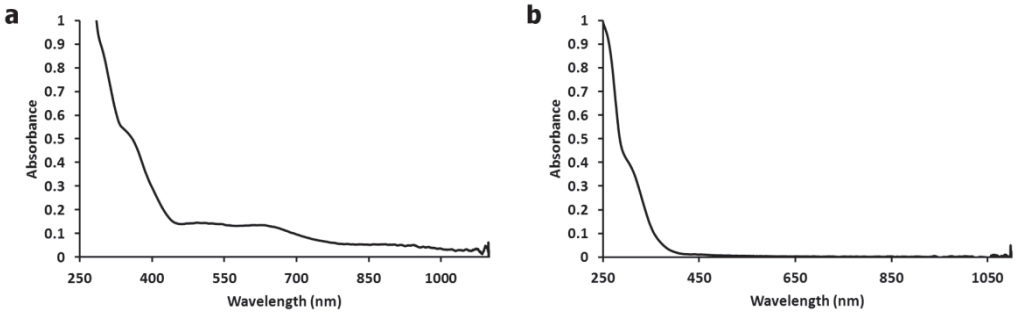

Figure AI.2: UV-vis absorption spectra of $[Cu^{II}_2(\mathbf{L^2S})_2](BF_4)_2$ (a) in dichloromethane and $[Cu^{I}_2(\mathbf{L^2SSL^2})](BF_4)_2$ (b) in acetonitrile at a concentration of 1 mM [Cu], recorded with a transmission dipprobe with a path length of 1.2 mm.

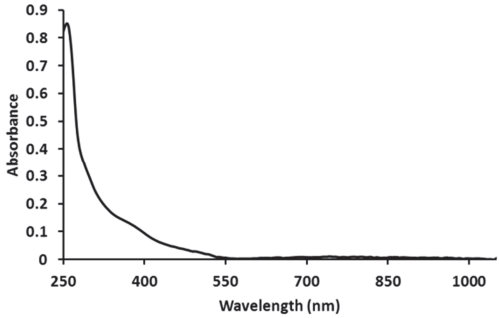

Figure AI.3: UV-vis absorption spectrum of $[Cu^{I}_2(\mathbf{L^4SSL^4})](BF_4)_2$ in methanol at a concentration of 1 mM [Cu], recorded with a transmission dipprobe with a path length of 1.2 mm.

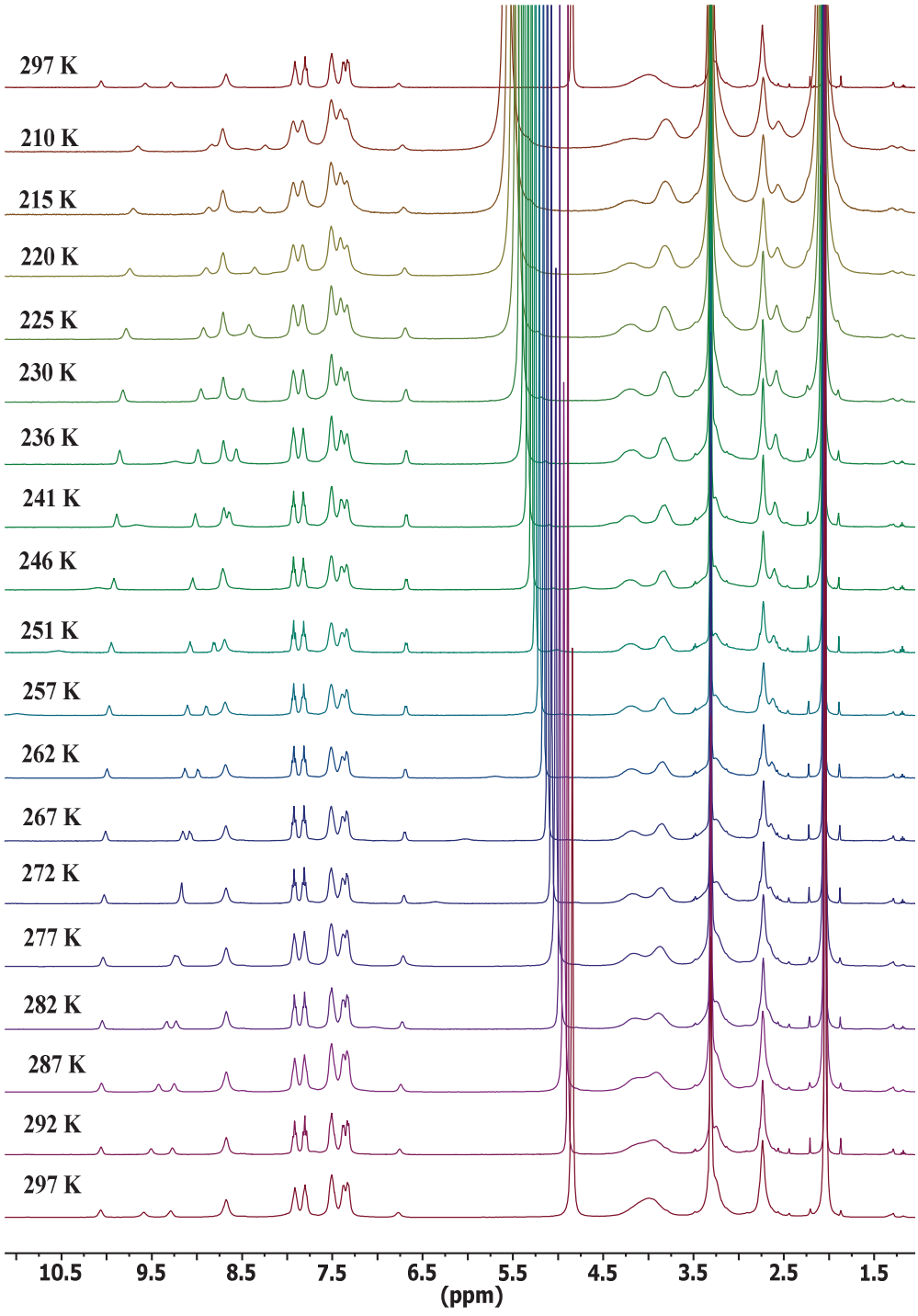

Figure AI.4: ^{1}H NMR spectra of **L^{2}SSL^{2}** and [Cu^{I}(CH$_3$CN)$_4$](BF$_4$) in CD$_3$OD measured first at 297 K, then cooled down and measured from 210 K to 297 K in steps of 5 K.

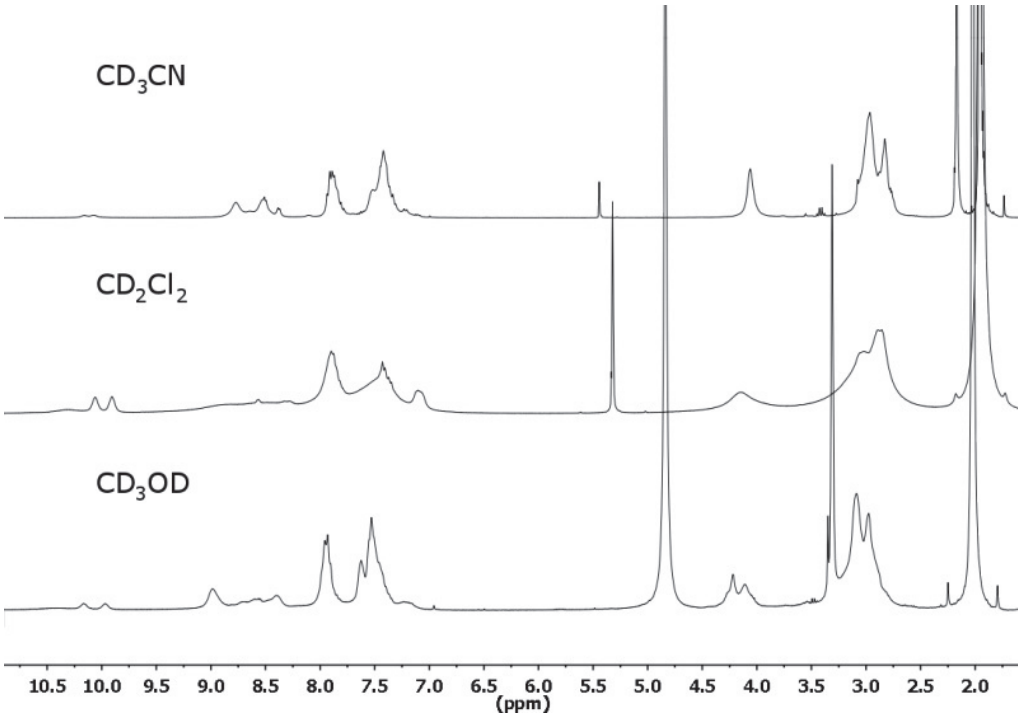

Figure AI.5: ^{1}H NMR spectra of $[Cu^{II}_2(\mathbf{L^4S})_2](BF_4)_2$ in CD_3CN, CD_2Cl_2 and CD_3OD at RT under argon.

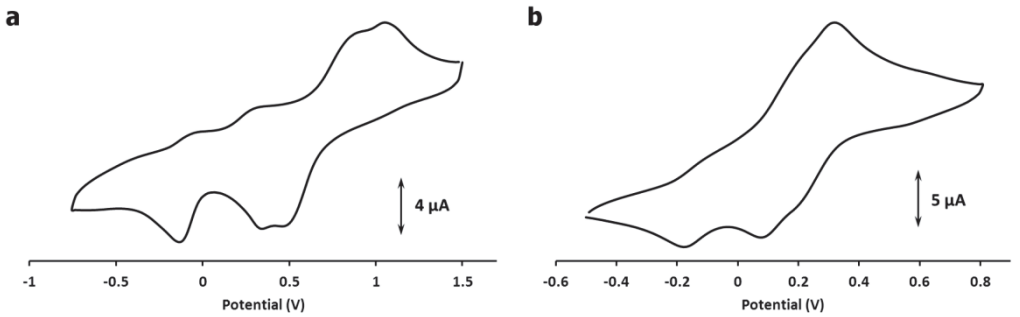

Figure AI.6: Cyclic voltammograms of (a) $[Cu^{II}_2(\mathbf{L^2S})_2](BF_4)_2$ in dichloromethane and (b) $[Cu^{II}_2(\mathbf{L^4S})_2](BF_4)_2$ in methanol at 1 mM [Cu] concentration at RT. The scanrate is 100 mV/s; potentials are given vs. Ag/AgCl.

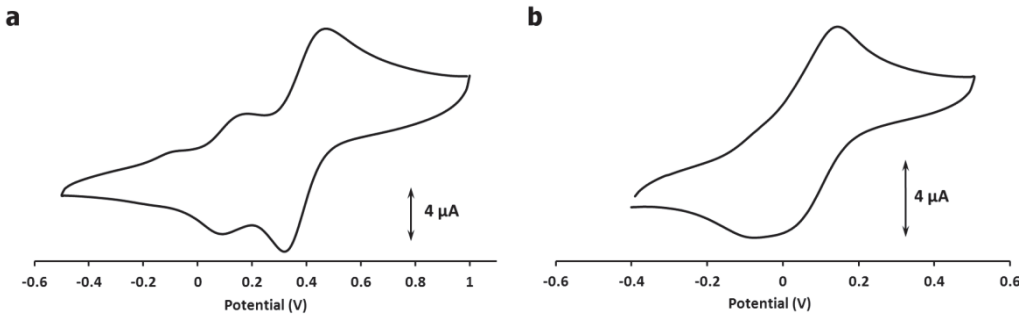

Figure AI.7: Cyclic voltammograms of (a) $[Cu^{I}_2(\mathbf{L^2SSL^2})](BF_4)_2$ in acetonitrile and (b) $[Cu^{I}_2(\mathbf{L^4SSL^4})](BF_4)_2$ in methanol at 1 mM [Cu] concentration at RT. The scanrate is 100 mV/s; potentials are given vs. Ag/AgCl.

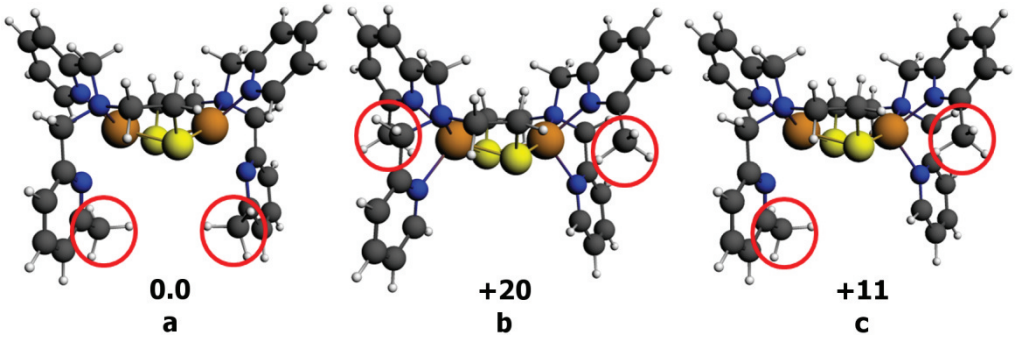

Figure AI.8: A projection of $[Cu^{II}_2(\mathbf{L^2S})_2]^{2+}$ with three different ways of coordination (a, b and c) of the two 6-methylpyridyl groups and the relative energies in kJ/mol, computed at OPBE/TZ2P in MeCN. The methyl groups are highlighted with a red circle.

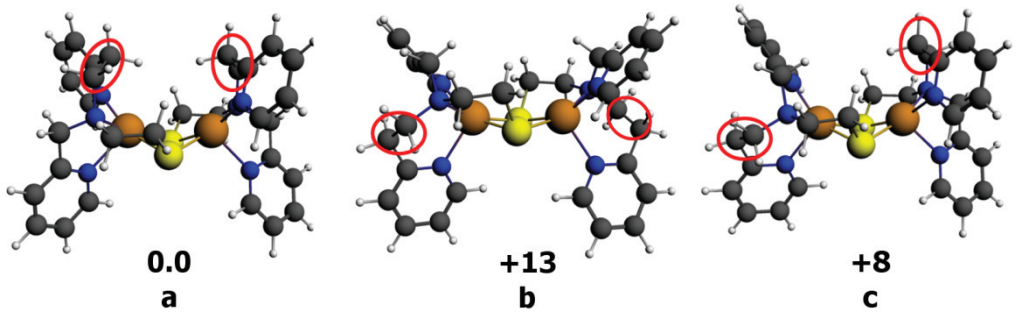

Figure AI.9: A projection of $[Cu^{II}_2(\mathbf{L^4S})_2]^{2+}$ with three different ways of coordination (a, b and c) of the two pyridyl groups with ethylene bridges and the relative energies in kJ/mol, computed at OPBE/TZ2P in MeCN. The ethylene bridges are highlighted with a red circle.

Table AI.3: ADF total energies (kJ mol^{-1}) of all Cu^{II} μ-thiolate complexes computed at ZORA-OPBE/TZ2P.

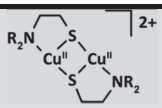 A		MeCN			gas phase		
		E_{SF}	E_1	E_0	E_{SF}	E_1	E_0
L^{1}SSL^1		–40988.3	–40986.8	–40989.9	–40493.5	–40494.2	–40492.9
L^{2}SSL^2	**a**	–44188.9	–44187.7	–44190.0	–43699.6	–43700.7	–43698.5
	b	–44171.2	–44172.7	–44169.7			
	c	–44179.7	–44180.5	–44178.9			
L^{3}SSL^3		–47375.1	–47377.2	–47373.0	–46901.0	–46904.7	–46897.2
L^{4}SSL^4	**a**	–44135.9	–44137.4	–44134.3	–43655.1	–43658.8	–43651.7
	b	–44122.0	–44122.9	–44121.0			
	c	–44128.2	–44130.1	–44126.3			
L^{5}SSL^5		–47253.1	–47257.3	–47248.9	–46785.3	–46791.1	–46779.6

Table AI.4: ADF total energies (kJ mol^{-1}) of all Cu^{I} disulfide complexes computed at ZORA-OPBE/TZ2P.

		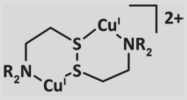 B		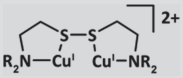 C	
		MeCN	gas phase	MeCN	gas phase
L^{1}SSL^1		–40993.5	–40509.2	–40982.9	–40507.9
L^{2}SSL^2	**a**	–44203.1	–43725.4	–44199.3	–43729.9
	b	–44205.7		–44197.2	
	c	–44204.9		–44198.9	
L^{3}SSL^3		–47412.1	–46942.7	–47406.9	–46944.2
L^{4}SSL^4	**a**	–44150.0	–43676.0	–44182.2	–43705.4
	b	–44145.7			
	c	–44148.1			
L^{5}SSL^5		–47296.2	–46835.0	–47359.1	–46898.8

Table AI.5: Energies of formation (kJ mol^{-1}) of Cu^{II} μ-thiolate (**A**) and Cu^{I} disulfide (**B** or **C**) complexes for different **LSSL** ligands with and without coordinated acetonitrile and with or without coordinated pyridyl or sulfur groups.[a]

	L^1SSL^1	**L^2SSL^2**	**L^3SSL^3**	**L^4SSL^4**	**L^5SSL^5**
A $[Cu^{II}_2(\mathbf{LS})_2]^{2+}$ + 2 CH_3CN	−80	−73	−63	−44	27
A $[Cu^{II}_2(\mathbf{LS})_2(CH_3CN)_2]^{2+}$ - N-pyr uncoordinated	x[b]	+33	+42	+87[d]	+108[d]
B $[Cu^{I}_2(\mathbf{LSSL})]^{2+}$ + 2 CH_3CN	−83	−86	−102	−60	−20
B $[Cu^{I}_2(\mathbf{LSSL})(CH_3CN)_2]^{2+}$ - N-pyr uncoordinated	−2	+10	−5	+70[d]	+26
C $[Cu^{I}_2(\mathbf{LSSL})]^{2+}$ + 2 CH_3CN	−73	−83	−97	−93	−83
C $[Cu^{I}_2(\mathbf{LSSL})(CH_3CN)_2]^{2+}$ - N-pyr uncoordinated	−6	x[c]	x[c]	−3	−19
$[Cu^{I}_2(\mathbf{LSSL})(CH_3CN)_2]^{2+}$ - S uncoordinated	−73	−79	−91[d]	−38	−20

[a] Computed at ZORA-OPBE/TZ2P in CH_3CN (COSMO).

[b] Acetonitrile dissociates from the complex

[c] Sulfur dissociates and pyridyl group re-coordinates

[d] Imaginary frequency (in the range of −23 to −134 cm^{-1}) which shows rotation of the methyl group of CH_3CN

Appendix II

Supplementary information on Chapter 3

Figure AII.1 Cyclic voltammogram of $[Cu^{I}(CH_3CN)_4](BF_4)$

Figure AII.2 UV-vis absorption spectra of $[Cu^{II}_2(\mathbf{L^{2*}S})_2](BF_4)_2$ and $[Cu^{I}_2(\mathbf{L^{2*}SSL^{2*}})](BF_4)_2$

Figure AII.3 UV-vis absorption spectra of $\mathbf{L^{1*}SSL^{1*}}$ with 0, 2 and 4 equivalents of HBF_4

Figure AII.4 UV-vis absorption spectra of $[Cu^{II}_2(\mathbf{L^{1*}S})_2]^{2+}$ with 0 - 4 equivalents of HBF_4

Figure AII.5 UV-vis absorption spectra of $[Cu^{II}_2(\mathbf{L^{1*}S})_2]^{2+}$ with 0 - 10 equivalents of HOTf

Figure AII.6 UV-vis absorption spectra of $[Cu^{II}_2(\mathbf{L^{2*}S})_2]^{2+}$ and $[Cu^{I}_2(\mathbf{L^{2*}SSL^{2*}})]^{2+}$ with 0 - 4 equivalents of HBF_4

Figure AII.7 ^1H NMR spectra of $[Cu^{II}_2(\mathbf{L^{1*}S})_2]^{2+}$ with 0, 2, 4 and 6 equivalents of HOTf

Figure AII.8 Schematic representation of the protonation of the pyridyl groups of **A**

Table AII.1 Relative geometry optimization energies of protonated **A**, **B** and **C**

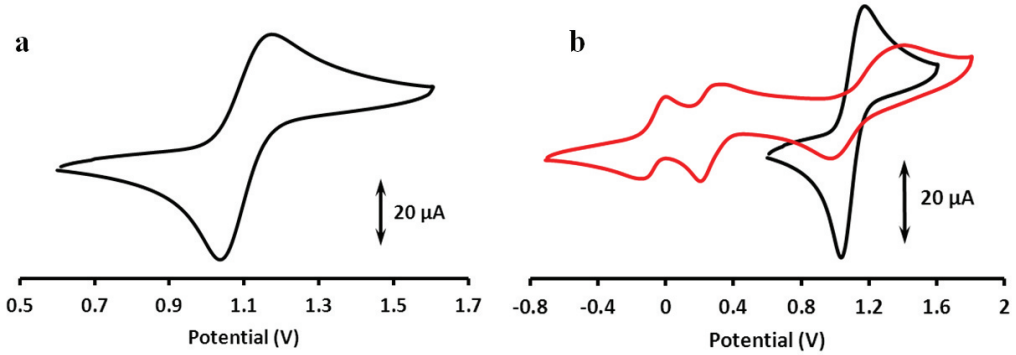

Figure AII.1: Cyclic voltammogram of $[Cu^{I}(CH_3CN)_4](BF_4)$ at a concentration of 2 mM [Cu] (a) compared with $[Cu^{I}_2Cu^{II}_2(\mathbf{L^{1*}S})_2(CH_3CN)_6]^{4+}$ (in red) at 4 mM [Cu] (b) in CH_3CN at RT. The scanrate is 100 mV/s; potentials are given vs. Ag/AgCl.

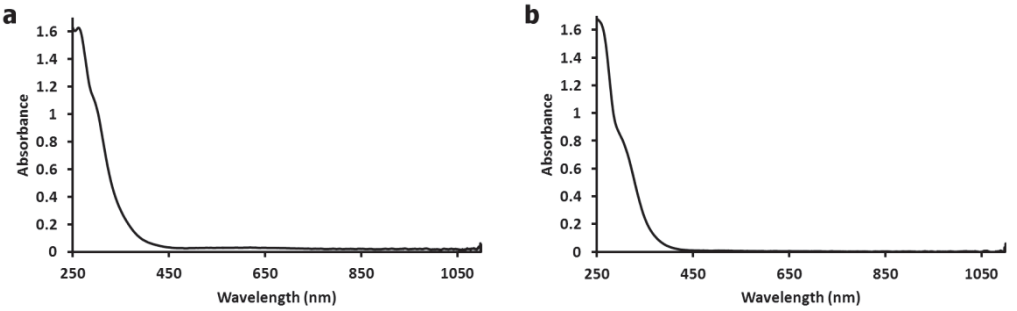

Figure AII.2: UV-vis absorption spectrum of $[Cu^{II}_2(\mathbf{L^{2*}S})_2]^{2+}$ in dichloromethane (a) and $[Cu^{I}_2(\mathbf{L^{2*}SSL^{2*}})]^{2+}$ in CH_3CN (b) at 2 mM [Cu] concentration recorded with a transmission dipprobe set at a pathlength of 1.2 mm.

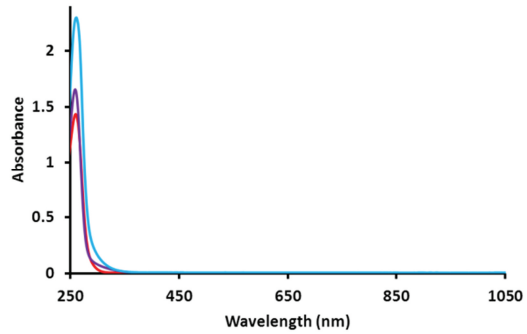

Figure AII.3: UV-vis absorption spectra of $\mathbf{L^{1*}SSL^{1*}}$ with zero (red), two (purple) and four (blue) equivalents of $HBF_4{\cdot}Et_2O$ in CH_3CN at 1 mM concentration recorded with a transmission dipprobe set at a pathlength of 1.2 mm.

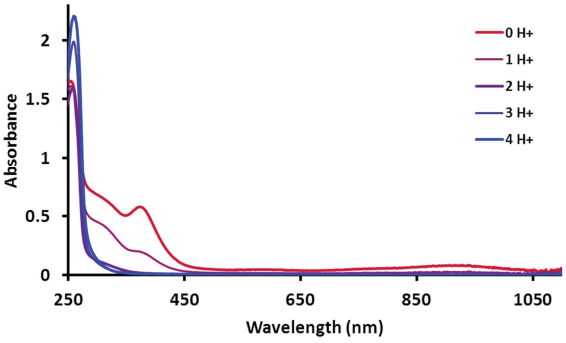

Figure AII.4: UV-vis absorption spectra of $[Cu^{II}_2(\mathbf{L^{1*}S})_2]^{2+}$ with 0 - 4 equivalents of $HBF_4{\cdot}Et_2O$ in CH_3CN at 2 mM [Cu] concentration recorded with a transmission dipprobe set at a pathlength of 1.2 mm.

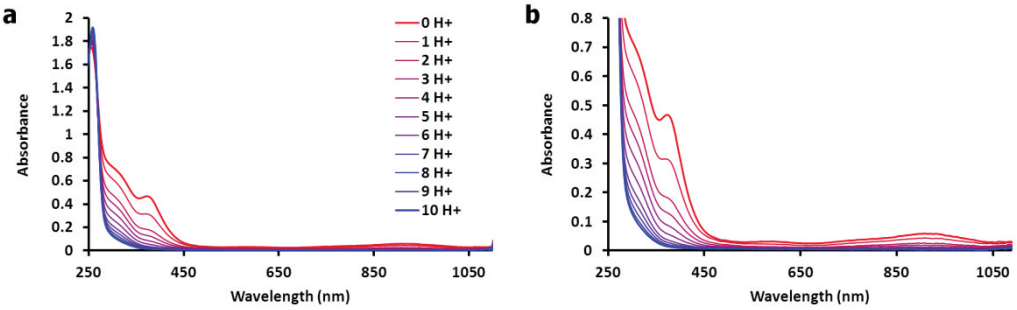

Figure AII.5: UV-vis absorption spectra of $[Cu^{II}_2(\mathbf{L^{1*}S})_2]^{2+}$ with 0 - 10 equivalents of HOTf in CH_3CN at 1 mM [Cu] concentration recorded with a transmission dipprobe set at a pathlength of 2.4 mm. (b) is a zoom of (a).

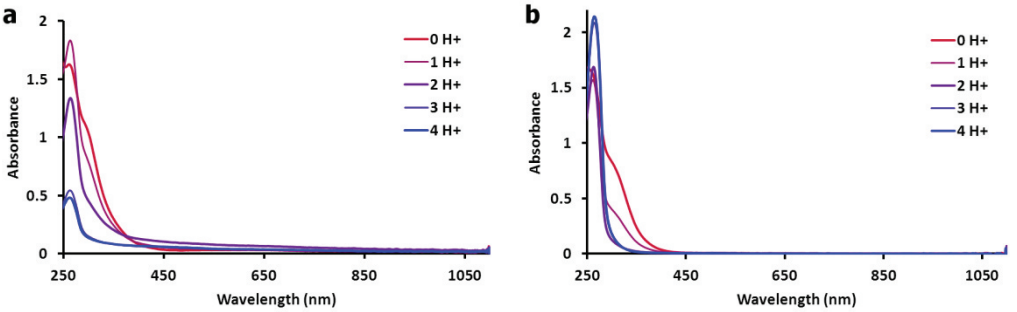

Figure AII.6: UV-vis absorption spectra of $[Cu^{II}_2(\mathbf{L^{2*}S})_2]^{2+}$ in dichloromethane (a) and $[Cu^{I}_2(\mathbf{L^{2*}SSL^{2*}})]^{2+}$ in CH_3CN (b) with 0 - 4 equivalents of $HBF_4{\cdot}Et_2O$ at 2 mM [Cu] concentration recorded with a transmission dipprobe set at a pathlength of 1.2 mm.

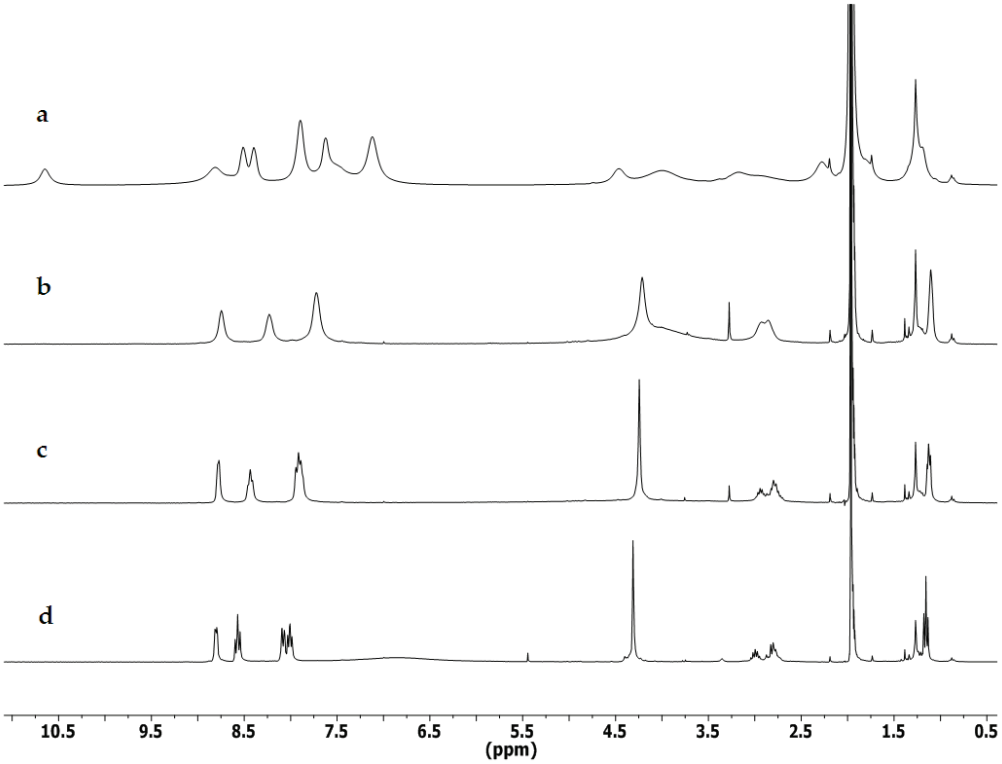

Figure AII.7: ^{1}H NMR spectra of **L^{1}*SSL^{1}*** in CD_3CN with 0 equivalents (a), 2 equivalents (b), 4 equivalents (c) and 6 equivalents (d) of HOTf at RT.

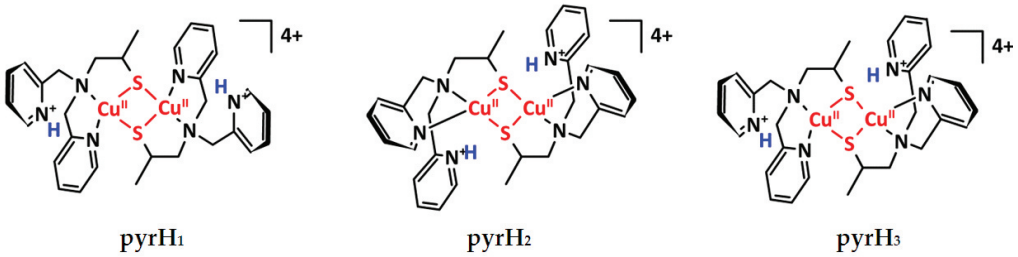

Figure AII.8: Schematic representation of three ways of protonation of two of the four pyridyl groups of $[Cu^{II}_2(\mathbf{L^{1}*S})_2]^{2+}$.

Table AII.1: Relative energies (kJ mol^{-1}) for Cu^{II} μ-thiolate (**A**) and Cu^{I} disulfide (**B** and **C**) complexes protonated in different ways (Figure AII.8) in two enantiomeric forms: *RR*/*SS* and *RS*/*SR* optimized at ZORA-OPBE/TZ2P solvated in CH_3CN (COSMO).

		X: *RR/SS*	**Z**: *RS/SR*
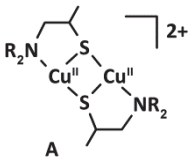 A	**A -** $pyrH_1$	**0**	18
	A - $pyrH_2$	90	25
	A - $pyrH_3$	2	19
	A - R_3NH	212	216
	A - SH	58	59
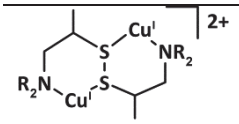 B	**B -** $pyrH_1$	54	37
	B - $pyrH_2$	46	60
	B - $pyrH_3$	27	30
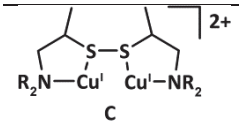 C	**C -** $pyrH_1$	57	51
	C - $pyrH_2$	58	59
	C - $pyrH_3$	78	52

Appendix III

Supplementary information on Chapter 4

Table AIII.1 Selected bond distances and angles of $[Cu^{II}_4Cu^{I}_4(\mathbf{L^{1*}S})_4(\mu\text{-}OH)_2(CH_3CN)_6](ClO_4)_6 \cdot 2\ CH_3CN$

Figure AIII.1 X-Band powder EPR spectra of $[Cu^{II}_2(\mathbf{L^{1*}SO_2})_2](BF_4)_2$ and $[Cu^{II}_2(\mathbf{L^{1*}SO_2})_2\ (OTf)_2]$

Figure AIII.2 X-Band powder EPR spectra of $Cu^{II}_2(\mathbf{L^{1*}SO_3})_2(BF_4)_2$ and $Cu^{II}_2(\mathbf{L^{1*}SO_3})_2(OTf)_2$

Figure AIII.3 X-Band EPR spectrum of $Cu^{II}_2(\mathbf{L^{1*}SO_3})_2(BF_4)_2$ dissolved in acetone

Figure AIII.4 UV-vis absorption spectra of $[Cu^{II}_2(\mathbf{L^{1*}SO_2})_2](BF_4)_2$ and $Cu^{II}_2(\mathbf{L^{1*}SO_3})_2(BF_4)_2$

Table AIII.1: Selected bond distances and angles of $[Cu^{II}_4Cu^{I}_4(\mathbf{L^{1*}S})_4(\mu\text{-}OH)_2(CH_3CN)_6](ClO_4)_6 \cdot 2\ CH_3CN$

	Bond distance (Å)		Bond angle (°)
Cu1 - S1A	2.3474(7)	S1A - Cu2 - S1D	128.55(3)
Cu2 - S1A	2.2174(8)	S1C - Cu3 - S1A	116.45(3)
Cu2 - S1D	2.2357(8)	S1B - Cu5 - S1C	129.27(3)
Cu3 - S1A	2.2967(8)	S1D - Cu6 - S1B	115.29(3)
Cu3 - S1C	2.2545(7)	O1A - Cu1 - S1A	92.93(7)
Cu4 - S1B	2.3408(8)	O1A - Cu4 - S1B	92.85(7)
Cu5 - S1B	2.2223(8)	O1B - Cu7 - S1C	93.88(6)
Cu5 - S1C	2.2257(7)	O1B - Cu8 - S1D	92.36(7)
Cu6 - S1D	2.2767(8)	Cu2 - S1A - Cu3	133.03(3)
Cu6 - S1B	2.2767(8)	Cu2 - S1A - Cu1	94.71(3)
Cu7 - S1C	2.3458(7)	Cu3 - S1A - Cu1	115.27(3)
Cu8 - S1D	2.3550(8)	Cu5 - S1B - Cu6	135.18(3)
Cu1 - O1A	1.924(2)	Cu5 - S1B - Cu4	101.19(3)
Cu4 - O1A	1.936(2)	Cu6 - S1B - Cu4	103.84(3)
Cu7 - O1B	1.909(2)	Cu5 - S1C - Cu3	117.97(3)
Cu8 - O1B	1.908(2)	Cu5 - S1C - Cu7	111.80(3)
Cu1 - N1A	2.039(2)	Cu3 - S1C - Cu7	113.15(3)
Cu1 - N11A	2.089(2)	Cu2 - S1D - Cu6	121.19(3)
Cu1 - N21A	2.118(2)	Cu2 - S1D - Cu8	115.89(3)
Cu2 - N2A	1.966(3)	Cu6 - S1D - Cu8	106.70(3)
Cu3 - N2C	2.041(3)		
Cu3 - N2B	2.077(3)		
Cu4 - N11B	2.034(3)		
Cu4 - N1B	2.047(2)		
Cu4 - N21B	2.135(2)		
Cu5 - N2D	1.964(3)		
Cu6 - N2F	2.019(3)		
Cu6 - N2E	2.092(3)		
Cu7 - N1C	2.036(2)		
Cu7 - N21C	2.083(2)		
Cu7 - N11C	2.143(2)		
Cu8 - N1D	2.031(2)		
Cu8 - N21D	2.104(2)		
Cu8 - N11D	2.129(2)		
O1A - H1H1	0.83(2)		
O1B - H1H2	0.73(2)		

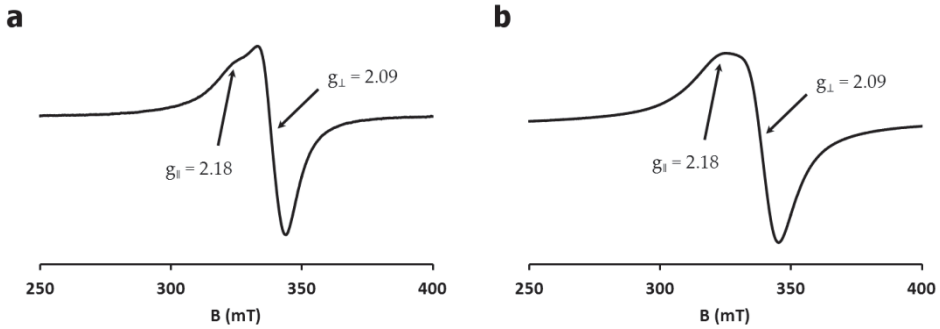

Figure AIII.1: X-Band powder EPR spectrum of $[Cu^{II}_2(\mathbf{L^{1*}SO_2})_2](BF_4)_2$ (ν = 9.881 GHz) (a) and $[Cu^{II}_2(\mathbf{L^{1*}SO_2})_2(OTf)_2]$ (ν = 9.883 GHz) (b) at RT.

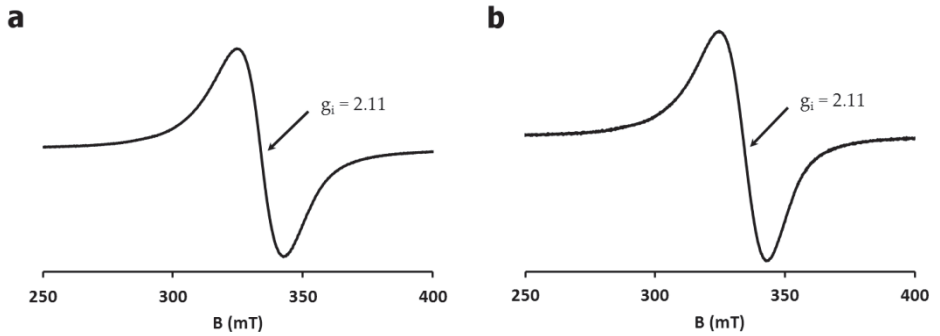

Figure AIII.2: X-Band powder EPR spectrum of $Cu^{II}_2(\mathbf{L^{1*}SO_3})_2(BF_4)_2$ (ν = 9.879 GHz) (a) and $Cu^{II}_2(\mathbf{L^{1*}SO_3})_2(OTf)_2$ (ν = 9.878 GHz) (b) at RT.

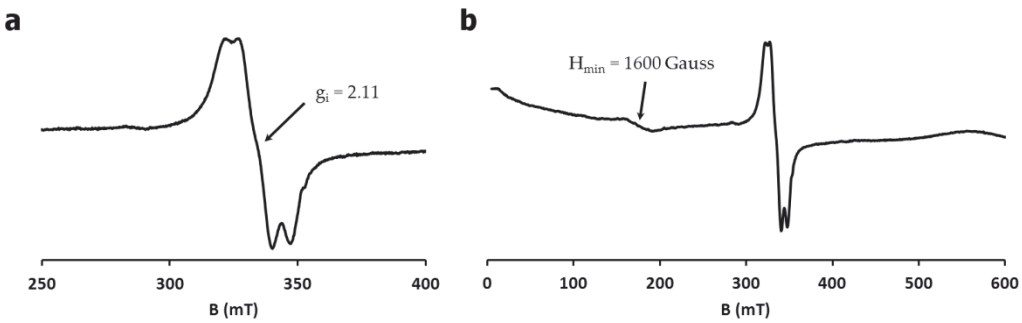

Figure AIII.3: X-Band EPR spectrum of $Cu^{II}_2(\mathbf{L^{1*}SO_3})_2(BF_4)_2$ dissolved in acetone (ν = 9.873 GHz) at RT depicted from 250 to 400 mT (a) and 0 to 600 mT (b).

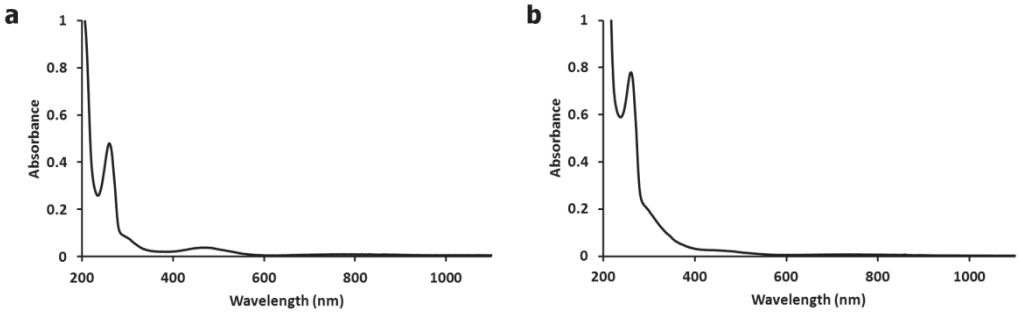

Figure AIII.4: UV-vis absorption spectra of $[Cu^{II}_2(\mathbf{L^{1*}SO_2})_2](BF_4)_2$ (a) and $Cu^{II}_2(\mathbf{L^{1*}SO_3})_2(BF_4)_2$ (b) at a concentration of 0.1 mM [Cu] in acetonitrile, recorded with a path length of 10 mm.

Appendix IV

Supplementary information on Chapter 5

Figure AIV.1 Displacement ellipsoid plot of **L^{1}SXSL^1**

Figure AIV.2 Displacement ellipsoid plot of [Cu$^{II}_2$(**L^{MPz}SSL^{MPz}**)(Cl)$_2$]$_n$(BF$_4$)$_{2n}$

Table AIV.1 Crystallographic data for **L^{1}SXSL^1** and [Cu$^{II}_2$(**L^{MPz}SSL^{MPz}**)(Cl)$_2$]$_n$(BF$_4$)$_{2n}$

Table AIV.2 Selected bond distances and angles for [Cu$^{II}_2$(**L^{MPz}SSL^{MPz}**)(Cl)$_2$]$_n$(BF$_4$)$_{2n}$

Figure AIV.3 ^{1}H NMR spectra of **L^{1}SXSL^1** and [Cu$^{I}_2$(**L^{1}SXSL^1**)(CH$_3$CN)](BF$_4$)$_2$

Figure AIV.4 ^{1}H NMR spectra of **L^{Pz}SSL^{Pz}** and [Cu$^{I}_2$(**L^{Pz}SSL^{Pz}**)](BF$_4$)$_2$

Figure AIV.5 ^{1}H NMR spectra of **L^{MPz}SSL^{MPz}** and [Cu$^{I}_2$(**L^{MPz}SSL^{MPz}**)](BF$_4$)$_2$

Figure AIV.6 Cyclic voltammograms of [Cu$^{I}_2$(**L^{Pz}SSL^{Pz}**)](BF$_4$)$_2$

Figure AIV.7 Cyclic voltammograms of [Cu$^{I}_2$(**L^{MPz}SSL^{MPz}**)](BF$_4$)$_2$

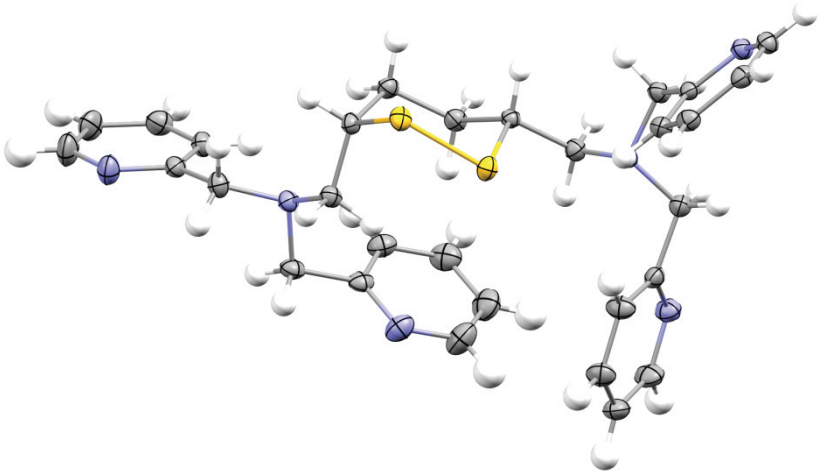

Figure AIV.1: Displacement ellipsoid plot (50% probability level) of **L^{1}SXSL^{1}**.

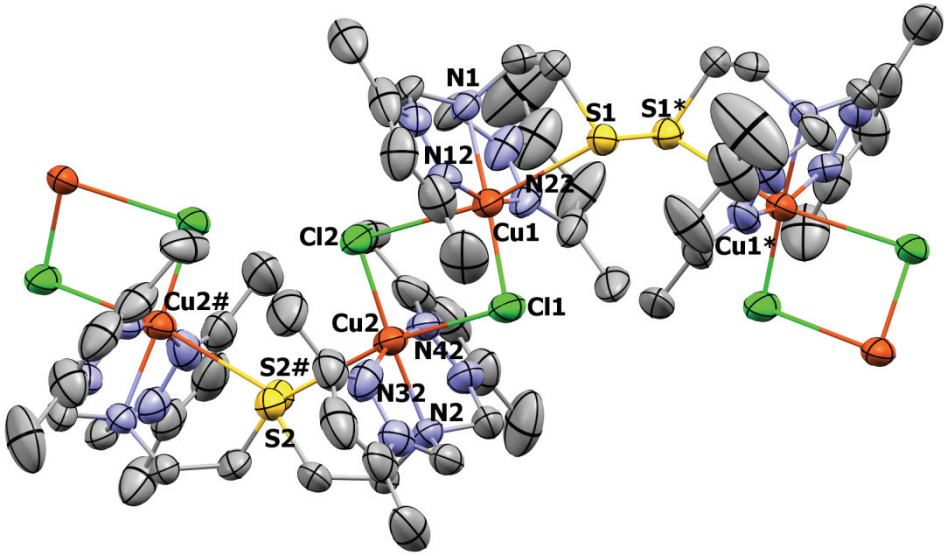

Figure AIV.2: Displacement ellipsoid plot (50% probability level) of $[Cu^{II}_2(\mathbf{L}^{MPz}\mathbf{SSL}^{MPz})(Cl)_2]_n(BF_4)_{2n}$. Hydrogen atoms, counterions and lattice solvent molecules are omitted for clarity. Symmetry operation * = [1–x, y, ½–z] and # = [–x, y, ½–z]

Synthesis of $[Cu^{II}_2(\mathbf{L^{MPz}SSL^{MPz}})(Cl)_2]_n(BF_4)_{2n}$

$\mathbf{L^{MPz}SSL^{MPz}}$ (0.103 g, 0.18 mmol) was dissolved in 5 mL CH_3CN. To this solution $[Cu^{II}(H_2O)_6](BF_4)_2$ (0.062 g, 0.18 mmol) and $CuCl_2 \cdot 2\ H_2O$ (0.032 g, 0.18 mmol) were added and the mixture was stirred for 10 minutes. Diethyl ether (10 mL) was added, which resulted in a precipitate that was filtered and washed with diethyl ether giving $[Cu^{II}_2(\mathbf{L^{MPz}SSL^{MPz}})(Cl)_2]_n(BF_4)_{2n}$ (0.130 g, 0.14 mmol, 76%) as a light green powder. ESI-MS found (calculated) for $[M - 2\ BF_4]^{2+}$ *m*/*z* 391.0 (391.1); $[½\ M - Cl - BF_4]^+$ *m*/*z* 355.0 (355.1); $[½\ M - BF_4 + Cl]^+$ *m*/*z* 426.9 (427.0). IR (neat, cm^{-1}): 2999*w*, 1553*m*, 1477*m*, 1418*m*, 1392*m*, 1280*m*, 1048*vs*, 1020*vs*, 1006*s*, 912*m*, 797*m*, 624*m*, 521*m* 468*m*. Elemental analysis calcd for $[Cu^{II}_2(\mathbf{L^{MPz}SSL^{MPz}})(Cl)_2](BF_4)_2$: C 35.16, H 4.64, N 14.64, S 6.70; Found: C 33.92, H 4.50, N 14.34, S 6.27. UV-vis in CH_3CN at 0.1 mM [Cu] concentration: 213 nm (18 000 $M^{-1}\ cm^{-1}$), 285 nm (ε = 3 300 $M^{-1}\ cm^{-1}$), 750 nm (ε = 100 $M^{-1}\ cm^{-1}$). X-band powder EPR spectrum (RT, ν = 9.855 GHz): g_{iso} = 2.10; X-band EPR spectrum in CH_3CN (RT, ν = 9.865 GHz): g_{iso} = 2.10.

Table AIV.1: Crystallographic and structure refinement data for $\mathbf{L^1SXSL^1}$ and $[Cu^{II}_2(\mathbf{L^{MPz}SSL^{MPz}})(Cl)_2]_n(BF_4)_{2n}$.

	$\mathbf{L^1SXSL^1}$	$[Cu^{II}_2(\mathbf{L^{MPz}SSL^{MPz}})(Cl)_2]_n(BF_4)_{2n}$
empirical formula	$C_{30}H_{34}N_6S_2$	$[C_{28}H_{44}Cl_2Cu_2N_{10}S_2](BF_4)_2 \cdot CH_3CN$
formula weight	542.75	994.48
crystal system	triclinic	monoclinic
space group	*P*-1	*C*2/*c*
a, Å	6.1886(2)	16.0760(4)
b, Å	14.4574(5)	30.5905(3)
c, Å	16.6963(5)	19.2993(5)
α, deg	104.490(3)	90
β, deg	98.618(3)	114.138(3)
γ, deg	95.211(3)	90
V, Å^3	1417.08(8)	8661.0(4)
Z, *Z'*	2, 1	8, 1
D_{calc}, g·cm^3	1.272	1.525
T, Kelvin	100(2)	110(2)
crystal size, mm	$0.27 \times 0.09 \times 0.06$	$0.53 \times 0.41 \times 0.34$
μ, mm^{-1}	1.933	3.885
no. of reflns measd	16387	30710
no. of unique reflns	5554	8476
no. of reflns obsd.	5229 [$I > 2\sigma(I)$]	7664 [$I > 2\sigma(I)$]
no. of parameters	343	689
R_1 / wR_2 [$I > 2\sigma(I)$]	0.0406/0.0984	0.0737/0.2156
R_1 / wR_2 [all refl.]	0.0432/0.1000	0.0789/0.2241
goodness of fit	1.118	1.056
$\Delta\rho$, e·Å^{-3}	−0.26 /0.50	−0.84 /1.09

Structure determination

The reflection intensities for **L^{1}SXSL^1** and [Cu$^{II}_2$(**L^{MPz}SSL^{MPz}**)(Cl)$_2$]$_n$(BF$_4$)$_{2n}$ were measured using a SuperNova diffractometer (equipped with Atlas detector) with Cu *K*α radiation (λ = 1.54178 Å) under the program CrysAlisPro (Versions 1.171.36.24 or 1.171.36.32 Agilent Technologies, 2012-2013). The same program was used to refine the cell dimensions and for data reduction. The structure was solved with the program SHELXS-2013 (Sheldrick, 2013) and was refined on F^2 with SHELXL-2013 (Sheldrick, 2013). Analytical numeric absorption correction based on a multifaceted crystal model was applied using CrysAlisPro. The temperature of the data collection was controlled using the system Cryojet (manufactured by Oxford Instruments). The H atoms were placed at calculated positions using the instructions AFIX 13, AFIX 23, AFIX 43 or AFIX 137 with isotropic displacement parameters having values 1.2 or 1.5 times *U*eq of the attached C atoms.

For [Cu$^{II}_2$(**L^{MPz}SSL^{MPz}**)(Cl)$_2$]$_n$(BF$_4$)$_{2n}$ the structure was solved and refined in the space group *C*2/*c*, and is found to be polymeric along the **a** direction with the repeating unit corresponding to the dicopper(II) complex $C_{28}H_{44}Cl_2Cu_2N_{10}S_2$. A first check with ADDSYM in Platon (Spek, 2003) suggests a *C*2/*c* to *Fddd* transformation *via* the transformation matrix (1 0 0 / 0 –1 0 / –1 0 –2), but such a transformation remains unlikely as the β angle would be *ca.* 90.47°. The space group *C*2/*c* remains the most likely space group as there are no strong evidences for wrong space group assignment (0 Systematic absence violations, 10 Inconsistent equivalents, *R*(int) = 0.0268, R(sigma) = 0.0201). The implementation of the twin matrix (–1 0 0 / 0 –1 0 / 1 0 1) (found *via* TwinRotMat in Platon) helps to drop the *R*1 factor a bit, and the BASF scale factor refines to 0.369(5). In the structure, the polymeric unit remains ordered while all counterions and lattice solvent molecules are significantly disordered. Two BF_4^- counterions are found at sites of twofold axial symmetry, and are constrained to be disordered with an occupancy factor of 0.5 for each counterion. The remaining BF_4^- counterion is found at no special position, but is disordered over 4 different orientations, whose occupancy factors refine to 0.314(3), 0.202(3), 0.230(3) and 0.254(3) (the SUMP instruction was used so that the sum of the four occupancy factors equals to 1). In the asymmetric unit, there is one lattice acetonitrile solvent molecule, which is found very disordered. Modelling of the disorder is very approximate (as it is likely that the molecule is disordered over more than 2 orientations), and the occupancy factor of the major component refines to 0.702(15). The H atoms of the very disordered acetonitrile lattice solvent molecule have been omitted in the final refinement. A SQUEEZE refinement was not possible as the different components of the disorder are close to the very disordered BF_4^- counterion.

Table AIV.2: Selected bond distances and angles for $[Cu^{II}_2(\mathbf{L^{MPz}SSL^{MPz}})(Cl)_2]_n(BF_4)_{2n}$.

Bond distance (Å)		Bond angle (°)	
Cu1 - Cu2	3.6500(15)	S1 - Cu1 - N1	81.24(19)
S1 - S1*	2.052(3)	S1 - Cu1 - N12	83.7(2)
S2 - S2#	2.046(4)	S1 - Cu1 - N22	92.5(2)
Cu1 - S1	2.977(2)	S1 - Cu1 - Cl2	163.74(7)
Cu1 - N1	2.124(5)	N1 - Cu1 - N12	81.3(2)
Cu1 - N12	1.986(6)	N1 - Cu1 - N22	80.4(2)
Cu1 - N22	1.967(7)	N1 - Cu1 - Cl1	176.13(17)
Cu1 - Cl1	2.235(2)	N12 - Cu1 - N22	161.7(3)
Cu1 - Cl2	2.895(3)	S2 - Cu2 - N2	81.57(19)
Cu2 - S1	2.972(2)	S2 - Cu2 - N32	83.1(2)
Cu2 - N2	2.083(5)	S2 - Cu2 - N42	93.8(2)
Cu2 - N32	1.963(8)	S2 - Cu2 - Cl1	164.65(7)
Cu2 - N42	1.968(7)	N2 - Cu2 - N32	81.4(3)
Cu2 - Cl1	2.899(3)	N2 - Cu2 - N42	82.4(2)
Cu2 - Cl2	2.402(19)	N2 - Cu2 - Cl2	176.35(18)
		N32 - Cu2 - N42	163.8(3)

Symmetry operation * = [1–x, y, ½–z], # = [–x, y, ½–z]

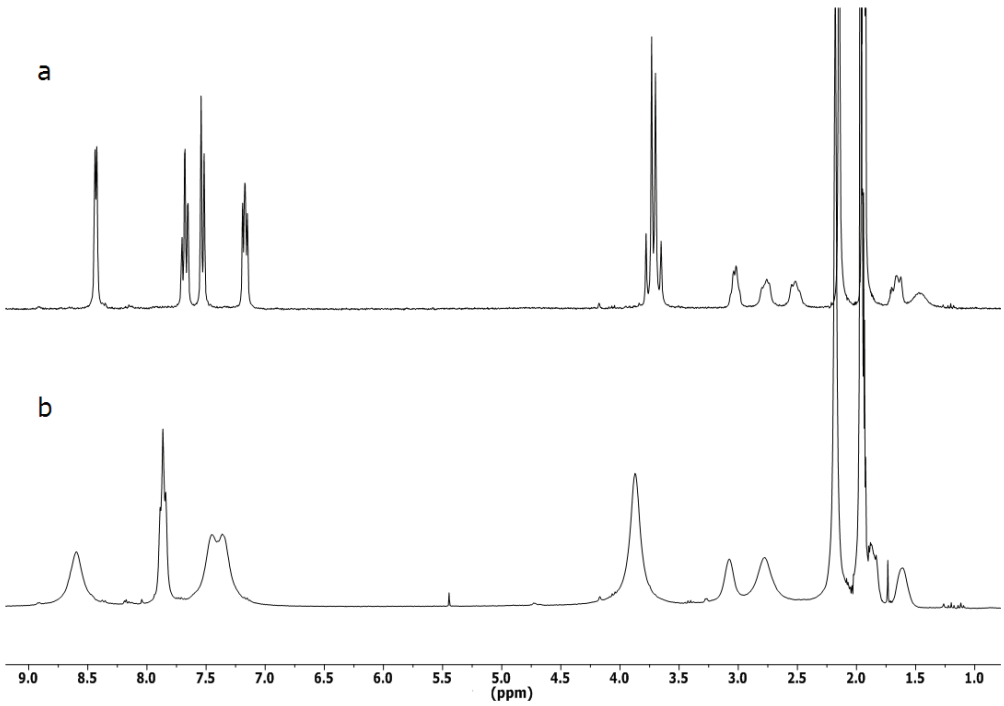

Figure AIV.3: ^{1}H NMR spectra of $\mathbf{L^1SXSL^1}$ (a) and $[Cu^I_2(\mathbf{L^1SXSL^1})(CH_3CN)](BF_4)_2$ (b) in CD_3CN.

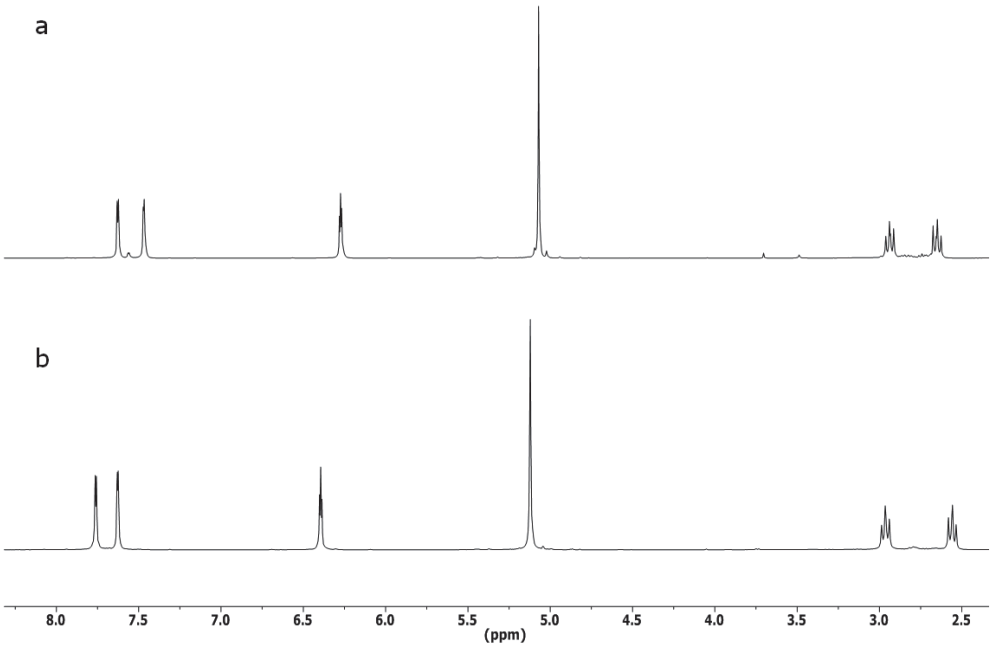

Figure AIV.4: ^{1}H NMR spectra of $\mathbf{L^{Pz}SSL^{Pz}}$ (a) and $[Cu^{I}_{2}(\mathbf{L^{Pz}SSL^{Pz}})](BF_4)_2$ (b) in CD_3CN.

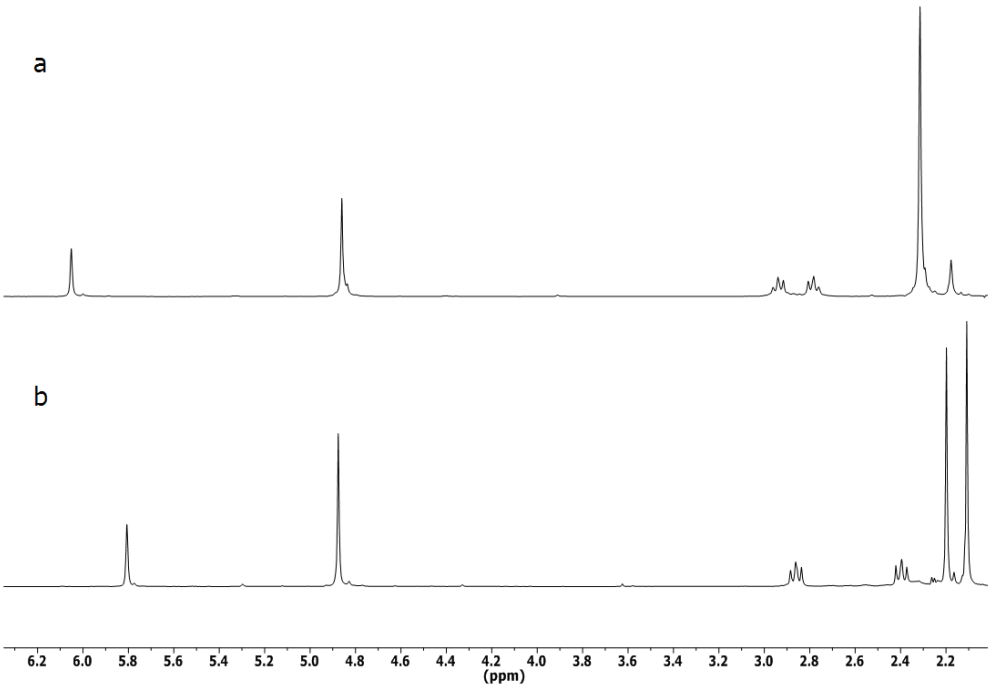

Figure AIV.5: ^{1}H NMR spectra of $\mathbf{L^{MPz}SSL^{MPz}}$ (a) and $[Cu^{I}_{2}(\mathbf{L^{MPz}SSL^{MPz}})](BF_4)_2$ (b) in CD_3CN.

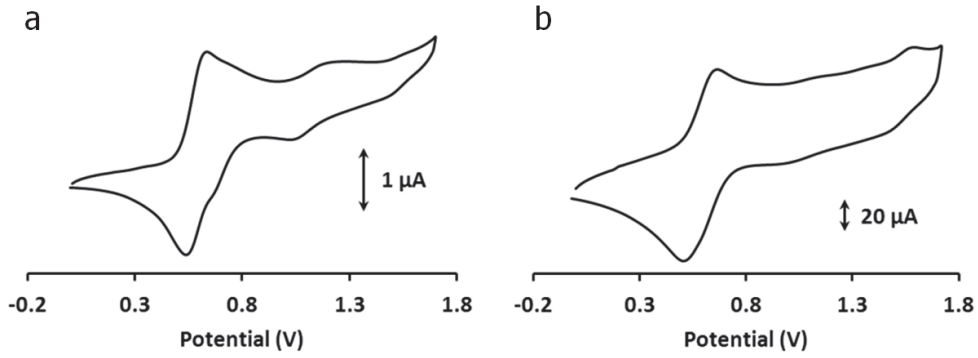

Figure AIV.6: Cyclic voltammograms of $[Cu^{I}_2(\mathbf{L^{Pz}SSL^{Pz}})](BF_4)_2$ in acetonitrile at 20 mV/s (a) and 1000 mV/s (b) at 2.0 mM [Cu] concentration. Potentials are given vs Ag/AgCl.

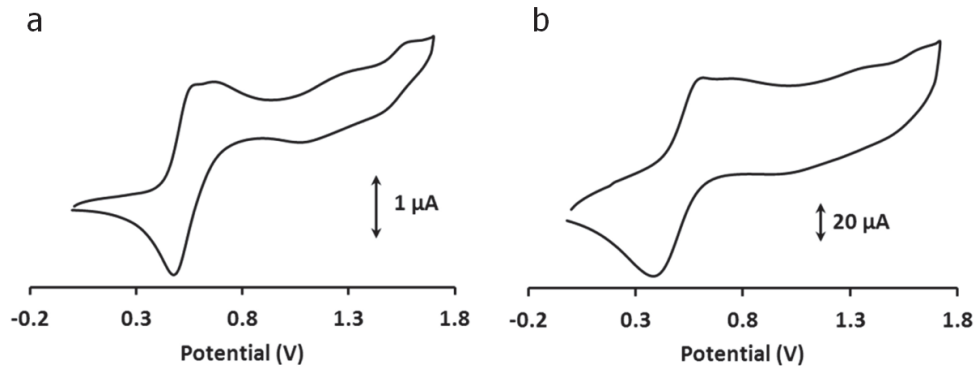

Figure AIV.7: Cyclic voltammograms of $[Cu^{I}_2(\mathbf{L^{MPz}SSL^{MPz}})](BF_4)_2$ in acetonitrile at 20 mV/s (a) and 1000 mV/s (b) at 2.0 mM [Cu] concentration. Potentials are given vs Ag/AgCl.

Appendix V

Supplementary information on Chapter 6

Figure AV.1 Raman spectra of $[Cu^{II}(\mathbf{L^1SCH_3})(OPh\text{-}X)]^+$ with different X substituents

Figure AV.2 X-band EPR spectrum of $[Cu^{II}(\mathbf{L^1SCH_3})(OPh)](SbF_6)$

Figure AV.3 Cyclic voltammograms of $[Cu^{II}(\mathbf{L^1SCH_3})(OPh\text{-}Me)](OTf)$ at different scanrates

Figure AV.4 Cyclic voltammograms of $[Cu^{II}(\mathbf{L^1SCH_3})(OPh\text{-}Me)](OTf)$ with different potential ranges

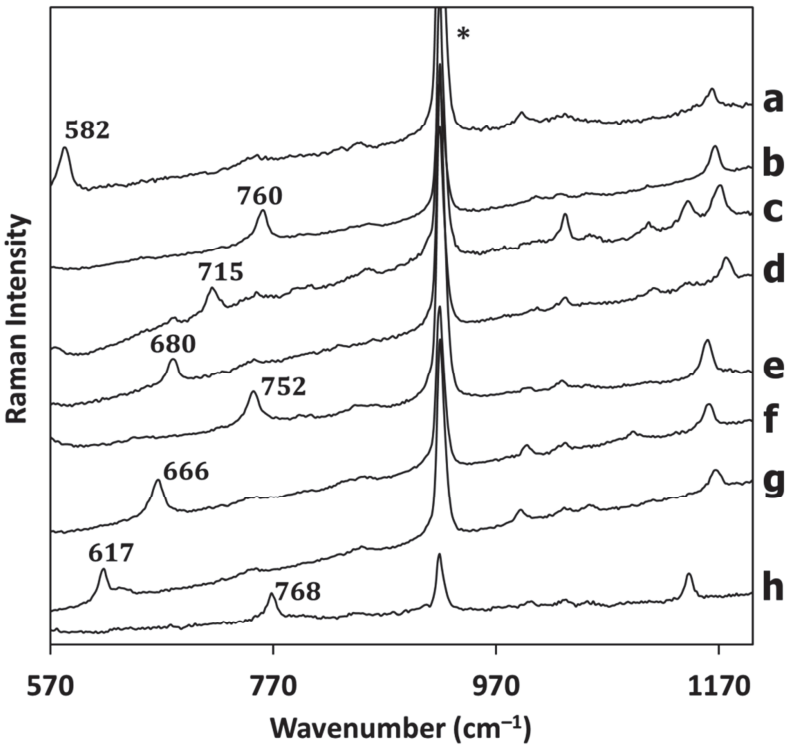

Figure AV.1: Raman spectra of $[Cu^{II}(\mathbf{L^1SCH_3})]^{2+}$ coordinated to X-PhO^- with different substituents on the *para*-position; X = (a) H, (b), CH_3, (c) *iso*-propyl, (d) *tert*-butyl, (e) OCH_3, (f) Cl, (g) I and (h) F. Spectra were recorded on a confocal Raman microscope at an excitation wavelength of 532 nm with 2 s exposure time. The spectra are the average of 25 accumulations. * = CH_3CN

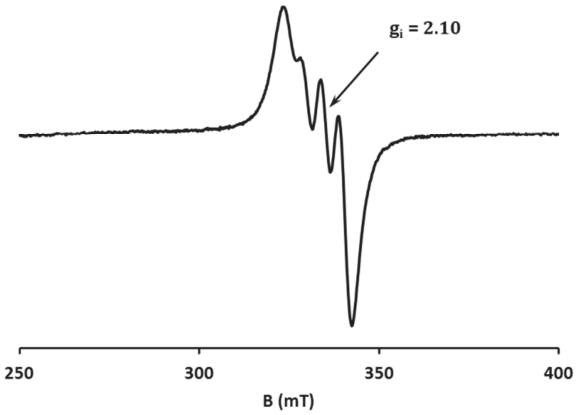

Figure AV.2: X-band EPR spectrum (ν = 9.863 GHz) of $[Cu^{II}(\mathbf{L^1SCH_3})(OPh)](SbF_6)$ at RT dissolved in CH_3CN; $g_i = 2.10$, $A_i = 52$ Gauss.

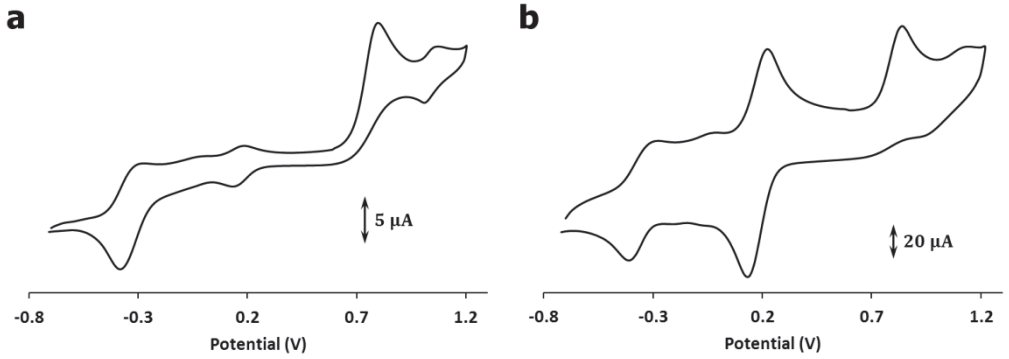

Figure AV.3: Cyclic voltammograms of [Cu^{II}(**L^1SCH_3**)(OPh-Me)](OTf) measured at a scanrate of (a) 20 mV/s and (b) 1000 mV/s in CH_3CN at 2.0 mM [Cu] concentration. Potentials are given vs Ag/AgCl.

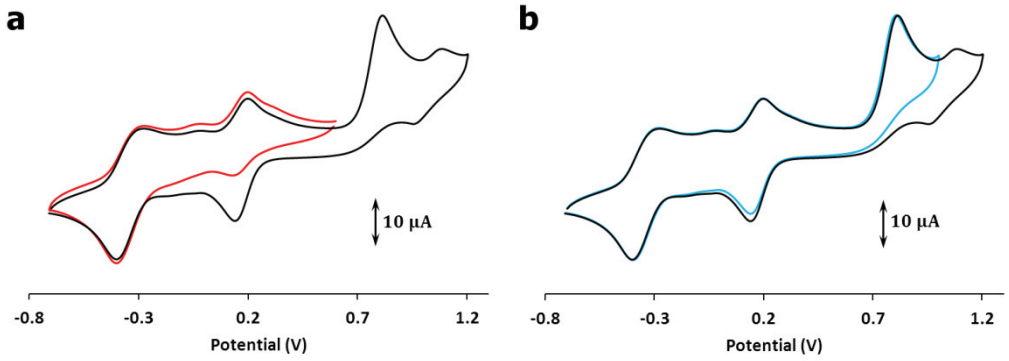

Figure AV.4: Cyclic voltammograms of [Cu^{II}(**L^1SCH_3**)(OPh-Me)](OTf) measured in a potential range of (a) –0.7 to 1.2 V (black) and –0.7 to 0.6 V (red); (b) –0.7 V to 1.2 V (black) and –0.7 to 1.0 V (blue) at a scanrate of 100 mV/s in CH_3CN at 2.0 mM [Cu] concentration. Potentials are given vs Ag/AgCl.

Appendix VI

Supplementary information on Chapter 7

Figure AVI.1 Displacement ellipsoid plots of $[Cu^{II}_2(\mathbf{L^1SSL^1})(Cl)_2]_n(BF_4)_{2n}$ and $[Cu^{II}_2(\mathbf{L^2SSL^2})(Cl)_2]_n(ClO_4)_{2n}$

Figure AVI.2 Displacement ellipsoid plots of $[Cu^{II}(\mathbf{L^1{*}SCH_3})(Cl)](BF_4)$ and $[Cu^{II}(\mathbf{L^1{*}SCH_3})(Cl)]_2(CuCl_4)$

Table AVI.1 Crystallographic data for $[Cu^{II}_2(\mathbf{L^1SSL^1})(Cl)_2]_n(BF_4)_{2n}$, $[Cu^{II}_2(\mathbf{L^2SSL^2})(Cl)_2]_n(ClO_4)_{2n}$, $[Cu^{II}(\mathbf{L^1{*}SCH_3})(Cl)](BF_4)$ and $[Cu^{II}(\mathbf{L^1{*}SCH_3})(Cl)]_2(CuCl_4)$

Table AVI.2 Selected bond distances and angles for $[Cu^{II}_2(\mathbf{L^1SSL^1})(Cl)_2]_n(BF_4)_{2n}$, $[Cu^{II}_2(\mathbf{L^2SSL^2})(Cl)_2]_n(ClO_4)_{2n}$, $[Cu^{II}(\mathbf{L^1{*}SCH_3})(Cl)](BF_4)$ and $[Cu^{II}(\mathbf{L^1{*}SCH_3})(Cl)]_2(CuCl_4)$

Figure AVI.3 UV-vis spectra of synthesized Cu^{II} complexes

Figure AVI.4 UV-vis spectra of 3,5-DTBQ formation catalyzed by $[Cu^{II}_2(\mathbf{L^{Pz}SSL^{Pz}})(Cl)_2]_n(BF_4)_{2n}$

Figure AVI.5 UV-vis spectra of $[Cu^{II}_2(\mathbf{L^{Pz}SSL^{Pz}})](BF_4)_4$ in the presence of different amounts of chlorides

Figure AVI.6 Absorption curves at 400 nm of 3,5-DTBQ formation catalyzed by $[Cu^{II}_2(\mathbf{L^{Pz}SSL^{Pz}})](BF_4)_4$ in the presence of different amounts of chlorides

Figure AVI.7 Absorption curves at 400 nm of 3,5-DTBQ formation catalyzed by $[Cu^{II}_2(\mathbf{L^1{*}SSL^{1*}})](BF_4)_4$ at different catalyst concentrations

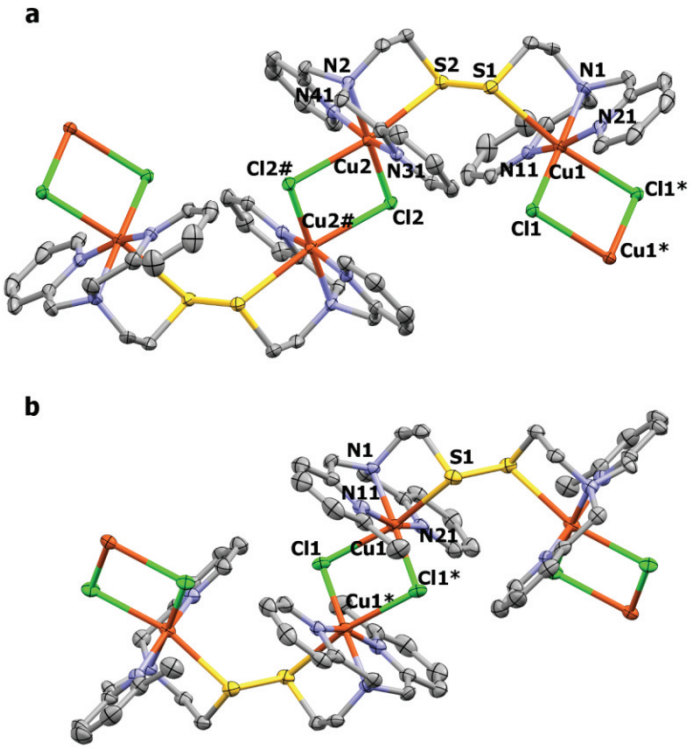

Figure AVI.1: Displacement ellipsoid plots (50% probability level) of (a) $[Cu^{II}_2(\mathbf{L^1SSL^1})(Cl)_2]_n(BF_4)_{2n}$ and (b) $[Cu^{II}_2(\mathbf{L^2SSL^2})(Cl)_2]_n(ClO_4)_{2n}$. Hydrogen atoms, lattice solvent molecules (only for $[Cu^{II}_2(\mathbf{L^1SSL^1})(Cl)_2]_n(BF_4)_{2n}$) and non-coordinating counterions are omitted for clarity. Symmetry operation * = [–x, 1–y, 1–z] and # = [–x, 1–y, –z] for $[Cu^{II}_2(\mathbf{L^1SSL^1})(Cl)_2]_n(BF_4)_{2n}$. Symmetry operation * = [1–x, 2–y, –z] for $[Cu^{II}_2(\mathbf{L^2SSL^2})(Cl)_2]_n(ClO_4)_{2n}$.

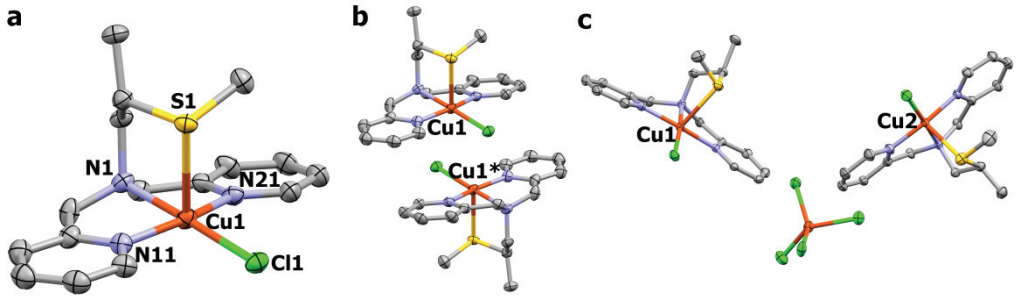

Figure AVI.2: Displacement ellipsoid plots (50% probability level) of one (a) and two (b) cationic subunits of $[Cu^{II}(\mathbf{L^{1*}SCH_3})(Cl)](BF_4)$ and of (c) $[Cu^{II}(\mathbf{L^{1*}SCH_3})(Cl)]_2(Cu^{II}Cl_4)$. Disorder (only for $[Cu^{II}(\mathbf{L^{1*}SCH_3})(Cl)](BF_4)$), hydrogen atoms and BF_4^- counterions have been omitted for clarity. Symmetry operation * = [2–x, –y, 1–z].

*Synthesis of [Cu^{II}(**L^1*SCH$_3$**)(Cl)]$_2$(CuCl$_4$)*

L^1*SCH$_3$ (690 mg; 2.40 mmol) and Cu^{II}Cl$_2$ · 2 H$_2$O (614 mg; 3.60 mmol) were dissolved in 50 mL methanol and refluxed for 1 hour. The solution was cooled down and left to evaporate until green crystals had formed. The crystals were filtered and washed with methanol and diethyl ether to give [Cu^{II}(**L^1*SCH$_3$**)(Cl)]$_2$(CuCl$_4$) (789 mg; 0.807 mmol; 67%). Crystals suitable for X-ray structure determination were originally obtained from 1 instead of 1.5 equiv of Cu^{II}Cl$_2$ · 2 H$_2$O. ESI-MS found (calculated) for [½ M – CuCl$_4$]$^+$ *m*/*z* 384.8 (385.0). IR (neat, cm^{-1}): 2932*w*, 1607*s*, 1573*w*, 1482*m*, 1440*s*, 1299*m*, 1284*m*, 1157*m*, 1053*m*, 1030*s*, 989*w*, 938*w*, 868*m*, 770*s*, 728*w*, 656*w*, 420*s*. Elemental analysis calcd for [Cu^{II}(**L^1*SCH$_3$**)(Cl)]$_2$(CuCl$_4$): C 39.29, H 4.33, N 8.59, S 6.56; Found: C 38.61, H 4.39, N 8.39, S 6.49. UV-vis in CH$_3$CN at 0.15 mM [Cu] concentration: 259 nm (ε = 12 100 M^{-1} cm^{-1}), 305 nm (ε = 5 100 M^{-1} cm^{-1}), 464 nm (ε = 750 M^{-1} cm^{-1}), 700 nm (ε = 130 M^{-1} cm^{-1}), 890 nm (ε = 190 M^{-1} cm^{-1}).

Structure Determination

The reflection intensities for [Cu^{II}(**L^1*SCH$_3$**)(Cl)](BF$_4$) were measured at 110(2) K using a SuperNova diffractometer (equipped with Atlas detector) with Cu *Kα* radiation (*λ* = 1.54178 Å) under the program CrysAlisPro (Version 1.171.36.32 Agilent Technologies, 2013). The same program was used to refine the cell dimensions and for data reduction. The structure was solved with the program SHELXS-2013 (Sheldrick, 2013) and was refined on F^2 with SHELXL-2013 (Sheldrick, 2013). Analytical numeric absorption corrections based on a multifaceted crystal model were applied using CrysAlisPro. The temperature of the data collection was controlled using the system Cryojet (manufactured by Oxford Instruments). The H atoms were placed at calculated positions using the instructions AFIX 13, AFIX 23, AFIX 43, AFIX 137 or AFIX 147 with isotropic displacement parameters having values 1.2 or 1.5 times *U*eq of the attached C atoms.

The reflection intensities for [Cu$^{II}_2$(**L^{1}SSL^1**)(Cl)$_2$]$_n$(BF$_4$)$_{2n}$, [Cu$^{II}_2$(**L^{2}SSL^2**)(Cl)$_2$]$_n$(ClO$_4$)$_{2n}$ and [Cu^{II}(**L^1*SCH$_3$**)(Cl)]$_2$(CuCl$_4$) were measured using a KM4/Xcalibur (detector: Sapphire3) with enhanced graphite-monochromated Mo *Kα* radiation (*λ* = 0.71073 Å) at 110(2) K under the program CrysAlisPro (Version 1.171.35.11 or 1.171.36.24 Agilent Technologies, 2011-2012). The same program was used to refine the cell dimensions and for data reduction. The structures were solved with the program SHELXS-97 (Sheldrick, 2008) and was refined on F^2 with SHELXL-97 (Sheldrick, 2008). Analytical numeric absorption corrections based on a multifaceted crystal model were applied using CrysAlisPro. The temperature of the data collection was controlled using the system Cryojet (manufactured by Oxford Instruments). The H atoms were placed at calculated positions using the instructions AFIX 13, AFIX 23, AFIX 43 or AFIX 137 with isotropic displacement parameters having 1.2 or 1.5 times *U*eq of the attached C atoms.

Table AVI.1: Crystallographic and structure refinement data for complexes $[Cu^{II}_2(\mathbf{L^1SSL^1})(Cl)_2]_n(BF_4)_{2n}$, $[Cu^{II}_2(\mathbf{L^2SSL^2})(Cl)_2]_n(ClO_4)_{2n}$, $[Cu^{II}(\mathbf{L^1{*}SCH_3})(Cl)](BF_4)$ and $[Cu^{II}(\mathbf{L^1{*}SCH_3})(Cl)]_2(CuCl_4)$.

	$[Cu^{II}_2(\mathbf{L^1SSL^1})(Cl)_2]_n(BF_4)_{2n}$	$[Cu^{II}_2(\mathbf{L^2SSL^2})(Cl)_2]_n(ClO_4)_{2n}$	$[Cu^{II}(\mathbf{L^1{*}SCH_3})(Cl)](BF_4)$	$[Cu^{II}(\mathbf{L^1{*}SCH_3})(Cl)]_2(CuCl_4)$
empirical formula	$[C_{28}H_{32}Cl_2Cu_2N_6S_2](BF_4)_2 \cdot 2\,CH_3CN$	$[C_{15}H_{18}ClCuN_3S](ClO_4)$	$[C_{16}H_{21}ClCuN_3S](BF_4)$	$[C_{16}H_{21}ClCuN_3S]_2(CuCl_4)$
formula weight	970.42	470.82	473.22	978.16
crystal system	triclinic	monoclinic	monoclinic	monoclinic
space group	*P*-1	*C*2/*c*	$P2_1/c$	$P2_1/n$
a, Å	12.4006(2)	21.2487(5)	13.4189(4)	13.6254(3)
b, Å	13.1923(3)	12.6146(2)	12.5086(3)	13.2651(3)
c, Å	14.4294(4)	14.6206(4)	12.8357(5)	22.7359(5)
α, deg	104.022(2)	90	90	90
β, deg	107.238(2)	110.200(3)	116.644(4)	102.954(2)
γ, deg	99.5150(18)	90	90	90
V, Å^3	2114.51(8)	3677.92(16)	1925.71(12)	4004.76(15)
Z	2	8	4	4
D_{calc}, g·cm^3	1.524	1.701	1.632	1.622
T, K	110(2)	110(2)	110(2)	110(2)
crystal size, mm	0.57×0.42×0.26	0.19×0.19×0.17	0.17×0.12×0.02	0.52×0.35×0.15
μ, mm^{-1}	1.301	1.618	4.297	2.116
no. of reflns measd	28931	13583	13585	27367
no. of unique reflns	9699	3708	3754	8080
no. of reflns obsd.	8706 [$I > 2\sigma(I)$]	3303 [$I > 2\sigma(I)$]	3206 [$I > 2\sigma(I)$]	6596 [$I > 2\sigma(I)$]
no. of parameters	669	282	294	446
R_1 / wR_2 [$I > 2\sigma(I)$]	0.0231/0.0620	0.0361/0.0930	0.0368/0.0889	0.0447/0.1218
R_1 / wR_2 [all refl.]	0.0266/0.0630	0.0413/0.0955	0.0455/0.0930	0.0573/0.1290
goodness of fit	1.074	1.058	1.041	1.051
$\Delta\rho$, e·Å^{-3}	−0.31/0.33	−0.39/0.87	−0.27/0.60	−1.08/2.62

Table AVI.2: Selected bond distances (Å) and bond angles (°) for complexes $[Cu^{II}_2(\mathbf{L^1SSL^1})(Cl)_2]_n(BF_4)_{2n}$, $[Cu^{II}_2(\mathbf{L^2SSL^2})(Cl)_2]_n(ClO_4)_{2n}$, $[Cu^{II}(\mathbf{L^{1*}SCH_3})(Cl)](BF_4)$ and $[Cu^{II}(\mathbf{L^{1*}SCH_3})(Cl)]_2(CuCl_4)$.

	$[Cu^{II}_2(\mathbf{L^1SSL^1})(Cl)_2]_n(BF_4)_{2n}$	$[Cu^{II}_2(\mathbf{L^2SSL^2})(Cl)_2]_n(ClO_4)_{2n}$	$[Cu^{II}(\mathbf{L^{1*}SCH_3})(Cl)](BF_4)$	$[Cu^{II}(\mathbf{L^{1*}SCH_3})(Cl)]_2(CuCl_4)$
Cu1 - Cu1*	3.5955(3)	3.6455(4)	3.7751(6)	3.9085(7)
Cu2 - Cu2#	3.6192(3)			
Cu1 - Cu2/Cu1#	5.6586(3)	5.6416(5)		
Cu1 - S1	2.8896(4)	2.7676(7)	2.645(3)	2.6608(11)
Cu1 - N1	2.0523(12)	2.041(2)	2.054(2)	2.054(3)
Cu1 - N11	1.9803(12)	2.074(2)	2.003(2)	1.987(3)
Cu1 - N21	1.9901(12)	2.028(2)	2.001(2)	1.985(3)
Cu1 - Cl1	2.2666(4)	2.2644(7)	2.2662(7)	2.2594(10)
Cu1 - Cl1*	2.7862(4)	2.7428(8)	3.0985(8)	3.2663(12)
Cu2 - S2	2.8619(4)			
Cu2 - N2	2.0601(12)			
Cu2 - N31	1.9713(11)			
Cu2 - N41	1.9868(12)			
Cu2 - Cl2	2.2693(3)			
Cu2 - Cl2#	2.7719(3)			
S1 - Cu1 - N1	84.11(4)	85.43(7)	86.52(8)	85.49(9)
S1 - Cu1 - N11	92.75(4)	77.40(7)	86.43(8)	102.36(10)
S1 - Cu1 - N21	87.29(4)	100.67(7)	101.32(8)	86.22(9)
S1 - Cu1 - Cl1/Cl1*	170.50(1)	164.24(2)	96.32(6)	101.22(4)
N1 - Cu1 - N11	81.65(5)	82.10(9)	82.86(9)	81.61(13)
N1 - Cu1 - N21	83.23(5)	81.20(9)	81.80(9)	84.00(13)
N1 - Cu1 - Cl1	179.10(4)	174.37(7)	177.11(6)	173.26(9)
N11 - Cu1 - N21	164.80(5)	163.29(9)	162.32(9)	162.57(14)
S2 - Cu2 - N2	83.68(3)			
S2 - Cu2 - N31	93.92(4)			
S2 - Cu2 - N41	85.95(4)			
S2 - Cu2 - Cl2#	171.24(1)			
N2 - Cu2 - N31	82.10(5)			
N2 - Cu2 - N41	83.37(5)			
N2 - Cu2 - Cl2	179.11(4)			
N31 - Cu2 - N41	165.39(5)			

Symmetry operation * = [–x, 1–y, 1–z] for $[Cu^{II}_2(\mathbf{L^1SSL^1})(Cl)_2]_n(BF_4)_{2n}$; [1–x, 2–y, –z] for $[Cu^{II}_2(\mathbf{L^2SSL^2})(Cl)_2]_n(ClO_4)_{2n}$; [2–x, –y, 1–z] for $[Cu^{II}(\mathbf{L^{1*}SCH_3})(Cl)](BF_4)$; [1–x, 1–y, –z] for $[Cu^{II}(\mathbf{L^{1*}SCH_3})(Cl)]_2(CuCl_4)$. Symmetry operation # = [–x, 1–y, –z] for $[Cu^{II}_2(\mathbf{L^1SSL^1})(Cl)_2]_n(BF_4)_{2n}$; [1–x, y, ½–z] for $[Cu^{II}_2(\mathbf{L^2SSL^2})(Cl)_2]_n(ClO_4)_{2n}$.

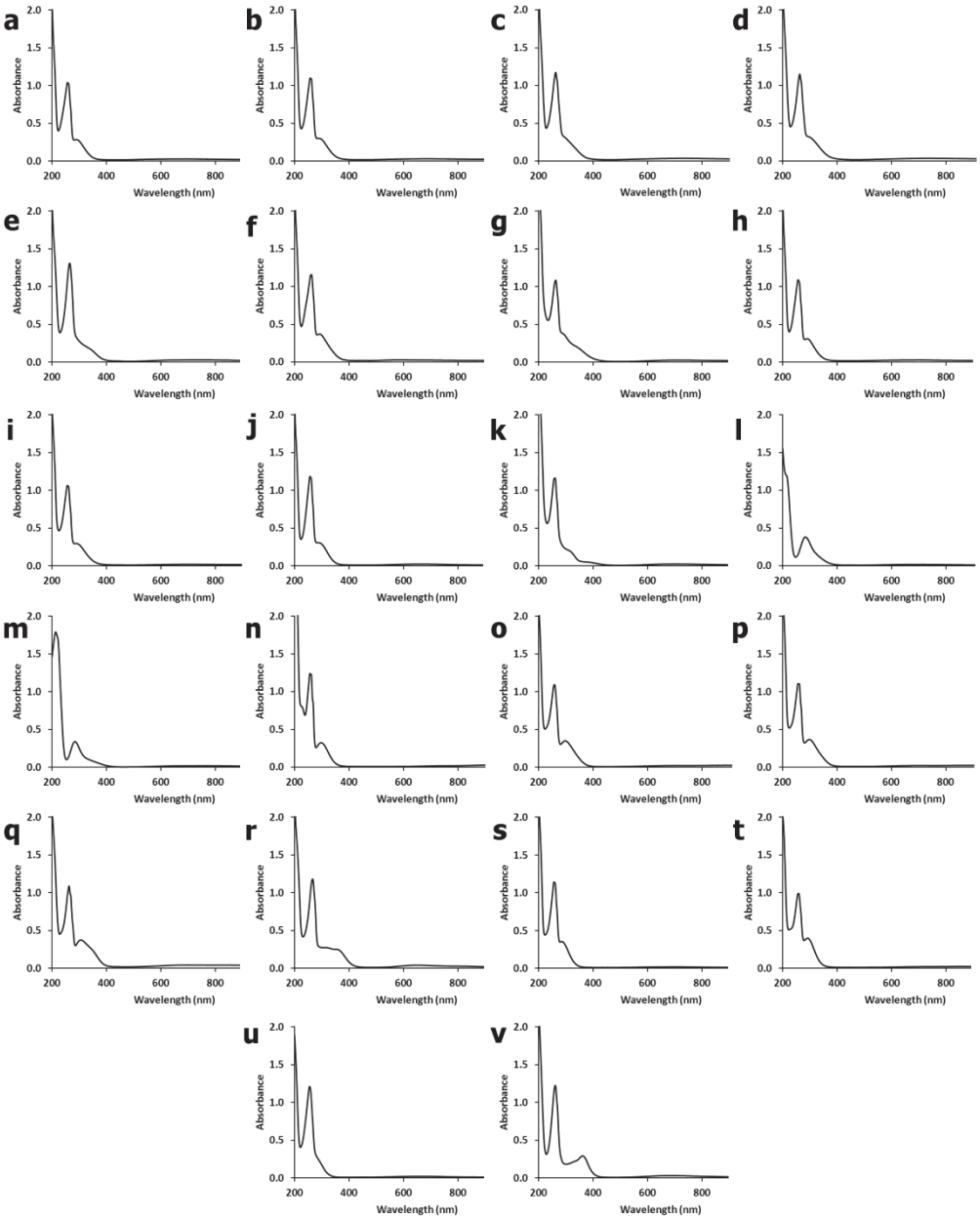

Figure AVI.3: UV-vis spectra of (a) $[Cu^{II}_2(\mathbf{L^1SSL^1})(Cl)_2]_n(BF_4)_{2n}$, (b) $[Cu^{II}_2(\mathbf{L^{1*}SSL^{1*}})(Cl)_2]_n(BF_4)_{2n}$, (c) $[Cu^{II}_2(\mathbf{L^2SSL^2})(Cl)_2]_n(BF_4)_{2n}$, (d) $[Cu^{II}_2(\mathbf{L^{2*}SSL^{2*}})(Cl)_2]_n(BF_4)_{2n}$, (e) $[Cu^{II}_2(\mathbf{L^3SSL^3})(Cl)_2]_n(BF_4)_{2n}$, (f) $[Cu^{II}_2(\mathbf{L^4SSL^4})(Cl)_2]_n(BF_4)_{2n}$, (g) $[Cu^{II}_2(\mathbf{L^5SSL^5})(Cl)_2]_n(BF_4)_{2n}$, (h) $[Cu^{II}_2(\mathbf{L^1SXSL^1})(Cl)_2]_n(BF_4)_{2n}$, (i) $[Cu^{II}_2(\mathbf{L^1SL^1})(Cl)_2]_n(BF_4)_{2n}$, (j) $[Cu^{II}_2(\mathbf{L^1C_6L^1})(Cl)_2]_n(BF_4)_{2n}$, (k) $[Cu^{II}_2(\mathbf{L^1PhL^1})(Cl)_2]_n(BF_4)_{2n}$, (l) $[Cu^{II}_2(\mathbf{L^{Pz}SSL^{Pz}})(Cl)_2]_n(BF_4)_{2n}$, (m) $[Cu^{II}_2(\mathbf{L^{MPz}SSL^{MPz}})(Cl)_2]_n(BF_4)_{2n}$, (n) $[Cu^{II}(\mathbf{Py_3N})(Cl)](BF_4)$, (o) $[Cu^{II}(\mathbf{L^1SCH_3})(Cl)](BF_4)$, (p) $[Cu^{II}(\mathbf{L^{1*}SCH_3})(Cl)](BF_4)$, (q) $[Cu^{II}(\mathbf{L^2SCH_3})(Cl)](BF_4)$, (r) $[Cu^{II}(\mathbf{L^3SCH_3})(Cl)](BF_4)$, (s) $[Cu^{II}(\mathbf{L^1OH})(Cl)](BF_4)$, (t) $[Cu^{II}(\mathbf{L^1NH_2})(Cl)](BF_4)$, (u) $[Cu^{II}(\mathbf{Py_2NH})(Cl)](BF_4)$ and (v) $[Cu^{II}(\mathbf{Py_2S})(Cl)](BF_4)$ in CH_3CN at 0.1 mM [Cu] concentration.

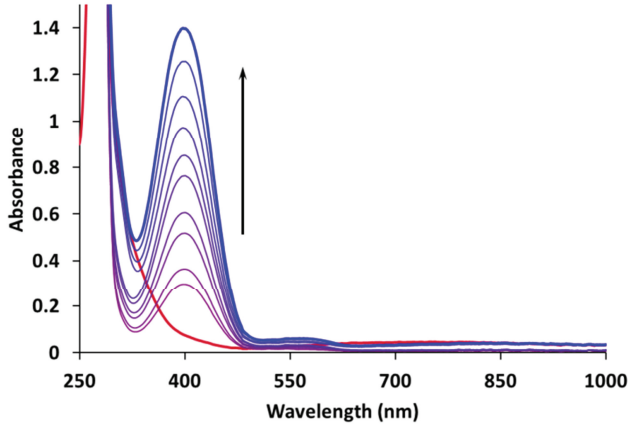

Figure AVI.4: UV-vis spectra of 3,5-DTBQ formation catalyzed by $[Cu^{II}_2(\mathbf{L}^{Pz}\mathbf{SSL}^{Pz})(Cl)_2]_n(BF_4)_{2n}$ at a concentration of 1.0 mM [Cu], 0.2 mM 3,5-DTBQ and 0.2 mM NEt_3 in CH_3CN over the course of 15 minutes. Spectra were recorded with a transmission dipprobe path length of 2.0 mm.

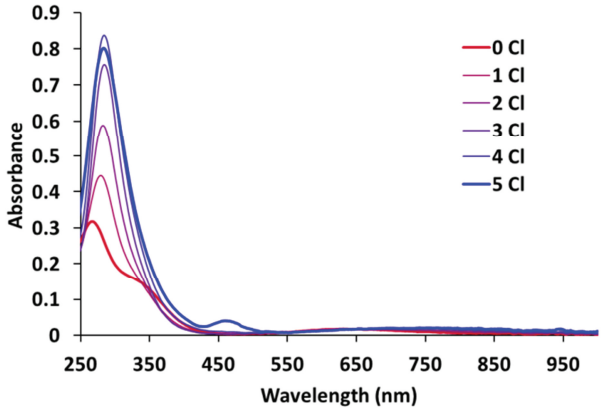

Figure AVI.5: UV-vis spectra of $[Cu^{II}_2(\mathbf{L}^{Pz}\mathbf{SSL}^{Pz})](BF_4)_4$ in CH_3CN at 1.0 mM [Cu] concentration with 0 to 5 equiv of Bu_4NCl in ratio to the whole complex. Spectra were recorded with a transmission dipprobe path length of 2.0 mm.

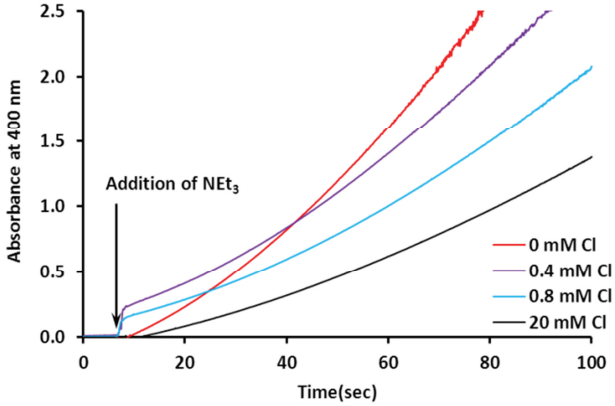

Figure AVI.6: Absorption curves at 400 nm of 3,5-DTBQ formation, catalyzed by $[Cu^{II}_2(\mathbf{L^{Pz}SSL^{Pz}})](BF_4)_4$ in the presence of 0 mM Cl^- (red), 0.4 mM Cl^- (purple), 0.8 mM Cl^- (blue) and 20 mM Cl^- (black).

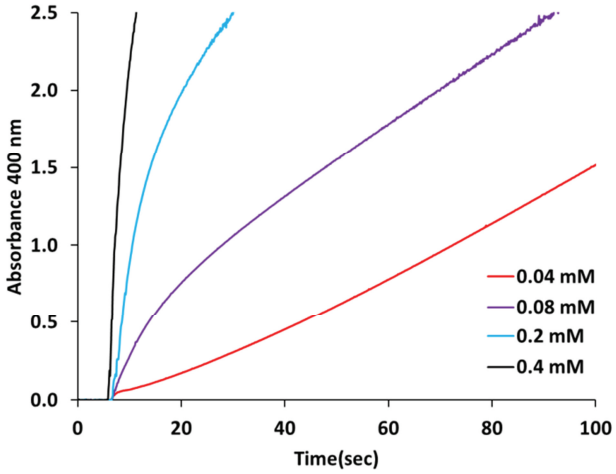

Figure AVI.7: Development in time of the absorption at 400 nm due to 3,5-DTBQ formation, catalyzed by $[Cu^{II}_2(\mathbf{L^{1*}SSL^{1*}})](BF)_4$ at different copper concentrations: 0.04 mM (red), 0.08 mM (purple), 0.2 mM (blue) and 0.4 mM (black).

Samenvatting

Biomimetische Redoxreacties van het Cu^{II} μ-Thiolaatcomplex

Inleiding

Een grote verscheidenheid aan enzymen katalyseert chemische reacties in biologische systemen. Veel van deze enzymen bevatten koper, omdat dit metaal eenvoudig in staat is te wisselen tussen de Cu^{II}– en Cu^{I}-oxidatietoestanden. Deze gekatalyseerde reacties zijn zeer snel en efficiënt en om deze processen beter te begrijpen worden synthetische modellen gebruikt om inzicht te krijgen in hoe deze reacties plaatsvinden in het enzym en om deze kennis te kunnen toepassen in andere katalytische processen. Onze interesse werd gewekt door het Cu_A-centrum, dat twee koperionen bevat die worden gebrugd door twee cysteïnethiolaatzwaveldonoren. Het Cu_A-centrum transporteert elektronen binnen het enzym en wordt gevonden in enzymen zoals cytochroom-c-oxidase en N_2O-reductase. Het is uitdagend om synthetische modellen te ontwerpen voor dit actieve centrum, omdat in veel gevallen een redoxreactie plaatsvindt wanneer een thiolaatverbinding wordt toegevoegd aan een Cu^{II}-ion, volgens de vergelijking: 2 Cu^{II} + 2 LS^- → 2 Cu^{I} + LSSL. Er is echter gerapporteerd dat deze redoxreactie eigenlijk een evenwicht is; de ligging van dit evenwicht kan worden beïnvloed door de structuur van het ligand, het oplosmiddel of de aanwezigheid van chloride-ionen. Een schematisch overzicht van dit evenwicht is weergegeven in Figuur 1.

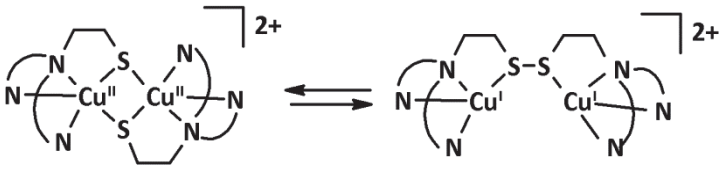

Figuur 1: Schematisch overzicht van het redoxevenwicht tussen een Cu^{II}-μ-thiolaatcomplex en een Cu^{I}-disulfideverbinding.

In Hoofdstuk 1 wordt een overzicht gegeven van de verschillende soorten koperenzymen en de structuur van hun actieve centra. Hierna volgt een overzicht van de gesynthetiseerde modellen voor het Cu_A-centrum, waarbij ook een aantal Cu^{II}-μ-thiolaatverbindingen besproken wordt. Tot slot worden verschillende

gerapporteerde Cu^{II}-μ-thiolaat/Cu^{I}-disulfide-evenwichten besproken alsmede een soortgelijk kobaltevenwicht. Hoofdstuk 1 besluit met de doelstellingen van het onderzoek beschreven in dit proefschrift.

Het Cu^{II}-μ-Thiolaat/Cu^{I}-Disulfide-Evenwicht

Het evenwicht tussen de Cu^{II}-μ-thiolaat– en de Cu^{I}-disulfideverbinding kan worden beïnvloed door kleine veranderingen in de ligandstructuur, het toevoegen van chloride-ionen of het veranderen van het oplosmiddel. Er is echter beperkte kennis over waarom of wanneer de Cu^{II}-μ-thiolaatcomplexen vormen. In Hoofdstuk 2 worden twee nieuwe liganden **L^2SSL^2** en **L^4SSL^4** geïntroduceerd, die samen met drie liganden uit de literatuur twee ligandseries vormen. Deze twee series hebben ofwel een toenemend aantal methylgroepen aan de pyridylringen van het ligand, die meer sterische hindering veroorzaken, of een toenemend aantal ethyleenbruggen naar de pyridylringen, die zorgen voor grotere chelaatringen. De twee nieuwe liganden kunnen beiden Cu^{II}-μ-thiolaatcomplexen vormen met koper, maar deze Cu^{II}-verbindingen verschillen in hoe zij worden omgezet naar een Cu^{I}-disulfideverbinding. In een reactie van het ligand **L^2SSL^2** met een Cu^{I}-zout, wordt een Cu^{II}-μ-thiolaatverbinding gevormd in apolaire oplosmiddelen terwijl een Cu^{I}-disulfidecomplex ontstaat in polaire oplosmiddelen. De Cu^{II}-μ-thiolaatverbinding, opgelost in het enigszins apolaire CH_2Cl_2, kan worden omgezet in een Cu^{I}-disulfidecomplex door het polaire oplosmiddel CH_3CN toe te voegen. Bovendien is gevonden dat in methanol de ligging van het evenwicht bij lagere temperaturen temperatuursafhankelijk is, waarbij de Cu^{I}-disulfideverbinding het thermodynamische product is dat wordt gevormd bij hogere temperaturen. Het ligand **L^4SSL^4** vormt een Cu^{II}-μ-thiolaatcomplex in reactie met een Cu^{I}-zout in elk oplosmiddel, maar kan onomkeerbaar omgezet worden naar een Cu^{I}-disulfideverbinding door de oplossing te verwarmen. Dit betekent dat in het geval van **L^4SSL^4**, de Cu^{II}-μ-thiolaatverbinding het kinetische product is, terwijl het Cu^{I}-disulfidecomplex het thermodynamische product is. Om inzicht te krijgen in de relatieve energieën van de verbindingen die betrokken zijn bij deze evenwichten en wat de waargenomen verschillen veroorzaakt, zijn DFT-berekeningen uitgevoerd voor alle Cu^{II}-thiolaat– en Cu^{I}-disulfideverbindingen van de twee ligandseries. Hieruit bleek dat de Cu^{I}-disulfideverbindingen inderdaad lager zijn in energie dan de corresponderende Cu^{II}-μ-thiolaatcomplexen, maar dat het energieverschil tussen de twee redoxisomeren groter wordt met toenemende sterische hindering of met een toenemend aantal grotere chelaatringen. Dit resultaat impliceert dat de deformatie-

energie van het ligand van zijn grondstructuur naar de geometrie in het complex bepaalt of een Cu^{II}-μ-thiolaatcomplex gevormd kan worden. De ligging van het evenwicht tussen de redoxisomere structuren is grotendeels afhankelijk van de activeringsenergie die nodig is om het thiolaatcomplex om te zetten naar het disulfidecomplex.

Een ander Cu^{II}-μ-thiolaat/Cu^{I}-disulfide-evenwicht met een vergelijkbaar ligand is gerapporteerd beïnvloedt te worden door de aanwezigheid van protonen. Het onderzoek naar deze proton-geïnduceerde omzetting is beschreven in Hoofdstuk 3. Isolatie van een Cu^{II}-thiolaatcluster dat ook gedissocieerde Cu^{I}-ionen bevat, wees ons op de mogelijkheid dat de proton-geïnduceerde omzetting van een Cu^{II}-thiolaatverbinding naar een Cu^{I}-disulfidecomplex mogelijk kan leiden tot liganddissociatie. ^{1}H NMR en UV-vis metingen lieten zien dat het ligand dissocieert van de koperionen na toevoeging van 4 equivalenten protonen aan het dinucleaire Cu^{II}-μ-thiolaatcomplex; dit betreft een aantal protonen gelijk aan één proton per pyridylgroep. Uit de experimentele gegevens werd echter niet duidelijk wat er gebeurt na toevoeging van twee protonen per dinuclear kopercomplex. Om hier duidelijkheid over te krijgen werd de protonering van dit complex computationeel bestudeerd met behulp van DFT. Uit de berekeningen bleek dat de pyridyl-stikstof inderdaad wordt geprotoneerd, maar bovendien bleek dat liganddissociatie met meer dan 100 kJ mol^{-1} gunstiger is dan omzetting naar een geprotoneerd Cu^{I}-disulfidecomplex. De liganddissociatiereactie is schematisch weergegeven in Figuur 2. Dat een soortgelijke liganddissociatie ook optreedt uitgaande van een Cu^{I}-disulfidecomplex is ook experimenteel aangetoond.

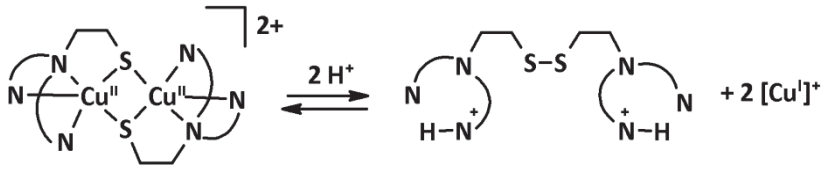

Figuur 2: Schematische representatie van de liganddissociatie, die plaatsvindt na protonering van een Cu^{II}-μ-thiolaatcomplex.

Cu^{II}-μ-Thiolaatoxidatie

Veel koperbevattende enzymen zijn betrokken bij zuurstofactiveringsreacties en veel van hen bevatten zwavelliganden in het actieve centrum. Het is daarom interessant om te weten hoe zuurstofgevoelig deze enzymen zijn. Bovendien spelen thiolverbindingen zoals cysteïne een belangrijke rol in biologische redoxreacties via

de vorming van disulfides, maar ook door de vorming van verder geoxideerde groepen zoals sulfaan–, sulfine– en sulfonzuren. In Hoofdstuk 4 wordt ons onderzoek naar de oxidatie van een Cu^{I}-thiolaatcomplex beschreven. De vorming van een multinucleair Cu^{II}-Cu^{I}-thiolaatcomplex, dat mogelijk een tussenproduct is van de oxidatiereactie, in combinatie met UV-vis metingen liet zien dat de oxidatie verloopt via een Cu^{II}-μ-thiolaatcomplex. Dit betekent dat in eerste instantie het koperion oxideert van Cu^{I} naar Cu^{II}, in tegenstelling tot de directe oxidatie van de thiolaatliganden. De oxidatie van een Cu^{I}-thiolaatverbinding leidt uiteindelijk tot de vorming van Cu^{II}-sulfinaat– en Cu^{II}-sulfonaatcomplexen; deze verbindingen zijn geïsoleerd en geanalyseerd en hun spectroscopische en elektrochemische eigenschappen zijn vergeleken. Hieruit bleek dat de sulfinaat– en sulfonaatcomplexen in spectroscopisch opzicht erg op elkaar lijken, maar dat hun elektrochemische eigenschappen erg verschillend zijn. Dit verschil wordt waarschijnlijk veroorzaakt door de relatieve hardheid van de sulfonaatgroep, die niet in staat is de Cu^{I}-oxidatietoestand te stabiliseren. Een schematisch overzicht van het oxidatieproces is weergegeven in Figuur 3.

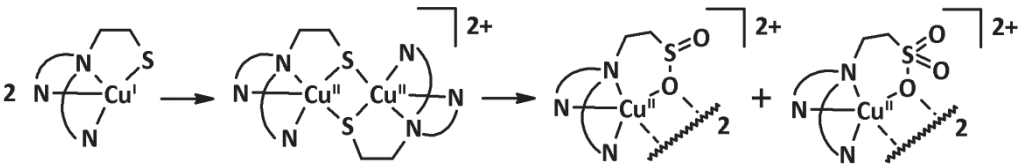

Figuur 3: Schematische voorstelling van de complete oxidatiereactie van een Cu^{I}-thiolaatcomplex naar Cu^{II}-sulfinaat– en sulfonaatverbindingen via de vorming van een Cu^{II}-μ-thiolaatcomplex.

Kleine Ligandveranderingen Verhinderen Cu^{II}-μ-Thiolaatvorming

Het Cu^{II}-μ-thiolaatcomplex vormt een synthetisch model voor het Cu_A-centrum, maar de synthese van dergelijke complexen wordt bemoeilijkt door de conversie naar Cu^{I}-disulfidecomplexen. Kleine veranderingen in de ligandstructuur kunnen bepalen of een Cu^{II}-μ-thiolaat– of een Cu^{I}-disulfideverbinding wordt gevormd. De synthese van drie nieuwe disulfideliganden is beschreven in Hoofdstuk 5. Met deze liganden zijn de effecten op Cu^{II}-μ-thiolaatvorming bestudeerd. Het ligand **L^1SXSL^1** lijkt in structuur op het ligand **L^1*SSL^1***, dat Cu^{II}-μ-thiolaatcomplexen vormt, maar is meer rigide door de aanwezigheid van een extra koolstof-koolstofbinding. Dit ligand verhindert Cu^{II}-μ-thiolaatvorming door de grote reorientatie die nodig is om intermoleculaire Cu^{II}-thiolaatvorming te laten plaatsvinden. De twee andere liganden

hebben verschillende elektronische eigenschappen als gevolg van de vervanging van een pyridinegroep door een pyrazool– of een 3,5-dimethylpyrazoolgroep. Wanneer deze pyrazoolliganden reageren met Cu^{I}-zouten vormen zij Cu^{I}-complexen, die dagenlang stabiel zijn in lucht. De redoxpotentialen van deze drie Cu^{I}-complexen zijn bepaald en vergeleken met dat van een Cu^{I}-complex, dat gevormd wordt door thermische omzetting van een Cu^{II}-μ-thiolaatcomplex (Hoofdstuk 2). Deze vergelijking laat zien dat voor de vorming van zowel de Cu^{II}-μ-thiolaat– en de Cu^{I}-disulfideverbindingen een redoxpotentiaal van ongeveer 0 V vs Ag/AgCl vereist is. Verder worden in Hoofdstuk 5 de structuren van een aantal Cu^{II}-complexen met de gesynthetiseerde disulfideliganden en verschillende tegenionen beschreven.

Overeenkomsten Tussen Koper-Thiolaat– en Koper-Zuurstofchemie

Een groot deel van het biomimetische koperonderzoek dat gerapporteerd wordt in de literatuur is gericht op aromatische ringoxidatie van fenolen en catecholen, omdat deze reacties de activiteit van enzymen als tyrosinase en catechol-oxidase modelleren. In Hoofdstuk 6 en 7 wordt de reactie tussen enkele kopercomplexen uit de eerdere hoofdstukken met fenolen of catechol beschreven; de soms verrassende resultaten onthullen de overeenkomsten tussen koper-thiolaat– en koper-zuurstofchemie.

Wanneer een oplossing van een Cu^{I}-complex met fenol aan de lucht wordt geopend, vormt een donkerpaarse mononucleaire Cu^{II}-fenolaatverbinding. De structuur van deze verbinding is vastgesteld met behulp van röntgen-kristallografie en wordt beschreven in Hoofdstuk 6. De vorming van deze verbinding is interessant, omdat oxidatie van dit soort complexen normaal gesproken leidt tot ringoxidatie of oxidatieve fenolkoppeling. Na verloop van tijd zet de paarse fenolaatverbinding zich om via een unieke redoxreactie naar een Cu^{I}-complex en een fenolaatradicaal dat verder reageert naar een diarylperoxide of een arylether. Dit is bevestigd door middel van NMR en UV-vis spectroscopie en het ontstaan van een nieuwe band in het Ramanspectrum. De omzettingssnelheid is afhankelijk van zowel de concentratie van het mononucleaire complex alsmede de *para*-substituent op de fenylgroep. Een schematische voorstelling van de omzetting is weergegeven in Figuur 4. Het ligand dat is gebruikt voor de bestudering van deze reactie, is vergelijkbaar met het ligand dat Cu^{II}-μ-thiolaatverbindingen kan vormen met een Cu^{I}-zout. Deze redoxreactie lijkt op de koperthiolaat/disulfide redoxreactie beschreven in Hoofdstuk 2, alleen wordt nu $R\text{-}O^{-}$ omgezet naar $R\text{-}O^{\bullet}$ in plaats van $R\text{-}S^{-}$ naar $R\text{-}S^{\bullet}$, dat verder reageert tot R-S-S-R.

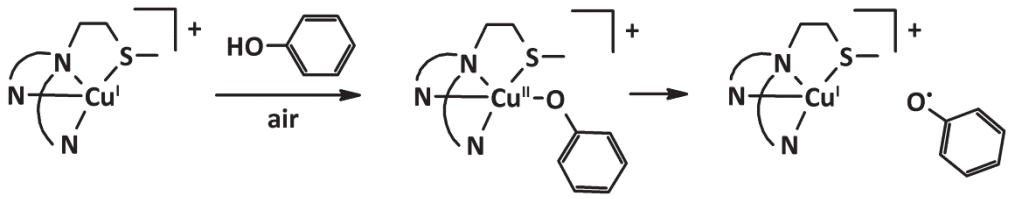

Figuur 4: Schematisch overzicht van de vorming van een Cu^{II}-fenolaatcomplex en de verdere redoxconversie naar een fenolaatradicaal en een Cu^{I}-verbinding.

Om verdere overeenkomsten tussen koper-zuurstof– en koper-zwavelchemie te onderzoeken, is de katalytische oxidatie van 3,5-di-*tert*-butylcatechol (3,5-DTBC) naar 3,5-di-*tert*-butyl-*o*-benzochinon (3,5-DTBQ) onderzocht; de resultaten worden omschreven in Hoofdstuk 7. Een grote bibliotheek van liganden die mononucleaire of polymere koperverbindingen vormen is gesynthetiseerd en met deze liganden zijn $[Cu^{II}(ligand)(Cl)](BF_4)$ complexen gemaakt om te testen in oxidatiekatalyse. Van een aantal van deze complexen kon een kristalstructuur verkregen worden. Deze structuren lieten voor de liganden die polymere complexen vormen relatief grote Cu…Cu-afstanden zien. De katalytische oxidatie van 3,5-DTBC vond plaats met een hogere omzettingsfrequentie (TOF) voor de katalytische systemen gebaseerd op liganden die polymere verbindingen geven, dan voor systemen met liganden die slechts één koperion binden, wat bevestigt dat voor de oxidatiekatalyse twee kopercentra nodig zijn. Daarnaast werden de hoogste TOFs gemeten voor de katalytische systemen gebaseerd op liganden die ook Cu^{II}-μ-thiolaatverbindingen kunnen vormen; de hoogste initiële snelheid met een dergelijk systeem was zelfs 7800 h^{-1}. De oxidatie van 3,5-DTBC vertraagt echter over de tijd, wat erop duidt dat de katalysator waarschijnlijk degradeert. Deze resultaten impliceren opnieuw dat er een relatie is tussen thiolaatvorming met koperionen en hun reactie met zuurstof. Er kan verondersteld worden dat de hoge activiteit veroorzaakt wordt door het vermogen van deze complexen om het Cu^{II}_2-μ-η^2:η^2-peroxide-intermediair te stabiliseren, gezien deze verbinding structureel vergelijkbaar is met het dinucleaire Cu^{II}-μ-thiolaatcomplex. De vorming van het Cu^{II}_2-μ-η^2:η^2-peroxide-intermediair is immers de gepostuleerde snelheidsbepalende stap van de reactie.

Samenvatting voor Niet-Chemici

Inleiding

Het werk aan *biomimetica* dat is beschreven in dit proefschrift betreft fundamenteel onderzoek. Dit betekent dat het onderzoek gericht is op het verwerven van kennis, zonder stil te staan bij mogelijke toepassingen van deze kennis. Uiteraard zou er een toepassing kunnen zijn, die we nog niet kennen. Het doel is echter om dingen beter te begrijpen en op zoek te gaan naar nieuwe verschijnselen. De speurtocht naar nieuwe planeten en sterrenstelsels bijvoorbeeld is ook fundamenteel onderzoek. Het is interessant en kan ons beter laten begrijpen hoe ons sterrenstelsel is ontstaan, maar of wij deze kennis toe kunnen passen zal de toekomst moeten uitwijzen. In deze samenvatting wordt een beknopte uitleg gegeven over wat biomimetica precies is en waar het onderzoek over gaat dat ik in de afgelopen vier jaar heb gedaan.

Enzymen

In elk levend wezen, dus zowel in het menselijk lichaam als in een bacterie, zijn enzymen aanwezig. Een enzym, ook wel een eiwit genoemd, is een katalysator. Dit wil zeggen dat het enzym allerlei biologische reacties versnelt zonder zelf verbruikt te worden. Een voorbeeld van zo'n reactie is de omzetting van suiker (wat je eet) en zuurstof (wat je inademt) naar energie (om te bewegen) en koolstofdioxide (wat je uitademt). Deze reactie wordt in stappen door een hele reeks enzymen gekatalyseerd. Wat houdt dit nu precies in? Een enzym verlaagt de hoeveelheid energie die nodig is om een reactie te laten plaatsvinden. Voordat de reactie $\mathbf{X} + \mathbf{Y} \rightarrow \mathbf{Z}$ kan gebeuren, moet deze eerst op gang gebracht worden: er moet energie (warmte) in gestoken worden, de activeringsenergie, voordat product **Z** wordt gevormd en er weer energie vrijkomt. Dit is schematisch weergegeven in Figuur A. Wanneer er een lagere activeringsenergie is, kan de reactie sneller plaatsvinden en/of bij een lagere temperatuur. Zo verbrandt het lichaam suiker bij 36 °C in plaats van de veel hogere temperatuur van ongeveer 200 °C die nodig is om suiker buiten je lichaam te verbranden.

Hoe ziet zo'n enzym er nou uit? Een enzym is een heel groot molecuul opgebouwd uit koolstof (C), waterstof (H), stikstof (N), zuurstof (O) en zwavel (S). In dit enzymmolecuul zitten metalen gebonden, meestal aan de stikstof en zuurstofatomen. Deze metalen zitten in het 'actieve centrum' van het enzym, wat wil zeggen dat deze metalen het echte werk doen en dus de reacties uitvoeren. Metalen die veel voorkomen in enzymen zijn bijvoorbeeld koper (Cu), ijzer (Fe) en zink (Zn).

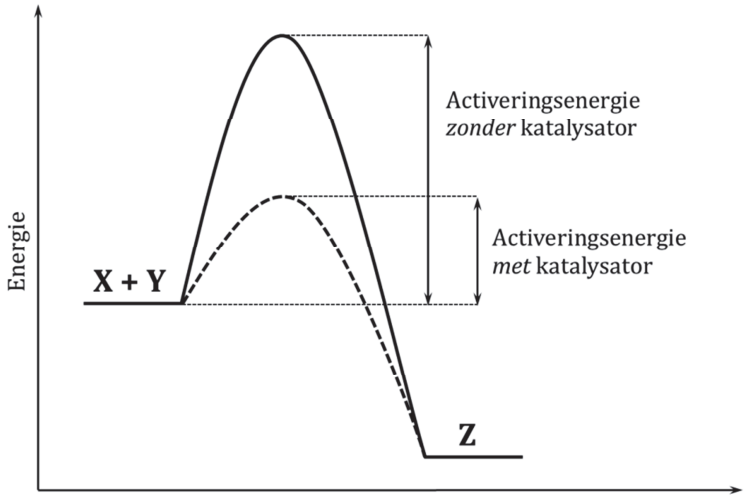

Figuur A: Schematische weergave van de activeringsenergie in de reactie **X** + **Y** → **Z** met en zonder de aanwezigheid van een katalysator.

Elk 'actief centrum' is precies zo ontworpen dat het één soort reactie kan katalyseren. Welke reactie dit is wordt bepaald door het enzymmolecuul dat aan het metaal gebonden is. De soort bindingen van het metaal met het enzymmolecuul bepalen welke reactie het metaal kan uitvoeren. Verder bepaalt het enzymmolecuul ook welke stoffen geactiveerd kunnen worden in het actieve centrum (in ons voorbeeld **X** en **Y**); de juiste stoffen passen in het enzymmolecuul als een sleutel in een slot.

Biomimetica

Enzymen kunnen reacties heel snel en efficiënt uitvoeren. Deze reacties zouden we graag even snel kunnen uitvoeren buiten een biologisch systeem, bijvoorbeeld in industriële toepassingen. Zo zou het energieprobleem opgelost kunnen worden wanneer we fotosynthese kunnen nabootsen, een proces waarin planten met behulp van energie uit zonlicht, koolstofdioxide en water omzetten naar zuurstof en brandstof (koolhydraten). Dit proces wordt gekatalyseerd door samenwerking van een groot aantal enzymen in de plant, en blijkt zeer ingewikkeld te zijn om na te doen in het laboratorium. Doordat enzymen zo groot en complex zijn, is het moeilijk om ze na te maken en te analyseren. Daarom wordt er onderzoek gedaan waarin niet het hele enzym wordt nagebouwd, maar slechts het actieve centrum: dit wordt biomimetica genoemd. Biomimetica betekent letterlijk 'nabootsen van biosystemen'. Het actieve centrum wordt nagebouwd met dezelfde metalen als in het enzym, maar

deze metalen worden gebonden aan veel kleinere moleculen. Deze moleculen worden liganden genoemd. Het geheel van het metaal met de ligand(en) wordt een metaalcomplex genoemd. Verschillende liganden zullen leiden tot verschillende eigenschappen van het metaalcomplex en op deze manier kunnen verschillende reacties gekatalyseerd worden. Over het algemeen is de snelheid van de nagebootste reacties nog altijd honderden malen langzamer dan in het enzym, maar een bijkomstig voordeel van het nabouwen van het actieve centrum is ook dat we het beter kunnen bestuderen. Doordat het metaalcomplex veel kleiner is dan het enzym kunnen we de effecten van kleine veranderingen beter waarnemen en onderzoek doen naar hoe de reactie werkt. Zo leren we meer over hoe de reacties gekatalyseerd worden en hoe we dit met een kleiner metaalcomplex beter na kunnen doen.

Het Cu_A-Centrum

In de afgelopen vier jaar heb ik biomimetische modellen gemaakt voor het Cu_A-centrum. Het Cu_A-centrum is een koperbevattend actief centrum en zit bijvoorbeeld in het enzym cytochroom *c* oxidase dat betrokken is bij de omzetting van zuurstof naar water, maar is ook te vinden in het enzym N_2O reductase dat N_2O omzet naar stikstof en water. Dit zijn beiden grote enzymen waarin verschillende actieve centra samenwerken. Het Cu_A-centrum functioneert als een elektronen-doorgeefluik, wat betekent dat het razendsnel (als een stroomdraad) elektronen van het ene actieve centrum naar het andere actieve centrum verplaatst. In het Cu_A-centrum zijn twee koperionen (Cu^+) aanwezig gebonden aan twee thiolaatgroepen (S^-) van het enzymmolecuul. De elektronen kunnen zich in dit actieve centrum zowel op de thiolaatgroepen als op de koperionen bevinden. Om het Cu_A-centrum na te bouwen is een ligand ontwikkeld dat samen met koper een koper-thiolaatcomplex vormt. Een schematische tekening van het Cu_A-centrum en het koper-thiolaatcomplex is te zien in Figuur B. Het biomimetische koper-thiolaatcomplex heeft net als het Cu_A-centrum twee koperionen, die gebrugd worden door twee thiolaatgroepen.

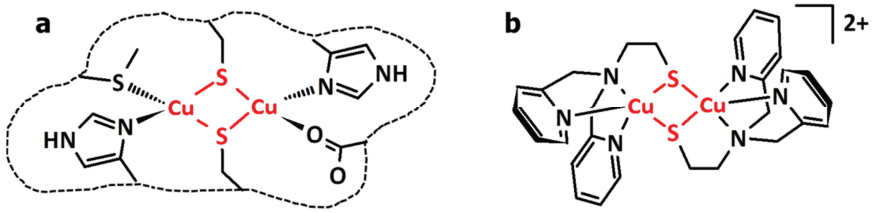

Figuur B: Schematische weergave van a) het Cu_A-centrum in cytochroom c oxidase en b) een biomimetisch koper-thiolaatcomplex.

Redoxreacties

Een reactie waarin alleen een elektron verplaatst van het ene atoom naar het andere, wordt een redoxreactie genoemd: het ene atoom raakt een elektron kwijt (wordt geoxideerd) en het andere atoom krijgt er een elektron bij (wordt gereduceerd). Het Cu_A-centrum ondergaat een redoxreactie wanneer het elektronen doorgeeft van het ene actieve centrum naar het volgende actieve centrum. In Hoofdstuk 2 van dit proefschrift wordt het onderzoek beschreven naar een soortgelijke redoxreactie binnen het biomimetische koper-thiolaatcomplex. Deze redoxreactie is schematisch weergegeven in Figuur C.

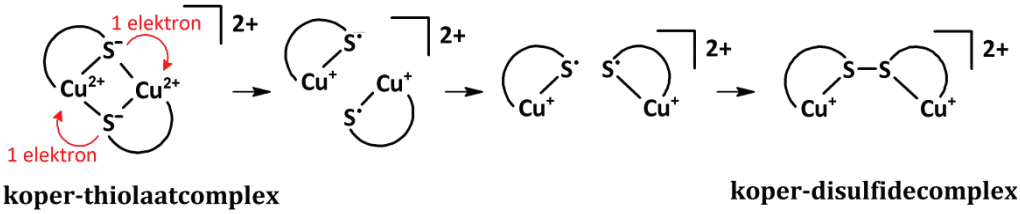

koper-thiolaatcomplex **koper-disulfidecomplex**

Figuur C: Voorgesteld mechanisme voor de omzetting van een koper-thiolaatcomplex naar een koper-disulfidecomplex.

Een elektron van het zwavelion (thiolaatgroep) verplaatst naar het koperion, waardoor een reactief zwavelradicaal ontstaat. Twee zwavelradicalen willen graag samen een binding vormen, waardoor een koper-disulfidecomplex ontstaat. Twee van de elektronen in dit kopercomplex kunnen zich dus of op het zwavelion bevinden (in het koper-thiolaatcomplex) of op het koperion (in het koper-disulfidecomplex). Ik heb onderzocht waarom het elektron juist op het koperion of op het zwavelion zit en wat veroorzaakt of het koper-thiolaatcomplex of het koper-disulfidecomplex vormt. Ik heb gevonden dat deze omzetting van het ene in het andere kopercomplex wordt beïnvloed door de temperatuur en door het oplosmiddel waarin het kopercomplex is opgelost. Ik heb ook berekeningen gedaan aan de kopercomplexen: hieruit blijkt dat ook het type ligand bepaalt welk complex gevormd wordt.

Ik heb gevonden dat er ook een redoxreactie plaatsvindt wanneer er zuur, ofwel protonen (H^+), worden toegevoegd aan het koper-thiolaatcomplex. Het onderzoek naar deze reactie staat beschreven in Hoofdstuk 3. Uit dit onderzoek bleek dat in aanwezigheid van protonen het koper-thiolaatcomplex niet alleen omzet naar het koper-disulfidecomplex, maar dat daarna ook het ligand loslaat (Figuur D). Dit is een zeer interessante vinding, omdat zuur en pH in biologische systemen een hele grote

rol spelen. De wetenschap dat een metaalion in een enzym kan loslaten in aanwezigheid van zuur is zeer belangrijk aangezien het iets kan vertellen over de invloed van zuur op het Cu_A-centrum.

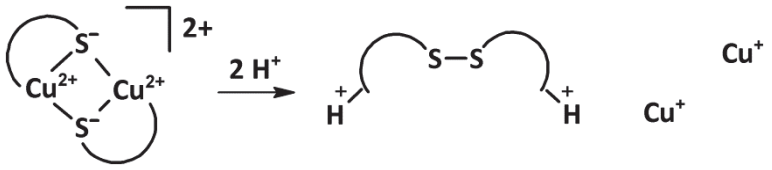

Figuur D: Schematische voorstelling van het loslaten van het ligand na toevoeging van twee protonen aan het koper-thiolaatcomplex.

Niet alleen protonen, maar ook zuurstof speelt een rol in de omgeving van het Cu_A-centrum. Zoals eerder vermeld wordt zuurstof (O_2) in cytochroom *c* oxidase met protonen en elektronen omgezet naar water. Daarom heb ik ook het effect van zuurstof op het koper-thiolaatcomplex bestudeerd; dit onderzoek is beschreven in Hoofdstuk 4. Wanneer het koper-thiolaatcomplex in contact komt met lucht, reageren de thiolaatzwavelatomen met zuurstof. Deze reactie kun je vergelijken met de reactie van ijzer met lucht, waarbij roest ontstaat. De thiolaatgroepen oxideren naar zogenoemde sulfinaat- en sulfonaatgroepen zoals weergegeven in Figuur E. Hierdoor kunnen de zwavelatomen niet meer een disulfide vormen (zoals in Figuur C). Dit zou kunnen betekenen dat wanneer zuurstof met de zwavelatomen in het Cu_A-centrum reageert, het enzym niet meer kan functioneren en dus vervangen moet worden.

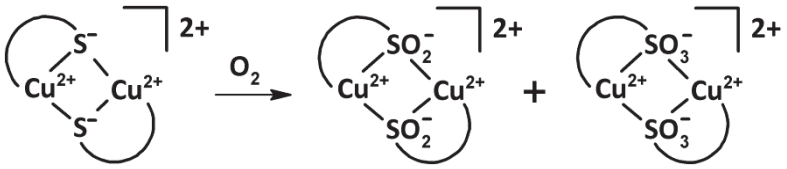

Figuur E: Schematische weergave van de oxidatie van het koper-thiolaatcomplex door zuurstof.

Tot slot heb ik onderzocht of de kopercomplexen gebruikt kunnen worden als biomimetische katalysator voor oxidatiereacties. In Hoofdstuk 6 en 7 is beschreven hoe de gemaakte kopercomplexen reageren met andere bioactieve stoffen zoals fenol en catechol.

CHEMISTRY
A European Journal

www.chemeurj.org

A Journal of ChemPubSoc Europe

2014-20/51

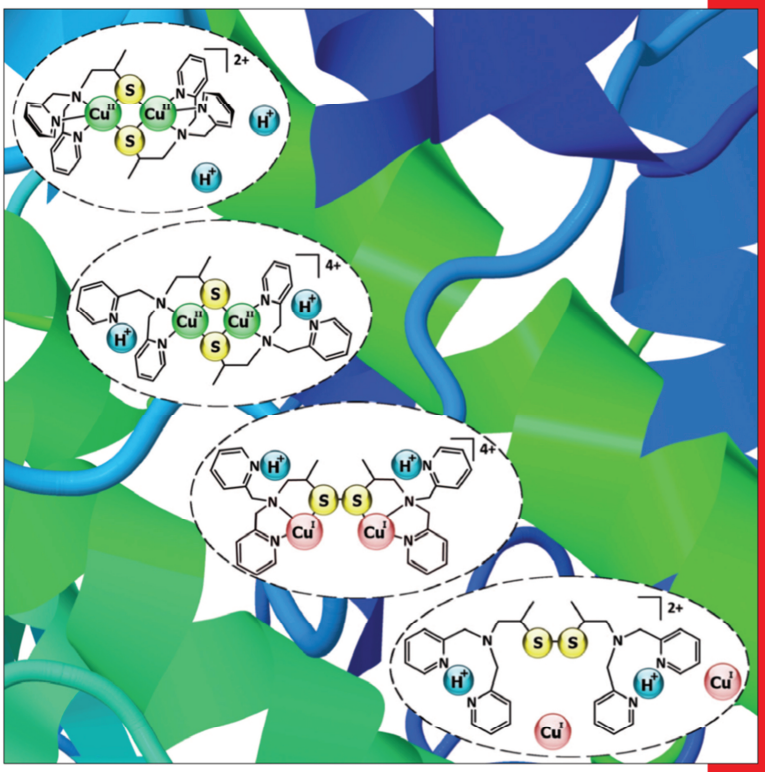

Protonation of a Cu^{II} μ-thiolate complex …

… induces an internal redox reaction by which a Cu^{I} disulfide compound is formed. The dinuclear Cu^{II} μ-thiolate species forms a model for the CuA site, which has been shown to be sensitive to pH changes. In their Full Paper on page 16913 ff., C. Fonseca Guerra, E. Bouwman et al. show, both experimentally and computationally, that, after addition of just one equivalent of acid per copper center, not only does this redox reaction occur, but ligand dissociation takes place as well. The results imply that pH can have a tremendous effect on the coordination environment of the metal center.

Supported by ACES

WILEY-VCH

List of Publications

'The Quest for Cobalt-Free Alkyd Paint Driers'
J. W. de Boer, P. V. Wesenhagen, E. C. M. Wenker, K. Maaijen, F. Gol, H. Gibbs, R. Hage, *Eur. J. Inorg. Chem.* **2013**, *21*, 3581-3591.

'Homogeneous Hydrogenation and Isomerization of 1-Octene Catalyzed by Nickel(II) Complexes with Bidentate Diarylphosphane Ligands'
T. Mooibroek, E. C. M. Wenker, W. Smit, I. Mutikainen, M. Lutz, E. Bouwman, *Inorg. Chem.* **2013**, *52*, 8190-8201.

'Cu^{I} Thiolate Reactivity with Dioxygen: The Formation of Cu^{II} Sulfinate and Cu^{II} Sulfonate Species via a Cu^{II} Thiolate Intermediate'
E. C. M. Ording-Wenker, M. A. Siegler, M. Lutz, E. Bouwman, *Inorg. Chem.* **2013**, *52*, 13113-13122.

'Thermodynamics of the Cu^{II} μ-Thiolate and Cu^{I} Disulfide Equilibrium: A Combined Experimental and Theoretical Study'
E. C. M. Ording-Wenker, M. van der Plas, M. A. Siegler, S. Bonnet, F. M. Bickelhaupt, C. Fonseca Guerra, E. Bouwman, *Inorg. Chem.* **2014**, *53*, 8494-8504.

'Protonation of a Biologically Relevant Cu^{II} μ-Thiolate Complex: Ligand Dissociation or Formation of a Protonated Cu^{I} Disulfide Species?'
E. C. M. Ording-Wenker, M. van der Plas, M. A. Siegler, C. Fonseca Guerra, E. Bouwman, *Chem. Eur. J.* **2014**, *20*, 16913-16921 (Inside Cover).

'Coordination of New Disulfide Ligands to Cu^{I} and Cu^{II}: Does a Cu^{II} μ-Thiolate Complex Form?'
E. C. M. Ording-Wenker, M. A. Siegler, E. Bouwman, *Inorg. Chim. Acta* **2015**, *in press*.

'Catalytic Catechol Oxidation by Copper Complexes: Development of a Structure-Activity Relationship'
E. C. M. Ording-Wenker, M. A. Siegler, M. Lutz, E. Bouwman, *submitted for publication*.

'The Study of Unprecedented Cu^{II} Phenolate Redox Chemistry'
E. C. M. Ording-Wenker, M. J. B. Moester, M. A. Siegler, E. Bouwman, *manuscript in preparation*.

Curriculum Vitae

The author of this thesis was born in Hoorn, the Netherlands, on July 31st in 1986. In 2004, she graduated from the Gymnasium at the Etty Hillesum College in Den Helder. Later that year she started her BSc study Chemistry at Leiden University. She finished her propaedeutic year *cum laude* and was involved in several extracurricular activities during her studies like being a board member of the study association 'Chemisch Dispuut Leiden' and a board member of the PAC symposium foundation. She was also a student member of the Education Committee and the Faculty Council. Her BSc internship was carried out in the field of organic synthesis under supervision of dr. Amar Ghisaidoobe, prof. dr. Gijs van der Marel and prof. dr. Hermen Overkleeft. After finishing her BSc studies she started the research master Chemistry in the track Design and Synthesis at Leiden University. During her masters she did an internship in homogeneous catalysis under supervision of dr. Tiddo Mooibroek and prof. dr. Lies Bouwman as well as an internship at the company Rahu Catalytics B.V. concerning paint-drying under supervision of dr. Ronald Hage. In addition, a summer internship at Occidental College in Los Angeles was done under supervision of prof. Tetsuo Otsuki in the field of organic chemistry. Based on the results obtained during her MSc study she was awarded the Unilever Research Prize in 2010 and the Oxford University Press Achievement in Chemistry Prize of 2010. She obtained her MSc degree in August 2010.

On the 1st of December in 2010, she started her PhD in the Metals in Catalysis, Biomimetics & Inorganic Materials group at Leiden University in the group of prof. dr. Lies Bouwman. During her PhD research she collaborated with dr. Sylvestre Bonnet (Leiden University), for the theoretical chemistry with dr. Célia Fonseca Guerra (VU University Amsterdam) and prof. dr. Matthias Bickelhaupt (VU University Amsterdam) and for Raman measurements with Miriam Moester, MSc (VU University Amsterdam). She has supervised several practical courses, a number of BSc students and two MSc students during the course of the research described in this thesis. Furthermore, she has participated in several courses like the NIOK course 'Catalysis – An Integrated Approach', the HRSMC course 'Molecular Modeling' and the Leiden Graduate school courses 'Time Management', 'Effective Communication', 'Scientific Integrity' and 'Communication in Science'.

The results reported in this thesis were presented at national conferences and meetings and at international conferences:

- Netherlands' Chemistry and Catalysis Conferences NCCC XIII – NCCC XV, 2012-2014 in Noordwijkerhout, 1x oral and 2x poster presentation
- NRSC-C Workshop, 2012 and 2014 in Utrecht, oral presentations
- Reedijk (LIC) Symposium, 2012 in Leiden, poster presentation
- HRSMC symposium, 2013 in Leiden, oral presentation
- Zing Coordination Chemistry Conference, 2013 in Playa del Carmen, Mexico, oral and poster presentation
- European Biological Inorganic Chemistry Conference EuroBIC 12, 2014 in Zürich, Switzerland, poster presentation